QUANTIFYING GLOBAL EXCHANGES OF METHANE AND CARBON MONOXIDE BETWEEN TERRESTRIAL ECOSYSTEMS AND THE ATMOSPHERE USING PROCESS-BASED BIOGEOCHEMISTRY MODELS

by

Licheng Liu

A Dissertation

Submitted to the Faculty of Purdue University

In Partial Fulfillment of the Requirements for the degree of

Doctor of Philosophy

Department of Earth, Atmospheric, and Planetary Sciences

West Lafayette, Indiana

May 2020

THE PURDUE UNIVERSITY GRADUATE SCHOOL
STATEMENT OF COMMITTEE APPROVAL

Dr. Qianlai Zhuang, Chair

Department of Earth, Atmospheric, & Planetary Sciences, and Agronomy

Dr. Robert Nowack

Department of Earth, Atmospheric, & Planetary Sciences

Dr. H. Harshvardhan

Department of Earth, Atmospheric and Planetary Sciences

Dr. Greg Michalski

Department of Earth, Atmospheric, & Planetary Sciences, and Analytical Chemistry

Approved by:

Dr. Daniel J. Cziczo

To my parents, wife and best friends.

ACKNOWLEDGMENTS

This work can be impossible to complete without the help and support from my advisors and colleagues. First of all, I would like to thank my major professor, Dr. Qianlai Zhuang. He provided me the great opportunity to come to USA and study in Ecosystem and Biogeochemical Dynamics Laboratory (EBDL) group. Prof. Zhuang is always the unshakeable light in my journey of research career. During a nearly six-year period time of pursuing my PhD degree at EAPS department, he has been always showing great patience and wisdom on guidance, assistance and encouragement. It is my great honor studying from and working under him. I would also like to express my sincere gratitude to Prof. Robert Nowack, Prof. H. Harshvardhan, and Prof. Greg Michalski for serving on my committee. They have followed my research progress seriously and has given me many invaluable comments.

Moreover, I want to thank everyone in EBDL group, including those graduated and those still striving for their degrees. They have provided me countless help on not only my research projects but also the daily life. I could not survive without their helps living in a different country. They also have provided the opportunities to enrich the daily life by gathering parties and holding exercises. Every minute with them will be shining all the time in my whole life.

Finally, I would like to express my sincere thankfulness to my family. My parents are living abroad in China. They have been supporting me all the time and reducing my homesick by contacting me every week. Especially, I would like to appreciate my loved wife, who has paused his own career in China and come to the US to take care of me. She helped me focusing on my research work without bothering by other daily issues.

TABLE OF CONTENTS

LIST OF TABLES 8
LIST OF FIGURES 10
ABSTRACT 14
CHAPTER 1. INTRODUCTION 17
CHAPTER 2. GLOBAL SOIL CONSUMPTION OF ATMOSPHERIC CARBON MONOXIDE: AN ANALYSIS USING A PROCESS-BASED BIOGEOCHEMISTRY MODEL 23
2.1 Abstract 23
2.2 Introduction 24
2.3 Method 27
2.3.1 Overview 27
2.3.2 Carbon Monoxide Dynamics Module (CODM) 28
2.3.3 Model Parameterization and Extrapolation 31
2.3.4 Data Organization 33
2.3.5 Model Experiment Design 34
2.4 Results 35
2.4.1 Site Evaluation 35
2.4.2 Global Soil CO Dynamics During 2000-2013 35
2.4.3 Global Soil CO Dynamics During 1901-2100 36
2.4.4 Sensitivity test 37
2.5 Discussion 37
2.5.1 Comparison with Other Studies 37
2.5.2 Major Controls to Soil CO Dynamics 38
2.5.3 Model Uncertainties and Limitations 40
2.6 Conclusions 42
CHAPTER 3. UNCERTAINTY QUANTIFICATION OF GLOBAL NET METHANE EMISSIONS FROM TERRESTRIAL ECOSYSTEMS USING A MECHANISTICALLY-BASED BIOGEOCHEMISTRY MODEL 64

3.1 Abstract 64
3.2 Introduction 65
3.3 Method 68
3.3.1 Overview 68
3.3.2 Model Modification 69
3.3.3 Model Parameterization and Extrapolation 71
3.3.4 Data Organization 72
3.3.5 Model Experimental Design 73
3.4 Results 74
3.4.1 Site Calibration and Evaluation 74
3.4.2 Sensitivity analysis 75
3.4.3 Global emission uncertainty due to uncertain parameters 75
3.4.4 Global emission uncertainty due to uncertain wetland type distribution 76
3.4.5 Uncertainty due to uncertain forcing data 76
3.4.6 Global land methane budget estimates during 1950-2012 77
3.5 Discussion 78
3.5.1 Major controls to the global land methane budget 78
3.5.2 Model Uncertainty Sources 79
3.5.3 Comparison with Other Studies 80
3.6 Conclusions 82
CHAPTER 4. INVENTORYING GLOBAL WETLAND METHANE EMISSIONS USING IN SITU DATA AND AN ARTIFICIAL NEURAL NETWORK APPROACH 109
4.1 Abstract 109
4.2 Introduction 110
4.3 Method 113
4.3.1 Overview 113
4.3.2 Data Organization 113
4.3.3 Neural Network Development 115
4.3.4 Regional Extrapolation 116
4.3.5 Sensitivity and Uncertainty Analysis 118
4.4 Results 119

4.4.1 Trained Artificial Neural Networks 119
4.4.2 Temporal and Spatial Variations of Regional CH_4 Dynamics 119
4.4.3 Sensitivity and Uncertainty of Regional CH_4 Estimates 121
4.5 Discussion 122
4.5.1 Effects of In Situ Data Availability and Wetland Distribution Data on the Inventory 122
4.5.2 Effects of Predictor Variables on the Inventory 124
4.6 Conclusions 126
CHAPTER 5. LARGE METHANE EMISSIONS FROM PALM TREE STEMS IN AMAZONIAN BASIN 143
5.1 Abstract 143
5.2 Introduction 143
5.3 Method 146
5.3.1 Overview 146
5.3.2 2D Diffusion Model 146
5.3.3 Model Parameterization and Extrapolation 147
5.3.4 Data Organization 148
5.4 Results 149
5.4.1 Methane emissions from single palm tree stem 149
5.4.2 Palm tree stem methane emissions from large regions 149
5.5 Discussion 150
5.5.1 Comparison with previous methane emission estimates 150
5.5.2 Uncertainties and limitations 151
5.6 Conclusions 152
CHAPTER 6. SUMMARY AND FUTURE WORK 158
6.1 Conclusions 158
6.2 Limitations and Future Work 159
APPENDIX A. SUPPORTING INFORMATION FOR CHAPTER 3 162
APPENDIX B. SUPPORTING INFORMATION FOR CHAPTER 5 169
REFERENCES 177
VITA 195

LIST OF TABLES

Table 2.1. Model parameterization sites for the thermal and hydrology modules (site No. 1-4) and for the CODM module (site No. 5-13) 44

Table 2.2. Ecosystem-specific parameters in the CODM module[a] 45

Table 2.3. Regional soil CO consumption, net flux and production (Tg CO yr-1) during 2000-2013 46

Table 2.4. Annual total soil CO consumption, net flux and production in different ecosystems during 2000-2013 (E1) and mean CO deposition velocity in different ecosystems during 1901-2013 (E2) 47

Table 2.5. Sensitivity of the global CO consumption, net flux and production (Tg CO yr^{-1}) to the changes in atmospheric CO, soil organic carbon (SOC), precipitation (Prec) and air temperature (AT) 48

Table 2.6. Correlation coefficients between forcing variables (precipitation (Prec), air temperature (Tair), soil organic carbon (SOC), soil temperature (Tsoil), soil moisture (Msoil) and atmospheric CO (CO air)) and absolute values of consumption, production and net flux for different regions and the globe 49

Table 3.1. Parameters related to methane production and oxidation process for wetlands in TEM 84

Table 3.2. Calibration (No.1-15) and validation sites (No.16-29) list 85

Table 3.3. Optimized parameters for different ecosystem types. 88

Table 3.4. Model evaluations with observations. Observation points are acceptable observed flux data at each site. RMSE is root mean square error between simulation and observation (mg CH_4 m^{-2} day^{-1}). R^2 is the coefficient of determination. P value is the probability value based on a two-sided t-test. T-value is the t statistic value. Regional results from site 28 and 29 are discussed in Section 3.4.1. 90

Table 3.5. Model sensitivity test during 2000-2012 using monthly CRU data and transient wetland fraction data. 91

Table 3.6. Correlations between simulated methane fluxes and environmental factors during 2000-2012 using monthly CRU data and transient wetland fraction data. Factors include net primary production (NPP), precipitation (PREP), air temperature (TAIR), wetland inundation area fraction (IN-AREA), soil temperature (SOILT) and volumetric soil moisture (VSOIL). 92

Table 3.7. Parameter uncertainties in different wetland types 93

Table 3.8. Simulated methane emission (Tg CH_4 $region^{-1}$ yr^{-1}) uncertainties due to uncertain parameters and wetland type distribution expressed with standard deviations (STD) in different regions. 94

Table 3.9. Modeled methane fluxes (Tg CH_4 yr^{-1}) uncertainties due to different forcing data 95

Table 3.10. Modeled methane fluxes (Tg CH_4 yr^{-1}) during 1950-2012 using CRU data 96

Table 3.11. Historical simulations compared with previous global wetland emission estimates..97

Table 4.1. Description of the site used in this study 127

Table 4.2. Description of the parameters in the ANN model 131

Table 4.3. Historical and future CH_4 emissions (Tg CH_4 yr^{-1}) estimated with the ANN model. The reference for other studies is Saunois et al. (2019).....132

Table 5.1. Estimated palm swamp area, methane emissions per tree, trees per unit area and total emissions from the study regions. For South America palm swamp, we assume soil methane concentrations are from 200ppm to 400ppm. For Pastaza-Marañon foreland basin in Peru (PMFB), we used soil methane concentration product from TEM model. PMFB methane emissions are estimated using palm swamp classification from remote sensing data of Draper (2014).....153

LIST OF FIGURES

Figure 2.1. The model framework includes a carbon and nitrogen dynamics module (CNDM), a soil thermal module (STM) from Terrestrial Ecosystem Model (TEM) 5.0 (Zhuang et al., 2001, 2003), a hydrological module (HM) based on a Land Surface Module (Bonan, 1996; Zhuang et al., 2004), and a carbon monoxide dynamics module (CODM). The detailed structure of CODM includes land surface CO concentration as top boundary and thirty 1 cm thick layers (totally 30 cm) where consumption and production take place. 50

Figure 2.2. Evaluation of thermal and hydrology module at four sites: (a) Boreal Evergreen Needle Leaf Forests, (b) Temperate Deciduous Broadleaf Forests. (1) shows the soil temperature comparison between the model simulations (gray line) and observations (black line) and (2) shows the soil moisture comparison between the model simulations (gray line) and observations (black line). Specifically, the volumetric soil moisture is converted from the water content reflectometry (WCR) probe output period using an empirical calibration function of Bourgeau-Chavez et al. (2012) for 5cm-30cm layer. Some of them resulted in calculations of values greater than 100% VSM in Nakai et al. (2013) study. Our model estimated high VSM (close to 80%) is due to top 10 cm moss in the model which has a saturation VSM of 0.8 51

Figure 2.3. Parameter ensemble experiment results: Each parameter has 50 calibrated values generated from running SCE-UA-R 50 times independently. Parameters are normalized to their largest potential values described in Table 2. (a1) and (a2) are temperate coniferous forest normalized parameter distribution boxplots and CO flux comparisons between the model simulations (solid line, using mean value of parameters) and observations (green diamond, red lines represent error bar, site No.8), respectively. For each box, line top, box top, horizontal line inside box, box bottom and line bottom represent maximum, third quartile, median, first quartile and minimum of 50 parameter values. Red dot represents the mean value of 50 parameter values. (b1) and (b2) are plots for temperate deciduous forest (site No.11).....53

Figure 2.4. Historical global land surface (excluding Antarctic area and ocean area) mean climate, and simulated global mean soil moisture, soil temperature and SOC for the period 1901-2013..55

Figure 2.5. CO surface concentration data from MOPITT satellite (ppbv): (a) the global mean CO surface concentrations from MOPITT during 2000-2013; (b) the CO annual surface concentrations from both MOPITT and empirical functions (Potter et al., 1996).....56

Figure 2.6. Global land surface (excluding Antarctic area and ocean area) mean climate from the RCP2.6, RCP4.5 and RCP8.5 data sets and simulated mean soil temperature, moisture and SOC: (a)-(g) are land surface air temperature (℃), soil temperature (°C), precipitation (mm), soil moisture (%), surface water vapor pressure (hpa), cloud fraction (%), and SOC (mg m^{-2}), respectively. 57

Figure 2.7. Global mean soil CO consumption, production and net flux: (a) the annual time series during 2000-2013and (b) the latitudinal distribution during 2000-2013. 58

Figure 2.8. Global annual mean soil CO fluxes (mg CO m^{-2} yr^{-1}) during 2000-2013 using the MOPITT CO atmospheric surface concentration data 59

Figure 2.9. Global mean annual time series of CO deposition velocity (mm s^{-1}) using constant in time and spatially distributed CO concentration data during 1901-2013 (left side of the dot line) and under the future climate scenarios RCP2.6, RCP4.5 and RCP8.5 during 2014-2100 (right side of the dot line) 60

Figure 2.10. Global annual mean CO deposition velocity using constant in time and spatially distributed CO concentration data (mm s^{-1}) a) during 1901-2013 and b), c), d) under the future climate scenarios RCP2.6, RCP4.5 and RCP8.5 during 2014-2100, respectively 61

Figure 2.11. Global mean monthly time series of the MOPITT surface atmospheric CO concentration (ppbv) and soil CO consumption from model simulations E1 (Tg CO mon^{-1}).....62

Figure 2.12. Daily mean vertical soil CO concentration profiles of top 30 cm. In the soil (depth < 0 cm), black diamonds represent the soil CO concentration (mg CO m^{-3}). Above the surface (depth>=0 cm), black diamonds represent the atmospheric CO concentration. a), b), c), d) and e) are the results from the same day when soils are a net sink of CO, but using different layer thickness (dz = 10 cm, 2 cm, 1 cm, 0.1 cm and 0.01 cm, respectively); f) is the result from the day when soils are a net source of CO, with dz = 1 cm. 63

Figure 3.1. Comparison between observed and simulated methane fluxes at calibration sites (upper panel) and evaluation sites (lower panel). Diamond symbol represents the boreal data. Triangle symbol represents the temperate data. Square symbols represent the tropical data. Dot line represents that the observed data equals the simulated data. Red solid line represents the linear regression line between all observed and simulated data. 98

Figure 3.2. Climate forcing data used in this study. Figure a)-d) represent the climate data from CRU (solid line), ECMWF (dash line) and NCEP (dash-dot line), respectively, during 2000-2012 99

Figure 3.3. Wetland distribution data used in this study 101

Figure 3.4. Parameter uncertainty analysis during 2000-2012: a) global monthly methane flux uncertainties, the black line represents the baseline results and the gray lines represent the 100 simulation results using parameters which were randomly chosen in optimized ranges; b) global annual methane flux uncertainties, the black line represents the baseline. For each box, line top, box top, horizontal line inside box, box bottom and line bottom represent maximum, third quartile, median, first quartile and minimum of 100 simulations; and c) the latitude distribution of global annual mean methane emissions, the black line represents the baseline results and the gray lines represents the 100 parameter uncertainty simulations. 102

Figure 3.5. Wetland type uncertainty analysis during 2000-2012: a) global monthly methane flux uncertainties, the black line represents the baseline results and the gray lines represent the 770 simulation results using different wetland distributions; b) global annual methane flux uncertainties, the black line represents the baseline. For each box, line top, box top, horizontal line inside box, box bottom and line bottom represent maximum, third quartile, median, first quartile and minimum of 770 simulation results, respectively; and c) the latitude distribution of global annual mean methane emission, the black line represents the baseline results and the gray lines represents the results of the 770 wetland type uncertainty simulations. 103

Figure 3.6. Forcing data uncertainty test results during 2000-2012: Upper panel represents global monthly methane flux uncertainties. Different colors and line styles represent different combinations of forcing data; lower panel represents global annual methane flux uncertainties. Different colors and line styles represent different combinations of forcing data. 104

Figure 3.7. Global distribution of annual wetland methane emissions during 2000-2012 when using different forcing data: a) the baseline using static wetland map and CRU climate data; b)-f) shows the differences (new flux value – baseline flux value) when using different wetland distribution data or using different climate data. Red regions represent emission increasing while blue regions represent emission decreasing.....105

Figure 3.8. Global distribution of annual upland methane consumption during 2000-2012 when using different forcing data: a) shows the baseline using static wetland map and CRU climate data; b)-f) show the difference (new flux value – baseline flux value) when using different wetland distribution data or using different climate data. Red regions represent consumption decreasing while blue regions represent consumption increasing. 106

Figure 3.9. Global simulation during 1950-2012 using CRU data and transient wetland fraction data: a) global distribution of annual wetland methane emissions; b) global distribution of annual upland methane consumption; and c) latitude distribution of methane emission, consumption and net fluxes. 107

Figure 3.10. Historical estimates and comparisons: Upper panel represents annual wetland methane emissions (black) and net fluxes (blue) during El Niño (yellow strip) and La Nina (blue) event periods; lower panel represents annual upland methane consumption (black) during El Niño (yellow strip) and La Nina (blue) event periods 108

Figure 4.1. Comparisons between the measured and modeled monthly CH_4 emissions at all sites. Upper panel: The ANN models were constructed based on the training dataset; and lower panel: the validation dataset was used to test the performance of the model. Diamond symbol represents the boreal data. Triangle symbol represents the temperate data. Square symbols represent the tropical data. The dashed line is the 1:1 line, and the solid red line is the fitted line. 133

Figure 4.2. ANN model estimated global CH_4 wetland emissions with the transient wetland inundation map during 2000-2012. Upper panel is the global wetland mean fluxes distribution; Lower panel is the global annual wetland emission. 134

Figure 4.3. ANN model estimated global CH_4 wetland emissions with the static wetland inundation map during 1979-2018. Upper panel is the global wetland mean fluxes distribution; Lower panel is the global annual wetland emission 135

Figure 4.4. ANN model future predictions of global mean wetland CH_4 emission distribution during 2080-2099 comparing with historical estimates during 2000-2018 (positive value means increase). (a)-(d) presented results using future climate forcing of RCP2.6, 4.5, 6.0 and 8.5, respectively 136

Figure 4.5. ANN model future predictions of annual wetland emissions from different regions. Green dots are interannual variation, red lines are fitted lines between years and blue shadows are uncertainties from four different GCMs in each RCP scenario 137

Figure 4.6. Sensitivity of the ANN model to changes in precipitation (PREC), surface air temperature (TAIR), surface solar radiation (SOLAR), elevation (ElEV), soil bulk density (BULK), soil clay content (CLPC), soil carbon/nitrogen ratio (CNRT), soil organic carbon (ORGC), soil pH (PHAQ), soil sand content (SDTO) and soil silt content (STPC). The values are for the period 2000-2012 and different regions. The changes are calculated based on the baseline simulation using the unchanged regional input data 138

Figure 4.7. Uncertainties of the estimated wetland CH_4 emissions from the different region with 100 ANN models. Probability distribution (red histograms), fitted Gaussian distribution line (blue lines), the center of the distribution (Center), the 95% confidence intervals (L_95%: lower boundary of the distribution; U_95%: upper boundary of the distribution) and the standard deviation (STD) of mean annual CH_4 emissions during year 2000-2012 are presented.....140

Figure 4.8. Uncertainties of the estimated annual wetland CH_4 emissions from the different region with 100 ANN models. Interannual variations of annual CH_4 emissions (black dots, fitted with red lines) and the 95% confidence intervals (blue error bars) from 2000 to 2012 are presented 141

Figure 4.9. Uncertainties of the estimated wetland CH_4 emission seasonality from the different region with 100 ANN models. Seasonality of wetland CH_4 emissions (black dots, fitted with red lines) and the 95% confidence intervals (blue error bars) from 2000 to 2012 are presented 142

Figure 5.1. Parameter posteriors of (a)soil methane concentration C_soil, (b) diffusivity coefficients in x direction (D_x), and (c) diffusivity coefficients in y direction (D_y), using the PySMC method (Bilionis, 2015). Y-axis represents number of optimized C_soil, D_x or D_y located in a specific range of parameter values, which showed in X-axis; (d) is comparison between simulations (solid lines) and observations (blue "x"), and blue area is the standard deviation of the simulations. There are two modes of parameter posteriors: a and b mode showed in figure d. Each mode represents the average value of a group of parameter posteriors, and detailed values showed in Table S3. 154

Figure 5.2. Ecosystem classification in PMFB in Peru. It is similar to the figure 5.4 in Draper (2015). Red areas represent distributions of palm swamp at a resolution of 90mx90m. 155

Figure 5.3. Mean methane flux distribution from palm tree stems in PMFB during 2000-2010: (a) the methane emission from palm swamp area and (b) the methane emission distribution from pole forest area. 156

Figure 5.4. Monthly methane emissions from palm tree stems in PMFB from 2000 to 2010. Solid lines and blue shadow represent the temporal variations and ranges of methane emission from palm swamp in PMFB, respectively. Dash lines and green shadow represent the temporal variations and ranges of methane emissions from pole forest in PMFB, respectively. 157

ABSTRACT

Methane (CH_4) is the second most powerful greenhouse gas (GHG) behind carbon dioxide (CO_2), and is able to trap a large amount of long-wave radiation, leading to surface warming. Carbon monoxide (CO) plays an important role in controlling the oxidizing capacity of the atmosphere by reacting with OH radicals that affect atmospheric CH_4 dynamics. Terrestrial ecosystems play an important role in determining the amount of these gases into the atmosphere. However, global quantifications of CH_4 emissions from wetlands and its sinks from uplands, and CO exchanges between land and the atmosphere are still fraught with large uncertainties, presenting a big challenge to interpret complex atmospheric CH_4 dynamics in recent decades. In this dissertation, I apply modeling approaches to estimate the global CH_4 and CO exchanges between land ecosystems and the atmosphere and analyze how they respond to contemporary and future climate change.

Firstly, I develop a process-based biogeochemistry model embedded in Terrestrial Ecosystem Model (TEM) to quantify the CO exchange between soils and the atmosphere at the global scale (Chapter 2). Parameterizations were conducted by using the CO *in situ* data for eleven representative ecosystem types. The model is then extrapolated to global terrestrial ecosystems. Globally soils act as a sink of atmospheric CO. Areas near the equator, Eastern US, Europe and eastern Asia will be the largest sink regions due to their optimum soil moisture and high temperature. The annual global soil net flux of atmospheric CO is primarily controlled by air temperature, soil temperature, SOC and atmospheric CO concentrations, while its monthly variation is mainly determined by air temperature, precipitation, soil temperature and soil moisture.

Secondly, to better quantify the global CH_4 emissions from wetlands and their uncertainties, I revise, parameterize and verify a process-based biogeochemical model for methane for various wetland ecosystems (Chapter 3). The model is then extrapolated to the global scale to quantify the uncertainty induced from four different types of uncertainty sources including parameterization, wetland type distribution, wetland area distribution and meteorological input. Spatially, the northeast US and Amazon are two hotspots of CH_4 emissions, while consumption hotspots are in the eastern US and eastern China. The relationships between both wetland emissions and upland consumption and El Niño and La Niña events are analyzed. This study highlights the need for more in situ methane flux data, more accurate wetland type and area distribution information to better constrain the model uncertainty.

Thirdly, to further constrain the global wetland CH_4 emissions, I develop a predictive model of CH_4 emissions using an artificial neural network (ANN) approach and available field observations of CH_4 fluxes (Chapter 4). Eleven explanatory variables including three transient climate variables (precipitation, air temperature and solar radiation) and eight static soil property variables are considered in developing the ANN models. The models are then extrapolated to the global scale to estimate monthly CH_4 emissions from 1979 to 2099. Significant interannual and seasonal variations of wetland CH_4 emissions exist in the past four decades, and the emissions in this period are most sensitive to variations in solar radiation and air temperature. This study reduced the uncertainty in global CH_4 emissions from wetlands and called for better characterizing variations of wetland areas and water table position and more long-term observations of CH_4 fluxes in tropical regions.

Finally, in order to study a new pathway of CH_4 emissions from palm tree stem, I develop a two-dimensional diffusion model. The model is optimized using field data of methane emissions

from palm tree stems (Chapter 5). The model is then extrapolated to Pastaza-Marañón foreland basin (PMFB) in Peru by using a process-based biogeochemical model. To our knowledge, this is among the first efforts to quantify regional CH_4 emissions through this pathway. The estimates can be improved by considering the effects of changes in temperature, precipitation and radiation and using long-period continuous flux observations. Regional and global estimates of CH_4 emissions through this pathway can be further constrained using more accurate palm swamp classification and spatial distribution data of palm trees at the global scale.

CHAPTER 1. INTRODUCTION

Methane (CH_4) is the second most powerful greenhouse gas behind CO_2 and has contributed to about 20% of the observed warming since pre-industrial times (Ciais et al., 2013). According to the latest Intergovernmental Panel on Climate Change report (IPCC), the global warming potential (GWP) of CH_4 is 28, about 25 times that of CO_2 on a 100-year time period (IPCC AR5, Myhre et al., 2013). Atmospheric CH_4 concentrations have risen from pre-industrial levels of 715 parts per billion (ppb) since the 1800s (Etheridge et al., 1998; MacFarling Meure et al., 2006) to over 1800 ppb at the present. The increase of atmospheric CH_4 concentrations has contributed ~23% (~0.62 Wm-2) to the additional radiative forcing accumulated in the lower atmosphere since 1750 (Etminan, et al., 2016). The growth rate of atmospheric CH_4 has decreased, however, from approximately 13 ppb yr^{-1} during the early 1980s to near zero between 1999 and 2006. Since 2007, the growth rate of atmospheric CH_4 has risen again (Dlugokencky et al., 2009; Nisbet, Dlugokencky, & Bousquet, 2014; Saunois et al., 2016; Schaefer et al., 2016; Zhang et al., 2018). The climatic sensitivity of biogenic CH_4 sources has significantly influenced the inter-annual variability of atmospheric CH_4 and the global wetland contributes 60–80% of natural CH_4 emissions (Quiquet et al., 2015; Hopcroft et al., 2017) and this large role is likely to persist into the future (Zhang et al., 2017). Therefore, it is important to improve existing CH_4 emission quantifications to better understand the role of global CH_4 cycling in the global climate system (Zhuang et al., 2004; Chen et al., 2013; Kirschke et al., 2013; Nisbet et al., 2014; Zhu et al., 2014).

Carbon monoxide (CO) plays an important role in controlling the oxidizing capacity of the atmosphere by reacting with OH radicals and can directly and indirectly influence the fate of critical greenhouse gases such as CH_4 and ozone (O_3) (Logan et al., 1981; Crutzen, 1987; Khalil

& Rasmussen, 1990; Prather et al., 1995; Prather & Ehhalt, 2001; Tan and Zhuang, 2012). Although CO itself absorbs only a limited amount of infrared radiation from the Earth, the cumulative indirect radiative forcing of CO may be even larger than that of the third powerful greenhouse gas, nitrous oxide (N_2O, Myhre et al., 2013). Current estimates of global CO emissions from both anthropogenic and natural sources range from 1550 to 2900 Tg CO yr^{-1}, which are mainly from anthropogenic and natural direct emissions and from the oxidation of methane and other Volatile Organic Compounds (VOC) (Prather et al., 1995; Khalil et al., 1999; Bergamaschi et al., 2000; Prather & Ehhalt, 2001, Stein et al., 2014). Chemical consumption of CO by atmospheric OH and the biological consumption of CO by soil microbes are two major sinks of the atmospheric CO (Conrad, 1988; Lu & Khalil, 1993; Yonemura et al., 2000; Whalen & Reeburgh, 2001). Annually, 10-25% of total earth surface CO emissions were consumed by soils (Sanhueza et al., 1998; King, 1999a; Chan & Steudler, 2006). Thus, the better quantification of soil CO consumption could improve the atmospheric CO and OH estimate and further improve the quantification of atmospheric CH_4.

To date, three approaches have been used in estimating CH_4 and CO exchanges between land and the atmosphere across different scales over the last few decades: 1) a bottom-up extrapolation approach by using simple empirical or statistical models and actual gas flux measurements; 2) a bottom-up approach with process-based models parameterized using flux measurements to quantify CH_4 and CO dynamics, and 3) a top-down approach, which uses atmospheric inverse models to estimate the distribution of CH_4 and CO sources and sinks by incorporating atmospheric observations, an atmospheric transport model and prior estimates of source distributions and magnitudes (Arneth et al., 2010; Anderson et al., 2010; Kirschke et al., 2013; Zhu et al., 2014; Saunois, et al., 2019). Although top-down approach is widely thought to

be more accurate than bottom-up approach, the current top-down approach may inadvertently include some incomplete observations and error amplifications during inverse modelling processes (Chen and Prinn, 2005; Stevenson et al., 2006; Ciais et al., 2013). Process-based models can be used to improve CH_4 and CO considering the effects of complex interactions between soil, vegetation, and hydrology on production and consumption processes.

Specifically, for CH_4 estimation, although great efforts have been made on estimating global natural wetland CH_4 emissions in all three kinds of approaches, current quantifications still have large uncertainties. The Global Carbon Project (GCP) and the Wetland and Wetland CH_4 Inter-comparison of Models Project (WETCHIMP) estimated the global CH_4 emission from natural wetlands, ranging from 102 to 284 Tg CH_4 yr^{-1} during 2000-2017 (Kirschke et al., 2013; Melton et al., 2013; Saunois et al., 2016; Saunois et al., 2019). The uncertainty in these estimates could result from many sources including model structures, assumptions, parameterization, and choice of forcing data. Among these uncertainty sources, the paucity of CH_4 flux measurements could be an important factor. The lack of sufficient measurements of CH_4 fluxes and related environmental factors may limit the understanding of ecological processes in specific wetland ecosystems, the model assumptions, and the parameterization of models. In addition to the large uncertainty present in wetland CH_4 emissions, the sensitivity of CH_4 fluxes to environmental controls is not well understood, which also limits explicit representations of many mechanistic processes in models. For instant, undisturbed tropical wetlands emit 85-184 Tg of CH_4 each year, accounting for two thirds of the global emissions from wetlands (Sjögersten, 2014). Recent studies indicate that plant stems are a particularly efficient means for releasing CH_4 from wetland soils because the pathway bypasses highly active populations of methanotrophic bacteria situated at the oxic-anoxic interface in the subsurface (Pangala et al., 2013, 2017). However, due to the lack of CH_4 flux observations

and understanding of palm tree stem CH_4 emission process, tropical region estimates of CH_4 emissions are challenging (Sjögersten, 2014). During the past decades, although most of the field measurements of CH_4 fluxes were made in high latitude regions, some measurements in temperate or tropical region started to accumulate. Currently, the *in situ* CH_4 flux data are accumulating and the coordination networks for ecosystem-scale CH_4 measurements at the global scale have been founded (e.g. FLUXNET, Knox et al., 2019). In addition, Artificial neural networks (ANN), one kind of bottom-up approaches, are among the most intelligent statistical methods and are widely used for a range of applications spanning across various scientific fields including Earth ecosystem modeling. ANNs have proved as robust surrogate models with flexible mathematical structure and is capable of identifying complex nonlinear behavior between model input and output (Delon et al., 2007; Dupont et al., 2008; Zhu et al., 2013; Liu et al., 2016; Bomers et al., 2019). With the CH_4 flux data and new techniques, it is the time to improve the estimate of wetland CH_4 emissions at the global scale.

For soil CO dynamics, all existing estimates have large uncertainties and range from -640 to -16 Tg CO yr^{-1} (negative values represent the uptake from the atmosphere to soils, Sanhueza et al., 1998; King, 1999; Bergamaschi et al., 2000). Similarly, the estimates of CO dry deposition velocities also have large uncertainties and range from 0 to 4.0 mm s^{-1}, here positive values represent deposition to soils (King, 1999a; Castellanos et al., 2011). Most top-down atmospheric models applied a dry deposition scheme based on the resistance model of Wesely (1989). Only a few models (MOZART-4, Emmons et al., 2010; CAM-chem, Lamarque et al., 2012) have extended their dry deposition schemes with a parameterization for CO and H_2 uptake through oxidation by soil microbes, following the work of Sanderson et al. (2003), which was based on extensive measurements from Yonemura et al. (2000). Current bottom-up CO modeling

approaches are mostly based on a limited number of CO *in situ* observations or laboratory studies to quantify regional and global soil consumption (Potter et al., 1996; Sanhueza et al., 1998; Khalil et al., 1999; King, 1999a; Bergamaschi et al., 2000; Prather & Ehhalt, 2001). To our knowledge, no detailed process-based model of soil-atmospheric exchange of CO has been published in the recent 15 years. The first study to report long-term and continuous field measurements of CO flux over grasslands using a micrometeorological eddy covariance (EC) method is Pihlatie et al. (2016). Laboratory studies on soil CO production and consumption processes have published in recent years, indicating that CO can be consumed by soil via microbial activities (Whalen and Reeburgh, 2001; King and Weber, 2007), and can be produced from soils by abiotic processes such as thermal- and photo-degradation of organic matter or plant materials (Conrad and Seiler, 1985b; Tarr et al., 1995; Schade et al., 1999; Derendorp et al., 2011; Lee et al., 2012; van Asperen et al., 2015; Fraser et al., 2015)), except for a few cases of anaerobic formation. CO *in situ* data accumulation and better understanding of consumption and production processes present the possibility to develop a better process-based bottom-up biogeochemical model and use it to better estimate global CO soil dynamics.

In this dissertation, I applied modeling approaches to assess global CH_4 and CO exchanges between land and the atmosphere under both contemporary and future climate conditions. I first developed a CO dynamics module (CODM) embedded in a process-based biogeochemistry model, the Terrestrial Ecosystem Model (TEM) to investigate global soil CO dynamics (Chapter 2). Then, I used existing flux data at multiple sites to improve our revised methane biogeochemistry model TEM and extrapolated it to global scale to quantify CH_4 emissions from wetland and consumptions into upland and locate their uncertainty sources (Chapter 3). Moreover, I developed and used a data-driven ANN approach to quantify wetland CH_4 emissions from wetlands to further constrain

the uncertainty (Chapter 4). Finally, I developed and used a two-dimensional (2D) diffusion model by considering horizontal and vertical transport of gases inside tree stem to quantify CH_4 fluxes from palm tree stem in Amazon Basin (Chapter 5).

CHAPTER 2. GLOBAL SOIL CONSUMPTION OF ATMOSPHERIC CARBON MONOXIDE: AN ANALYSIS USING A PROCESS-BASED BIOGEOCHEMISTRY MODEL

2.1 Abstract

Carbon monoxide (CO) plays an important role in controlling the oxidizing capacity of the atmosphere by reacting with OH radicals that affect atmospheric methane (CH_4) dynamics. We develop a process-based biogeochemistry model to quantify the CO exchange between soils and the atmosphere with a 5-minute internal time step at the global scale. The model is parameterized using the CO flux data from the field and laboratory experiments for eleven representative ecosystem types. The model is then extrapolated to global terrestrial ecosystems using monthly climate forcing data. Global soil gross consumption, gross production, and net flux of the atmospheric CO are estimated to be from -197 to -180, 34 to 36, and -163 to -145 Tg CO yr^{-1} (1Tg = 1012 g), respectively, when the model is driven with satellite-based atmospheric CO concentration data during 2000-2013. Tropical evergreen forest, savanna and deciduous forest areas are the largest sinks at 123 Tg CO yr^{-1}. The soil CO gross consumption is sensitive to air temperature and atmospheric CO concentration while the gross production is sensitive to soil organic carbon (SOC) stock and air temperature. By assuming that the spatially-distributed atmospheric CO concentrations (~128 ppbv) are not changing over time, the global mean CO net deposition velocity is estimated to be 0.16-0.19 mm s-1 during the 20th century. Under the future climate scenarios, the CO deposition velocity will increase at a rate of 0.0002-0.0013 mm s-1 yr^{-1} during 2014-2100, reaching 0.20-0.30 mm s^{-1} by the end of the 21st century, primarily due to the increasing temperature. Areas near the equator, Eastern US, Europe and eastern Asia will be the largest sinks due to optimum soil moisture and high temperature. The annual global soil net flux

of atmospheric CO is primarily controlled by air temperature, soil temperature, SOC and atmospheric CO concentrations, while its monthly variation is mainly determined by air temperature, precipitation, soil temperature and soil moisture.

2.2 Introduction

Carbon monoxide (CO) plays an important role in controlling the oxidizing capacity of the atmosphere by reacting with OH radicals (Logan et al., 1981; Crutzen, 1987; Khalil & Rasmussen, 1990; Prather et al., 1995; Prather & Ehhalt, 2001). CO in the atmosphere can directly and indirectly influence the fate of critical greenhouse gases such as methane (CH_4) and ozone (O_3) (Tan and Zhuang, 2012). Although CO itself absorbs only a limited amount of infrared radiation from the Earth, the cumulative indirect radiative forcing of CO may be even larger than that of the third powerful greenhouse gas, nitrous oxide (N_2O, Myhre et al., 2013). Current estimates of global CO emissions from both anthropogenic and natural sources range from 1550 to 2900 Tg CO yr^{-1}, which are mainly from anthropogenic and natural direct emissions and from the oxidation of methane and other Volatile Organic Compounds (VOC) (Prather et al., 1995; Khalil et al., 1999; Bergamaschi et al., 2000; Prather & Ehhalt, 2001, Stein et al., 2014). Chemical consumption of CO by atmospheric OH and the biological consumption of CO by soil microbes are two major sinks of the atmospheric CO (Conrad, 1988; Lu & Khalil, 1993; Yonemura et al., 2000; Whalen & Reeburgh, 2001).

Soils are globally considered as a major sink for CO due to microbial activities (Whalen and Reeburgh, 2001; King and Weber, 2007). A diverse group of soil microbes including carboxydotrophs, methanotrophs and nitrifiers are capable of oxidizing CO (King and Weber, 2007). Annually, 10-25% of total earth surface CO emissions were consumed by soils (Sanhueza

et al., 1998; King, 1999a; Chan & Steudler, 2006). Potter et al. (1996) reported the global soil consumption to be from -50 to -16 Tg CO yr^{-1} (negative values represent the uptake from the atmosphere to soil), by using a single-box model over the upper 5 cm of soils. All existing estimates have large uncertainties and range from -640 to -16 Tg CO yr^{-1} (Sanhueza et al., 1998; King, 1999; Bergamaschi et al., 2000). Similarly, the estimates of CO dry deposition velocities also have large uncertainties and range from 0 to 4.0 mm s^{-1}, here positive values represent deposition to soils (King, 1999a; Castellanos et al., 2011). Soils also produce CO mainly via abiotic processes such as thermal- and photo-degradation of organic matter or plant materials (Conrad and Seiler, 1985b; Tarr et al., 1995; Schade et al., 1999; Derendorp et al., 2011; Lee et al., 2012; van Asperen et al., 2015; Fraser et al., 2015, Pihlatie et al., 2016), except for a few cases of anaerobic formation. Photo-degradation is identified as radiation-dependent degradation due to absorbing radiation (King et al., 2012). Thermal-degradation is identified as the temperature-dependent degradation of carbon in the absence of radiation and possibly oxygen (Derendorp et al., 2011; Lee et al., 2012; van Asperen et al., 2015; Pihlatie et al., 2016). These major soil CO production processes, together with soil CO consumption processes, have not been adequately considered in global soil CO budget estimates.

To date, most top-down atmospheric models applied a dry deposition scheme based on the resistance model of Wesely (1989). Such schemes provided a wide range of dry deposition velocities (Stevenson et al., 2006). Only a few models (MOZART-4, Emmons et al., 2010; CAM-chem, Lamarque et al., 2012) have extended their dry deposition schemes with a parameterization for CO and H_2 uptake through oxidation by soil microbes, following the work of Sanderson et al. (2003), which was based on extensive measurements from Yonemura et al. (2000). Potter et al. (1996) developed a bottom-up model to simulate CO consumption and production at the global

scale. Their model is a single box model, only considers top 5 cm depth of soil and does not have explicit microbial factors, therefore might have underestimated CO consumption (Potter et al., 1996; King, 1999a). Current bottom-up CO modeling approaches are mostly based on a limited number of CO in situ observations or laboratory studies to quantify regional and global soil consumption (Potter et al., 1996; Sanhueza et al., 1998; Khalil et al., 1999; King, 1999a; Bergamaschi et al., 2000; Prather & Ehhalt, 2001). To our knowledge, no detailed process-based model of soil-atmospheric exchange of CO has been published in the recent 15 years. One reason is that there is an incomplete understanding of biological processes of uptake (King & Weber, 2007; Vreman et al., 2011; He and He, 2014; Pihlatie et al., 2016). Another reason is that there is a lack of long-term CO flux measurements for different ecosystem types to calibrate and evaluate the models. CO flux measurements are mostly from short-term field observations or laboratory experiments (e.g. Conrad and Seiler, 1985a; Funk et al., 1994; Tarr et al., 1995; Zepp et al., 1997; Kuhlbusch et al., 1998; Moxley and Smith, 1998; Schade et al., 1999; King and Crosby, 2002; Varella et al., 2004; Lee et al., 2012; Bruhn et al., 2013; van Asperen et al., 2015). The first study to report long-term and continuous field measurements of CO flux over grasslands using a micrometeorological eddy covariance (EC) method is Pihlatie et al. (2016).

To improve the quantification of the global soil CO budget for the period 2000-2013 and the CO deposition velocity for the 20th and 21st centuries, this study developed a CO dynamics module (CODM) embedded in a process-based biogeochemistry model, the Terrestrial Ecosystem Model (TEM) (Zhuang et al., 2003, 2004, 2007). CODM was then calibrated and evaluated using laboratory experiments and field measurements for different ecosystem types. The atmospheric CO concentration data from MOPITT (Gille, 2013) were used to drive model simulations from 2000 to 2013. A set of century-long simulations of 1901-2100 were also conducted using the

atmospheric CO concentrations estimated with an empirical function (Badr & Probert, 1994; Potter et al., 1996). Finally, the effects of multiple forcings on the global CO consumption and production, including the changes of climate and atmospheric CO concentrations at the global scale were evaluated with the model.

2.3 Method

2.3.1 Overview

We first developed a soil CO dynamics module (CODM) on a daily time step that considers: (1) the soil-atmosphere CO exchange and diffusion process between soil layers, (2) the consumption by soil microbial oxidation, (3) the production by soil chemical oxidation, and (4) the effects of temperature, soil moisture, soil CO substrate and surface atmospheric CO concentration on these processes. Second, we used the observed soil temperature and moisture to evaluate TEM hydrology module and the soil thermal module in order to estimate soil physical variables. Then we used the data from laboratory experiments and CO flux measurements to parameterize the model using the Shuffled Complex Evolution (SCE-UA) method (Duan et al., 1993). Finally, the model was extrapolated to the globe at a 0.5° by 0.5° resolution. We conducted three sets of model experiments to investigate the impact of climate and atmospheric CO concentrations on soil CO dynamics: 1) Simulations for 2000-2013 with MOPITT satellite atmospheric CO concentration data; 2) Simulations for 1901-2100 with constant atmospheric CO concentrations estimated from an empirical function and the historical climate data (1901-2013) and three future climate scenarios (2014-2100); and 3) Eight sensitivity simulations by increasing and decreasing a) constant CO surface concentrations by 30%, b) SOC by 5%, c) precipitation by 20% and d) air temperature by 3℃ for each pixel, respectively, while holding other forcing data as they were, during 1999-2000.

2.3.2 Carbon Monoxide Dynamics Module (CODM)

Embedded in TEM (Figure 2.1), CODM is mainly driven by: (1) soil organic carbon availability based on a carbon and nitrogen dynamics module (CNDM) (Zhuang et al., 2003); (2) soil temperature profile from a soil thermal module (STM) (Zhuang et al., 2001, 2003); and (3) soil moisture profile from a hydrological module (HM) (Bonan, 1996; Zhuang et al, 2004). The net exchange of CO between the atmosphere and soil is determined by the mass balance approach (net flux = total production – total oxidation – total soil CO concentration change). According to previous studies, we separated active soils (top 30 cm) for CO consumption and production into 1 cm thickness layers (King, 1999a, 1999b; Whalen & Reeburgh, 2001; Chan & Steudler, 2006). Between the soil layers, the changes of CO concentrations were calculated as:

$$\frac{\partial(C(t,i))}{\partial t} = \frac{\partial}{\partial z}\left(D(t,i)\frac{\partial\big(C(t,i)\big)}{\partial z}\right) + P(t,i) - O(t,i) \qquad (2.1)$$

Where $C(t,i)$ is the CO concentration (mg m^{-3}) in layer i and at time t. z is the depth of the soil (m). $D(t,i)$ is the diffusion coefficient (m^2 s^{-1}) for layer i. $P(t,i)$ is the CO production rate (mg m^{-3} s^{-1}) and $O(t,i)$ is the CO consumption rate (mg m^{-3} s^{-1}). $D(t,i)$ is calculated using the method from Potter et al. (1996), which is a function of soil temperature, soil texture and soil moisture. The upper boundary condition is the atmospheric CO concentration, which is estimated with an empirical function of latitude (Potter et al., 1996) or directly measured by the MOPITT satellite during 2000-2013. The lower boundary condition is assumed to have no diffusion exchange with the layer underneath. This partial differential equation (PDE) is solved using the Crank-Nicolson method for less time-step-sensitive solution.

The CO consumption was modeled in unsaturated soil pores as:

$$O(t,i) = V_{max} \cdot f_1\big(C(t,i)\big) \cdot f_2\big(T(t,i)\big) \cdot f_3\big(M(t,i)\big) \qquad (2.2)$$

Where V_{max} is the ecosystem specific maximum oxidation rate and was estimated previously ranging from 0.3 to 11.1 µg CO g^{-1} h^{-1} for different ecosystems (Whalen & Reeburgh, 2001). f_i represents the effects of soil CO concentration $C(t,i)$, temperature $T(t,i)$ and moisture $M(t,i)$ on the CO soil consumption. Considering the CO consumption as the result of microbial activities, we calculated $f_1\big(C(t,i)\big)$, $f_2\big(T(t,i)\big)$ and $f_3\big(M(t,i)\big)$ in a similar way to Zhuang et al. (2004):

$$f_1\big(C(t,i)\big) = \frac{C(t,i)}{C(t,i) + k_{CO}} \qquad (2.2.1)$$

$$f_2\big(T(t,i)\big) = Q_{10}^{\frac{T(t,i)-T_{ref}}{10}} \qquad (2.2.2)$$

$$f_3\big(M(t,i)\big) = \frac{(M(t,i) - M_{min})(M(t,i) - M_{max})}{(M(t,i) - M_{min})(M(t,i) - M_{max}) - (M(t,i) - M_{opt})^2} \qquad (2.2.3)$$

Where $f_1\big(C(t,i)\big)$ is a multiplier that enhances the oxidation rate with increasing soil CO concentrations using a Michaelis-Menten function with a half-saturation constant k_{CO}, and their values were previously estimated ranging from 5 to 51 µl CO l^{-1} for different ecosystems (Whalen & Reeburgh, 2001); $f_2\big(T(t,i)\big)$ is a multiplier that enhances the CO oxidation rate with increasing soil temperature using a Q10 function with Q_{10} coefficients (Whalen & Reeburgh, 2001). T_{ref} is the reference temperature, units are °C (Zhuang et al., 2004, 2013). $f_3\big(M(t,i)\big)$ is a multiplier to estimate the biological limiting effect that diminishes the CO oxidation rates if the soil moisture is not at an optimum level (M_{opt}). M_{min}, M_{max} and M_{opt} are the minimum, maximum and optimum volumetric soil moistures of oxidation reaction, respectively. Equation (2.2.2) will overestimate the CO consumption at high temperature because in reality the CO consumption will decrease when temperature is higher than optimum temperature, while f_2 will keep increasing with rising temperature. However, the CO consumption is constrained by the CO production, and equation (2.1) is used to represent this constraint.

We modeled the CO production rate ($P(t,i)$) as a process of chemical oxidation constrained by the soil organic carbon (SOC) decay (Conrad and Seiler,1985; Potter et al. 1996; Jobbagy & Jackson, 2000; van Asperen et al., 2015):

$$P(t,i) = P_r(t,i) \cdot E_{SOC} \cdot C_{SOC}(t) \cdot F_{SOC} \qquad (3)$$

Where $P_r(t,i)$ is a reference soil CO production rate which has been normalized to the rate at reference temperature (the production rate at temperature (t,i) divided by the production rate at the reference temperature), which is affected by soil moisture and soil temperature (Conrad and Seiler,1985; van Asperen et al., 2015). E_{SOC} is an estimated nominal CO production factor of 3.5 ± 0.9 X 10^{-9} mg CO m^{-2} s^{-1} per g SOC m^{-2} (to 30 cm soil depth) (Potter et al., 1996). $C_{SOC}(t)$ is a SOC content (mg m^{-2}), which is provided by CNDM module in TEM. F_{SOC} is a constant fraction of top 30cm SOC compared to the total amount of SOC, which is 0.33 for shrubland areas, 0.42 for grassland areas and 0.50 for forest areas, respectively (Jobbagy & Jackson, 2000). $P_r(t,i)$ was calculated as:

$$P_r(t,i) = \exp\left(f_4\big(M(t,i)\big) \cdot Ea_{ref}/R \cdot \left(\frac{1}{273.15 + PT_{ref}} - \frac{1}{T(t,i) + 273.15}\right)\right) \qquad (2.3.1)$$

$$f_4\big(M(t,i)\big) = \frac{PM_{ref}}{M(t,i) + PM_{ref}} \qquad (2.3.2)$$

Where equation (2.3.1) is derived from the Arrhenius equation for chemical reactions and normalized using the reference temperature PT_{ref}. Ea_{ref}/R is the reference activation energy divided by gas constant R, units are K. $f_4\big(M(t,i)\big)$ is the multiplier that reduces activation energy using a regression approach based on the laboratory experiment of moisture influences on CO production (Conrad and Seiler,1985). PM_{ref} is the reference volumetric soil moisture, ranging from 0.01 to 0.5 volume/volume (v/v). We assumed the thermal-degradation as the main CO

producing process due to lack of photo-degradation data and hard to distinguish photo-degradation from observations. In order to reduce the bias from the thermal-degradation to the total abiotic degradation, the equation (2.3.1) is parameterized by comparing with the total production rate. For instance, $P_r(t, i)$ calculation can perfectly fit the experiment results in Van Asperen et al. (2015) with proper PT_{ref}(18℃), Ea_{ref}/R(14000 K), and PM_{ref}(0.5 v/v).

The CO deposition velocity was modeled in the same way as equation (19.1) in Seinfeld et al. (1998):

$$v_d = -F_{net}/C_{CO,air} \qquad (2.4)$$

Where v_d is the CO deposition velocity (mm s-1). F_{net} is the model estimated CO net flux rate (mg CO m^{-2} day^{-1}). $C_{CO,air}$ is the CO surface concentration (ppbv). $C_{CO,air}$ can be MOPITT CO surface concentration data or the derived CO surface concentrations using the same method as Potter et al. (1996). Positive values of v_d represent soil uptake (deposition from air to soils) and negative values represent soil emissions.

2.3.3 Model Parameterization and Extrapolation

The model parameterization was conducted in two steps: 1) Thermal and hydrology modules embedded in TEM were revised, calibrated and evaluated by running model driven by corresponding local meteorological or climatic data at four representative sites, including boreal forest, temperate forest, tropical forest and savanna (Table 2.1, site No.1 to 4, Figure 2.2) to minimize model-data mismatch in terms of soil temperature and moisture. 2) CODM module was parameterized by running TEM for observational periods driven with the corresponding local meteorological or climatic data at each reference site (Table 2.1, Figure 2.3), and using the Shuffled Complex Evolution Approach in R language (SCE-UA-R) (Duan et al., 1993) to minimize the difference between the simulated and observed net CO flux. Eleven parameters

including k_{CO}, V_{max}, T_{ref}, Q_{10}, M_{min}, M_{max}, M_{opt}, E_{SOC}, Ea_{ref}/R, PM_{ref} and PT_{ref} were optimized (Table 2.2). To be noticed, F_{SOC} was not involved in the calibration process. Parameter priors were decided based on previous studies (Conrad & Seiler, 1985; King, 1999b; Whalen & Reeburgh, 2001; Zhuang et al., 2004). The SCE-UA-R was used for site No. 6, 8, 10, 11 (Table 2.1). In parameter ensemble simulations, we have run 50 times SCE-UA-R with 10000 maximum loops for each site, and all of them have reached stable state before the end of the loops. For wetlands, the only available data for calibration is from site No.12. We used the trial-and-error method to make the simulated results in the range of observed flux rates, with a 10% tolerance. For tropical sites, since tropical savanna vegetation type is treated as a combination type of tropical forest and grassland in our simulations, we first used Site No. 13 to set priors to fit the experiment results with a 10% tolerance and then evaluated by running our model comparing with site No.7 results. Site No. 9 and 5 were used to evaluate our model results for temperate forest and grassland. Besides the observed climatic and soil property data, we used the ERA-Interim reanalysis data from The European Centre for Medium-Range Weather Forecasts (ECMWF) (Dee et al., 2011), AmeriFlux observed meteorology data (http://ameriflux.lbl.gov/) and reanalysis climatic data from Climatic Research Unit (CRU, Harris et al., 2014) to fill the missing environmental data. To sum up, parameters for various ecosystem types in Table 2.2 were the final results of our parameterization. Model parameterization was conducted for ecosystem types including boreal forest, temperate coniferous forest, temperate deciduous forest, and grassland using SCE-UA-R. In contrast, for tropical forest and wet tundra, we used a trial-and-error method to adjust parameters to allow model simulation best fit the observed data. Due to limited data availability, we assumed temperate evergreen broadleaf forests have the same parameters as temperate deciduous forest ecosystems.

2.3.4 Data Organization

To get the spatially and temporally explicit estimates of the CO consumption, production and net flux at the global scale, we used the data of land cover, soils, climate and leaf area index (LAI) from various sources at a spatial resolution of 0.5° latitude X 0.5° longitude to drive TEM. The land cover data include the potential vegetation distribution (Melillo et al., 1993) and soil texture (Zhuang et al., 2003), which were used to assign vegetation- and texture-specific parameters to each grid cell.

For the simulation of the period 1901-2013, the monthly air temperature, precipitation, clouds fraction and vapor pressure data sets from CRU were used to estimate the soil temperature, soil moisture and SOC with TEM (Figure 2.4). The monthly LAI data from TEM were required to simulate soil moisture (Zhuang et al., 2004). During this period time, we used an empirical function of latitude, which was derived from the observed latitudinal distribution of tropospheric carbon monoxide (Badr and Probert, 1994) to calculate static CO surface concentration distribution (equation (2.7), Potter et al., 1996):

$$C_{CO,air} = 82.267856 + 0.8441503L + 1.55934 \times 10^{-2}L^2 + 2.37 \times 10^{-5}L^3 - 2.3 \times 10^{-6}L^4 \quad (2.5)$$

Where $C_{CO,air}$ is the derived surface CO concentration (ppbv), L represents latitudes with negative degrees for southern hemisphere and positive degrees for northern hemisphere. We also used the atmospheric CO data from MOPITT satellite during 2000-2013 (Figure 2.5). We averaged day-time and night-time monthly mean values of CO surface level 3 retrieval data (variables mapped on 0.5° latitude X 0.5° longitude grid scales with monthly time step, Gille, 2013) to represent the CO surface concentration level in each month. The pixels with missing values were filled with the average values of those pixels that were inside 1.5 times of the distance between the

missing-value pixel and the nearest pixel with values. These global mean values shown in Figure 2.5 do not include ocean surfaces, thus there are differences between our surface CO concentration results and Yoon and Pozzer's report in 2014, which is as low as 99.8 ppb. From 2014 to 2100, we used the Intergovernmental Panel on Climate Change (IPCC) future climate scenarios from Representative Concentration Pathways (RCPs) climate forcing data sets RCP2.6, RCP4.5 and RCP8.5 (Figure 2.6). RCP2.6, 4.5 and 8.5 datasets are future climate projections with anthropogenic greenhouse gas emission radiative forcing of 2.6 W m^{-2}, 4.5 W m^{-2} and 8.5 W m^{-2}, respectively, by 2100. Since RCPs did not have water vapor pressure data, we used the specific humidity and sea level air pressure from the RCPs and elevation of surface to estimate the monthly surface vapor pressure (Seinfeld & Pandis, 1998).

2.3.5 Model Experiment Design

We conducted two sets of core simulations and eight sensitivity test simulations for a historical period. The two core sets of simulations were driven with the MOPITT CO surface concentrations data for the period 2000-2013 (experiment E1) and with the spatially distributed CO surface concentrations assuming as constant over time estimated from an empirical function of latitude for the period 1901-2100 (experiment E2), respectively. Specifically, in experiment E2 we used the CRU climate forcing for the historical period 1901-2013 and the climate data of RCP2.6, RCP4.5 and RCP8.5 for different future scenarios to examine the responses of CO flux to changing climates. Eight sensitivity simulations were driven with varying different forcing variables while keeping others as they were: 1) with constant CO surface concentrations ± 30%, 2) SOC ± 5%, 3) precipitation ± 20% and 4) air temperature ± 3℃ for each pixel, respectively, during 1999-2000 (E3).

2.4 Results

2.4.1 Site Evaluation

Both the magnitude and variation of the simulated soil temperature and moisture from cold areas to warm areas are compared well to the observations (Figure 2.2). The magnitude of the simulated CO flux is comparable and correlated with the observations (R is about 0.5, p-value < 0.001, Figures 2.3, a2, b2, c2, d2). Estimated CO fluxes for different ecosystem types range from -28.4 to 1.7 mg CO m^{-2} day^{-1}, and the root mean square error (RMSE) between simulation and observation at all sites is below 1.5 mg CO m^{-2} day^{-1}. RMSE for site No. 7 is bigger than 2.0 mg CO m^{-2} day^{-1} when compared with transparent chamber observations. For boreal forest site, we only had 8 acceptable points in 1994 and 1996 (Figure 2.3c2).

2.4.2 Global Soil CO Dynamics During 2000-2013

Using the MOPITT CO surface concentration data during 2000-2013 (E1), the estimated mean soil CO consumption, production and net flux (positive values indicate CO emissions from soils to the atmosphere) are from -197 to -180, 34 to 36 and -163 to -145 Tg CO yr^{-1}, respectively (Figure 2.7a). The consumption is about 4 times larger than the production. The annual consumption and net flux trends follow the atmospheric CO concentration trends (Figure 2.5b, Figure 2.7a), with a small interannual variability (< 10%). The latitudinal distributions of the consumption, production and net fluxes share the same spatial pattern. Around 20°S-20°N and 20-60°N are the largest and second largest areas for production and consumption, while the 45°S-45°N area accounts for nearly 90% of the total consumption and production (Figure 2.7b, Table 2.3). The Southern and Northern Hemispheres have 41% and 59% of the total consumption, and 47% and 53% of the total production, respectively (Table 2.3). The highest rates of the consumption and production are located in areas close to the equator, and the consumption from

areas such as eastern US, Europe and eastern Asia also is high (< -1000 mg m^{-2} yr^{-1}) (Figure 2.8a, b). Global soils serve as an atmospheric CO sink (Figure 2.8c). Some areas, such as western US and southern Australia, are CO sources, all of which are grasslands or experiencing dry climate. Tropical evergreen forests are the largest sinks, consuming 86 Tg CO yr^{-1}, and tropical savanna and deciduous forest are the second and third largest sinks, consuming a total of 37 Tg CO yr^{-1} (Table 2.4). These three ecosystems account for 66% of the total consumption. Tropical evergreen forests are also the largest source of soil CO production, producing 16 Tg CO yr^{-1}, while tropical savanna has a considerable production of 6 Tg CO yr^{-1} (Table 2.4). Moreover, tropical areas, including forested wetlands, forested floodplain and evergreen forests, are most efficient for the CO consumption, ranging from -18 to -13 mg CO m^{-2} day^{-1}. They are also most efficient for the CO production at over 2 mg CO m^{-2} day^{-1} (Table 2.4, calculated by fluxes divided by area).

2.4.3 Global Soil CO Dynamics During 1901-2100

Using the constant CO surface concentration, the estimated global mean CO deposition velocities are 0.16-0.19 mm s^{-1} for the period 1901-2013. For the period 2014-2100, the deposition velocities are 0.18-0.21, 0.18-0.24 and 0.17-0.31 for RCP2.6, 4.5 and 8.5 scenarios, respectively (Figure 2.9). During 2014-2100, there are significant trends of increasing deposition velocities for nearly all scenarios (Figure 2.9). The rates of increasing are 0.0002, 0.0005 and 0.0013 mm s-1 yr^{-1}, and will reach 0.20, 0.23 and 0.30 mm s^{-1} by the end of the 21st century for the RCP2.6, RCP4.5 and RCP8.5 scenarios, respectively (Figure 2.9). These increasing trends are similar to the air temperature increasing trends (Figure 2.6a). The global distribution patterns of the CO deposition velocity are similar to the net flux distribution for the period 2000-2013 but there are significant differences among the 1901-2013, RCP2.6, RCP4.5 and RCP8.5 scenarios (Figure 2.10). The deposition velocities are increasing from the RCP2.6 to RCP8.5 and larger than that in the

historical periods in areas near the equator (Figure 2.10). Areas near the equator and eastern Asia become big sinks of the atmospheric CO, while northeastern US becomes a small source in the 21st century (Figure 2.10). Different vegetation types have a large range of the deposition velocity, from 0.008 to 1.154 mm s^{-1} (Table 2.4). The tropical forested wetland, tropical forested floodplain and tropical evergreen forest have top three largest deposition velocity of 1.154, 1.117 and 0.879 mm s^{-1}, respectively, while desert, short grasslands, and wet tundra have the smallest deposition velocity of 0.008, 0.010 and 0.015 mm s^{-1}, respectively.

2.4.4 Sensitivity test

The soil CO consumption is most sensitive (changing 29%) to air temperature while the production is most sensitive to both air temperature (changing up to 36%) and SOC (5%). The net CO fluxes have the similar sensitivities as the consumption. The annual CO consumption, production and net flux follow the change of air temperature (Table 2.5). In addition, a 30% change in precipitation will not lead to large changes in the CO flux (< 3%).

2.5 Discussion

2.5.1 Comparison with Other Studies

Previous studies estimated a wide range of the global CO consumption from -16 to -640 Tg CO yr^{-1}. Our estimates are from -197 to -180 Tg CO yr^{-1} for 2000-2013 using the MOPITT satellite CO surface concentration data. Previous studies also provided a large range for the CO production from 0 to 7.6 mg m^{-2} day^{-1} (reviewed in Pihlatie et al., 2016). Our results showed the averaged CO production ranging from 0.01 to 2.29 mg m^{-2} day^{-1}. The existing estimates of the CO deposition velocities for different vegetation types ranged from 0.0 to 4.0 mm s^{-1} while our simulations showed an averaged CO deposition velocity ranging from 0.006 to 1.154 mm s^{-1} for different

vegetation types. The large uncertainty of these estimates is mainly due to different considerations of the microbial activities, the depth of the soil, and the parameters in the model. In contrast to the estimates of -57 to -16 Tg CO yr^{-1} which were based on top 5 cm soils (Potter et al., 1996), our estimates considered 30 cm soils, which were used in Whalen & Reeburgh (2001). In addition, we used a thinner layer division (1 cm each layer) for diffusion process, and used the Crank-Nicolson method to solve partial differential equations to avoid time step influences. We also included the microbial CO oxidation process to remove the CO from the soil and considered the effects of soil moisture, soil temperature, vegetation type and soil CO substrate on microbial activities. Our soil thermal, soil hydrology and carbon and nitrogen dynamics simulated in TEM provided carbon substrate spatially and temporally for estimating the soil CO dynamics. Overall, although a few previous studies have examined the long-term impacts of climate, land use and nitrogen deposition on the CO dynamics (Chan & Steudler, 2006, Pihlatie et al., 2016), the global prediction of the soil CO dynamics still has a large uncertainty.

2.5.2 Major Controls to Soil CO Dynamics

The sensitivity tests indicate that the consumption is normally much larger than the CO production so that the former will determine the dynamics of the net flux (Table 2.5). Model being sensitive to air temperature explains the small increasing trends after the 1960s, the significant increasing trend in the 21st century and the large sinks over tropical areas (Table 2.5, Figure 2.9). SOC did not directly influence the CO consumption. For instance, increasing SOC led to an increase in soil CO substrate, implying that more CO in soils can be consumed. To be noticed, an extra 3 Tg CO yr^{-1} was taken up from the atmosphere to the soil in the sensitivity test when SOC increasing by 5% (Table 2.5), which will be discussed in detail in Section 2.5.3. CO surface

concentrations will only influence the uptake rate and soil CO substrate concentrations, thus influencing the soil CO consumption rate.

The annual CO consumption and net flux have a similar correlation coefficient with forcing variables and both are significantly correlated with air temperature, soil temperature SOC and atmospheric CO concentration ($R > 0.91$ globally, Table 2.6). Increasing temperature will increase microbial activities, while more SOC will increase soil CO substrate level. The annual CO consumption and net flux have low correlations with annual precipitation and soil moisture, especially at 45°N-45°S ($R < 0.54$ Table 2.6). The annual CO production is strongly correlated with annual mean SOC, air temperature and soil temperature ($R > 0.91$), while is less correlated with precipitation, soil moisture and atmospheric CO concentration. Meanwhile, the monthly CO consumption, production and net flux are well correlated with air temperature, soil temperature, precipitation, and soil moisture ($R > 0.69$ globally Table 2.6). The soil moisture is significantly influenced by temperature at a monthly time step since the increasing temperature would induce higher evapotranspiration. The monthly CO consumption, production and net flux have low correlations with SOC because it will not change greatly within a month.

The R between the annual soil CO consumption and atmospheric CO concentration is 0.91 at the global scale because the atmospheric CO concentration, air temperature, and soil temperature dominate the annual consumption rate. At monthly scale, this R is -0.48 because the global atmospheric CO concentrations are high in winter and low in summer while the simulated soil CO consumption shows an opposite monthly variation (Table 2.6, Figure 2.11), suggesting that other factors such as precipitation, air temperature, and soil temperature are major controls for the monthly CO fluxes.

2.5.3 Model Uncertainties and Limitations

There are a number of limitations, contributing to our simulation uncertainties. First, due to lacking long-period observational data of the CO flux and associated environmental factors, the model parameterization can only be conducted for 4 ecosystem types including boreal forest, temperate coniferous forest, temperate deciduous forest and grassland. Tropical forest calibration is only conducted using a very limited amount of laboratory experiment data, but tropical areas are hotspots for CO soil-atmosphere exchanges. Besides, the amount of tropical forest SOC for top 30 cm can be very large according to observations. TEM model may underestimate the top 30 cm SOC, which will underestimate the production rates, especially in tropical regions. Tropical regions typically have high temperature during the whole year, which may result in overestimation of the CO consumption using equation (2.2.2). The large deviation of model simulations to observations in tropical savanna (which is mosaic of tropical forest and grassland ecosystems) may be due to using outside air temperature to represent inside air temperature of transparent chamber observations (Varella et al., 2004), and uncertain tropical forest parameterization. Second, we used the conclusion from van Asperen et al. (2015) and only considered the thermal-degradation process for the CO production in this study. The photo-degradation process and biological formation process were not considered due to lacking the understanding of these processes. Third, the static CO surface concentration derived from the empirical function is lower than the MOPITT CO surface concentration, which will lead to underestimation of CO deposition velocity during 1901-2100. Fourth, from the sensitivity test (Table 2.5) we notice that an increase in SOC by 5% resulted in a net flux increase from the atmosphere to the soil by 2.57%. The SOC increase enhanced CO production (Equation 2.3), CO concentrations (Equation 2.1), and CO oxidation (Equation 2.2). When the change of total oxidation is larger than the difference between the change of total

production and the change of total soil CO concentration (Equation 2.1), the estimate of the net flux change is negative (from the atmosphere to soil) using a mass balance approach (Section 2.3.2), which leads to a 2.57% increase in the net flux in our SOC sensitive test. This is due to the fact that CO production (Equation 2.3) is calculated independently from oxidation (Equation 2.2). This will not influence our general findings since SOC varies only slightly during our simulation periods with a 3% increase from 1900 to 2013 (Figure 2.4d) and up to a 4% increase from 2014 to 2100 (Figure 2.6g). This model artifact that is apparent in the SOC sensitivity test can be alleviated using a very fine time step (e.g., 1 second), because in this case CO concentrations change only slightly within the short time. Therefore, when a short time step is used, the net flux roughly equals the difference between production and oxidation. If the change of production is bigger than the change of oxidation, the change of net flux will be positive, leading to a decrease of deposition to the soil. The downside is that running the model at a time step of one second will require a significantly large amount of computing time. Fifth, our model structure still has a large potential to improve. In this study we divided the top 30 cm soil into 30 layers (layer thickness dz = 1 cm), but a finer division will increase the accuracy (Figure 2.12). We chose 1 cm thickness because if thicker than 1 cm, the model vertical CO concentration profile will deviate from reality and diffusion process will be influenced significantly. If thinner than 1 cm, it will need much more computing time but doesn't have much improvement compared to thickness set to 1 cm (Figure 2.12a-e). We notice that the 30-layer division well represents the soil CO concentration profile not only in the days of soil CO net uptake, but also in the days of CO net emission (Figure 2.12c, f). Sixth, Michaelis-Menten function (equation 2.2.1) is used in this model and we notice that k_{CO} is normally much larger than $C(t,i)$ in those days of net soil uptake (over ten times larger, Figure 2.12). However, we can't simplify equation (2.2.2) to $f_1\big(C(t,i)\big) = \frac{C(t,i)}{k_{CO}}$, because the CO

concentrations in the soil can be larger than in the atmosphere in the days of net emissions and $C(t,i)$ may be close to k_{CO}, and then the simplified equation may lead to overestimation of CO oxidation (Figure 2.12f). Finally, although we focused on natural ecosystems in this study, the land-use change, agriculture activity, and nitrogen deposition also affect the soil CO consumption and production (King, 2002; Chan & Steudler, 2006). For instance, the soil CO consumption in agriculture ecosystems is from 0 to 9 mg CO m-2 day-1 in Brazil (King & Hungria, 2002). In this study, we used grassland or forest ecosystem to represent agriculture areas in CODM module. Our future study shall include these processes and factors.

2.6 Conclusions

We analyzed the magnitude, spatial pattern, and the controlling factors of the atmosphere-soil CO exchanges at the global scale for the 20th and 21st centuries using a process-based biogeochemistry model. Major processes include the atmospheric CO diffusion from the atmosphere to the soil and inside the soil of terrestrial ecosystems, microbial oxidation removal of CO, and CO production through chemical reaction. We found that air temperature and soil temperature play a dominant role in determining the annual soil CO consumption and production while precipitation, air temperature, and soil temperature are the major controls for the monthly consumption and production. The atmospheric CO concentrations are important for annual CO consumption. We estimated that the global annual CO consumption, production and net fluxes for 2000-2013 are from -197 to -180, 34 to 36 and -163 to -145 Tg CO yr^{-1}, respectively, when using the MOPITT CO surface concentration data. Tropical evergreen forest, savanna and deciduous forest areas are the largest sinks accounting for 66% of the total CO consumption, while the Northern Hemisphere consumes 59% of the global total. During the 20th century, the estimated

CO deposition velocity is 0.16-0.19 mm s^{-1}. The predicted CO deposition velocity will reach 0.20-0.30 mm s^{-1} in the 2090s, primarily because of the increasing air temperature. The areas near the equator, eastern Asia, Europe and eastern US will become the hotspots of sink because they have warm and moist soils. This study calls for long-period observations of CO flux for various ecosystem types and better projection of atmospheric CO surface concentrations from 1901-2100 to improve future estimates of global soil CO consumption. The effects of land-use change, agriculture activities, nitrogen deposition, photo-degradation and biological formation shall also be considered to improve future quantification of soil CO fluxes.

Acknowledgments: This study is supported through projects funded to Q.Z. by Department of Energy (DE-SC0008092 and DE-SC0007007) and the NSF Division of Information and Intelligent Systems (NSF-1028291). The supercomputing resource is provided by Rosen Center for Advanced Computing at Purdue University. We acknowledge Dr. Stephen C. Whalen made the observational CO flux data available to this study. We are also grateful to University of Tuscia (dep. DIBAF), Italy, and their affiliated members, for their help and the use of their field data. All data used in this manuscript can be accessed in Purdue University Research Repository (PURR) through the link: https://doi.org/10.4231/JGZ8-9C75

Table 2.1. Model parameterization sites for the thermal and hydrology modules (site No. 1-4) and for the CODM module (site No. 5-13)

No.	Site Name	Location	Vegetation	Driving Climate	Observed Data	Source and Comments
1	Poker Flat Research Range Black Spruce Forest (US_PRR)	147°29'W/65°7'N	Boreal Evergreen Needle Leaf Forests	Site Observation & ERA Interim	Soil Temperature and Moisutre of 2011-2014	Suzuki (2016)
2	Morgan Monroe State Forest (US_MMS)	86°25W/39°19'N	Temperate Deciduous Broadleaf Forests	Site Observation & ERA Interim	Soil Temperature and Moisutre of 1999-2014	Philip and Novick (2016)
3	Santarem, Tapajos National Forest (STM_K83)	54°56'W/3°3'S	Tropical Moist Forest	Site Observation & ERA Interim	Soil Temperature and Moisutre of 2000-2004	SALESKA et al. (2013)
4	Bananal Island Site (TOC_BAN)	50°08'W/9°49'S	Tropical Forest-Savanna	Site Observation & ERA Interim	Soil Temperature and Moisutre of 2003-2006	SALESKA et al. (2013)
5	Eastern Finland (EF)	27°14E/63°9'N	Boreal Grassland	Site Observation & ERA Interim	CO flux of April-November,2011	Pihlatie et.al. (2016)
6	Viterbo, Italy (VI)	11°55'E/42°22'N	Mediterranean Grassland	Site Observation & ERA Interim	CO flux of August, 2013	van Asperen et al. (2015)
7	Brasilia, Brazil (BB)	47°51'W/15°56'S	Tropical Savanna	Site Observation & CRU	CO flux of October 1999 to July 2001	Varella et al. (2004)
8	Orange County, North Carolina (OC)	79°7'W/35°58'N	Temperate Coniferous Forest	AMF_US-Dk3 2002-2003	CO flux of March 2002 to March 2003	Fisher (2003)
9	Tsukuba Science City, Japan (TSC)	140°7'E/36°01'N	Temperate Mixed Forest	Site Observation & ERA Interim	CO flux of July 1996 to September 1997	Yonemura et. al. (2000)
10	Manitoba, Canada (CBS)	96°44'W/56°09'N	Boreal Pine Forest	Site Observation & AMF_CA-Man	CO flux of June-August, 1994	Kuhlbusch et. al (1998)
11	Scotland, U.K. (SUK)	3°12'W/55°51'N	Temperate Deciduous Forests	ERA Interim 1995	CO flux of 1995	Moxley and Smith (1998)
12	Alaska, USA (AUS)	147°41'W/64°52'N	Boreal wetland	CRU 1991	CO flux of Lab Experiment,1991	Funk et al. (1994)
13	Guayana Shield,Bolivar State,Venezuela (GBV)	62°57'W/7°51'N	Tropical Smideciduous Forest	CRU 1985	CO flux of Lab Experiment,1985	Scharffe et al. (1990)

Table 2.2. Ecosystem-specific parameters in the CODM module[a]

	Ecosystem Type	k_{CO} $(ul\ CO\ l^{-1})$	$Vmax$ $(ug\ CO\ g^{-1}h^{-1})$	T_{ref} (℃)	$Q10$ $(Unitless)$	M_{min} $(\frac{v}{v})$	M_{max} $(\frac{v}{v})$	M_{opt} $(\frac{v}{v})$	E_{SOC}	F_{SOC} $(\frac{g}{g})$	$\frac{Ea_{ref}}{R}$ (K)	PM_{ref} $(\frac{v}{v})$	PT_{ref} (℃)
1	Alpine Tundra & Polar Desert	36.00	0.78	4.00	1.80	0.10	1.00	0.55	3.00	0.33	7700	0.25	30.00
2	Wet Tundra	36.00	0.70	4.00	1.80	0.25	1.00	0.55	3.00	0.42	7700	0.25	30.00
3	Boreal Forest	27.34	1.18	9.81	1.60	0.15	0.64	0.53	2.98	0.50	8827	0.35	26.99
4	Temperate Coniferous Forest	42.64	2.15	6.90	1.87	0.02	0.96	0.53	2.86	0.50	8404	0.38	31.52
5	Temperate Deciduous Forest	40.16	2.43	8.54	1.51	0.17	0.81	0.51	2.45	0.50	8801	0.35	37.44
6	Grassland	42.41	0.49	11.27	1.65	0.16	0.82	0.51	3.09	0.42	14165	0.24	12.29
7	Xeric Shrublands	8.00	0.30	4.00	1.50	0.10	1.00	0.55	3.00	0.33	7700	0.25	30.00
8	Tropical Forest	45.00	2.00	4.00	1.50	0.10	1.00	0.55	3.80	0.50	14000	0.50	18.00
9	Xeric Woodland	8.00	0.30	4.00	1.50	0.10	1.00	0.55	3.00	0.50	7700	0.25	30.00
10	Temperate Evergreen Broadleaf Forest	40.16	2.43	8.54	1.51	0.17	0.81	0.51	2.45	0.50	8801	0.35	37.44
11	Mediterranean Shrubland	45.00	1.50	4.00	1.50	0.10	1.00	0.55	3.00	0.33	7700	0.25	30.00
**	Largest Potential Value	51.00	11.1	15.00	2.00	0.30	1.00	0.60	3.80	--	15000	0.60	40.00

[a] k_{CO} is the half-saturation constant for soil CO concentration; $Vmax$ is the specific maximum CO oxidation rate; T_{ref} is the reference temperature to account for the soil temperature effects on the CO consumption; $Q10$ is the an ecosystem-specific Q10 coefficient to account for soil temperature effects on the CO consumption; M_{min}, M_{max}, M_{opt} are the minimum, optimum, and maximum volumetric soil moistures of oxidation reaction to account for soil moisture effects on the CO consumption; E_{SOC} is an estimated nominal CO production factor, similar as Potter et al. (1996) (10^{-4} mg CO m^{-2} d^{-1} per g SOC m^{-2}); F_{SOC} is a constant fraction of top 20cm SOC compared to total amount of SOC to account for SOC effects on the CO production; Ea_{ref}/R is the is the ecosystem-specific activation energy divided by gas constant to account for the reaction rate of production; PM_{ref} is the reference moisture to account for soil temperature effects on the CO production; PT_{ref} is the reference temperature to account for soil temperature effects on the CO production

Table 2.3. Regional soil CO consumption, net flux and production (Tg CO yr-1) during 2000-2013

	South-45S	45S-0	0-45N	45N-North	Global
Consumption	0.22	75.77	91.66	18.90	186.55
Net flux	0.13	59.34	77.17	14.63	151.27
Production	0.09	16.43	14.49	4.27	35.28

Table 2.4. Annual total soil CO consumption, net flux and production in different ecosystems during 2000-2013 (E1) and mean CO deposition velocity in different ecosystems during 1901-2013 (E2)

Vegetation Type	Area (10^6 km^2)	Pixels	Consumption (Tg CO yr^{-1})	Net flux (Tg CO yr^{-1})	Production (Tg CO yr^{-1})	Deposition velocity (mm s^{-1})
Alpine Tundra & Polar Desert	5.28	3580	-0.92	-0.69	0.23	0.023
Wet Tundra	5.24	4212	-1.00	-0.42	0.58	0.015
Boreal Forest	12.47	7578	-7.76	-6.01	1.75	0.070
Forested Boreal Wetland	0.23	130	-0.14	-0.09	0.04	0.109
Boreal Woodland	6.48	4545	-2.48	-1.54	0.94	0.036
Non-Forested Boreal Wetland	0.83	623	-0.35	-0.18	0.17	0.029
Mixed Temperate Forest	5.25	2320	-10.49	-9.98	0.51	0.204
Temperate Coniferous Forest	2.49	1127	-3.51	-3.21	0.30	0.185
Temperate Deciduous Forests	3.65	1666	-5.07	-4.83	0.25	0.151
Temperate Forested Wetland	0.15	60	-0.35	-0.35	0.01	0.281
Tall Grassland	3.63	1567	-1.66	-0.65	1.01	0.021
Short Grassland	4.71	2072	-1.05	-0.27	0.78	0.010
Tropical Savanna	13.85	4666	-21.86	-15.88	5.98	0.234
Xeric Shrubland	14.71	5784	-1.95	-1.64	0.31	0.021
Tropical Evergreen Forest	17.77	5855	-85.90	-69.66	16.24	0.879
Tropical Forested Wetland	0.55	178	-3.59	-3.09	0.50	1.154
Tropical Deciduous Forest	4.69	1606	-14.81	-11.78	3.03	0.532
Xeric Woodland	6.85	2387	-8.48	-7.44	1.04	0.246
Tropical Forested Floodplain	0.15	50	-0.89	-0.77	0.12	1.117
Desert	11.61	4170	-0.62	-0.57	0.05	0.008
Tropical Non-forested Wetland	0.06	19	-0.03	-0.02	0.01	0.067
Tropical Non-forested Floodplain	0.36	120	-0.35	-0.24	0.10	0.083
Temperate Non-Forested Weland	0.34	120	-0.33	-0.20	0.14	0.089
Temperate Forested Floodplain	0.10	48	-0.13	-0.12	0.00	0.197
Temperate Non-forested Floodplain	0.10	45	-0.05	-0.03	0.02	0.050
Wet Savanna	0.16	59	-0.39	-0.32	0.07	0.434
Salt Marsh	0.09	35	-0.05	-0.03	0.03	0.035
Mangroves	0.12	38	-0.49	-0.41	0.08	0.809
Temperate Savannas	6.83	2921	-3.83	-3.22	0.61	0.076
Temperate Evergreen Broadleaf	3.33	1268	-7.17	-6.95	0.22	0.252
Mediterranean Shrubland	1.47	575	-0.86	-0.71	0.16	0.100
Total	133.56	59424	-186.55	-151.27	35.28	--

Table 2.5. Sensitivity of the global CO consumption, net flux and production (Tg CO yr^{-1}) to the changes in atmospheric CO, soil organic carbon (SOC), precipitation (Prec) and air temperature (AT)

	Baseline	CO +30%	CO -30%	SOC +5%	SOC -5%	Prec +30%	Prec -30%	AT +3°C	AT -3°C
Consumption	-147.65	-164.14	-131.12	-152.27	-143.03	-150.72	-143.50	-190.59	-114.83
Change (%)	0.00	11.17	-11.19	3.13	-3.13	2.08	-2.81	29.09	-22.23
Net flux	-113.65	-130.15	-97.12	-116.58	-110.73	-116.97	-109.32	-144.23	-89.58
Change (%)	0.00	14.51	-14.54	2.57	-2.57	2.92	-3.81	26.90	-21.18
Production	33.99	33.99	33.99	35.69	32.29	33.74	34.17	46.36	25.25
Change (%)	0.00	0.00	0.00	5.00	-5.00	-0.75	0.53	36.39	-25.72

Table 2.6. Correlation coefficients between forcing variables (precipitation (Prec), air temperature (Tair), soil organic carbon (SOC), soil temperature (Tsoil), soil moisture (Msoil) and atmospheric CO (CO air)) and absolute values of consumption, production and net flux for different regions and the globe

		Monthly					Annual				
		North-45°N	45°N-0°	0°-45°S	45°S-South	Global	North-45°N	45°N-0°	0°-45°S	45°S-South	Global
Prec	Consumption	0.91	0.96	0.92	-0.34	0.87	0.65	0.21	0.26	0.13	0.52
	Production	0.91	0.70	0.45	-0.34	0.82	0.63	0.10	0.15	-0.11	0.47
	Net flux	0.91	0.97	0.94	-0.33	0.87	0.65	0.25	0.31	0.32	0.54
Tair	Consumption	0.97	0.98	0.91	0.96	0.95	0.92	0.93	0.88	0.84	0.91
	Production	0.96	0.83	0.72	0.98	0.94	0.92	0.92	0.91	0.95	0.91
	Net Flux	0.97	0.97	0.88	0.90	0.95	0.91	0.92	0.85	0.62	0.91
SOC	Consumption	-0.19	0.07	0.21	-0.01	0.15	0.68	0.90	0.92	0.47	0.92
	Production	-0.19	0.31	0.47	-0.02	0.24	0.72	0.92	0.92	0.50	0.93
	Net Flux	-0.19	0.03	0.14	0.00	0.13	0.67	0.88	0.91	0.38	0.91
Tsoil	Consumption	0.97	0.98	0.92	0.96	0.95	0.94	0.93	0.88	0.85	0.95
	Production	0.97	0.83	0.72	0.98	0.94	0.94	0.92	0.91	0.96	0.95
	Net Flux	0.98	0.97	0.88	0.90	0.95	0.93	0.93	0.86	0.63	0.95
Msoil	Consumption	0.85	0.96	0.92	0.19	0.76	0.03	0.22	0.14	0.26	0.22
	Production	0.85	0.75	0.44	0.14	0.69	-0.02	0.12	0.02	0.05	0.17
	Net Flux	0.84	0.96	0.95	0.25	0.77	0.04	0.26	0.19	0.40	0.24
CO Air	Consumption	-0.66	-0.76	-0.29	0.14	-0.48	0.87	0.88	0.81	0.98	0.91
	Production	-0.70	-0.66	0.08	-0.40	-0.66	-0.36	-0.48	-0.54	-0.44	-0.57
	Net Flux	-0.64	-0.73	-0.35	0.55	-0.41	0.92	0.91	0.88	0.99	0.94

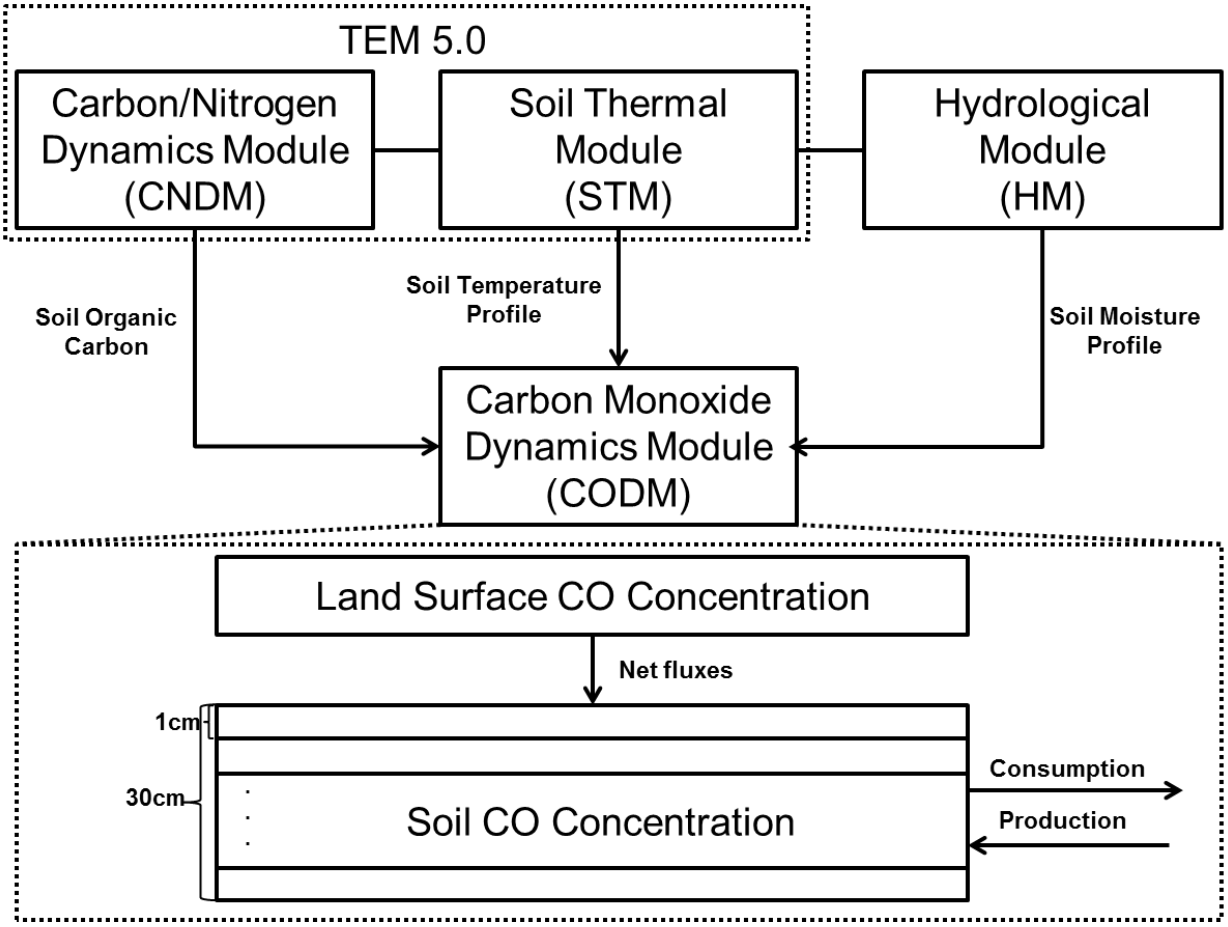

Figure 2.1. The model framework includes a carbon and nitrogen dynamics module (CNDM), a soil thermal module (STM) from Terrestrial Ecosystem Model (TEM) 5.0 (Zhuang et al., 2001, 2003), a hydrological module (HM) based on a Land Surface Module (Bonan, 1996; Zhuang et al., 2004), and a carbon monoxide dynamics module (CODM). The detailed structure of CODM includes land surface CO concentration as top boundary and thirty 1 cm thick layers (totally 30 cm) where consumption and production take place.

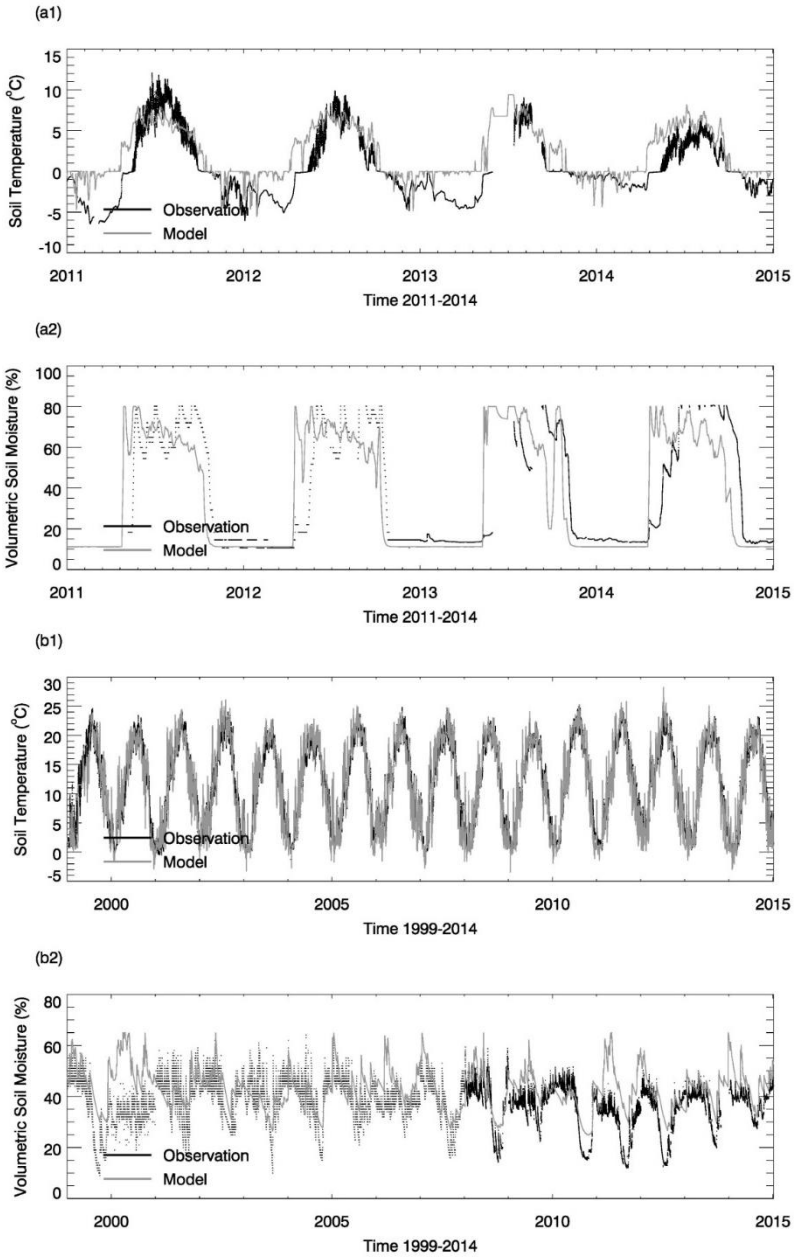

Figure 2.2. Evaluation of thermal and hydrology module at four sites: (a) Boreal Evergreen Needle Leaf Forests, (b) Temperate Deciduous Broadleaf Forests. (1) shows the soil temperature comparison between the model simulations (gray line) and observations (black line) and (2) shows the soil moisture comparison between the model simulations (gray line) and observations (black line). Specifically, the volumetric soil moisture is converted from the water content reflectometry (WCR) probe output period using an empirical calibration function of Bourgeau-Chavez et al. (2012) for 5cm-30cm layer. Some of them resulted in calculations of values greater than 100% VSM in Nakai et al. (2013) study. Our model estimated high VSM (close to 80%) is due to top 10 cm moss in the model which has a saturation VSM of 0.8

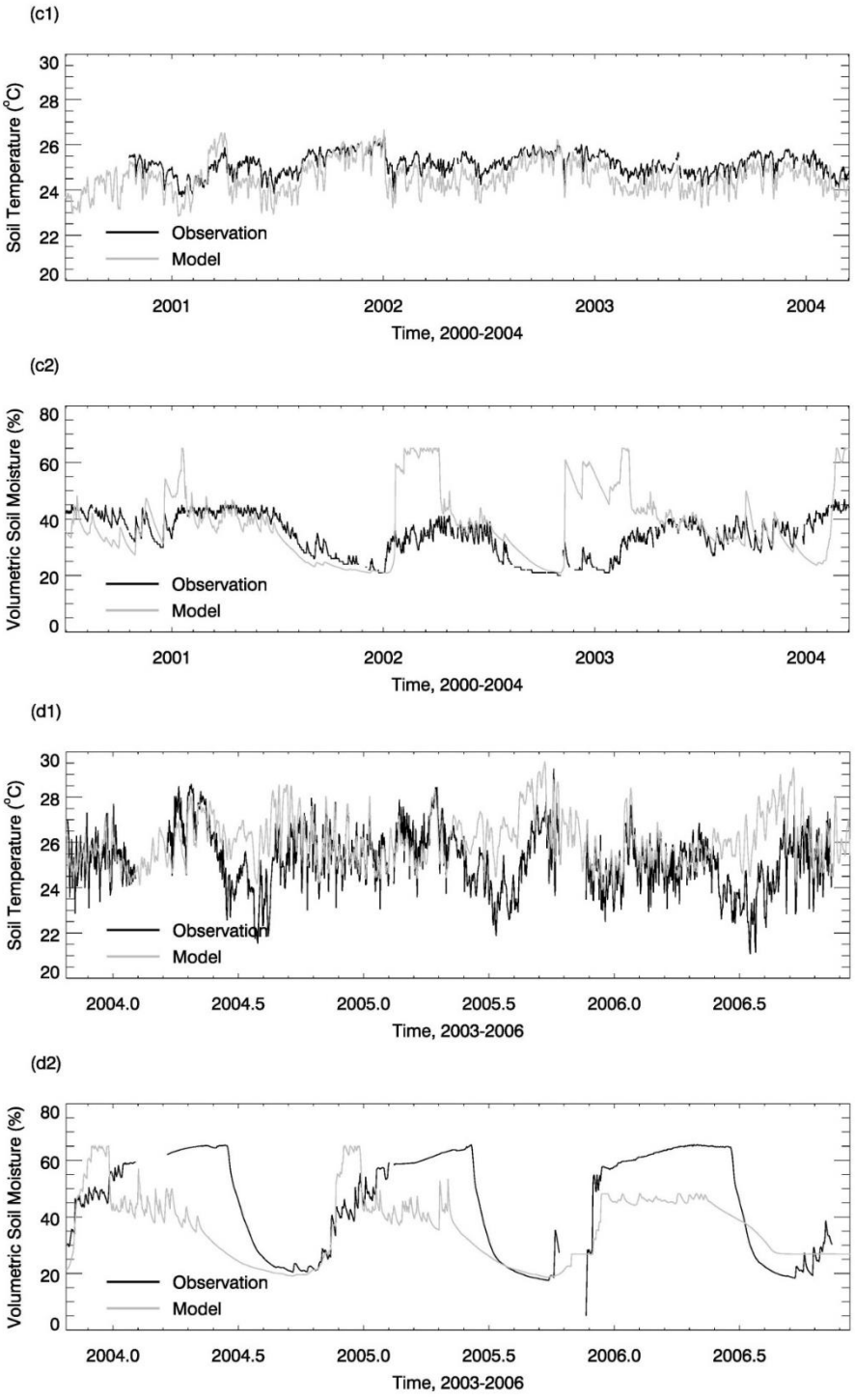

Figure 2.2.Contd. Evaluation of thermal and hydrology module at four sites: (c) Tropical Moist Forest, (d) Tropical Forest-Savanna. (1) shows the soil temperature comparison between the model simulations (gray line) and observations (black line) and (2) shows the soil moisture comparison between the model simulations (gray line) and observations (black line)

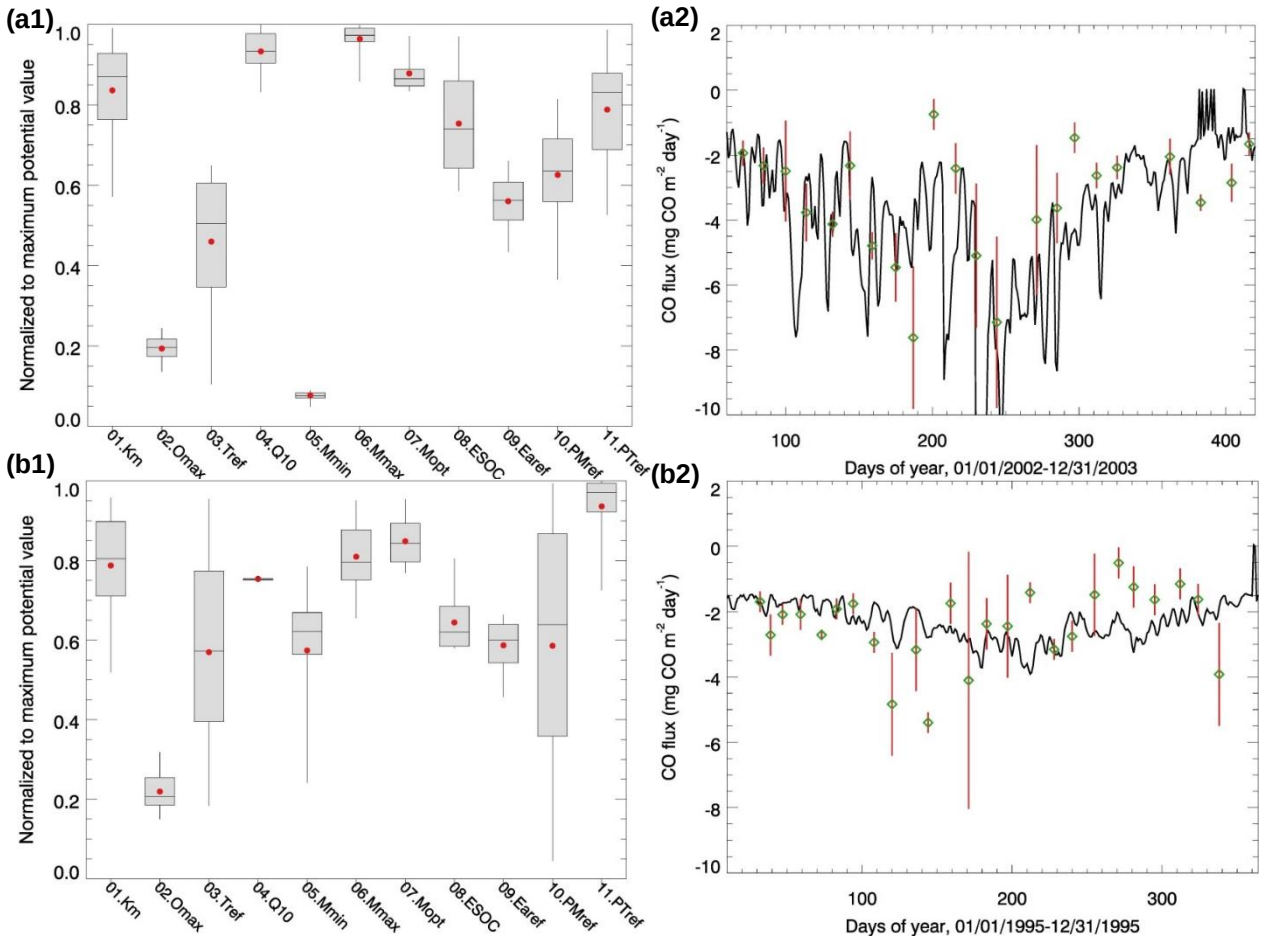

Figure 2.3. Parameter ensemble experiment results: Each parameter has 50 calibrated values generated from running SCE-UA-R 50 times independently. Parameters are normalized to their largest potential values described in Table 2. (a1) and (a2) are temperate coniferous forest normalized parameter distribution boxplots and CO flux comparisons between the model simulations (solid line, using mean value of parameters) and observations (green diamond, red lines represent error bar, site No.8), respectively. For each box, line top, box top, horizontal line inside box, box bottom and line bottom represent maximum, third quartile, median, first quartile and minimum of 50 parameter values. Red dot represents the mean value of 50 parameter values. (b1) and (b2) are plots for temperate deciduous forest (site No.11).

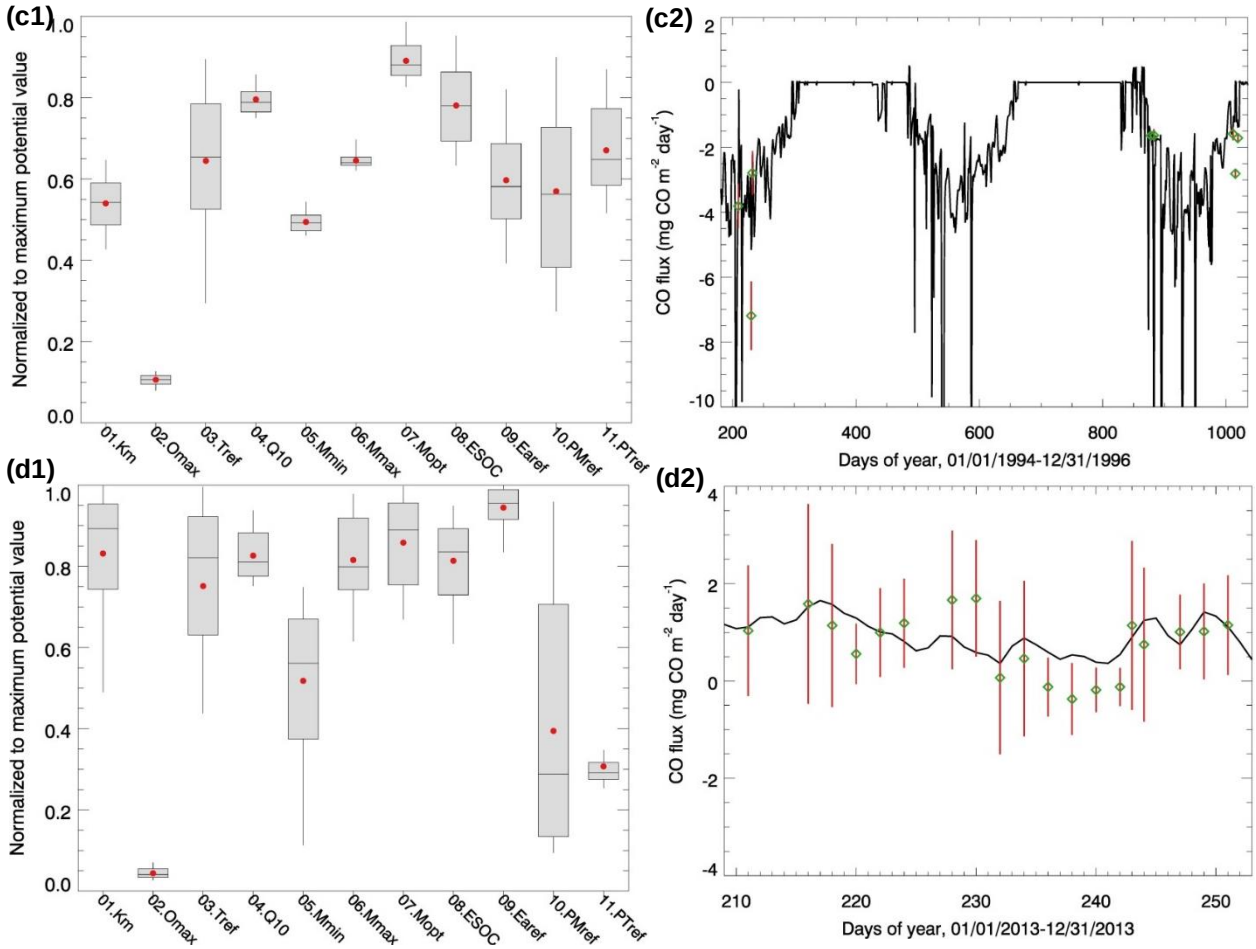

Figure 2.3. Contd. Parameter ensemble experiment results: Each parameter has 50 calibrated values generated from running SCE-UA-R 50 times independently. Parameters are normalized to their largest potential values described in Table 2. (c1) and (c2) are boreal forest normalized parameter distribution boxplots and CO flux comparisons between the model simulations (solid line, using mean value of parameters) and observations (green diamond, red lines represent error bar, site No. 12), respectively. For each box, line top, box top, horizontal line inside box, box bottom and line bottom represent maximum, third quartile, median, first quartile and minimum of 50 parameter values. Red dot represents the mean value of 50 parameter values. (d1) and (d2) are for grassland (site No.6). Grassland observation data is the sum of hourly observations so error bar represented the standard deviation.

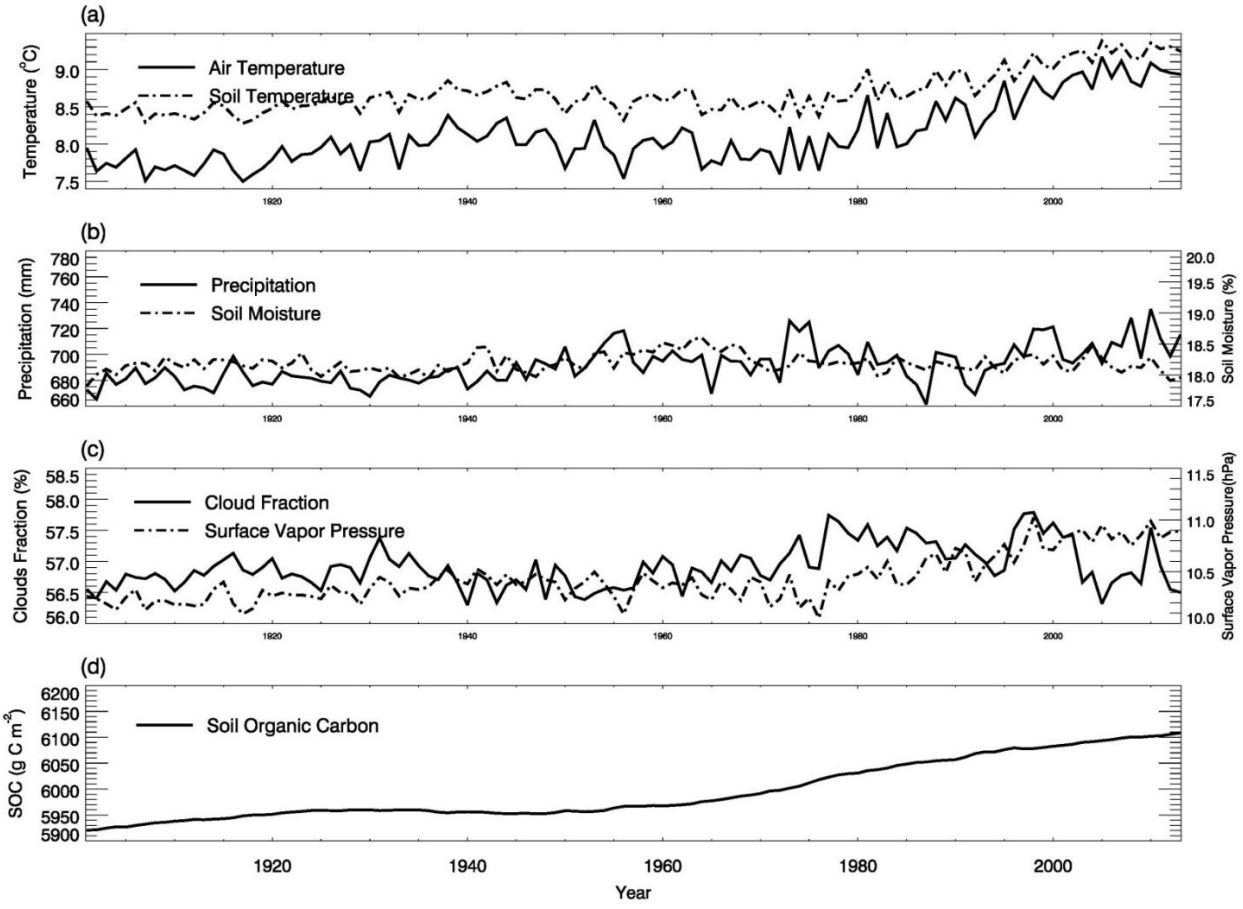

Figure 2.4. Historical global land surface (excluding Antarctic area and ocean area) mean climate, and simulated global mean soil moisture, soil temperature and SOC for the period 1901-2013.

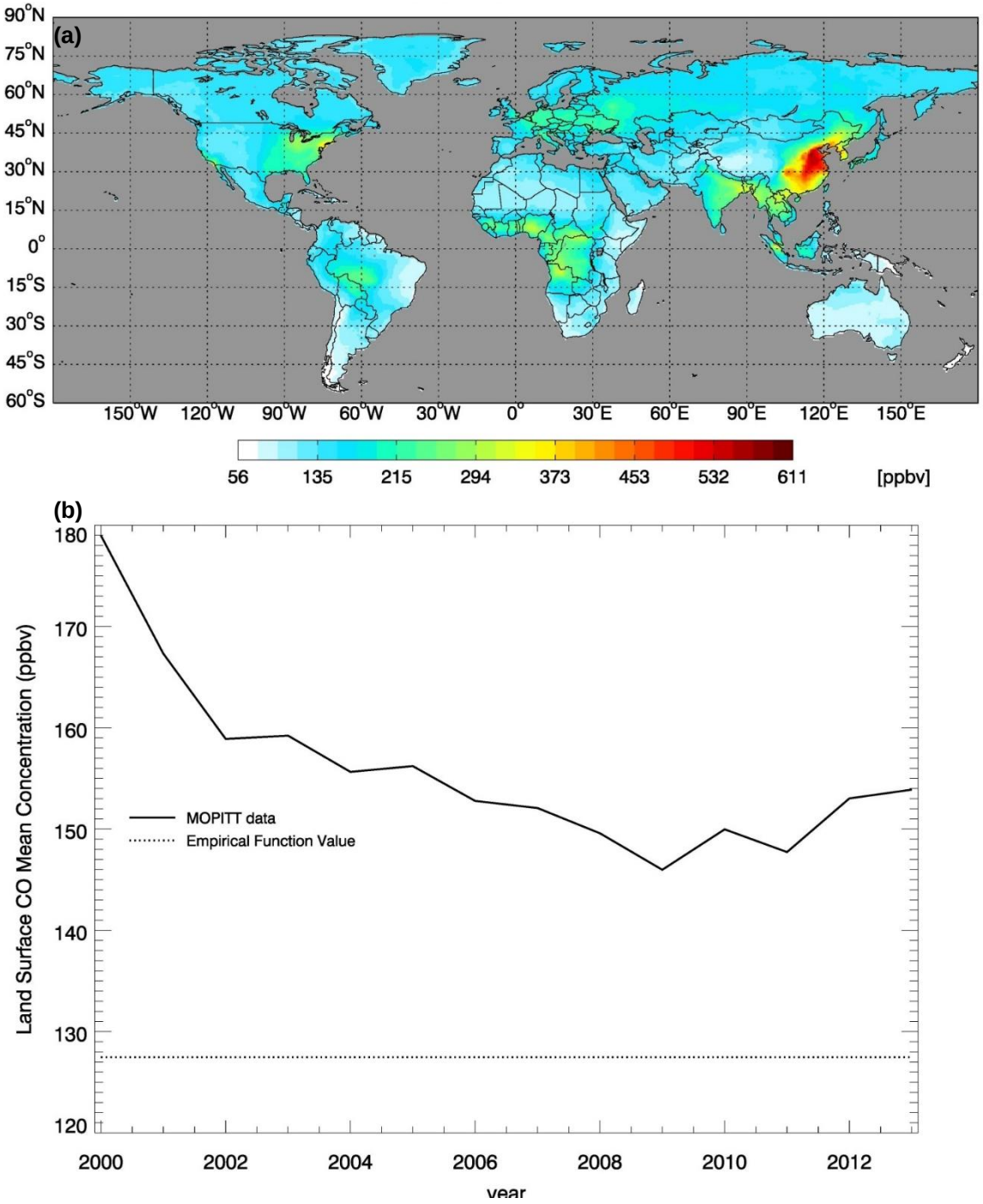

Figure 2.5. CO surface concentration data from MOPITT satellite (ppbv): (a) the global mean CO surface concentrations from MOPITT during 2000-2013; (b) the CO annual surface concentrations from both MOPITT and empirical functions (Potter et al., 1996).

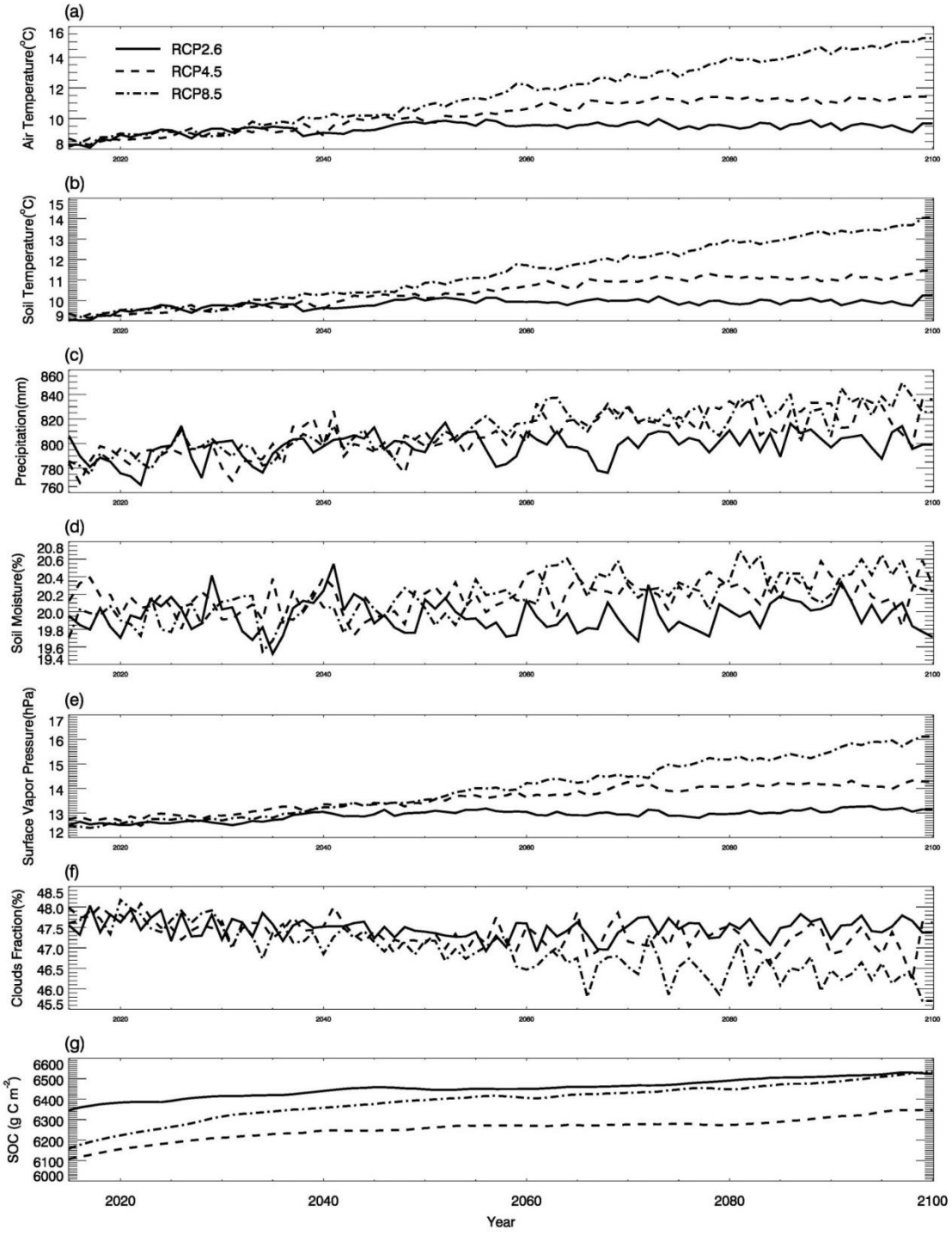

Figure 2.6. Global land surface (excluding Antarctic area and ocean area) mean climate from the RCP2.6, RCP4.5 and RCP8.5 data sets and simulated mean soil temperature, moisture and SOC: (a)-(g) are land surface air temperature (°C), soil temperature (°C), precipitation (mm), soil moisture (%), surface water vapor pressure (hpa), cloud fraction (%), and SOC (mg m^{-2}), respectively.

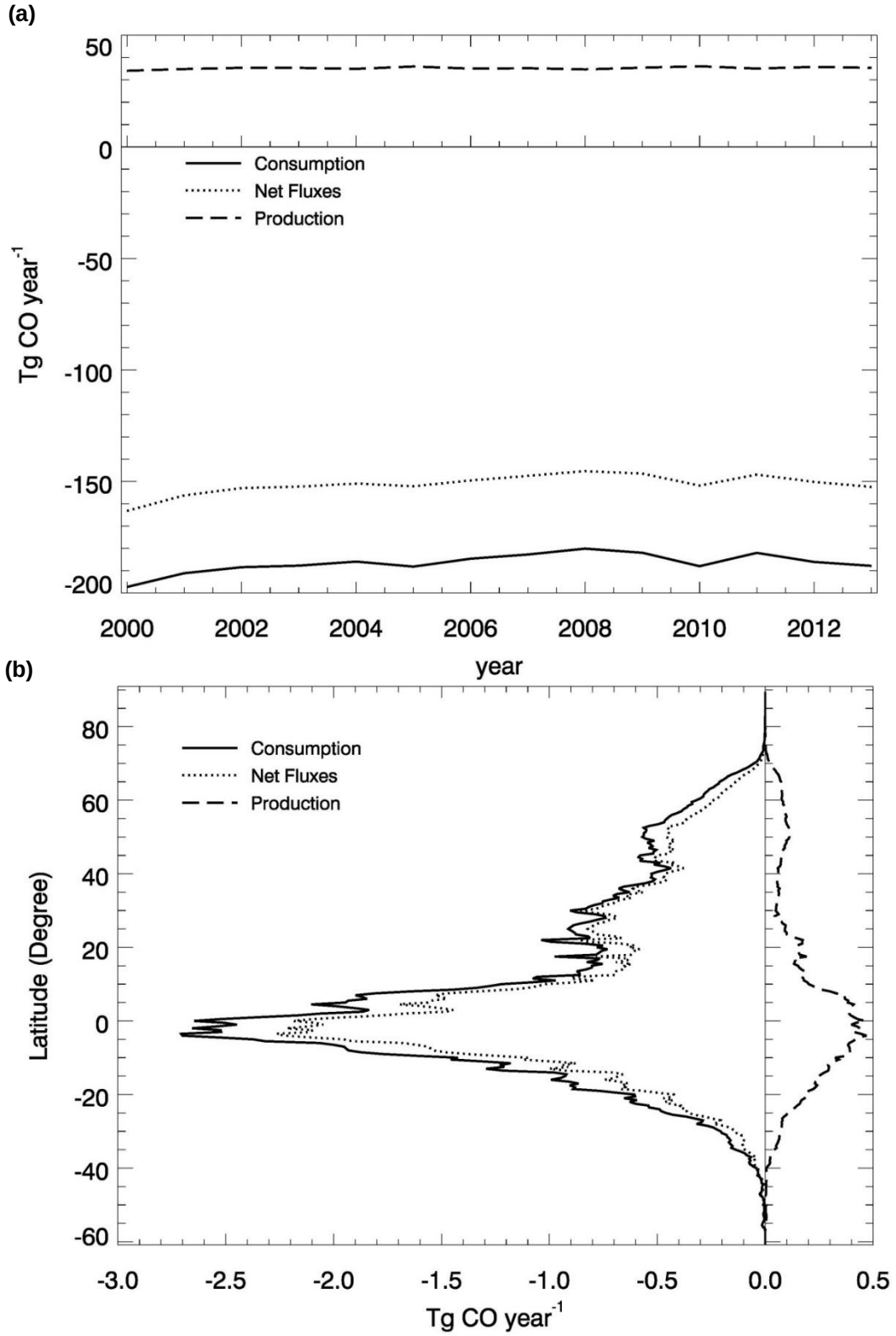

Figure 2.7. Global mean soil CO consumption, production and net flux: (a) the annual time series during 2000-2013and (b) the latitudinal distribution during 2000-2013.

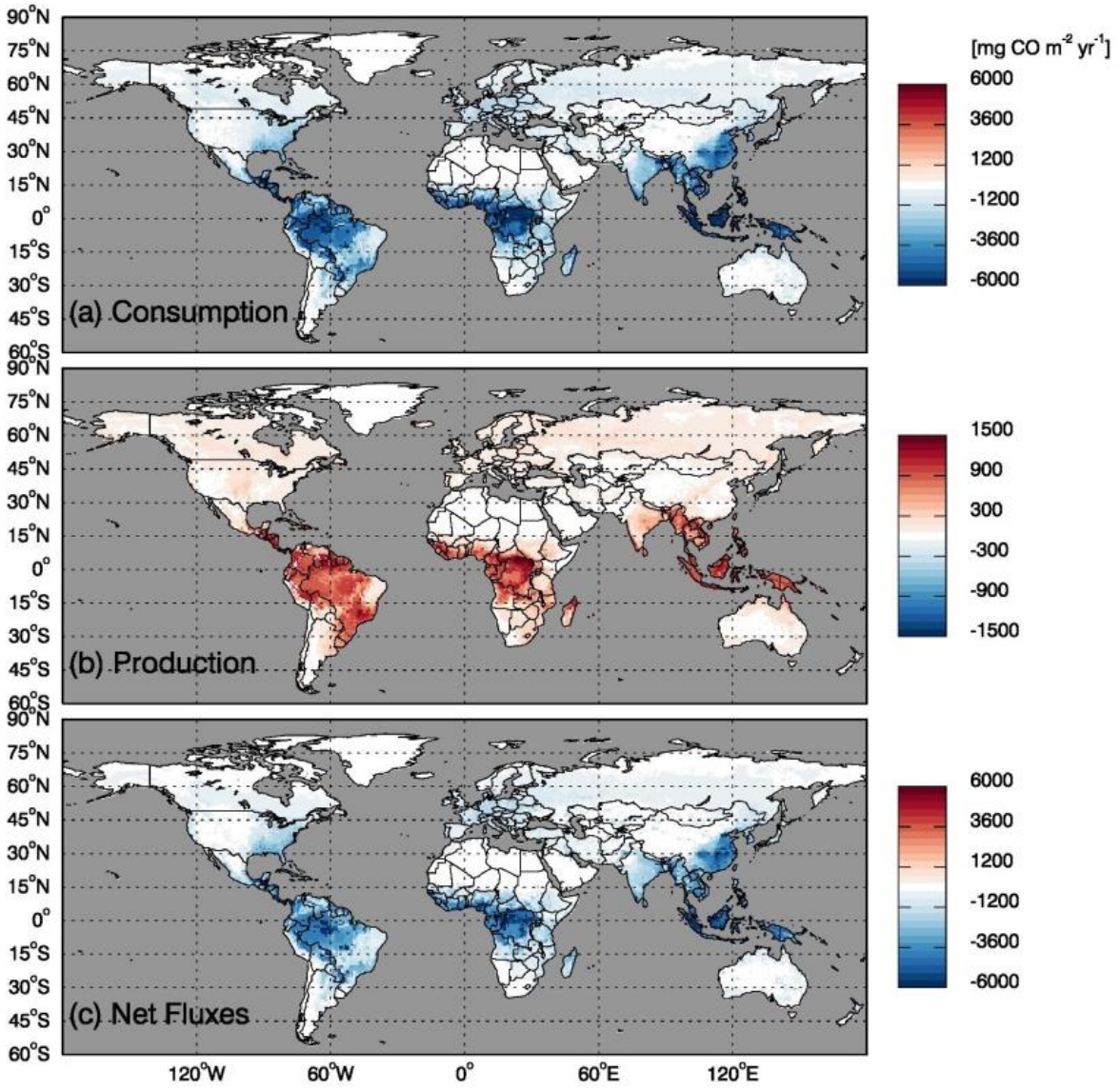

Figure 2.8. Global annual mean soil CO fluxes (mg CO m^{-2} yr^{-1}) during 2000-2013 using the MOPITT CO atmospheric surface concentration data

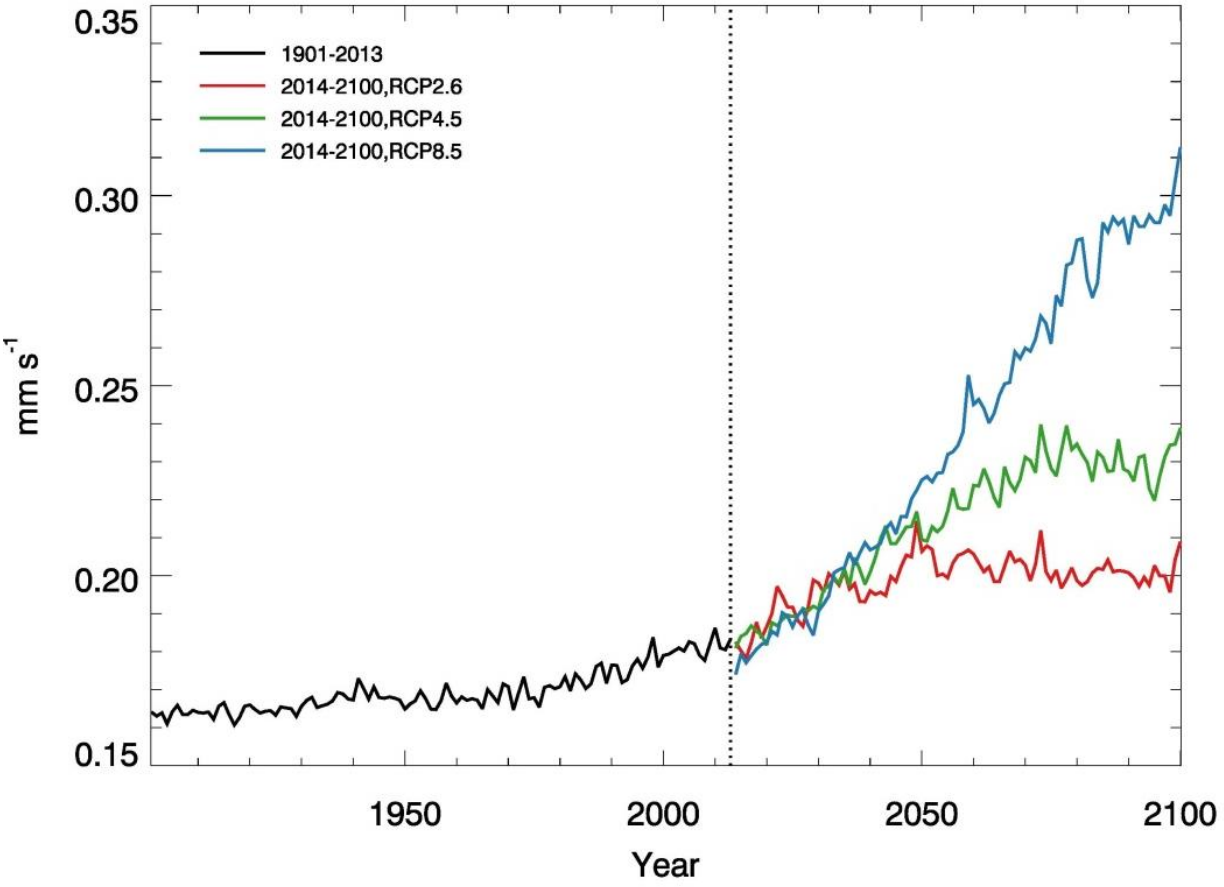

Figure 2.9. Global mean annual time series of CO deposition velocity (mm s^{-1}) using constant in time and spatially distributed CO concentration data during 1901-2013 (left side of the dot line) and under the future climate scenarios RCP2.6, RCP4.5 and RCP8.5 during 2014-2100 (right side of the dot line)

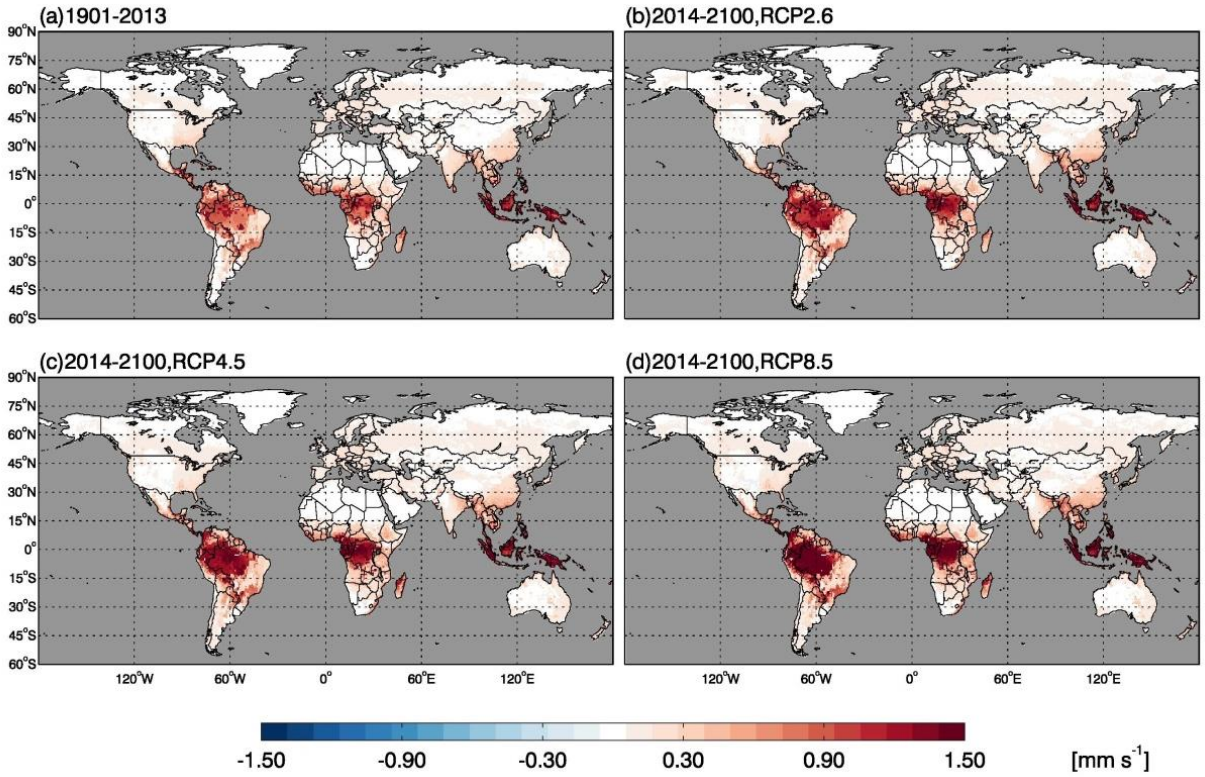

Figure 2.10. Global annual mean CO deposition velocity using constant in time and spatially distributed CO concentration data (mm s^{-1}) a) during 1901-2013 and b), c), d) under the future climate scenarios RCP2.6, RCP4.5 and RCP8.5 during 2014-2100, respectively

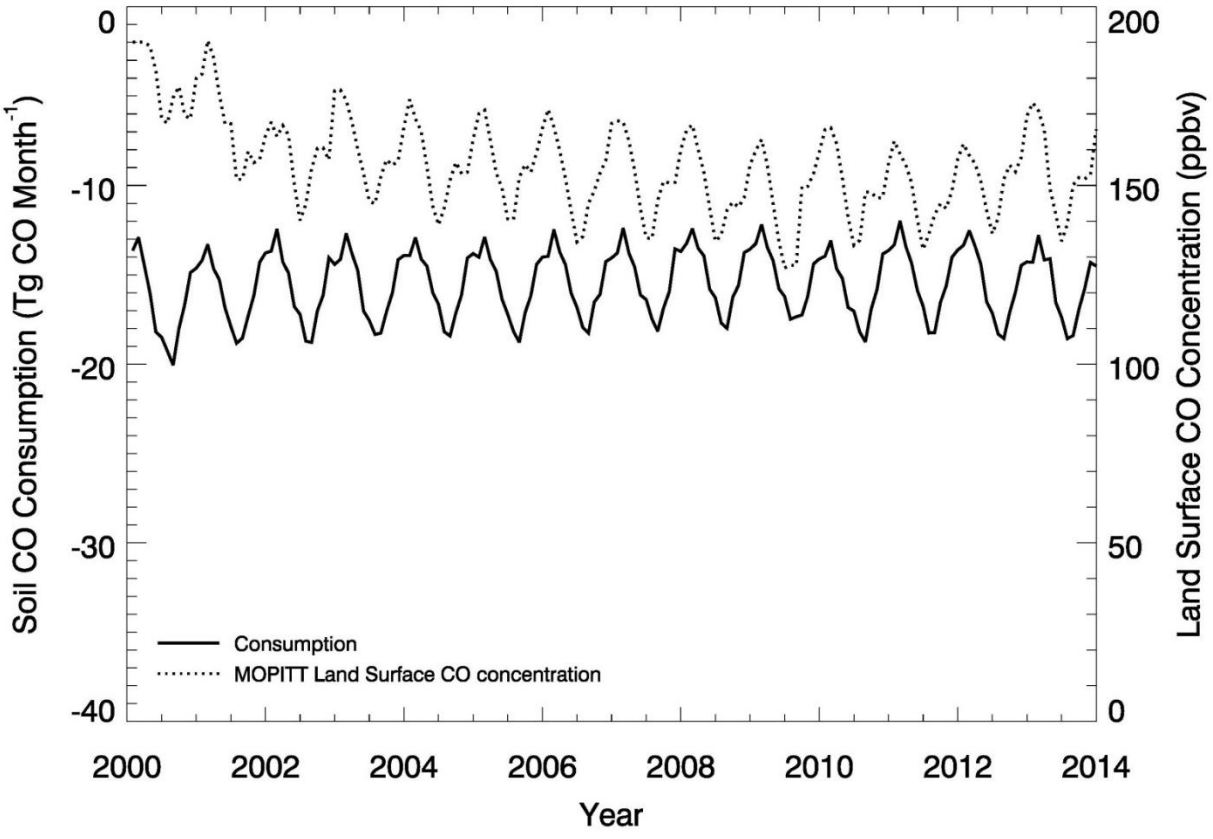

Figure 2.11. Global mean monthly time series of the MOPITT surface atmospheric CO concentration (ppbv) and soil CO consumption from model simulations E1 (Tg CO mon^{-1})

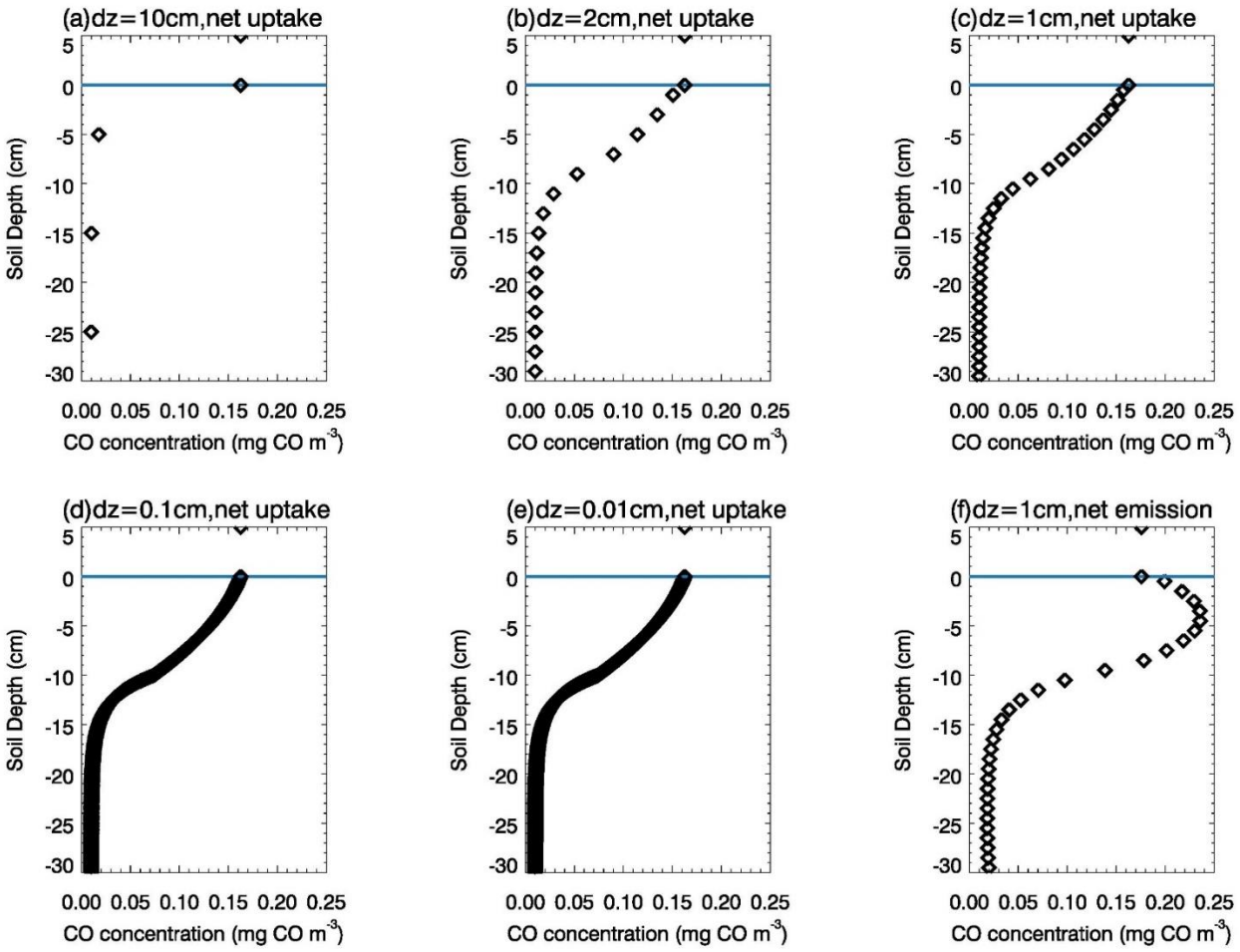

Figure 2.12. Daily mean vertical soil CO concentration profiles of top 30 cm. In the soil (depth < 0 cm), black diamonds represent the soil CO concentration (mg CO m^{-3}). Above the surface (depth>=0 cm), black diamonds represent the atmospheric CO concentration. a), b), c), d) and e) are the results from the same day when soils are a net sink of CO, but using different layer thickness (dz = 10 cm, 2 cm, 1 cm, 0.1 cm and 0.01 cm, respectively); f) is the result from the day when soils are a net source of CO, with dz = 1 cm.

CHAPTER 3. UNCERTAINTY QUANTIFICATION OF GLOBAL NET METHANE EMISSIONS FROM TERRESTRIAL ECOSYSTEMS USING A MECHANISTICALLY-BASED BIOGEOCHEMISTRY MODEL

3.1 Abstract

Quantification of methane (CH_4) emissions from wetlands and its sinks from uplands is still fraught with large uncertainties. Here, a methane biogeochemistry model was revised, parameterized and verified for various wetland ecosystems across the globe. The model was then extrapolated to the global scale to quantify the uncertainty induced from four different types of uncertainty sources including parameterization, wetland type distribution, wetland area distribution and meteorological input. We found that global wetland emissions are 212 ± 62 and 212 ± 32 Tg CH_4 yr^{-1} (1Tg = 1012 g) due to uncertain parameters and wetland type distribution, respectively, during 2000-2012. Using two wetland distribution datasets and three sets of climate data, the model simulations indicated that the global wetland emissions range from 186 to 212 CH_4 yr^{-1} for the same period. The parameters were the most significant uncertainty source. After combining the global methane consumption in the range of -34 to -46 Tg CH_4 yr^{-1}, we estimated that the global net land methane emissions are 149 - 176 Tg CH_4 yr^{-1} due to uncertain wetland distribution and meteorological input. Spatially, the northeast US and Amazon were two hotspots of methane emission, while consumption hotspots were in the eastern US and eastern China. During 1950-2016, both wetland emissions and upland consumption increased during El Niño events and decreased during La Niña events. This study highlights the need for more in situ methane flux data, more accurate wetland type and area distribution information to better constrain the model uncertainty.

3.2 Introduction

Methane (CH_4) is the second most powerful greenhouse gas behind CO_2 and has contributed to about 20% of the observed warming since pre-industrial times (Ciais et al., 2013). Atmospheric CH_4 concentrations have risen from pre-industrial levels of 715 parts per billion (ppb) since the 1800s (Etheridge et al., 1998; MacFarling Meure et al., 2006) to over 1800 ppb at the present. The growth rate of atmospheric CH_4 has decreased, however, from approximately 13 ppb yr^{-1} during the early 1980s to near zero between 1999 and 2006. Since 2007, the growth rate of atmospheric CH4 has risen again (Dlugokencky et al., 2009; Nisbet, Dlugokencky, & Bousquet, 2014; Saunois et al., 2016; Schaefer et al., 2016; Zhang et al., 2018). The inter-annual variability of atmospheric CH_4 is strongly related to the climatic sensitivity of biogenic CH_4 sources, of which global wetland CH_4 contributes 60–80% of natural emissions (Quiquet et al., 2015; Hopcroft et al., 2017) and this large role is likely to persist into the future (Zhang et al., 2017). Wetlands are an important component of the earth system and play a vital role in the global CH_4 cycling (Zhang et al., 2002; Zhuang et al., 2004; Ciais et al., 2013). CH_4 emissions from natural wetlands are the main drivers of the global interannual variability of CH_4 emissions with high confidence and contribute largely to interannual variations and anomalies of atmospheric CH_4 concentrations (Zhuang et al., 2004; Ciais et al., 2013). Therefore, it is important to improve existing CH_4 emission quantifications to better understand the role of global CH_4 cycling in the global climate system (Zhuang et al., 2004; Chen et al., 2013; Kirschke et al., 2013; Nisbet et al., 2014; Zhu et al., 2014).

To date, three approaches have been used in estimating CH_4 emissions from wetlands across different scales over the last few decades: 1) an extrapolation of flux measurements approach, which uses actual CH_4 emission measurements to scale up to global wetlands; 2) a bottom-up approach, which uses process-based models to quantify CH_4 fluxes, and 3) a top-down approach,

which uses atmospheric inverse models to estimate the distribution of CH_4 sources and sinks by incorporating atmospheric observations, an atmospheric transport model and prior estimates of source distributions and magnitudes (Arneth et al., 2010; Anderson et al., 2010; Kirschke et al., 2013; Zhu et al., 2014). Although top-down approach is widely thought to be more accurate than bottom-up approach, the current top-down approach may inadvertently include some incomplete observations and error amplifications during inverse modelling processes (Chen and Prinn, 2005; Ciais et al., 2013).

Process-based models can be used to improve CH_4 emission estimation considering the effects of complex interactions between soil, vegetation, and hydrology on CH_4 production and consumption processes. Process-based modeling became a practical alternative approach to scaling up site-level observation to regional or global scales (Cao et al., 1996; Li, 2000; Zhang et al., 2002; Zhuang et al., 2004). To date, a number of process-based models have been developed. Each has its own ways to implement wetland system complexity and CH_4 flux processes (Li, 2000; Walter and Heimann, 2000; Zhuang et al., 2004; Meng et al., 2012; Zhu et al., 2014). For instance, Cao et al. (1995, 1996) developed a CH_4 emission model for rice paddies based on C substrate level, soil organic matter (SOM) degradation and environmental control factors and improved it for global natural wetland simulation; but the model has no specific CH_4 emission process. Walter and Heimann (2000) and Walter et al. (2001a, b) developed a 1-D process-based climate sensitive model to estimate global long-term CH4 emissions from natural wetlands, forced with net primary production derived from a separate model. Li (2000) developed a denitrification–decomposition model (DNDC) to simulate CH_4 emissions but only for rice paddies. Later, Zhang et al. (2002) adopted the DNDC model and some of its key components to simulate wetland ecosystem emissions. A process model (PEATLAND) was developed to simulate CH_4 flux from peat soils

(van Huissteden et al., 2006) and up-scaled for boreal and Arctic wetland simulations (Petrescu et al., 2010), although the model did not include explicit soil biogeochemical processes. Wania et al. (2010) integrated a CH_4 emission module into the modified dynamic global vegetation model Lund-Potsdam-Jena (LPJ) to simulate CH_4 emissions from northern peatlands with consideration of permafrost dynamics, peatland hydrology and peatland vegetation. This model was then modified to simulate global net CH_4 emissions for northern peatlands, naturally inundated wetlands and rice agriculture soils (Spahni et al., 2011). To characterize uncertainties and feedbacks between CH_4 flux and climate, Riley et al. (2011) developed a CH_4 biogeochemistry model (CLM4Me) and integrated it into the land component of the Community Earth System Model (CESM) and further analyses were conducted by Meng et al. (2012), but specific plant functional types have not been incorporated in their wetlands. In contrast, Zhu et al. (2014) developed a processed CH_4 biogeochemistry model based on the Integrated Biosphere Simulator (IBIS) (TRIPLEX-GHG), considering plant functional types, but didn't consider the emissision differences between various wetland types across the landscape. The Global Carbon Project (GCP) and the Wetland and Wetland CH_4 Inter-comparison of Models Project (WETCHIMP) estimated the global methane emission from natural wetlands, ranging from 102 to 284 Tg CH_4 yr^{-1} during 2000-2017 (Kirschke et al., 2013; Melton et al., 2013; Saunois et al., 2016; Saunois et al., 2019).

The above review of the past study suggests that, although significant efforts have been made on development of bottom-up process models, current quantifications of methane emission from natural sources still have large uncertainties. Zhuang et al. (2004) have considered the important freeze-thaw processes and integrated methanogenesis modules into the Terrestrial Ecosystem Model (TEM) to estimate net CH_4 emissions from northern high latitudes. Zhuang et al. (2013) further revised the model and extrapolate it to the global scale to quantify soil methane

consumption. The hydrology and soil thermal model (HM and STM) in TEM were revised and evaluated in Liu et al. (2018). In summary, the existing bottom-up estimates still have large uncertainties using various models (Cao et al., 1996; Woodward and Lomas 2004; Hodson et al., 2011; Spahni et al., 2011; Ringeval et al., 2010; Kleinen et al., 2012; Ito and Inatomi, 2012; Melton and Arora, 2016). Further those estimates have not fully taken advantage of multiple in situ flux data for parameterizing and evaluating their models before conducting global simulations, although a few recent studies have used some site level observations (Riley et al., 2011; Zhu et al., 2014; Tian et al., 2010, 2015; Xu et al., 2016).

In this study, we made a step forward to use existing flux data at multiple sites to improve our revised methane biogeochemistry model TEM. The revised model was extensively parameterized and verified and then extrapolated to the global scale. To investigate the uncertainty sources of methane emissions, model simulations were conducted with different sets of parameters and climate forcing and wetland distribution data for the period 2000-2012. Land methane sources and sinks during 1950-2016 were then analyzed.

3.3 Method

3.3.1 Overview

We first revised the TEM-MDM model (Zhuang et al., 2003, 2004, 2007, 2013) by considering: 1) various types of wetlands based on their plant functional types and climates in boreal, temperate and tropical regions; 2) the influence of standing water above the surface on methane transport; 3) accumulated vertical methane concentrations in soils; and 4) finer time step in the MDM model (1 hour) and hydrological model (5 minutes). Second, we used the data of CH_4 flux measurement to calibrate the model with the Shuffled Complex Evolution (SCE-UA) method (Duan et al., 1993) for different wetland types in different climatic regions (Arctic, temperate and

tropical regions). The model was then evaluated using in situ data from different climatic regions. Finally, the model was extrapolated to the globe at a 0.5° by 0.5° resolution. We conducted five sets of model experiments to investigate the impact of parameters, wetland type distribution, climate, atmospheric CH_4, and wetland distribution data on soil CH_4 dynamics: 1) Ten sensitivity simulations by increasing and decreasing: a) CH_4 surface concentrations by 30%, b) NPP by 30%, c) precipitation by 30%, d) air temperature by 3°C and e) inundation area fraction by 30% for each pixel, respectively, while holding other forcing data as they were, during 2000-2012; 2) parameter uncertainty test simulations during 2000-2012; 3) wetland type uncertainty test simulations during 2000-2012; 4) forcing data uncertainty simulations using three sets of climate forcing data and two sets of wetland distribution data during 2000-2012; and 5) historical methane emission and consumption simulations during 1950-2012 to analyze CH4 responses during El Niño and La Niña events.

3.3.2 Model Modification

We revised the previous version of TEM-MDM (Zhuang et al., 2003, 2004, 2007, 2013) by considering several more detailed land methane cycling processes. First, standing water effects have not been explicitly modeled previously in TEM-MDM. However, the standing water limits atmospheric oxygen diffusion into soils, reducing oxidation, and affecting methane transport from soils and water column to the atmosphere. In this revision, a new algorithm to account for the effects on methane dynamics was incorporated into TEM-MDM. Specifically, the standing water results in smaller methane diffusivity in water (Tang et al., 2010):

$$D_w = 1.5 \times 10^{-9} \times \left(\frac{T}{298.0}\right) \qquad (3.1)$$

$$D_a = 1.9 \times 10^{-5} \times \left(\frac{T}{298.0}\right)^{1.82} \qquad (3.2)$$

$$D = \frac{1}{\tau}\frac{\epsilon D_a + \alpha\theta D_w}{\epsilon + \alpha\theta} \qquad (3.3)$$

$$\alpha = H \times \frac{T}{12.2} \qquad (3.4)$$

$$H = \ 1.3 \times 10^{-3}\exp[-1700(\frac{1}{T} - \frac{1}{298.0})] \qquad (3.5)$$

Where the Dw is the diffusivity of methane in water ($m^2\ s^{-1}$); T is the temperature at each layer (K); D is the combined diffusivity of methane in specific bulk medium ($m^2\ s^{-1}$); Da is the diffusivity of methane in air (m^2 s-1); τ is the tortuosity factor in the soil, taken as 1.5 throughout the study (Arah and Stephen, 1998); ϵ is air-filled porosity (m^3 air m^{-3} soil); α is the Bunsen coefficient for methane; θ is the volumetric soil moisture (m^3 water m^{-3} soil); H is the Henry's law constant (M atm^{-1}). The D is used as diffusivity of methane in the model. We can notice that normally Da is 1000 times larger than Dw. Thus, when there is standing water above soil surface, the D will be much smaller. Besides, the standing water supplies water to soils and change soil moisture in two situations: 1) when there is standing water above the soil surface, the soil will always be saturated; 2) when there is no standing water, the previous day's standing water will seep into soils and be treated as extra water supply besides precipitation. In the revised TEM-MDM, the simulated transient standing water is used to account for these effects.

Second, previous TEM-MDM has not considered the effects of accumulated methane in soil columns on methane fluxes. In this revision, this effect on soil methane oxidation and transport are incorporated into the model. Third, in this revision, a finer time step (5 minutes) instead of 1 hour is used for methane dynamics because gases and water would change rapidly at fine time steps. Finer time steps will reduce partial differential equation (PDE) solution errors.

For regional simulations, we used the five wetland types from Matthews and Fung (1987), including forested bog, non-forested bog, forested swamp, non-forested swamp and alluvial

formations to represent wetland types across the landscape. In addition, using a static wetland distribution data, we also used wetland inundation area data that vary across space and time. These detailed model developments and applications were documented in Appendix A.

3.3.3 Model Parameterization and Extrapolation

Wetland methane production and oxidation processes involve fifteen key parameters in TEM-MDM (Table 3.1). TEM-MDM was calibrated by running it for observational periods driven with the corresponding meteorological data at each site (Table 3.2, Figure 3.1 upper panel), and using the Shuffled Complex Evolution Approach in R language (SCE-UA-R) (Duan et al., 1993) to minimize the difference between the simulated and observed net CH_4 fluxes. Each site was run 50 times using the SCE-UA-R with 10,000 maximum loops, and all of them reached a stable state before the end of the loops. In addition to using in situ meteorological and soil data, we also used the ERA-Interim reanalysis data from the European Centre for Medium-Range Weather Forecasts (ECMWF), and reanalysis climatic data from Climatic Research Unit (CRU TS4.01, Harris et al., 2014, CRU for short) to fill any missing environmental data. Parameter values for various wetland types were summarized in Table 3.3.

The parameterized model was then evaluated at 14 sites (no. 16-29 in table 3.2), located in different climatic regions. For sites no.16-23, 26 and 27, we used nearest stations to the evaluation sites in the global data set of Global Summary of the Day (GSOD) (http://www7.ncdc.noaa.gov/CDO/cdoselect.cmd?datasetabbv=GSOD&countryabbv=&georegionabbv=) to drive the model, and the station IDs are 020200, 020200, 022740, 029290, 029450, 716278, 718270, 718113, 724675, and 948990, respectively. For sites no.18, we used the station 022860 together with 022740 to fill the missing data of precipitation. If the data from GSOD missed a few days of observation, we would fill the missing points by linear interpolation. For

longer data gaps (longer than 15 days), we filled the data with CRU data. For other sites, we used CRU data to drive the model. Since the GSOD data didn't provide cloud fraction or solar radiation data, we used the CRU cloud fraction data for all sites. Vegetation type, wetland type, soil texture, and elevation information have been set based on site observations.

3.3.4 Data Organization

To get the spatially and temporally explicit estimates of CH_4 consumption and emission at the global scale, we used the data of land cover, soils, climate and leaf area index (LAI) from various sources at a spatial resolution of 0.5° latitude X 0.5° longitude to drive TEM-MDM. The land cover data include the potential vegetation distribution (Melillo et al., 1993) and soil texture (Zhuang et al., 2003), which were used to assign vegetation- and texture-specific parameters to each grid cell.

In order to map the global methane fluxes from natural wetland and investigate the uncertainties from different sources, we used climate forcing data including the monthly CRU data during 1950-2012, the daily ERA Interim data from European Centre for Medium-Range Weather Forecasts (ECMWF; Dee et al., 2011), during 2000-2012, and the daily reanalysis data from National Centers for Environmental Prediction (NCEP; Kalnay et al., 1996) during 2000-2012 (Figure 3.2). The resolutions of CRU and ECMWF data are 0.5° latitude X 0.5° longitude. The NCEP data with an original spatial resolution of 2.5° latitude X 2.5° longitude were re-gridded to 0.5° latitude X 0.5° longitude resolution. We also used wetland distribution data including static wetland map from Matthews and Fung (1987) (M&F), and the transient wetland inundation area fraction data derived from previous study of merging Surface WAter Microwave Product Series (SWAMPS; Schroeder et al 2015) with the static inventory of wetland area from the Global Lakes and Wetlands Database (GLWD; Lehner and Doll 2004) by Poulter et al. (2017) (SWAMPS-

GLWD) during 2000-2012, (Figure 3.3). The spatial resolutions of these datasets are 0.5° latitude X 0.5° longitude. Observed CO_2 concentrations from in situ air measurements taken at Mauna Loa Observatory by Earth System Research Lab of National Oceanic and Atmospheric Administration (NOAA/ESRL, https://www.esrl.noaa.gov/gmd/ccgg/trends/data.html) were used for the period covering 1958–2012. Observed atmospheric CH_4 concentration data from NOAA/ESRL (www.esrl.noaa.gov/gmd/ccgg/trends_ch4/) cover 1984-2012. CO2 data before 1984 were from summary of United States Environment Protection Agency (EPA, https://www.epa.gov/climate-indicators/climate-change-indicators-atmospheric-concentrations-greenhouse-gases). El Niño and La Niña event data were derived from Zhu et al. (2017).

3.3.5 Model Experimental Design

To investigate the uncertainty from different sources, we conducted five experiments: 1) the sensitivity and correlations during 2000-2012 using CRU and SWAMPS_GLWD data. Ten sensitivity simulations were driven with varying different forcing variables while keeping others as they were, by increasing or decreasing: a) CH_4 surface concentrations by 30%, b) NPP by 30%, c) precipitation by 30%, d) air temperature by 3°C and e) inundation area fraction by 30% for each pixel, respectively, during 2000-2012. The magnitudes of changes in the input data were chosen to ensure they do not exceed the values identified in the field or based on previous model studies (Zhuang et al., 2004; Zhuang et al., 2013; Liu et al., 2018). Modifications were applied to the forcing data by multiplying a factor (e.g., 1.3 to NPP) to every value used in model simulations. Correlations were calculated from sensitivity baseline simulation (experiment E1).; 2) the uncertainty of parameters during 2000-2012 using CRU and SWAMPS-GLWD data. We conducted 100 simulations with parameters randomly chosen in optimized ranges and compared the results with the baseline simulation which uses the mean value of each parameter (experiment

E2); 3) the uncertainty of wetland type distribution during 2000-2012 using CRU and SWAMPS-GLWD data. M&F wetland data could only identify the wetland type for half of the pixels. Other pixels could have a period with inundated area as SWAMPS-GLWD indicated and were first grouped by their climate and vegetation types. Each group would then randomly choose possible wetland types. In this way, totally 770 simulations were conducted with different wetland type distributions (experiment E3); 4) the uncertainty from forcing data using CRU, ECMWF, NCEP, M&F wetland data and SWAMPS-GLWD inundation data during 2000-2012. Six forcing data uncertainty test simulations were driven with different forcing data sets while keeping others as they were: a) using CRU climate data with static M&F wetland data and transient SWAMPS-GLWD inundation data, b) using ECMWF climate data with static M&F wetland data and transient SWAMPS-GLWD inundation data, and c) using NCEP climate data with static M&F wetland data and transient SWAMPS-GLWD inundation data (experiment E4); and 5) historical methane emission and consumption simulation using CRU data during 1950-2012 and compare to El Niño and La Niña events. The inundation area fraction data for the period 2000-2012 are from SWAMPS-GLWD data. We used the inundation data of year 2000 to represent the inundation distribution and area for each year during 1950-1999 (experiment E5).

3.4 Results

3.4.1 Site Calibration and Evaluation

We use p-value < 0.05, t-value > 2.0, and relatively large R^2 to determine if the model simulations are well correlated with the observation at calibration sites. Our overall calibration and evaluation results are significant. The R^2 is 0.44 with p-value < 0.01 and T value = 24.8 for overall calibration results. R^2 is 0.41 with p-value<0.01 and t-value=16.7 for overall evaluation results. For most sites, the model captures the magnitude and the variation of the observation in model

evaluations (Table 3.4). Significant correlations are found for most sites except three sites from the boreal region (site 16, 17 and 22) and one site from the temperate region (site 24, Table 3.4). The poor performance for those sites is discussed in Appendix A Text A.2. The simulated and observed mean values are comparable with root mean square errors (RMSE) less than 270 mg CH_4 m^{-2} day^{-1}. For site 28 and 29, simulations indicate the average emissions are 25 mg CH_4 m^{-2} day^{-1} with variation of 14 mg CH_4 m^{-2} day^{-1}, while observations range from 4 to 217 mg CH_4 m^{-2} day^{-1}.

3.4.2 Sensitivity analysis

Modeled methane emissions are sensitive to NPP, air temperature and inundation area fraction globally, and also sensitive to precipitation in 45°S-0 latitude regions. Simulated methane consumption is sensitive to atmospheric methane concentration, precipitation and air temperature (Table 3.5). Simulated methane emissions are highly correlated with NPP, air temperature, inundation area fraction and soil temperature globally, while methane consumption is highly correlated with NPP, precipitation, air temperature, inundation area fraction and soil temperature globally. Annual correlations showed that the interannual variability of methane emissions are correlated with air temperature and soil temperature, while the interannual variability of methane consumption is correlated with inundation area fraction and soil moisture (Table 3.6).

3.4.3 Global emission uncertainty due to uncertain parameters

Global gross methane emission uncertainty increases during summer and decreases in winter, with a large uncertainty range surrounding the baseline simulation (Figure 3.4a). Globally, annual methane emission mean values (red dots) are close to the baseline with standard deviation (STD) of 62 Tg CH_4 yr^{-1} (Figure 3.4b, Table 3.7). Temperate forest bog (type 6), tropical forested swamps (type 13) and boreal forested bog (type 1) contribute most of the uncertainty due to their uncertain parameters, with annual mean STDs of 23, 22 and 15 Tg CH_4 yr^{-1}, respectively (Table 3.7). The

temperate region (0-45°N) in Northern Hemisphere contributes most to the parameter uncertainties while boreal region (45°N-90°N) in the Northern Hemisphere contributes second most, with annual mean STDs of 40 and 19 Tg CH_4 yr^{-1}, respectively (Figure 3.4c, Table 3.8).

3.4.4 Global emission uncertainty due to uncertain wetland type distribution

Global gross methane emission uncertainty due to uncertain wetland type distribution increases during summer and decreases in winter, with a large uncertainty range surrounding the baseline simulation (Figure 3.5a). Globally, methane emissions are lower than the baseline with STD of 32 Tg CH_4 yr^{-1} (Figure 3.5b, Table 3.8). The temperate region (0-45° N) in the Northern Hemisphere contributes most to the wetland type uncertainty (Figure 3.5c, Table 3.8).

3.4.5 Uncertainty due to uncertain forcing data

Driven with CRU data, the global wetland methane emissions are 186 and 212 Tg CH_4 yr^{-1} by using M&F static wetland distribution data and SWAMPS-GLWD dynamical inundation data, respectively, during 2000-2012. The respective emissions using static and dynamic inundation data are 195 and 210 Tg CH_4 yr^{-1} driven by NCEP data, and 195 and 212 Tg CH_4 yr^{-1} driven by ECMWF data (Table 3.9, Figure 3.6). These result in the global wetland emissions ranging from 186 to 212 Tg CH_4 yr^{-1} for the study period. The global soil consumption ranges from -34 to -46 Tg CH_4 yr^{-1}, resulting in global net land methane budget ranging from 149 to 176 Tg CH_4 yr^{-1} during 2000 – 2012 (Table 3.9). Among these simulations the seasonal emissions and consumption are similar, while emissions from using transient inundation area fraction data are always higher during summer and lower during winter comparing with the simulations using static wetland data (Figure 3.6 upper panel). The peak value of seasonal emissions has shifted a little from July to June when using transient wetland data (Figure 3.6 upper panel). Using different wetland distribution data result in large differences in global emissions (Figure 3.6 lower panel). Methane

emissions from simulations using CRU and static wetland map are lowest in all simulations (Figure 3.6 lower panel, figure 3.7a, c, e). Methane emissions are similar when using different climate forcing data, but have large differences when using different inundation data (Figure 3.7a, c, e). Methane emission flux increases in regions like middle of Northern America and eastern Asia, and decreases in regions like northern high latitudes (Figure 3.7b, d, f). Methane consumptions increase in Europe, Eastern US and Eastern Asia when using ECMWF and NCEP climate forcing and comparing with baseline with CRU climate forcing (Figure 3.8a, c, e). When using transient wetland inundation data, the methane consumption fluxes increases in temperate region of the Northern hemisphere and Eastern Australia, and decrease in boreal region of the Northern Hemisphere and tropical regions (Figure 3.8b, d, f).

3.4.6 Global land methane budget estimates during 1950-2012

Model estimates of annual methane emissions are 198 Tg CH_4 yr^{-1} and consumption is -32 Tg CH_4 yr^{-1} during 1950-2012 (Table 3.10). Temperate regions (0-45° N) contribute most to the global methane emission and consumption (Table 3.10). Eastern US, Eastern Asia and Amazonia regions are emission hotspots, while consumption hotspots are eastern US, middle east and eastern China (Figure 3.9a, b). For instance, three methane emission peaks show up around 30° N, 45° N and the equator, while one consumption peak shows around 35° N (Figure 3.9c). Temporally, both methane emission and the consumption increased during El Niño events and decreased during La Niña events (Figure 3.10).

3.5 Discussion

3.5.1 Major controls to the global land methane budget

Methane emissions are globally sensitive to changes in NPP, air temperature and wetland distributions (Table 3.5). The global annual emissions are more than 5 times larger than consumption. Of the three major controls, methane emissions are relatively more sensitive to air temperature, varying 46% or -31% when temperature is increased by 3 or decreased by -3 ℃ (Table 3.5). Methane emissions are also sensitive to the change in wetland distribution, resulting in 25% or -30% changes when the inundation area increased or decreased by 30% (Table 3.5). Methane emissions are not sensitive to the precipitation globally, which only change 1.5% and -2.4% when adjusting precipitation by 30%, but are sensitive in some specific regions such as 45° S-0, which change 3.0% and 7.6% (Table 3.5). The reason is that only the water table depth or standing water will influence the methane production in soils, and the water table depth is not calculated linearly in our model, which is significantly influenced by temperature (Zhuang et al., 2004, 2013). Besides, the wetland distribution overlaps with the sensitivities of precipitation to some extent. The correlations show that methane emissions are highly correlated with NPP, air temperature, wetland inundation area fraction and soil temperature ($R>0.9$, Table 3.6). This is mainly due to the fact that most of these variables share the same pattern as air temperature, which is high in summer and low in winter. Methane emissions are only correlated well with air temperature and soil temperature ($R>0.6$, Table 3.6).

Methane consumption is most sensitive to air temperature (change 53% and -26%, Table 3.5). This is mainly due to the treatment that Q10 function used in the model as temperature influences methane consumption (Zhuang et al., 2004, 2013). Methane consumption is sensitive to atmospheric methane concentration (changes by 16% and -16%, Table 3.5). The methane

consumption is also sensitive to precipitation globally comparing with the emission sensitivity (changes by 4% and -5%, Table 3.5) (Zhuang et al., 2004, 2013). The monthly methane consumption is well correlated with NPP, air temperature, soil temperature and wetland inundation fraction (|R| >= 0.9). In contrast, annual methane consumption is only correlated with wetland inundation area fraction and soil moisture (|R| > 0.6, Table 3.6). Wetland inundation area fraction influences the area of upland in each pixel, affecting methane consumption.

3.5.2 Model Uncertainty Sources

Methane emissions have a larger uncertainty during summer and lower uncertainty during winter (Figure 3.4a, Figure 3.5a). The reason is that methane emissions are higher during summer in the northern hemisphere which has higher wetland inundation area fraction (Figure 3.3), with large anomalies (75%-100% quantile) below base line estimates (Figure 3.5b). Globally the uncertain parameters result in 62 Tg CH_4 yr^{-1} methane emissions while the uncertain wetland type results in 32 Tg CH_4 yr^{-1} in our estimates. The temperate forested bog, tropical forested swamp and boreal forested bog are three main sources of the parameter uncertainties due to their relatively high rate of methane emissions and a large number of pixels (Table 3.7). There are some types containing a small number of pixels, such as boreal forested swamp, boreal alluvial formations, temperate alluvia formations and tropical forested bog. Northern temperate regions (0-45° N) contribute most to the parameter and wetland type uncertainty, due to the biggest emissions over this region and their diverse vegetation types (Table 3.8).

In order to investigate the forcing data influences on methane emission and production, we used different sources of climate and wetland distribution data (Figure 3.2, 3.3). CRU data have higher global average air temperature and lower precipitation. We used cloud fraction data instead of solar radiation (Figure 3.2). It shall be noticed that the ECMWF solar radiation data are lower

than NCEP data. We use 12 hours average solar radiation data from ECMWF and use average of daily data from NCEP. The wetland distribution data from different sources vary significantly (Figure 3.3). Wetland inundation area fraction data showed a high peak during summer and a low peak during winter. The M&F data have the biggest global average value but the SWAMPS-GLWD data can be higher than M&F data during summer (Figure 3.3). The M&F data don't have seasonal variation and provide the same amount of inundated area during winter as in summer without considering soil frozen. TEM-MDM will not stop produce methane when soil temperature is lower than 0℃ and this process will increase the winter estimate when using M&F data to some extent. Using different sets of climate forcing data, the emission estimates using CRU data are lower than using ECMWF and NCEP data (Figure 3.6). When using different wetland distribution data, the methane emission estimates vary up to 26 Tg CH_4 yr^{-1} (Table 3.9, Figure 3.6). Global distribution of methane emissions and consumptions don't change significantly when using different climate forcing data but will change significantly when using different wetland distribution data (Figure 3.7, 3.8). Global methane emission and consumption changes indicate that SWAMPS-GLWD has smaller wetland inundated area in boreal regions and larger area in tropical regions in comparison to M&F data (Figure 3.7, 3.8).

3.5.3 Comparison with Other Studies

The previous global estimates of methane emissions from wetlands range from 127 to 284 Tg CH_4 yr^{-1} for various historical periods (Table 3.11). This study estimates the global methane emissions of 185-217 Tg CH_4 yr^{-1} from wetlands, when using CRU climate data and SWAMPS-GLWD wetland inundation area fraction data (Table 3.11). For boreal regions, our model showed relatively lower mean emissions (~6 Tg CH_4 yr^{-1}, figure 3.9c) than previous mean estimates (14-16 Tg CH_4 yr^{-1}, Saunois et al., 2016, Kirschke et al., 2013). This might be due to wetland

inundation area uncertainty, such as inclusion of inland water in Poulter et al. (2017); and due to the lack of long-term methane fluxes observations from higher latitudes (>60°N, Table 3.2), resulting in methane emissions from boreal regions varying from 1 to 25 Tg CH_4 yr^{-1}. For temperate regions, our model showed a large peak and higher emissions when comparing with previous studies in latitudinal distributions (figure 3.9c, Saunois et al., 2016, Kirschke et al., 2013). This should be due to lacking long-term methane flux observation data from the region close to tropics (30°N-40°N) in our modeling. Regions including eastern US, middle east and eastern China showed large emissions during summer, at 29 and 27 Tg CH_4 yr^{-1}, respectively, because of high temperature (Figure 3.9a). Although regional results from previous works (Saunois et al., 2016, Kirschke et al., 2013) also indicated that eastern US and eastern China are hotspots, South America should be the biggest source. We estimate that methane emissions from South America are relatively lower than previous studies (Saunois et al., 2016, Kirschke et al., 2013). This is mainly due to extremely lack of the observation data from tropical regions and large uncertainties in wetland inundation area identifications (Table 3.2, Poulter et al., 2017). Besides, Amazon basin observations have recently found that tropical trees act as significant conduits for wetland CH_4 emissions (Pangala et al., 2017). Our current estimates however have not accounted for these effects. In the simulations during 1950-2012, both emission and consumption increased during El Niño events and decreased during La Niña events (Figure 3.10). Zhu et al. (2017) showed an opposite result, indicating there were less emissions from tropical regions during El Niño events and more emissions during La Niña events. This discrepancy might be due to that methane emissions and consumptions are more sensitive to air temperature change in our model. During El Niño events, the global mean air temperature would increase so the methane emission and consumption would increase. During La Niña events, global mean temperature is generally

relatively low and would decrease methane emission and consumption. Compared to previous modeling studies (Cao et al., 1995, 1996; Li, 2000; Walter and Heimann, 2000; Zhuang et al., 2004; Meng et al., 2012; Zhu et al., 2014), this study considers wetland types in different climatic regions and the influence of standing water for methane emissions. We use a finer time step (1 hour for methane module and 5 minutes for hydrology module) than before to reduce partial differential equation solution errors.

3.6 Conclusions

This study quantifies the uncertainty sources and magnitudes of global land methane emissions and consumption. We find that parameters, wetland type distribution and wetland area distribution are three major uncertainty sources for methane emissions, inducing emission uncertainty 62, 32 and up to 26 Tg CH_4 yr^{-1}, respectively. Climate forcing uncertainties result in the emission uncertainty up to 9 Tg CH_4 yr^{-1}. Driven with CRU forcing data and SWAMPS-GLWD inundation area fraction data, our model estimates that the global wetlands emit 198 Tg CH_4 yr^{-1} and uplands consume 32 Tg CH_4 yr^{-1} during 1950-2012. Global methane emissions and consumption increase during El Niño events and decrease during La Niña events. Our estimates can be improved by using more in situ data in parameterization and more accurate dynamical wetlands and inundation distribution data to drive our model. This study provided an improved process-based methane biogeochemistry model to the research community and helped identify important uncertainty sources and controlling factors for quantifying global wetland methane emissions. By organizing and using a large field dataset of methane fluxes for model parameterization and evaluation, this study helped significantly constrain the global wetland emission uncertainty.

Acknowledgment: This study is supported by NASA (NNX17AK20G), the Department of Energy (DESC0008092 and DE-SC0007007), and the NSF Division of Information and Intelligent Systems (NSF-1028291). The supercomputing is provided by the Rosen Center for Advanced Computing at Purdue University. We are also grateful to the University of Tuscia (dep. DIBAF), Italy, and their affiliated members, for their help and the use of their field data. All data used in this manuscript can be accessed in Purdue University Research Repository (PURR) through the link: https://doi.org/10.4231/W1M6-4651.

Table 3.1. Parameters related to methane production and oxidation process for wetlands in TEM

Name	Meaning	Units	Upper bounds	Lower bounds
M_{GO}	ecosystem-specific maximum potential CH production rate	µM h^{-1}	1	0.1
K_{PCH4}	methane ecosystem-specific half saturation constant used in Michaelis- Menten kinetics of methane production process	µM	0.2	0.05
P_{Q10}	ecosystem-specific Q10 coefficient indicating the dependency of CH_4 production to soil temperature	unitless	9	1.5
NPP_{MAX}	the maximum monthly NPP expected for a particular vegetation type	gC m^{-2} mon^{-1}	400	50
L_{MAXB}	prescribed maximum lower boundary	mm	2500	900
T_{PR}	the reference temperature for methanogenesis that varies across ecosystems	°C	30	0
O_{MAX}	ecosystem-specific maximum oxidation coefficient	µM h^{-1}	360	0.3
K_{OCH4}	methane ecosystem-specific half saturation constant used in Michaelis- Menten kinetics of methane oxidation process	µM	66.2	1
O_{Q10}	ecosystem-specific Q10 coefficient indicating the soil temperature dependency of methanotrophy	unitless	9	1.5
K_O	oxygen ecosystem-specific half saturation constant of oxygen used in Michaelis-Menten kinetics of methane oxidation process	µM	200	37
afp	air filled porosity of the soil	v/v	0.3	0.1
M_{VMAX}	maximum volumetric soil moisture for methanotrophy	v/v	1	0.6
M_{VMIN}	minimum volumetric soil moisture for methanotrophy	v/v	0.3	0
M_{VOPT}	optimum volumetric soil moisture for methanotrophy	v/v	0.6	0.3
T_{OR}	the reference temperature for methanotrophy that varies across ecosystems	C	30	0

Table 3.2. Calibration (No.1-15) and validation sites (No.16-29) list

No.	Site name	Location (Degree)	Type	Climate	Time	Reference
1	SSA-fen	104.62W, 53.8N	Peatland, Fen	Boreal	Daily 1994-1995	Sellers, et al., (1997)
2	NSA-fen	98.42W, 55.92N	Peatland, Fen	Boreal	Daily 1994/1996	Sellers, et al., (1997)
3	Plotnikovo Bog	82.85E, 56.85N	nonforested Bog	Boreal	Biweekly, Jun-Aug in 1997-1998	Glagolev, et al., (2011)
4	Plotnikovo Mire	82.85E, 56.85N	Mire, near river	Boreal	Biweekly, Jun-Aug in 2006	Glagolev, et al., (2011)
5	Muhrino	68.70E, 60.89N	nonforested Bog	Boreal	Biweekly, Jun-Aug in 2009-2010	Glagolev, et al., (2011)
6	Sallie's Fen	71.06W, 43.21N	Peatland Fen	Temperate	Weekly, 1994-2001	Zhuang, et al., (2008)
7	Buck Hollow Bog	84.02W,42.45N	Non forested wetland	Temperate	monthly,1991-1993	shannon,et al., (1994)
8	Minnesota peatland	93.47W,47.53N	Peatland bog	Temperate	Weekly,1991-1992	Clement et al., (1995); Shurpali, et al., (1993,1998)
9	Mer Bleue Bog	75.48W,45.41N	Non forested Peatland bog	Temperate	Weekly, 2004-2007	Moore, et al., (2011)
10	Minnesota peatland	93.47W,47.53N	Peatland bog	Temperate	Monthly,1988-1990	Dise (1993)
11	Cuini	64.10W, 0.48-1.14S	Interfluvial wetlands	Tropical	Monthly 200502-200601	Belger, et al., (2014)

Table 3.2 continued

12	Itu	63.56W, 0.29S	Interfluvial wetlands	Tropical	Monthly 200502-200601	Belger, et al., (2014)
13	EARTH	83.57W, 10.22N	Secondary forest	Tropical	6 visit 2006-2009	Nahlik and Mitsch, (2011)
14	La Selva	84.01W, 10.42N	Flooded forest	Tropical	6 visit 2006-2009	Nahlik and Mitsch, (2011)
15	Palo Verde	85.33W, 10.34N	Coastal plains	Tropical	6 visit 2006-2009	Nahlik and Mitsch, (2011)
16	Stordalen	19.05E, 68.33N	Subarctic micre	Boreal	monthly, 1974/1994/1995	Svensson et al., (1999)
17	Stordalen	19.05E, 68.33N	Subarctic micre	Boreal	Daily, 2006-2007	Jackowicz-Korczynski et al., (2010)
18	Degero Stormyr	19.55E, 64.18N	Boreal mire, fen	Boreal	Daily, 1995-1997	Grandberg, et al., (2001)
19	Salmisue mire	30.93E, 62.78N	Boreal fen	Boreal	Daily, 1997	Saarnio, et al., (1997)
20	Ruovesi	24.02E, 61.83N	Boreal fen	Boreal	Daily, 2006	Rinne, et al., (2007)
21	Quebec	78.77W, 53.9N	Peatland	Boreal	Daily, 2003	Pelletier, et al., (2007)
22	Quebec	77.72W, 53.63N	Peatland	Boreal	Daily, 2003	Pelletier, et al., (2007)
23	Quebec	76.13W, 53.57N	Peatland	Boreal	Daily, 2003	Pelletier, et al., (2007)
24	Sanjiang Plain	133.52E, 47.58N	Marshland/natural freshwater wetland	Temperate	Annually, 2002-2005	Huang, et al., (2010); Song, et al., (2009)

Table 3.2 continued

25	Sanjiang Plain	133.52E, 47.58N	Marshland/freshwater marsh	Temperate	Monthly, 1995-1996, 2001-2003	Wang, et al., (2002); Cui, et al., (1997); Ding, et al., (2004); Yang, et al., (2006); Hao, et al., (2004)
26	Loch Vale	105.65W, 40.28N	Subalpine wetland	Temperate	Daily, 1996-1998	WicKland, et al., (2001)
27	Ryans 1 Billagong	146.97E, 36.12N	Freshwater wetland	Temperate	Monthly, Apr 1993-May 1994	Boon and Mitchel, (1995)
28	Florida	81.00W, 25.00N	Everglade	Tropical	Averaged range using few visits during 1980-1987	Bartlett, et al., (1989); Burke Jr., et al., (1988); Harriss , et al., (1988)
29	Amazon	Amazon Basin	Flooded plain	Tropical	Averaged range using few visits during 1979-1987	Melack, et al., (2004); Devol, et al., (1988); Bartlett, et al., (1988); Bartlett., et al., (1990);

Table 3.3. Optimized parameters for different ecosystem types.

No.	Climate	Subtype	Category	M_{GO}	K_{PCH4}	P_{Q10}	NPP_{MAX}	L_{MAXB}	T_{PR}	O_{MAX}	K_{OCH4}	O_{Q10}	K_O	afp	M_{VMAX}	M_{VMIN}	M_{VOPT}	T_{OR}
1	Boreal	Forested Bog	mean	0.57	0.12	4.45	181.84	1641.66	15.48	175.48	34.63	5.19	118.39	0.2	0.79	0.15	0.46	16.16
			range	0.27-0.89	0.06-0.17	2.62-8.31	50.00-318.98	979.15-2499.86	8.13-21.43	4.07-355.18	12.39-64.05	2.19-8.51	59.07-196.18	0.13-0.28	0.64-0.94	0.02-0.28	0.31-0.57	3.49-29.76
2	Boreal	Nonforested Bog	mean	0.6	0.13	6.29	370.15	1965.68	16.1	176.74	30.58	5.01	118.13	0.2	0.82	0.16	0.45	15.54
			range	0.31-0.95	0.06-0.19	5.21-7.32	284.13-400.00	1721.92-2498.80	12.64-18.94	10.07-346.41	2.05-62.96	1.70-8.37	39.42-193.66	0.11-0.30	0.63-0.96	0.01-0.30	0.30-0.59	0.23-29.52
3	Boreal	Forested Swamp	mean	0.55	0.13	4.89	140.78	1739.22	17.89	105.16	39.71	5.05	110.47	0.2	0.86	0.19	0.46	19.83
			range	0.24-0.82	0.05-0.20	3.80-6.99	76.96-284.53	1331.57-2488.15	13.41-22.49	0.30-358.21	8.71-66.19	1.55-8.91	40.09-182.96	0.11-0.30	0.71-1.00	0.00-0.30	0.31-0.59	3.30-29.91
4	Boreal	Nonforested Swamp	mean	0.59	0.12	1.51	165.11	1366.7	18.18	175.68	30.44	4.6	108.56	0.2	0.83	0.14	0.47	15.43
			range	0.29-0.99	0.05-0.20	1.50-1.58	97.14-356.47	995.89-2479.50	4.16-29.48	13.19-358.06	1.22-64.60	1.60-7.74	37.87-197.99	0.10-0.29	0.60-0.97	0.00-0.30	0.31-0.60	0.19-29.35
5	Boreal	Alluvial Formations	mean	0.59	0.12	4.99	204.53	1878.88	20.73	126.72	30.52	4.6	116.47	0.2	0.85	0.13	0.44	20.04
			range	0.29-0.87	0.07-0.18	3.66-8.53	82.57-352.33	1442.66-2271.02	16.70-25.15	0.78-221.12	1.90-49.93	2.29-6.36	60.44-160.77	0.11-0.29	0.80-0.98	0.03-0.21	0.35-0.54	8.99-28.25
6	Temperate	Forested Bog	mean	0.61	0.13	6.21	334.19	1796.13	9.98	127.1	37.37	5.37	117.73	0.19	0.78	0.17	0.47	18.55
			range	0.27-0.98	0.07-0.20	5.32-6.89	223.48-398.98	1135.43-2497.48	5.64-13.09	0.31-351.21	11.49-65.83	1.82-8.81	42.50-186.97	0.10-0.29	0.63-1.00	0.01-0.30	0.30-0.60	2.27-29.95
7	Temperate	Nonforested Bog	mean	0.66	0.13	3.91	355.95	1652.22	10.11	191.25	34.73	5.39	127.16	0.19	0.8	0.12	0.42	13.06
			range	0.37-1.00	0.07-0.20	3.68-4.23	216.74-399.92	901.80-2435.60	5.81-12.78	45.35-356.57	1.44-63.64	2.32-8.87	59.68-199.04	0.11-0.28	0.63-0.99	0.02-0.25	0.30-0.58	0.14-23.68
8	Temperate	Forested Swamp	mean	0.61	0.13	6.21	334.19	1796.13	9.98	127.1	37.37	5.37	117.73	0.19	0.78	0.17	0.47	18.55
			range	0.27-0.98	0.07-0.20	5.32-6.89	223.48-398.98	1135.43-2497.48	5.64-13.09	0.31-351.21	11.49-65.83	1.82-8.81	42.50-186.97	0.10-0.29	0.63-1.00	0.01-0.30	0.30-0.60	2.27-29.95
9	Temperate	Nonforested Swamp	mean	0.66	0.13	3.91	355.95	1652.22	10.11	191.25	34.73	5.39	127.16	0.19	0.8	0.12	0.42	13.06
			range	0.37-1.00	0.07-0.20	3.68-4.23	216.74-399.92	901.80-2435.60	5.81-12.78	45.35-356.57	1.44-63.64	2.32-8.87	59.68-199.04	0.11-0.28	0.63-0.99	0.02-0.25	0.30-0.58	0.14-23.68

Table 3.3 continued

10	Temperate	Alluvial Formations	mean	0.75	0.12	1.53	382.92	1852.6	11.94	120	38.18	6.43	126.81	0.2	0.81	0.16	0.48	20
			range	0.47-1.00	0.05-0.20	1.50-1.63	251.26-400.00	1162.27-2493.35	0.69-19.52	0.30-342.86	4.47-65.14	2.81-9.00	37.90-196.69	0.10-0.30	0.60-1.00	0.01-0.29	0.32-0.60	0.83-29.96
11	Tropical	Forested Bog	mean	0.41	0.12	2.84	62.45	1744.61	25.52	129.3	29.01	4.99	122.46	0.2	0.85	0.14	0.46	14.91
			range	0.12-0.64	0.05-0.20	1.64-6.83	50.00-196.05	913.70-2315.90	18.87-29.98	0.33-349.74	1.80-63.36	1.74-8.94	44.17-197.16	0.11-0.30	0.62-1.00	0.01-0.28	0.35-0.60	1.03-28.47
12	Tropical	Nonforested Bog	mean	0.43	0.13	1.68	232.85	1649.91	25.78	192.55	31.53	4.76	122.64	0.19	0.79	0.14	0.45	14.89
			range	0.33-0.58	0.05-0.18	1.50-2.99	153.04-398.90	1260.12-2295.02	19.66-28.38	3.23-354.08	4.40-59.57	1.85-8.71	65.10-197.91	0.10-0.28	0.64-0.95	0.00-0.27	0.30-0.60	0.24-29.63
13	Tropical	Forested Swamp	mean	0.34	0.12	5.34	356.03	1752.12	26.43	157.48	29.32	5.33	115.08	0.21	0.8	0.16	0.44	15.66
			range	0.15-0.65	0.05-0.20	3.75-6.97	212.62-400.00	900.85-2496.07	22.00-30.00	0.56-352.83	1.65-63.63	1.54-8.99	40.48-197.12	0.11-0.29	0.61-0.98	0.01-0.30	0.32-0.60	1.23-30.00
14	Tropical	Nonforested Swamp	mean	0.2	0.13	7.25	393.95	1659.53	27.48	163.85	34.68	4.74	115.96	0.2	0.78	0.15	0.46	16.09
			range	0.12-0.30	0.06-0.20	3.90-9.00	335.57-400.00	930.73-2318.31	25.00-29.80	1.00-359.41	1.88-65.52	1.54-8.71	38.10-199.91	0.10-0.30	0.62-0.98	0.00-0.30	0.31-0.60	0.00-29.95
15	Tropical	Alluvial Formations	mean	0.51	0.12	1.53	80.31	1654.54	24.52	131.58	26.75	4.99	122.13	0.19	0.82	0.12	0.45	17.8
			range	0.30-0.92	0.06-0.20	1.50-1.72	59.61-222.76	916.68-2244.78	9.18-29.83	1.53-334.90	1.15-65.99	1.66-8.96	39.19-195.81	0.11-0.29	0.61-0.99	0.00-0.30	0.30-0.59	1.06-29.33

Table 3.4. Model evaluations with observations. Observation points are acceptable observed flux data at each site. RMSE is root mean square error between simulation and observation (mg CH_4 m^{-2} day^{-1}). R^2 is the coefficient of determination. P value is the probability value based on a two-sided t-test. T-value is the t statistic value. Regional results from site 28 and 29 are discussed in Section 3.4.1.

	site16	site17	site18	site19	site20	site21	site22	site23	site24	site25	site26	site27
Observation points	9	42	24	80	127	7	7	7	6	31	53	14
Observed mean value	77.81	117.19	72.27	190.30	53.51	79.94	28.01	28.11	117.84	383.15	172.67	186.48
RMSE	64.90	104.31	46.81	153.40	42.68	91.92	68.99	48.96	83.96	270.59	101.78	83.33
R^2	0.30	0.00	0.24	0.07	0.55	0.49	0.19	0.72	0.18	0.18	0.56	0.66
P-value	0.12	0.95	0.02	0.01	0.00	0.08	0.33	0.02	0.40	0.02	0.00	0.00
T-test	1.75	0.07	2.61	2.49	12.29	2.17	1.08	3.62	0.95	2.53	8.20	4.73

Table 3.5. Model sensitivity test during 2000-2012 using monthly CRU data and transient wetland fraction data.

Flux type	Region	Value category	Baseline ($Tg\ CH_4\ yr^{-1}$)	CH_4 +30%	CH_4 -30%	NPP +30%	NPP -30%	Precipitation +30%	Precipitation -30%	Air T +3°C	Air T -3°C	Inundation Fraction +30%	Inundation Fraction -30%
Consumption	Global	Value	-35.33	-40.83	-29.61	-35.92	-34.75	-36.74	-33.62	-54.11	-25.62	-35.02	-35.73
		Change %	0.00	15.57	-16.19	1.67	-1.64	3.99	-4.84	53.16	-27.48	-0.88	1.13
	90S-45S	Value	-0.14	-0.18	-0.1	-0.14	-0.14	-0.15	-0.14	-0.15	-0.13	-0.14	-0.14
		Change %	0.00	28.57	-28.57	0.00	0.00	7.14	0.00	7.14	-7.14	0.00	0.00
	45S-0	Value	-5.95	-7.22	-4.65	-6	-5.9	-6.42	-5.5	-7.76	-5.09	-5.93	-5.99
		Change %	0.00	21.34	-21.85	0.84	-0.84	7.90	-7.56	30.42	-14.45	-0.34	0.67
	0-45N	Value	-22.62	-25.34	-19.7	-23.04	-22.2	-23.41	-21.61	-37.37	-15.36	-22.39	-22.86
		Change %	0.00	12.02	-12.91	1.86	-1.86	3.49	-4.47	65.21	-32.10	-1.02	1.06
	45N-90N	Value	-6.62	-8.09	-5.15	-6.74	-6.51	-6.76	-6.37	-8.83	-5.05	-6.55	-6.73
		Change %	0.00	22.21	-22.21	1.81	-1.66	2.11	-3.78	33.38	-23.72	-1.06	1.66
Emission	Global	Value	211.93	210.5	213.36	222.27	201.59	215.15	206.89	309.54	146.03	266.51	148.33
		Change %	0.00	-0.67	0.67	4.88	-4.88	1.52	-2.38	46.06	-31.10	25.75	-30.01
	90S-45S	Value	0.57	0.57	0.58	0.6	0.54	0.58	0.57	0.92	0.38	0.74	0.4
		Change %	0.00	0.00	1.75	5.26	-5.26	1.75	0.00	61.40	-33.33	29.82	-29.82
	45S-0	Value	44.71	44.33	45.09	47.29	42.13	46.05	41.3	60.38	33.1	54.22	31.29
		Change %	0.00	-0.85	0.85	5.77	-5.77	3.00	-7.63	35.05	-25.97	21.27	-30.02
	0-45N	Value	124.72	124.11	125.32	129.24	120.19	126.11	123.32	184.34	85.32	157.51	87.29
		Change %	0.00	-0.49	0.48	3.62	-3.63	1.11	-1.12	47.80	-31.59	26.29	-30.01
	45N-90N	Value	41.93	41.5	42.37	45.14	38.73	42.41	41.69	63.91	27.23	54.03	29.35
		Change %	0.00	-1.03	1.05	7.66	-7.63	1.14	-0.57	52.42	-35.06	28.86	-30.00

Table 3.6. Correlations between simulated methane fluxes and environmental factors during 2000-2012 using monthly CRU data and transient wetland fraction data. Factors include net primary production (NPP), precipitation (PREP), air temperature (TAIR), wetland inundation area fraction (IN-AREA), soil temperature (SOILT) and volumetric soil moisture (VSOIL).

Variable name	CH_4 Dynamics	Month Correlation					Year Correlation				
		South-45S	45S-0	0-45N	45N-North	Global	South-45S	45S-0	0-45N	45N-North	Global
NPP	Consumption	-0.86	-0.87	-0.86	-0.96	-0.95	0.52	0.04	0.23	0.17	0.38
	Emission	0.70	0.83	0.89	0.99	0.99	-0.04	0.23	0.30	-0.32	0.10
PREC	Consumption	0.15	-0.91	-0.94	-0.90	-0.84	-0.56	0.31	-0.20	-0.20	-0.04
	Emission	-0.28	0.90	0.94	0.87	0.78	-0.05	-0.35	0.18	-0.05	-0.24
TAIR	Consumption	-0.83	-0.85	-0.88	-0.96	-0.89	0.08	-0.54	0.27	-0.77	-0.27
	Emission	0.83	0.91	0.93	0.88	0.90	0.71	0.58	0.38	0.53	0.73
IN_AREA	Consumption	0.68	-0.41	-0.64	-0.93	-0.89	-0.07	-0.71	-0.42	-0.42	-0.68
	Emission	-0.49	0.48	0.76	0.87	0.92	-0.15	0.68	-0.21	0.60	0.41
TSOIL	Consumption	-0.83	-0.85	-0.89	-0.99	-0.92	0.07	-0.54	0.30	-0.71	-0.10
	Emission	0.83	0.91	0.94	0.92	0.92	0.71	0.59	0.42	0.70	0.74
VSOIL	Consumption	0.52	-0.77	-0.52	-0.88	-0.77	-0.45	-0.67	-0.72	-0.20	-0.80
	Emission	-0.48	0.76	0.48	0.79	0.77	-0.25	0.51	-0.14	-0.09	-0.10

Table 3.7. Parameter uncertainties in different wetland types

Type numbers	Climate	Subtype	Pixels	Annual Mean Emission (Tg CH_4 yr^{-1})	Annual Mean STD (Tg CH_4 yr^{-1})
1	Boreal	Forested Bog	11475	13.95	14.96
2	Boreal	Nonforested Bog	10050	3.14	1.68
3	Boreal	Forested Swamp	52	0.01	0.01
4	Boreal	Nonforested Swamp	164	0.25	0.14
5	Boreal	Alluvial Formations	1	0.00	0.00
6	Temperate	Forested Bog	6754	48.12	23.42
7	Temperate	Nonforested Bog	4340	18.72	7.34
8	Temperate	Forested Swamp	1101	23.54	11.87
9	Temperate	Nonforested Swamp	741	4.56	2.19
10	Temperate	Alluvial Formations	72	1.07	0.42
11	Tropical	Forested Bog	55	1.58	1.02
12	Tropical	Nonforested Bog	8538	19.72	6.70
13	Tropical	Forested Swamp	12791	37.13	21.78
14	Tropical	Nonforested Swamp	5431	7.11	2.32
15	Tropical	Alluvial Formations	206	7.73	4.68
Total	--	--	61771	211.93	62.04

Table 3.8. Simulated methane emission (Tg CH_4 $region^{-1}$ yr^{-1}) uncertainties due to uncertain parameters and wetland type distribution expressed with standard deviations (STD) in different regions.

	90S-45S	45S-0	0-45N	45N-90N	global
Emission baseline	0.58	44.84	124.28	41.7	211.93
Emission parameter uncertainty STD	0.34	15.11	40.44	19.3	61.82
Emission wetland type uncertainty STD	0.11	7.24	25.77	3.61	31.93

Table 3.9. Modeled methane fluxes (Tg CH_4 yr^{-1}) uncertainties due to different forcing data

Flux Type	Region	CRU static	CRU transient	ECMWF static	ECMWF transient	NCEP static	NCEP transient
Consumption	90S-45S	-0.19	-0.14	-0.26	-0.16	-0.29	-0.19
Consumption	45S-0	-7.49	-5.99	-9.86	-6.93	-10.38	-7.1
Consumption	0-45N	-16.76	-22.72	-20.9	-27.27	-23.22	-27.51
Consumption	45N-90N	-9.44	-6.64	-11.69	-7.54	-12.14	-7.64
Emission	90S-45S	0.22	0.57	0.2	0.55	0.14	0.55
Emission	45S-0	53.76	44.67	51.39	40.05	53.73	42.59
Emission	0-45N	52.24	124.75	55.31	122	51.75	121.22
Emission	45N-90N	79.57	41.96	87.89	47.4	89.18	47.91
Consumption	Global	-33.89	-35.48	-42.71	-41.89	-46.04	-42.43
Emission	Global	185.78	211.93	194.78	210.01	194.81	212.27

Table 3.10. Modeled methane fluxes (Tg CH4 yr-1) during 1950-2012 using CRU data

	90S-45S	45S-0	0-45N	45N-90N	Global
Emission value	0.55	41.60	116.65	38.90	197.70
Emission %	0.28	21.04	59.00	19.67	100.00
consumption value	-0.14	-5.16	-20.49	-5.86	-31.65
consumption %	0.44	16.29	64.76	18.51	100.00

Table 3.11. Historical simulations compared with previous global wetland emission estimates

Studies	Period	Comments	Emission Value ($Tg\ CH_4\ yr^{-1}$)
Our study	1950-2012	Bottom-up approach, process-based model considering multiple natural wetland types	185-217
Zhang et al., 2017	2000-2007	Bottom-up approach, using same model as Tian et al., 2015 but using five different wetland distribution data sets	127-227
Saunois et al., 2016	2000-2012	Top-down and bottom-up approach, multiple model approaches, natural wetland emissions, tropical regions are hot spots	125-227
Tian et al., 2015	1981-2010	Bottom-up approach, land surface emissions considered agriculture, tropical and Asia are hot spots	131-157
Zhu et al., 2015	1901-2012	Bottom-up approach, wetland emissions considered agriculture, primarily controlled by tropical wetlands, peak occurring in 1991-2012	209-245
Kirschke et al., 2013	2000-2009	Top-down and bottom-up approach, multiple model approaches, natural wetland emissions	142-284

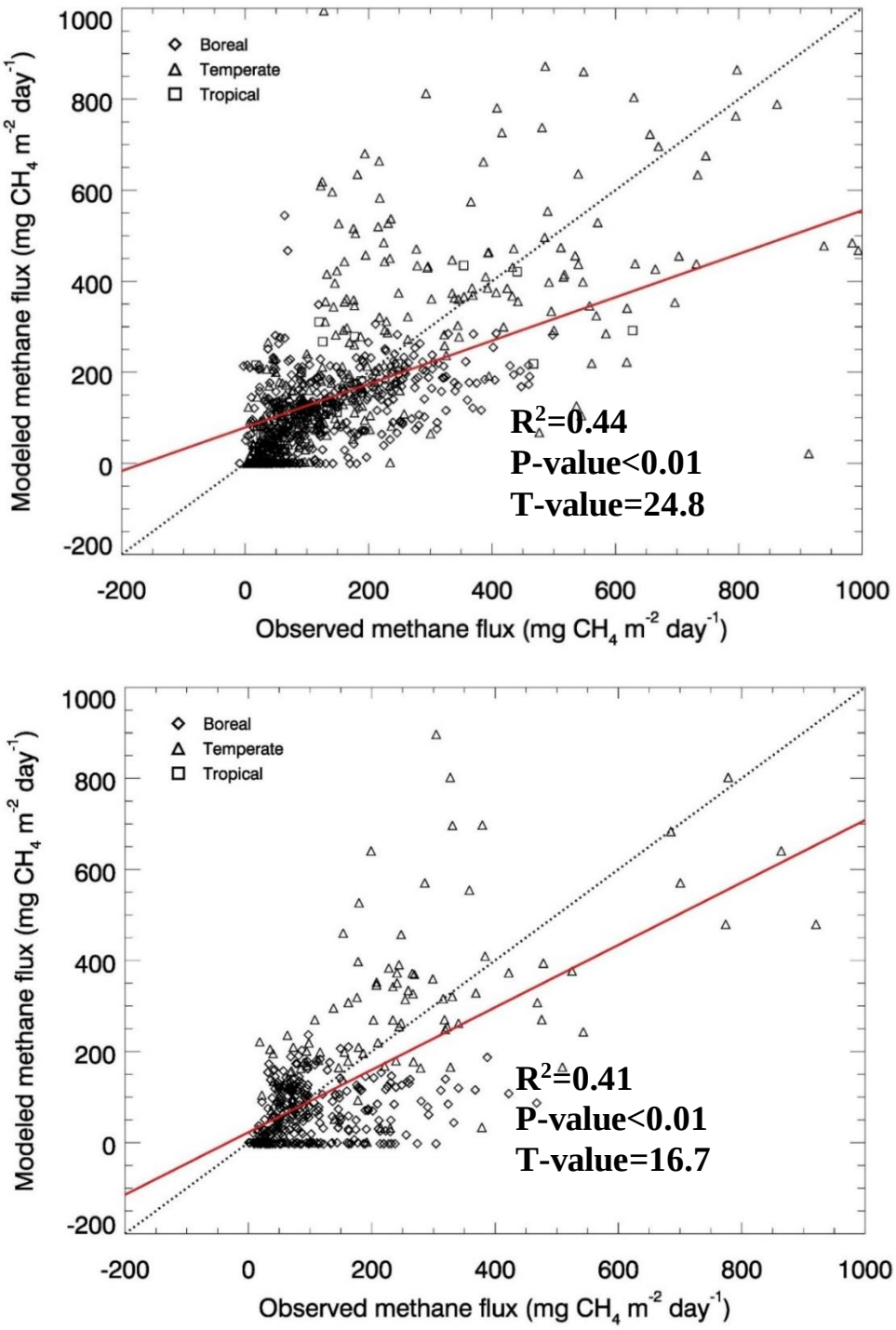

Figure 3.1. Comparison between observed and simulated methane fluxes at calibration sites (upper panel) and evaluation sites (lower panel). Diamond symbol represents the boreal data. Triangle symbol represents the temperate data. Square symbols represent the tropical data. Dot line represents that the observed data equals the simulated data. Red solid line represents the linear regression line between all observed and simulated data.

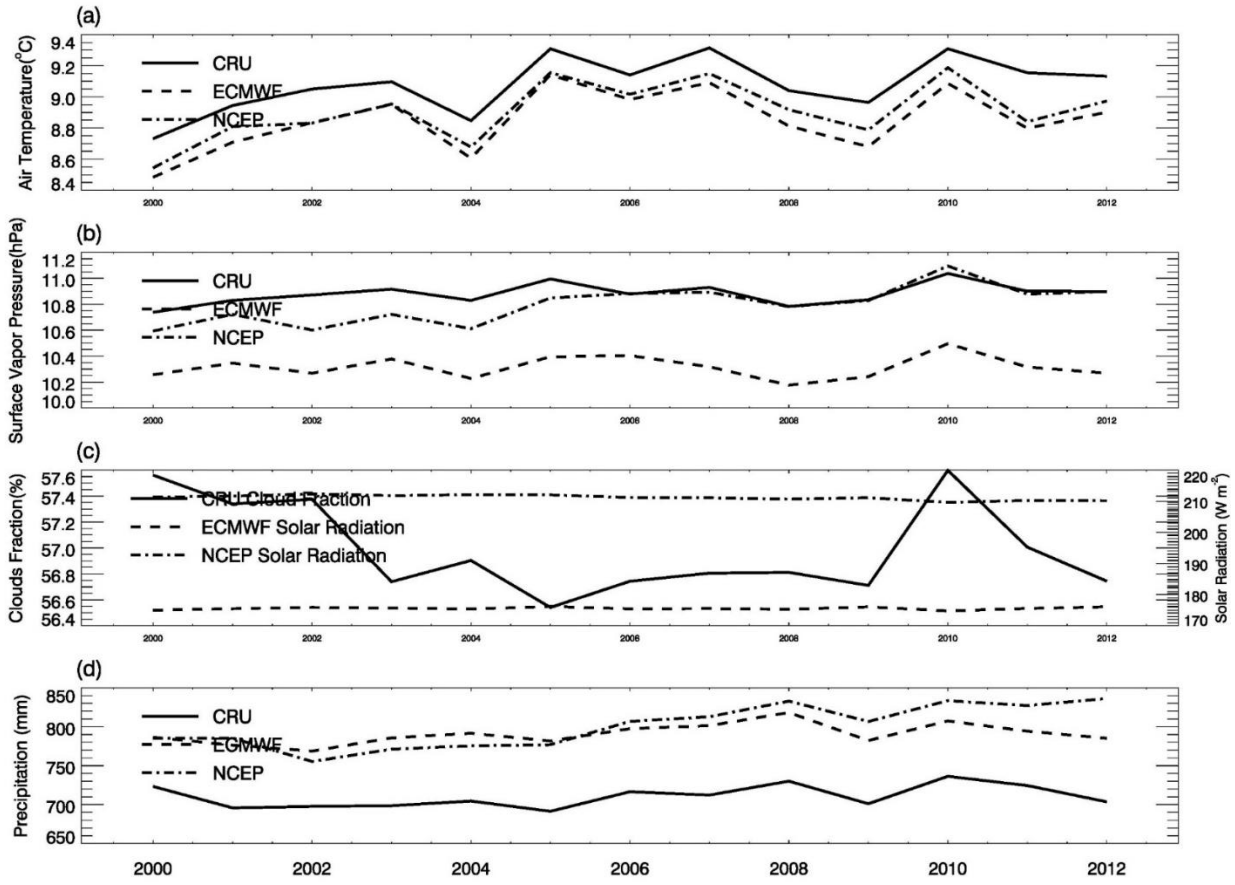

Figure 3.2. Climate forcing data used in this study. Figure a)-d) represent the climate data from CRU (solid line), ECMWF (dash line) and NCEP (dash-dot line), respectively, during 2000-2012

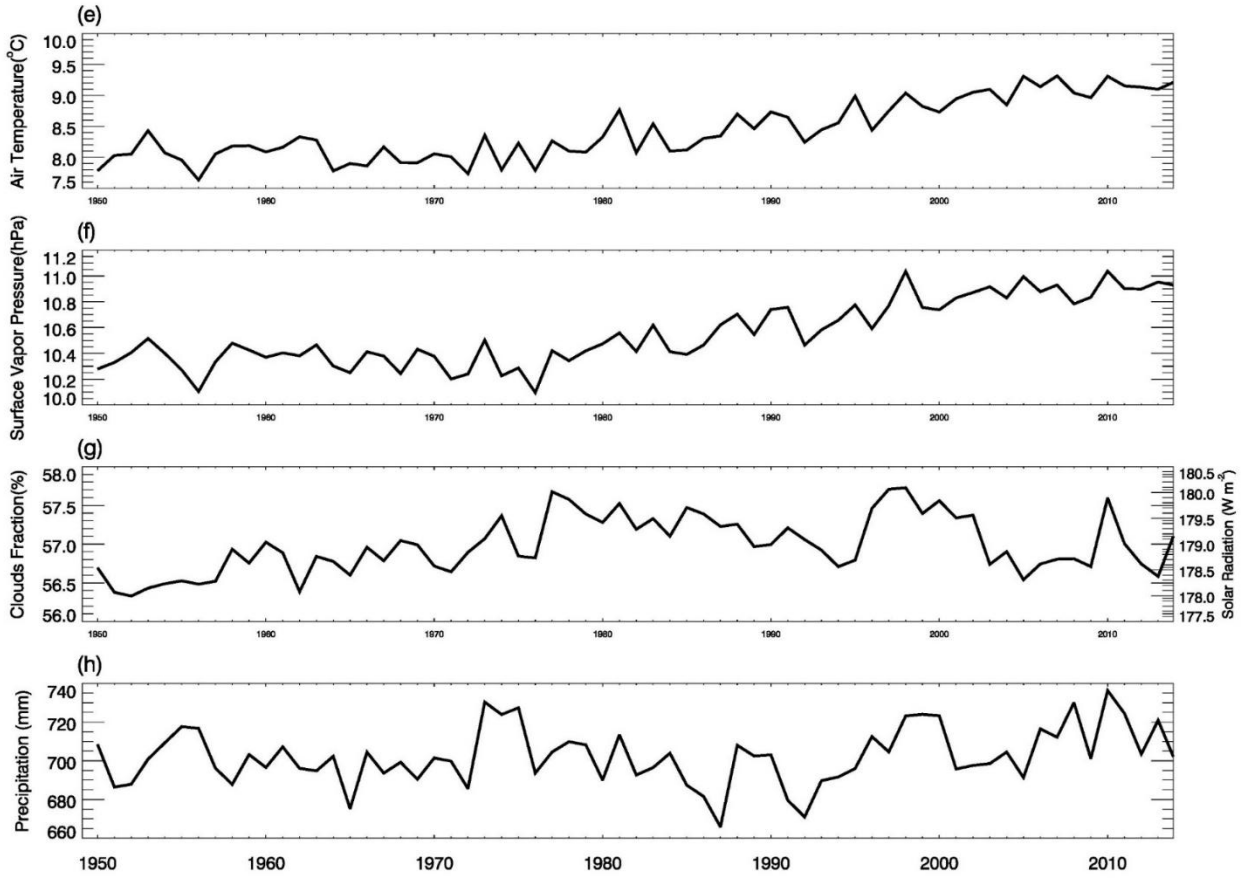

Figure 3.2.contd. Climate forcing data used in this study. Figure e-h represent the climate data from CRU during 1950-2012 (solid line)

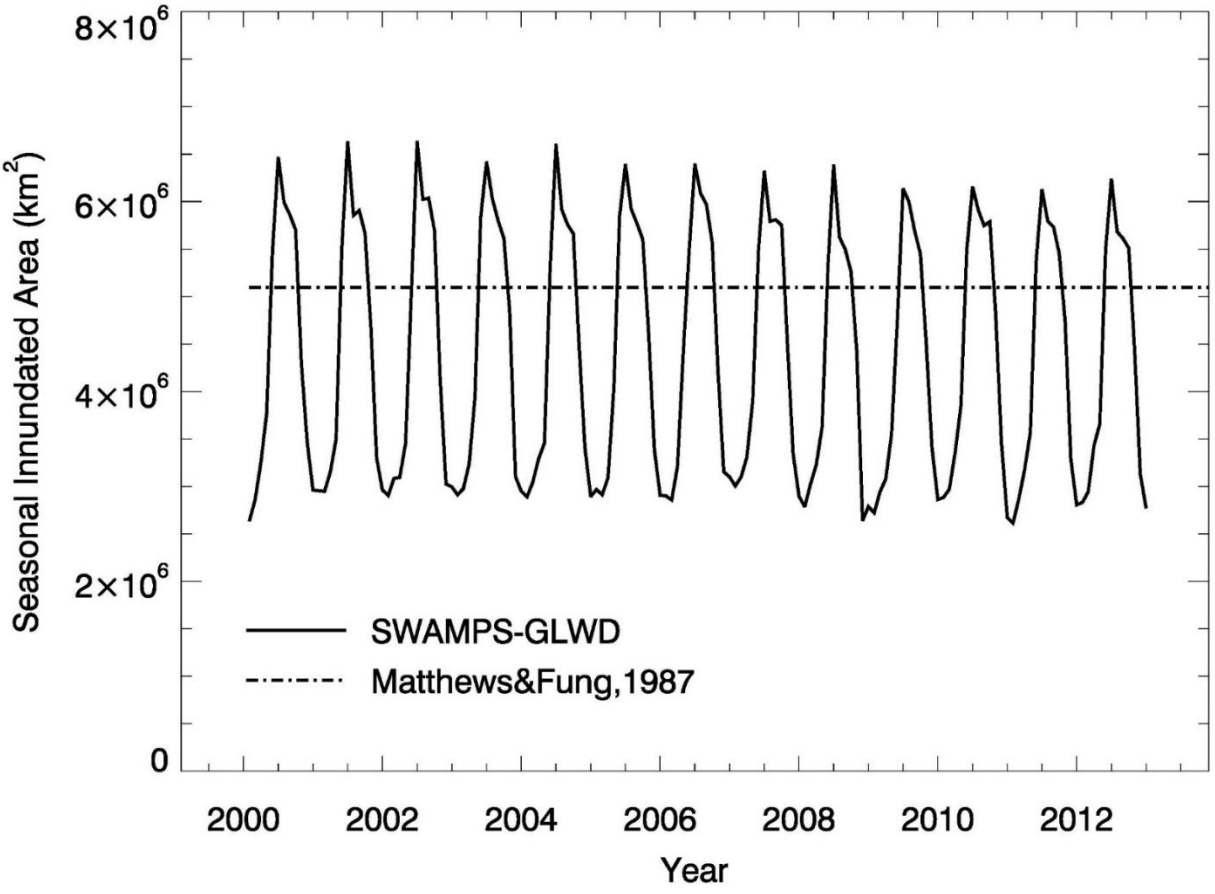

Figure 3.3. Wetland distribution data used in this stud

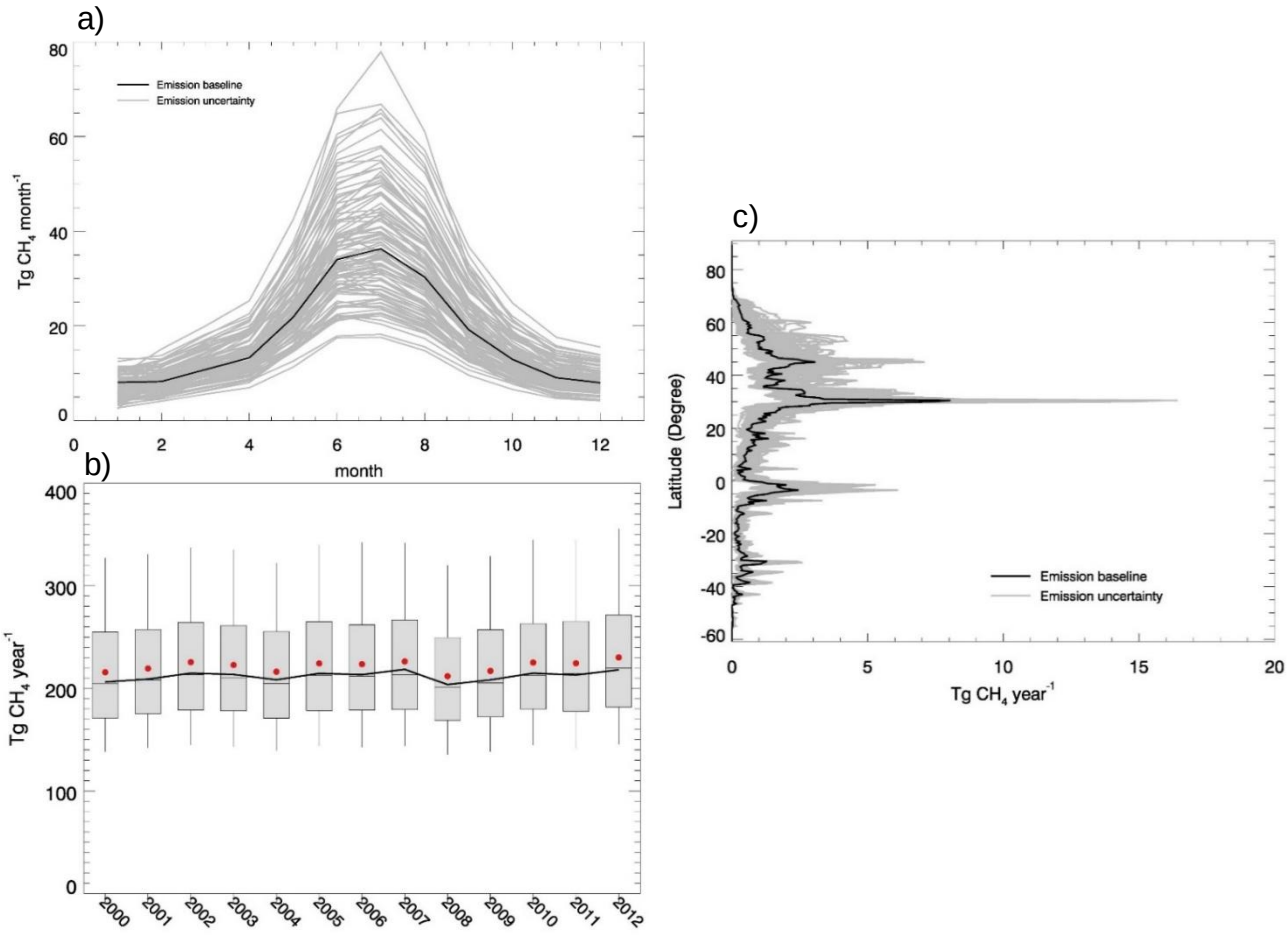

Figure 3.4. Parameter uncertainty analysis during 2000-2012: a) global monthly methane flux uncertainties, the black line represents the baseline results and the gray lines represent the 100 simulation results using parameters which were randomly chosen in optimized ranges; b) global annual methane flux uncertainties, the black line represents the baseline. For each box, line top, box top, horizontal line inside box, box bottom and line bottom represent maximum, third quartile, median, first quartile and minimum of 100 simulations; and c) the latitude distribution of global annual mean methane emissions, the black line represents the baseline results and the gray lines represents the 100 parameter uncertainty simulations.

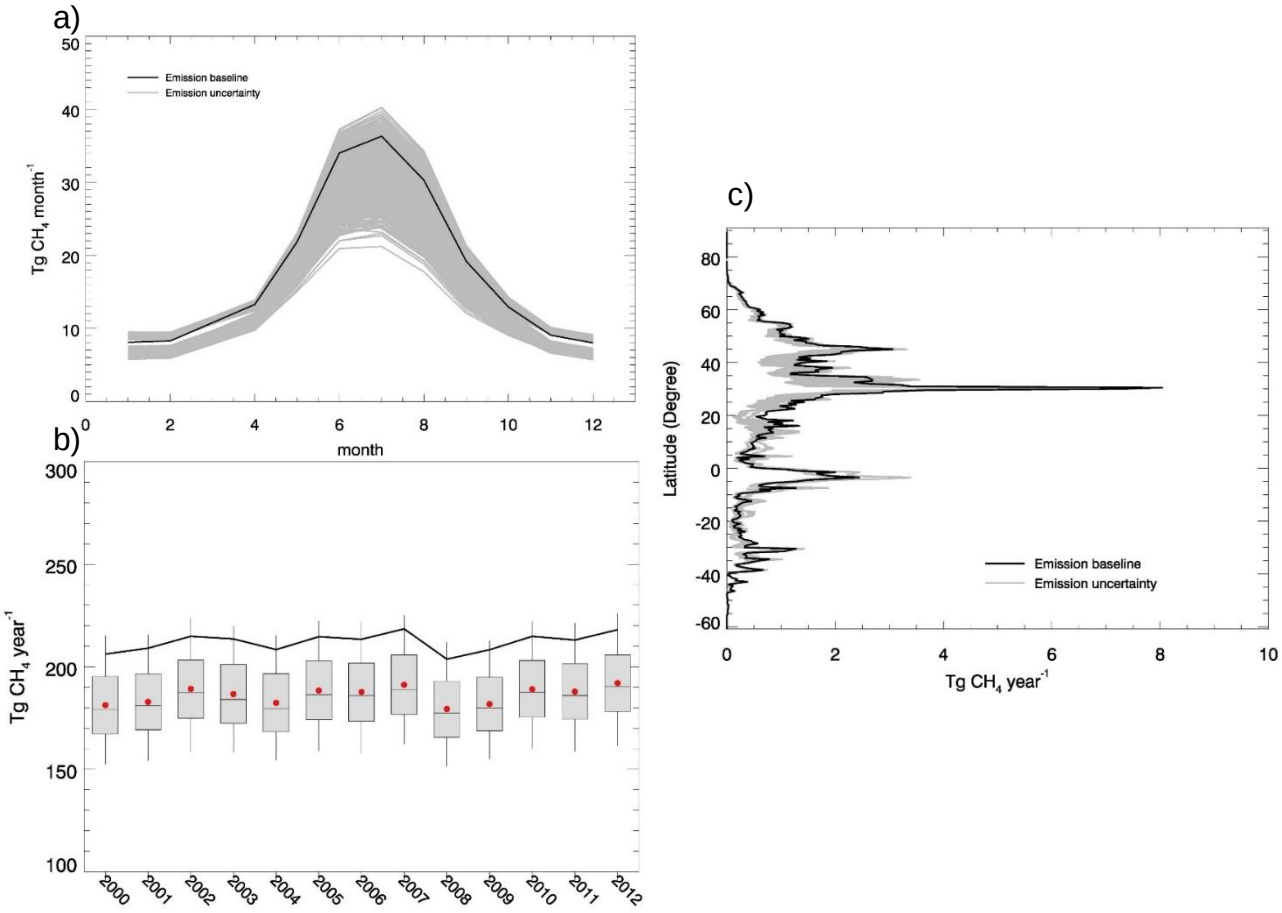

Figure 3.5. Wetland type uncertainty analysis during 2000-2012: a) global monthly methane flux uncertainties, the black line represents the baseline results and the gray lines represent the 770 simulation results using different wetland distributions; b) global annual methane flux uncertainties, the black line represents the baseline. For each box, line top, box top, horizontal line inside box, box bottom and line bottom represent maximum, third quartile, median, first quartile and minimum of 770 simulation results, respectively; and c) the latitude distribution of global annual mean methane emission, the black line represents the baseline results and the gray lines represents the results of the 770 wetland type uncertainty simulations.

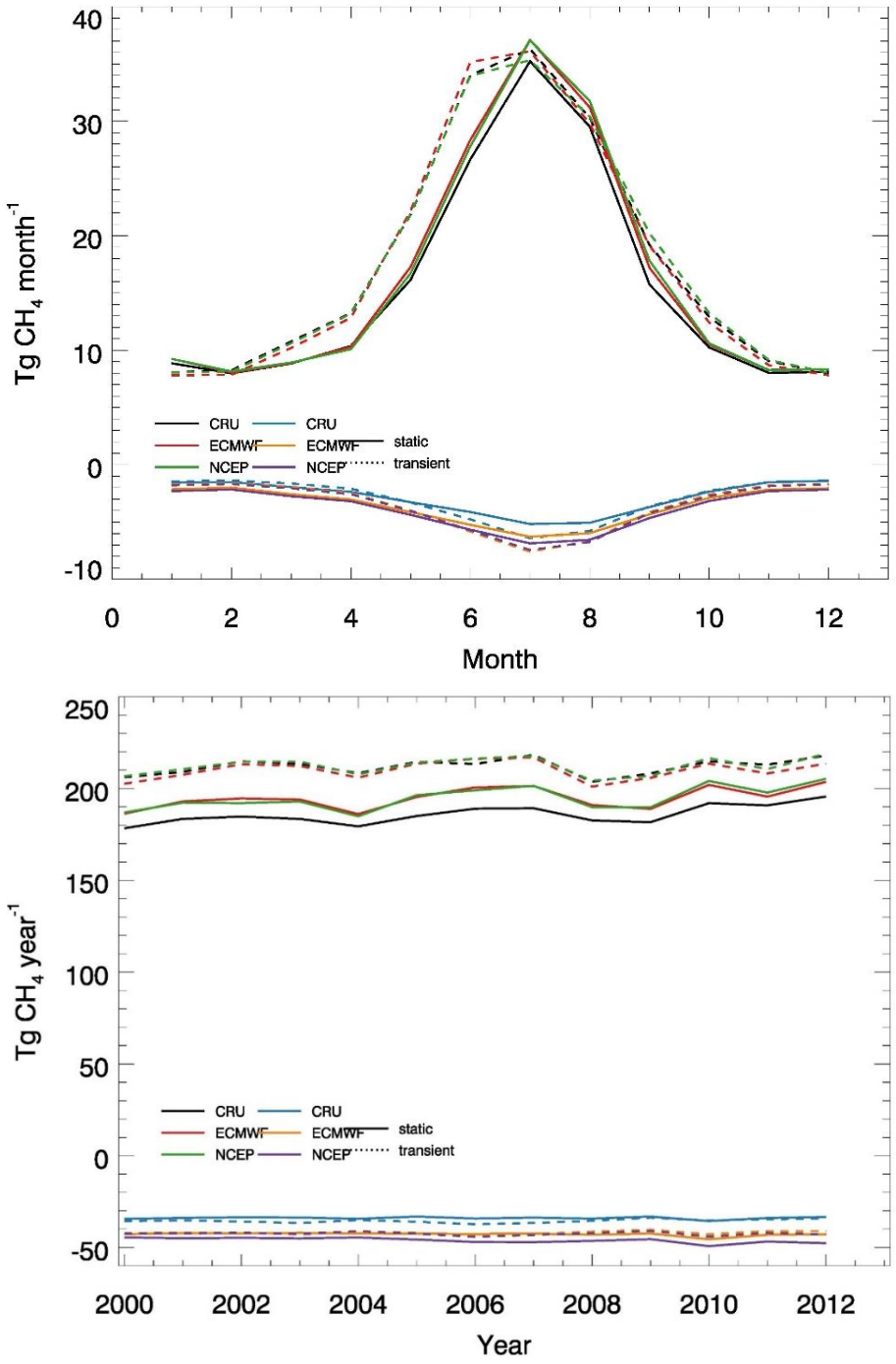

Figure 3.6. Forcing data uncertainty test results during 2000-2012: Upper panel represents global monthly methane flux uncertainties. Different colors and line styles represent different combinations of forcing data; lower panel represents global annual methane flux uncertainties. Different colors and line styles represent different combinations of forcing data.

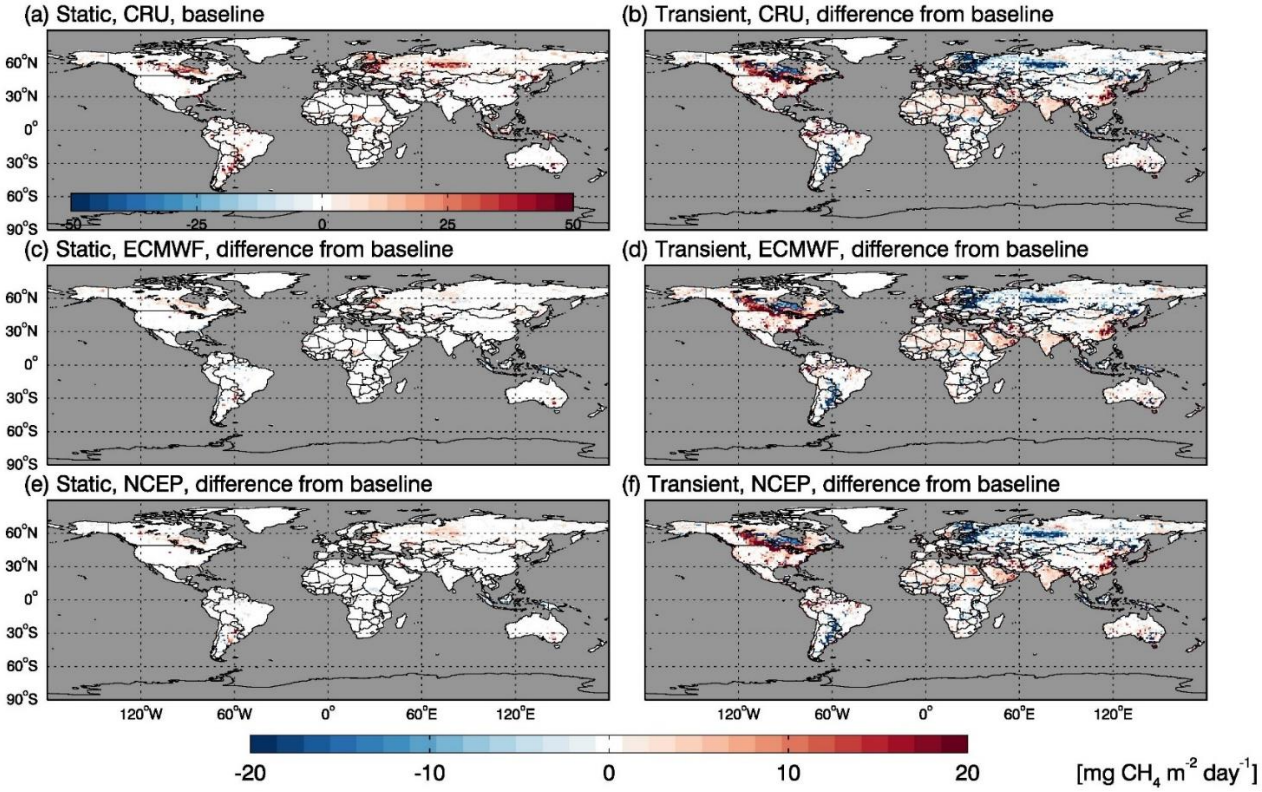

Figure 3.7. Global distribution of annual wetland methane emissions during 2000-2012 when using different forcing data: a) the baseline using static wetland map and CRU climate data; b)-f) shows the differences (new flux value – baseline flux value) when using different wetland distribution data or using different climate data. Red regions represent emission increasing while blue regions represent emission decreasing.

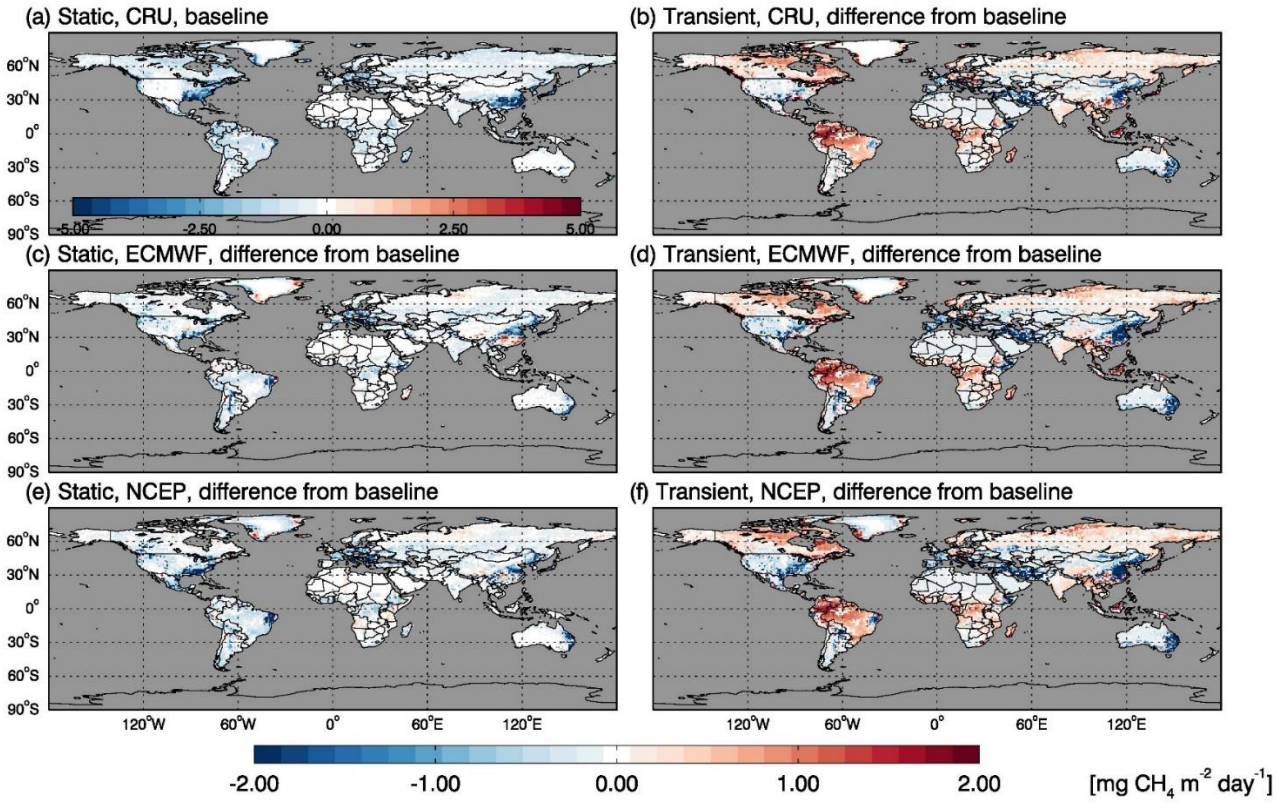

Figure 3.8. Global distribution of annual upland methane consumption during 2000-2012 when using different forcing data: a) shows the baseline using static wetland map and CRU climate data; b)-f) show the difference (new flux value – baseline flux value) when using different wetland distribution data or using different climate data. Red regions represent consumption decreasing while blue regions represent consumption increasing.

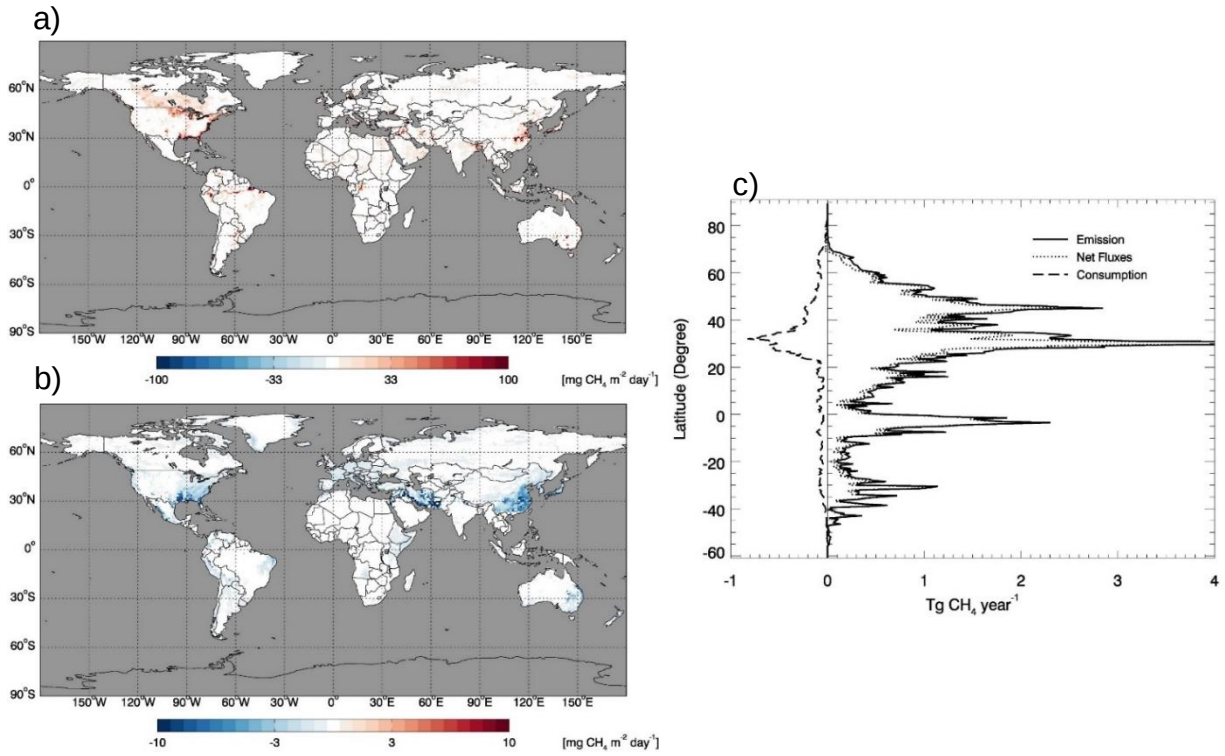

Figure 3.9. Global simulation during 1950-2012 using CRU data and transient wetland fraction data: a) global distribution of annual wetland methane emissions; b) global distribution of annual upland methane consumption; and c) latitude distribution of methane emission, consumption and net fluxes.

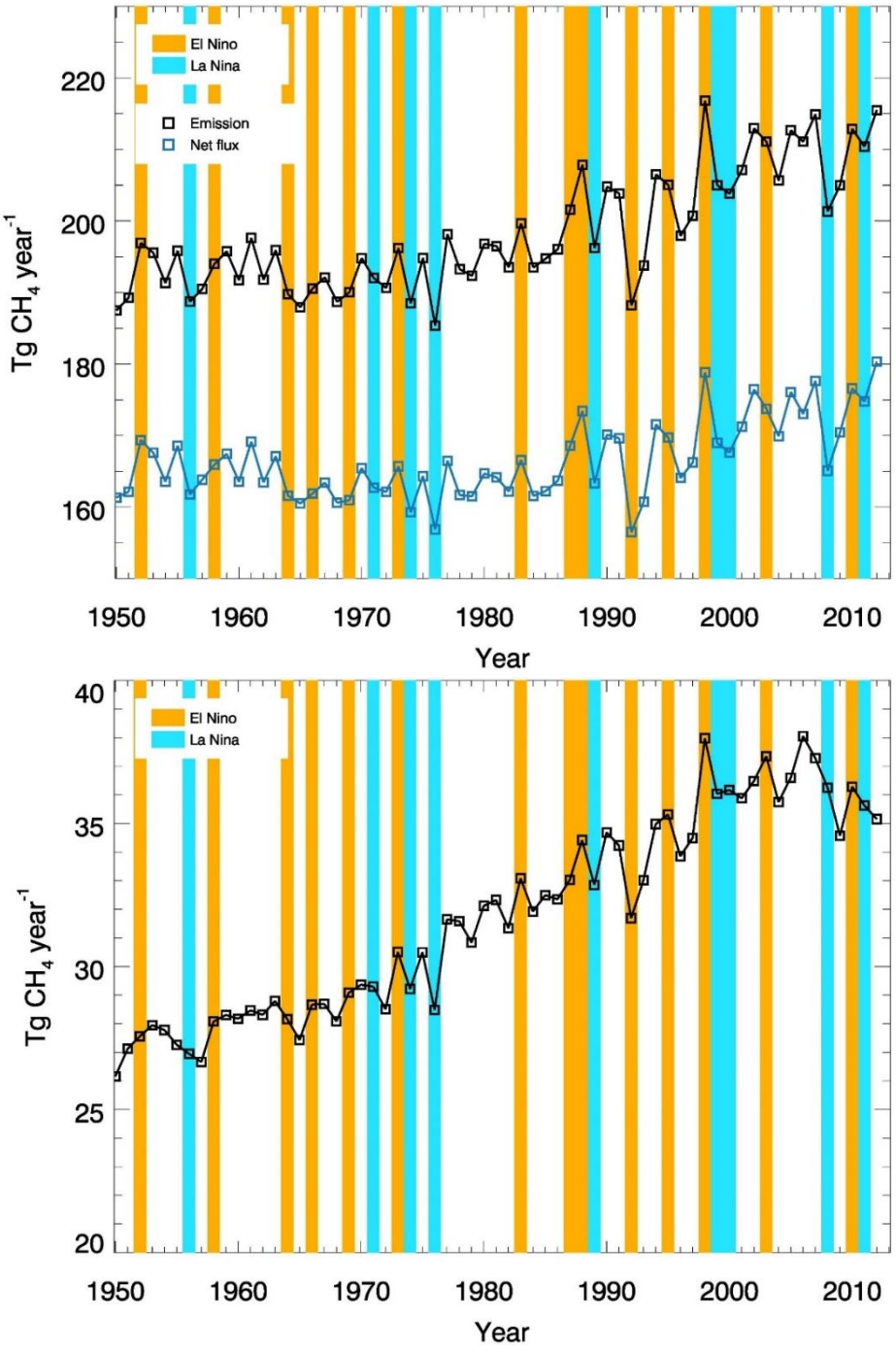

Figure 3.10. Historical estimates and comparisons: Upper panel represents annual wetland methane emissions (black) and net fluxes (blue) during El Niño (yellow strip) and La Nina (blue) event periods; lower panel represents annual upland methane consumption (black) during El Niño (yellow strip) and La Nina (blue) event periods

CHAPTER 4. INVENTORYING GLOBAL WETLAND METHANE EMISSIONS USING IN SITU DATA AND AN ARTIFICIAL NEURAL NETWORK APPROACH

4.1 Abstract

Methane (CH_4) emissions from wetland ecosystems exert large positive feedbacks to the global climate system. However, the estimation of wetland CH_4 emissions at the global scale still has large uncertainties. Here we develop a predictive model of CH_4 emissions using an artificial neural network (ANN) approach and available field observations of CH_4 fluxes. Eleven explanatory variables including three transient climate variables (precipitation, air temperature and solar radiation) and eight static soil property variables are considered in developing ANN models. The models are then extrapolated to the global scale to estimate monthly CH_4 emissions from 1979 to 2099. We estimate that the annual wetland CH_4 emissions are 186 Tg CH_4 yr^{-1} (1 Tg = 1012 g) with an uncertainty range of 169-190 Tg CH_4 yr^{-1} in the historical period. The future predicted emissions are 199-209 Tg CH_4 yr^{-1} in the last two decades of the 21st century. The estimated wetland CH_4 emissions show a large spatial variability, due to variations in hydrology, climate, and soil conditions. Significant interannual and seasonal variations of wetland CH_4 emissions exist in the past four decades, and the emissions in this period are most sensitive to variations in solar radiation and air temperature. To improve future quantifications, research priorities should be directed to better detecting water table position by using improved radar technology, characterizing temporal and spatial dynamics of wetland areas, and strengthening tropical wetland CH_4 flux observations.

4.2 Introduction

Methane (CH_4) is the second most potent greenhouse gas after carbon dioxide (CO2). It has contributed to about 20% of the observed warming since pre-industrial times (Ciais et al., 2013). According to the latest Intergovernmental Panel on Climate Change report (IPCC), the global warming potential (GWP) of CH_4 is 28, about 25 times that of CO2 on a 100-year time period (IPCC AR5, Myhre et al., 2013). The atmospheric concentration of CH_4 has increased from a preindustrial value of about 700 ppb to a current value of about 1850 ppb (Saunois, et al., 2019). The increase of atmospheric CH_4 concentrations has contributed ~23% (~0.62 Wm-2) to the additional radiative forcing accumulated in the lower atmosphere since 1750 (Etminan, et al., 2016). The growth rate of atmospheric CH_4 has decreased, however, from approximately 13 ppb yr-1 during the early 1980s to near zero between 1999 and 2006. Since 2007, the growth rate of atmospheric CH_4 has risen again (Dlugokencky et al., 2009; Nisbet, Dlugokencky, & Bousquet, 2014; Saunois et al., 2016; Schaefer et al., 2016; Zhang et al., 2018). The climatic sensitivity of biogenic CH_4 sources has significantly influenced the inter-annual variability of atmospheric CH_4 and the global wetland contributes 60–80% of natural CH_4 emissions (Quiquet et al., 2015; Hopcroft et al., 2017) and this large role is likely to persist into the future (Zhang et al., 2017).

The balance between CH_4 production and consumption determines the amount of CH_4 emitted from wetland soils. In wetland soils, CH_4 is normally produced by methanogens in anoxic environments, and is oxidized by methanotrophic bacteria in the presence of oxygen (Hanson and Hanson, 1996). Both CH_4 production and oxidation are mainly controlled by soil temperature, pH, and substrate availability (Christensen et al., 1995; MacDonald et al., 1998; Wagner et al., 2005). Besides, three pathways have been widely considered when quantifying CH_4 emissions from soils, including the diffusion process, plant-mediated transport and ebullition process (Zhuang, et al., 2004, 2013).

To date, three approaches have been used in estimating CH_4 emissions from wetlands across different scales over the last few decades: 1) a bottom-up extrapolation approach by using simple empirical or statistical models and actual CH_4 emission measurements; 2) a bottom-up approach with process-based models parameterized using flux measurements to quantify CH_4 fluxes, and 3) a top-down approach, which uses atmospheric inverse models to estimate the distribution of CH_4 sources and sinks by incorporating atmospheric observations, an atmospheric transport model and prior estimates of source distributions and magnitudes (Arneth et al., 2010; Anderson et al., 2010; Kirschke et al., 2013; Zhu et al., 2014; Saunois, et al., 2019). Although top-down approach is widely thought to be more accurate than bottom-up approach, the current top-down approach may inadvertently include some incomplete observations and error amplifications during inverse modelling processes (Chen and Prinn, 2005; Ciais et al., 2013). Process-based models can be used to improve CH_4 emission estimation considering the effects of complex interactions between soil, vegetation, and hydrology on CH_4 production and consumption processes. A number of process-based models have been developed previously to better quantify the wetland CH_4 emission and its influence on the climate (Cao et al., 1996; Li, 2000; Zhang et al., 2002; Zhuang et al., 2004; Meng et al., 2012; Zhu et al., 2014; Zhang, et al., 2017; Saunois et al., 2019).

Although great efforts have been made on estimating global natural wetland CH_4 emissions, current quantifications still have large uncertainties. The Global Carbon Project (GCP) and the Wetland and Wetland CH_4 Inter-comparison of Models Project (WETCHIMP) estimated the global CH_4 emission from natural wetlands, ranging from 102 to 284 Tg CH_4 yr^{-1} during 2000-2017 (Kirschke et al., 2013; Melton et al., 2013; Saunois et al., 2016; Saunois et al., 2019). The uncertainty in these estimates could result from many sources including model structures, assumptions, parameterization, and choice of forcing data. Among these uncertainty sources, the

paucity of CH_4 flux measurements could be an important factor. The lack of sufficient measurements of CH_4 fluxes and related environmental factors may limit the understanding of ecological processes in specific wetland ecosystems, the model assumptions, and the parameterization of models. In addition to the large uncertainty present in wetland CH_4 emissions, the sensitivity of CH_4 fluxes to environmental controls is not well understood, which also limits explicit representations of many mechanistic processes in models.

Artificial neural networks (ANN) are bottom-up approaches, among the most intelligent statistical methods and are widely used for a range of applications spanning across various scientific fields including Earth ecosystem modeling. ANNs have proved as robust surrogate models with flexible mathematical structure and is capable of identifying complex nonlinear behavior between model input and output (Delon et al., 2007; Dupont et al., 2008; Zhu et al., 2013; Liu et al., 2016; Bomers et al., 2019). The ANN model is created by a learning process, usually 75% percent of the total input/output data is reserved for training stage and 25% for evaluation. The learning process consists of the determination of suitable weight values according to real input/output data pairs and is an iterative process (Karkalos et al., 2019). During the past decades, although most of the field measurements of CH_4 fluxes were made in high latitude regions, some measurements in temperate or tropical region started to accumulate. Currently, with the accumulation of available in situ CH_4 flux data and formation of coordination network for ecosystem-scale CH_4 measurements at the global scale (e.g. FLUXNET, Knox et al., 2019), it is time to use a data-driven ANN approach to quantify wetland CH_4 emissions. This study first used an ANN approach to find the optimal nonlinear regression between CH_4 fluxes and key environmental controls. Driven with the spatially explicit data of climate, hydrology and soil

properties, the developed ANN was then extrapolated to the global scale to estimate wetland CH_4 emissions during a historical period 1979-2018 and a future period of 2006-2099.

4.3 Method

4.3.1 Overview

We first collected wetland CH_4 flux observation data from different climate regions and soil property data (Table 4.1; Section 4.3.2). These data were used to develop the relations between input variables and output CH_4 fluxes using an ANN model (Table 4.2; Section 4.3.3). We then evaluated the ANN model and extrapolated to the global scale by using the data of climate, soil property and wetland inundation area to estimate natural wetland CH_4 emissions during a historical period 1979-2018. Moreover, we used a well-trained ANN model to predict future wetland CH_4 emissions during 2006-2099 (Section 4.3.4). The sensitivity and uncertainty analysis were conducted for this period (Section 4.3.5).

4.3.2 Data Organization

We compiled CH_4 flux chamber measurements and eddy covariance measurements of wetland ecosystems at the global scale. Some of them are from peer-reviewed literature (e.g., Zhuang et al., 2008; Nahlik and Mitsch, 2011) and others are from AmeriFlux network (https://ameriflux.lbl.gov; e.g., Sonnentag and Quinton, 2016; Baldocchi, 2018; site 25-45). Only the long-term observations covering at least one-year period (except tropical regions) were collected. CH_4 measurements can be challenging in tropical regions due to unstable environments, resulting in only short-term observations (e.g. Nahlik and Mitsch, 2011). Our data contain CH_4 flux measurements from 56 sites, covering a range of wetland types under various field conditions (Table 4.1). Each site contains a collection of CH_4 flux measurement records together with some

environment variables like temperature, precipitation and soil properties. The original data were recorded as half hourly, hourly, daily, weekly or monthly. We converted them into monthly values by simply averaging non-monthly data within a month and aggregating to monthly values without considering within-month flux variations.

In addition to the observed CH_4 flux data, the site-level data of precipitation (PREC), surface air temperature (TAIR), surface downward solar radiation (SOLAR), elevation (ELEV), bulk density of the soil (BULK), clay content in soil (CLPC), carbon/nitrogen ration in soil (CNRT), organic carbon content in soil (ORGC), soil reaction pH (PHAQ), sand content in soil (SDTO) and silt content in soil (STPC) were also organized (Table 4.2). We did not include water table depth (WTD), which has been considered as a key factor controlling CH_4 emissions from wetland in most of previous bottom-up models (Zhuang el al., 2004; Zhu et al., 2013; Zhu et al., 2014). The WTD were not observed transiently at some sites. Regional water table depth data were often estimated using hydrology models, and their accuracy was temporally or spatially limited, which will introduce new uncertainties to an ANN model. In order to have enough amount of data points for global ANN model training and prepare for further global simulation, we replaced WTD with a set of variables which were normally considered in process-based WTD hydrology model, including TAIR, PREC, SOLAR and soil properties. Additionally, we used climate type (1. Boreal, 2. Temperate, 3. Tropical) and wetland type (1. Forested, 2. Non-forested) as input variables. The site-level data were first retrieved from original studies or AmeriFlux network websites and then complemented with other spatially explicit data sets based on the geographic coordinates and observation dates. When there were no observed meteorological data, climate data were derived from a reanalysis historical climatic dataset, Climatic Research Unit (CRU TS4.01; Harris et al., 2014; CRU for short). Especially, SOLAR data of ERA-Interim reanalysis climatic data from the

European Centre for Medium-Range Weather Forecasts (ECMWF; Dee et al., 2011) were used to fit the missing SOLAR data for each site. Site-level ElEV data were all retrieved from original site information. Soil property data including BULK, CLPC, CNRT, ORGC, PHAQ, SDTO and STPC were first retrieved from site information and then complemented using a harmonized soil property values from International Soil Reference and Information Centre World Inventory of Soil Emission Potentials (ISRIC-WISE) spatial soil database (WISE30sec; Batjes, 2016). We used the depth average method for soil property values from WISE30sec to derive the mean value for each variable for depth 0-200cm. Climate types were determined by site description and its latitude. Wetland types were determined by the site description and the classification from Matthews and Fung (1987). We simplified 5 categories (1. Forested Bog, 2. Non-forested Bog, 3. Forested Swamp, 4. Non-forested Swamp, 5. Alluvial Formations) to 2 categories (1. Forested, including Forested Bog, Forested Swamp and Alluvial Formations; 2. Non-forested, including Non-forested Bog and Non-forested Swamp). After processing, 3062 data points were retrieved for ANN model development.

4.3.3 Neural Network Development

We applied a generalized regression neural network (GRNN) algorithm (Specht, 1991) to represent the non-linear mapping between the independent variables (environmental variables) and the dependent variable (CH_4 fluxes). GRNN is similar to other kinds of neural networks, which is a data-driven model to estimate the underlying nonlinear relationship between model inputs and outputs, requiring no prior knowledge of the inputs. GRNN has some advantages including fast learning (without an interactive training procedure) and good convergence with a large amount of training data when comparing with other neural networks (Specht, 1991). GRNN model is a suitable mathematical model to develop a relation between CH_4 fluxes and the related

environmental factors. The model has a four-layer network architecture consisting of input, pattern, summation, and output layers (Zhuang et al., 2012). The multilayer neural network is trained using training dataset, including input and output values of measurements, to obtain a set of optimized interconnected network weights which can be used to produce the most probable value for the outputs.

A popular neural network validation method was adopted to validate the performance of the developed ANN model. Specifically, a set of training data (75%; N=2296) was randomly chosen from the whole measurement dataset to construct the ANN model and the rest of the dataset (25%; N= 766) was used to validate the constructed model. MATLAB codes were used for developing the ANN model (The MathWorks Inc., Natick, MA, USA).

Since we randomly chosen the training dataset from the measurement dataset, the constructed ANN model could be different and determined by the training dataset. In order to choose one representative model for stable global extrapolation, we first ran the normal ANN model 1000 times with randomly chosen training dataset. Then the best-run ANN was determined by the best evaluation results with largest coefficients of determination (R^2).

4.3.4 Regional Extrapolation

The developed best-run ANN model was used to simulate monthly CH_4 emissions from natural wetland ecosystems at the global scale at a spatial resolution of 0.5° x 0.5°. The climate type in each pixel was determined by the potential vegetation distribution (Melillo et al., 1993) and its latitude location. For instance, if no extra climate information, 30°S-30°N would be determined as tropical climate; 60°S-30°S and 30°N-60°N would be treated as temperate climate; and 90°S-60°S and 60°N-90°N would be regarded as boreal climate. The wetland type was defined in each pixel by vegetation distribution and wetland distribution from Matthews and Fung (1987)

(MF for short). The spatially explicit soil properties of the 0-200cm soil were retrieved from WISE30sec, including BULK, CLPC, CNRT, ORGC, PHAQ, SDTO and STPC. The elevation data were extracted from the Global, 1 arc second Digital Elevation Model (GDEM; Toutin, 2002).

To get the spatially and temporally explicit estimates of CH_4 consumption and emission at the global scale for historical and future scenarios, we designed three experiments: 1) for the period of 2000-2012, we used the transient wetland inundation area fraction data derived from previous study of merging Surface WAter Microwave Product Series (SWAMPS; Schroeder et al 2015) with the static inventory of wetland area from the Global Lakes and Wetlands Database (GLWD; Lehner and Doll 2004) by Poulter et al. (2017) (SWAMPS-GLWD). Precipitation, air temperature and solar radiation from ERA interim were processed into 0.5° x 0.5° spatial resolution and monthly time step to drive the model; 2) during 1979-2018, we used the static wetland distribution map from MF and climate forcing from ERA interim to drive the best-run ANN model to investigate the historical wetland CH_4 emission at the 0.5° x 0.5° spatial resolution and monthly time step; 3) for 2006-2099, we conducted the ANN model simulations using the static wetland distribution map from MF. The IPCC future climate scenarios from Representative Concentration Pathways (RCPs) climate forcing data sets RCP2.6, RCP4.5, RCP6.0 and RCP8.5 were retrieved from four global circulation models (GCMs) of the Inter-Sectoral Impact Model Inter-comparison Project (ISIMIP2b; Frieler et al, 2017), including GFDL-ESM2M, HadGRM2-ES, IPSL-CM5A-LR and MIROC5. ISIMIP2b bias-adjusted not only the multi-year monthly mean values and daily anomalies for most climate variables, but also adjusted them to a newly compiled reference dataset EWEMBI (E2OBS, WFDEI and ERAI data merged and bias-corrected for ISIMIP; Lange, 2016), which covers the entire globe at 0.5° horizontal and daily temporal resolution from 1979 to 2013. The climate forcing and wetland distribution data were processed into 0.5° x 0.5° spatial resolution

and monthly time step to conduct the best-run ANN model simulations with consideration of climate forcing data uncertainties from different models.

4.3.5 Sensitivity and Uncertainty Analysis

To identify key environmental variables in determining CH_4 fluxes, the sensitivity analysis of the ANN model to input data was conducted. The best-run ANN model involved 3 transient variables (temporal and spatial explicit) including PREC, TAIR and SOLAR, and 8 static variables (only spatial explicit) including ELEV, BULK, CLPC, CNRT, ORGC, PHAQ, SDTO and STPC. We therefore conducted 66 other regional simulations by altering the climate and soil input data uniformly for each grid cell at regional scales while keeping others as they were during 2000-2012, with same data input as experiment I described in section 4.3.4. Each of the 11 variables was individually increased or decreased at three levels including ±10%, ±25%, and ±50%. The sensitivity was then calculated as the percentage change between the estimated mean CH_4 fluxes of each sensitivity and the baseline simulation (experiment I).

The uncertainty of ANN model simulation is mainly from three sources including input variables, ANN model structure, and model parameters. Due to the lack of accurate prior knowledge of regional model inputs, we excluded regional forcing uncertainty analysis by only focusing on the uncertainties associated with ANN model structures and parameters. The ANN model was a data-driven and nonlinear system with optimized weight values. Thus, it was challenging to directly quantify the uncertainty range of the model through parametric inference since the model parameters were determined on the basis of the training dataset. In our study the structures and parameters model uncertainty were assessed through developing a number of alternative models using a "delete-one″ cross-validation method (Zhuang et al., 2012; Zhu et al., 2013). Specifically, we randomly sampled 75% of the measurement dataset as the training dataset

to develop a new ANN model. Each possible training set was used to construct a different set of network parameters or weights, which was then used for regional simulation of CH_4 fluxes during 2000-2012. During this step, the uncertainties in ANN model structures and parameters were quantified in an implicit manner. These steps were repeated 100 times to obtain 100 sets of regional estimation. The 95% confidence intervals of all estimates of CH_4 emissions were considered to be the range of model uncertainty and were thus used to define the lower and upper uncertainty bounds of the regional wetland CH_4 inventory.

4.4 Results

4.4.1 Trained Artificial Neural Networks

We conducted 1000 randomly chosen training sets to find the best-run ANN model with the largest validated R^2 value. The 1000 ANN models produced training R^2 values ranging from 0.98 to 0.99 and validated R^2 ranging from 0.2 to 0.42 (at a significance level of $p<0.01$). The root-mean square errors (RMSEs) for 1000 ANN models were ranging from 9.3 to 15.7 mg CH_4 m^{-2} day^{-1} for training and ranging from 91.0 to 129.5 mg CH_4 m^{-2} day^{-1} for validation. Thus, the best-run ANN model was determined as the one with training R^2=0.99 and validated R^2=0.42 (figure 4.1). The best-run ANN model simulated CH_4 fluxes are close to the observed data. The RMSE is 12.7 mg CH_4 m^{-2} day^{-1} for the training set and 91.0 mg CH_4 m^{-2} day^{-1} for the validation set (figure 4.1). The linear regression between the simulated and measured CH_4 fluxes is close to the 1:1 line, but with some underestimation at higher fluxes for the testing set (figure 4.1).

4.4.2 Temporal and Spatial Variations of Regional CH_4 Dynamics

For the historical period simulation with transient wetland inundation data SWAMPS-GLWD during 2000-2012, the Canadian lowlands, Alaska, northern eastern US, middle and east

Siberia, Amazon Basin, east of the Middle East, northern Asia, east Australia and areas near the equators acted as hotspots for CH_4 wetland emissions (Figure 4.2 upper panel). Simulated global annual wetland CH_4 fluxes are with a significant interannual variability from 2000 to 2012 (Figure 4.2, lower panel). Global mean annual emissions during this period are estimated to be 186 Tg CH_4 yr^{-1}, with the peak of 193 Tg CH_4 yr^{-1} in 2005 and the valley of 178 Tg CH_4 yr^{-1} in 2011 (Figure 4.2, lower panel). The region of 30°S-60°N contribute the most wetland CH_4 emission of 155 Tg CH_4 yr^{-1}, holding 84% of the global total wetland emissions (Table 4.3).

During 1979-2018, static wetland map MF was used for ANN best-run model simulation. Canadian lowlands, Alaska, Florida of the US, west Siberia, south side of the South America, and areas near the equators showed as hotspots for CH_4 wetland emissions (Figure 4.3 upper panel). Simulated global annual wetland CH_4 fluxes have a significant interannual variability from 1979 to 2018 (Figure 4.3, lower panel) with mean annual emissions of 188 Tg CH_4 yr^{-1} and a peak of 195 Tg CH_4 yr^{-1} in 2007 and a valley of 179 Tg CH_4 yr^{-1} in 1981 (Figure 4.3, lower panel). The region of 30°S-0 contributes the most wetland CH_4 emission of 68 Tg CH_4 yr^{-1} comparing with other regions, holding 36% of the global total wetland emission (Table 4.3).

Our model simulations during 2080-2099 from RCP2.6, 4.5, 6.0 and 8.5 were compared with a baseline simulation (2000-2018). (Figure 4.4). West Siberia and areas near the equator increased most comparing with the baseline, while the emissions in most areas of Canadian lowlands and south side of the South America decreased (Figure 4.4). From RCP2.6 to RCP8.5, the increased emissions become stronger (showed as red) and emission areas were larger, especially in western Siberia (Figure 4.4). Under the RCP2.6, the emissions did not change significantly with the emissions of 199 Tg CH_4 yr^{-1} during 2080-2099. In contrast, under the RCP8.5, the increase is significant, reaching 209 Tg CH_4 yr^{-1} during 2080-2099 (Figure 4.5a-d, Table 4.3). The uncertainty

from different models are smaller under the RCP2.6, 4.5 and 6.0 than under the RCP8.5 (Figure 4.5a-d). The region of 60°S-30°N did not increase under all RCPs in the 2090s, but contributed most uncertainties (Figure 4.5e-p). The region of 30°N-90°N increased significantly under the RCP6.0 and 8.5 scenarios by the 2090s.

4.4.3 Sensitivity and Uncertainty of Regional CH_4 Estimates

At the global scale, SOLAR stands out as the most sensitive one among 11 input variables (Figure 4.6). Increasing SOLAR favors CH_4 emissions while decreasing SOLAR inhibits emissions. Emissions vary uniformly with SOLAR at ±10% and ±25% changing levels but stop increasing with large decreases at ±50% changing levels (Figure 4.6a-c). Other sensitive variables include TAIR and ELEV. Higher TAIR stimulates emissions while lower TAIR inhibits emissions. CH_4 emissions rise or lower with increasing or decreasing ELEV. PREC, CLPC and ORGC are slightly sensitive, while the rest variables including BULK, CNRT, PHAQ, SDTO and STPC are not sensitive (Figure 4.4.6a-c). Sensitivities to variable changes in most regions are similar, except: 1) PREC can be significant sensitive in regions of 30°N-90°N, higher PREC favors more emissions (Figure 4.6m-r), while lower PREC favors higher emissions in the regions of 60°S-30°S and 0-30°N (Figure 4.6d-f; Figure 4.6j-l); 2) SOLAR changes can have opposite effects on emissions in the region of 0-30°N (Figure 4.6j-l); 3) Higher ELEV can have opposite effects on emissions in the region of 30°S-0 (figure 4.6g-i); 4) SDTO and STPC can be slightly sensitive in the regions of 60°S-0, 30°N-60°N (figure 4.6d-I; figure 4.6m-o); 5) ORGC becomes very sensitive in the regions of 60°N-90°N (figure 4.6p-r); 6) some variable changes can have very different effects at the ±50% changing level comparing with ±10% and ±25% levels, such as SOLAR in the regions of 60°S-30°S and 0-30°N (figure 4.6d-f; figure 4.6j-l).

The 100 ANN models provide a probability distribution of regional CH_4 emissions (Figure 4.7). The uncertainties of regional CH_4 emissions from ANN model structures and parameters are defined as the range between the lower bound and the upper bound of the 95% confidence intervals. At the global scale the mean of the Gaussian probability distribution is 179 Tg CH_4 yr^{-1} with a range of 168-190 Tg CH_4 yr^{-1}. The standard deviation (STD) is 5.52 Tg CH_4 yr^{-1} (Figure 4.7a). The region with biggest uncertainty is 0-30°N, contributing a 2. Tg CH_4 yr^{-1} to STD (Figure 4.7d). For interannual variability or seasonality, we calculate the probability distribution for each year or each month and then use Gaussian fitted distribution to find the lower bound and the upper bound of the 95% confidence intervals, respectively. The interannual variability indicates a peak close to 200 Tg CH_4 yr^{-1} in 2005 and a value of 160 Tg CH_4 yr^{-1} in 2011 by considering the structures and parameters uncertainty during 2000-2012 at the global scale (figure 4.8a). The peak and valley years vary significantly in the regions of 60°S-30°S and 30°N-90°N (Figure 4.8b, e, f). Global CH_4 emissions are higher during summer and lower during winter and have a higher uncertainty during summer (Figure 4.9a). The Southern Hemisphere has the opposite seasonality comparing to global results (Figure 4.9b). The tropical regions including 30°S-0 and 0-30°N have a two-peak shape and a two-valley shape, respectively (Figure 4.9c, d). The regions over 30°N are very similar to global results, with a small peak shift from June to May in the 30°N-60°N region (Figure 4.9e, f).

4.5 Discussion

4.5.1 Effects of In Situ Data Availability and Wetland Distribution Data on the Inventory

Our ANN model presents R^2 ranging from 0.2 to 0.42 when randomly choosing the training dataset from the measurements, which is relatively low comparing with a previous study using an ANN model to map CH_4 emissions from high latitudes (R^2=0.68; Zhu et al., 2013). There are a few reasons for this discrepancy. Firstly, we use more data points (3000 vs 1000 in the previous

study) covering the globe including temperate and tropical regions. Temperate regions (triangle) show the largest biases in model simulations (Figure 4.1 lower panel). This might also be due to observation data uncertainty. In particular, when we converted observation data from smaller time steps (e.g., hourly, daily and weekly) to monthly, we simply used the mean flux values of all data located in that month to represent the monthly CH_4 flux, introducing errors to the data. In addition, some data points used in model training were fitted using reanalysis data (e.g. ERA-interim and WISE30sec) since some environmental variables are missing at observation sites. This might also lead to unrealistic relationships built in the ANN model, leading to poor performance in model evaluation (Figure 4.1 lower panel).

From our analysis of uncertainty due to model structures and parameters (Figure 4.7, 4.8, 4.9), the probability distribution of the mean emissions during 2000-2012 indicates that 0-30°N and 30°S-0 contribute the first and second largest uncertainties (Figure 4.4c, d). Both are located in tropical regions, where we collected the least data. Thus, the ANN model was not well trained in these regions. In addition, the wetland distribution map can substantially influence the regional extrapolation of ANN model (Zhu et al., 2011; Table 4.3). The regional total of CH_4 emissions may be greatly affected by the choice of wetland dataset being used. For instance, when using static map to replace the transient map, the CH_4 emission estimates increase from 19 to 30 Tg CH_4 yr^{-1}.

At the global scale, the ANN models estimate the global emissions of 169-190 Tg CH_4 yr^{-1} with a mean value of 186 Tg CH_4 yr^{-1} during 2000-2012 with transient wetland inundation data. When using the static wetland distribution, the global emissions are 188 Tg CH_4 yr^{-1} during 1978-2018. The Previous estimates with multiple approaches during 2000-2017 range from 102 to 200 Tg CH_4 yr^{-1} (Table 4.3; Saunois et al., 2019). Our estimates are within the range of previous

estimates. However, in the regions of 30°N-60°N, the ANN model presents 52 Tg CH_4 yr^{-1} and 44 Tg CH_4 yr^{-1} for the period 2000-2012 and 1979-2018, respectively, exceeding the upper bound of previous estimates by Saunois et al. (2019) at 11-44 Tg CH_4 yr^{-1}. In addition, we estimated 19 Tg CH_4 yr^{-1} and 30 Tg CH_4 yr^{-1} in the region of 60°N-90°N for 2000-2012 and 1979-2018, respectively, exceeding the upper bound estimate by Saunois et al. (2019) with 2-18 Tg CH_4 yr^{-1}. The higher emissions from the ANN models might be due to different wetland maps used in different studies. The SWAMPS-GLWD and MF wetland distribution maps may overestimate the wetland area by including some lakes and rivers (Poulter et al., 2017). Indeed, there are large differences between SWAMPS-GLWD and MF wetland distribution maps, resulting in different regional distributions of CH_4 fluxes (figure 4.2a and 4.3a). Different wetland maps have significantly different wetland areas. For instance, the MF indicates global wetland area is 5.3 Mkm^2, while the SWAMPS-GLWD estimates a maximum of 10.5 Mkm^2 (Poulter et al., 2017; Matthews and Fung, 1987). Another wetland area map from Wetland Area Dynamics for Methane Modeling (WAD2M) shows the global wetland area is 14.9 Mkm^2 during the peak season, and 8.4 Mkm^2 on annual average, with a range of 8.0 - 8.9 Mkm^2 during 2000-2017, which accounts for 5.5% of the global land surface (Saunois et al., 2019).

4.5.2 Effects of Predictor Variables on the Inventory

The trends of increasing of emissions at the global and regional scales over 30°N, and the trends of steady emission in the region of 60°S-30°N in RCP8.5 can be explained with the predictor variable sensitivity test (Figure 4.5, 4.6). Globally, the CH_4 emission increases significantly under the RCP6.0 and 8.5 because of increasing TAIR and SOLAR (Figure 4.5a-c, 4.6a-c). In the regions of 60°S-30°N, TAIR and SOLAR are not very sensitive when exceeding a certain level like +25% or even having an opposite effect (Figure 4.6d-l). This is because that CH_4

production has its optimal TAIR and SOLAR. When optimal TAIR and SOLAR reached, further increase in those variables will not increase CH_4 emissions significantly or even decrease the emissions (e.g., 0-30°N, figure 4.6j-k). Thus, the future prediction of CH_4 emissions will not increase significantly during the 21st century with increasing TAIR and SOLAR under the RCP8.5 and RCP6.0 in these regions. The regions over 30°N in Northern Hemisphere have a similar global emission trend under all RCPs since they have very similar sensitivities (figure 4.5q-x, 4.6q-x). The big uncertainty in future prediction in some regions like 30°S-0 is due to RCPs from different models have big variances over these regions. The ELEV variable is sensitive in all regions (figure 4.6). Normally lower ELEV favors higher CH_4 emissions because lower altitude and ELEV regions have larger possibilities to be dominated by wetlands.

To avoid using WTD variable in global estimation, we replaced WTD with several key variables which used in soil hydrology calculation in process-based models Terrestrial Ecosystem Model (TEM; Zhuang et al., 2003, 2004, 2007). The sensitivity analysis results indicate that the PREC, TAIR, SOLAR, ELEV, ORGC are significant sensitive and should be considered in future ANN modelling work (figure 4.6). CLPC, SDTO and STPC can be relatively sensitive in some regions and should be useful in future spatially explicit ANN modelling. BULK, CNRT and PHAQ are not sensitive in global modelling but can be widely found in previous process-based models. We used the static values for these three variables. In fact, BULK, CNRT and PHAQ are largely determined by soil hydrology conditions and will vary significantly as time goes by. Transient BULK, CNRT and PHAQ measurement data should be included in future ANN model training work and global simulations.

4.6 Conclusions

This study uses an artificial neural network approach and CH_4 flux measurements in wetland ecosystems and associated environmental data to inventory global wetland CH_4 emissions. We find that global mean annual wetland CH_4 emissions are 186 Tg CH_4 yr^{-1} with an uncertainty range of 169-190 Tg CH_4 yr^{-1}, and there are both significant interannual and seasonal variations of emissions during 2000-2012 when using a transient wetland inundation map. By using the static wetland distribution data, the emissions are estimated to be 188 Tg CH_4 yr^{-1} during 1979-2018 but have large differences in regional distributions. The estimated emissions will reach 199, 201, 204, and 209 Tg CH_4 yr^{-1} at the last two decades of the 21st century when using RCP2.6, 4.5, 6.0 and 8.5, respectively. The global wetland CH_4 emissions are most sensitive to variations in solar radiation and temperature. The large spatial variability in CH_4 emissions is due to variations in hydrology, climate, and soil conditions. This study calls for better characterizing variations of wetland areas and water table position and more long-term observations of CH_4 fluxes in tropical regions so as to improve future inventorying wetland CH_4 emissions at the global scale.

Acknowledgment: This study is supported by NASA (NNX17AK20G), the Department of Energy (DESC0008092 and DE-SC0007007), and the NSF Division of Information and Intelligent Systems (NSF-1028291). The supercomputing is provided by the Rosen Center for Advanced Computing at Purdue University. We are also grateful to the University of Tuscia (dep. DIBAF), Italy, and their affiliated members, for their help and the use of their field data. All data used in this manuscript can be accessed in Purdue University Research Repository (PURR) through the link: https://doi.org/10.4231/3YX4-EY30.

Table 4.1. Description of the site used in this study

No.	Site Name	Longitude	Latitude	Climate	Wetland Type	Time period	Reference
1	Cuini	-64.10	-0.81	Tropical	Nonforested	Monthly 2005	Belger, et al. (2014)
2	Itu	-63.56	-0.29	Tropical	Nonforested	Monthly 2005	Belger, et al. (2014)
3	EARTH	-83.57	10.22	Tropical	Forested	Few visits 2006-2009	Nahlik and Mitsch (2011)
4	La Selva	-84.01	10.42	Tropical	Forested	Few visits 2006-2009	Nahlik and Mitsch (2011)
5	Palo Verde	-85.33	10.34	Tropical	Forested	Few visits 2006-2009	Nahlik and Mitsch (2011)
6	SSA-fen	-104.62	53.80	Boreal	Forested	Daily 1994-1995	Sellers, et al. (1997)
7	NSA-fen	-98.42	55.92	Boreal	Forested	Daily 1994/1996	Sellers, et al. (1997)
8	Sallie's Fen	-71.06	43.21	Temperate	Forested	Weekly, 1994-2001	Zhuang, et al. (2008)
9	Buck Hollow Bog	-84.02	42.45	Temperate	Nonforested	monthly,1991-1993	shannon,et al. (1994)
10	Minnesota peatland1	-93.47	47.53	Temperate	Forested	Weekly,1991-1992	Clement et al. (1995); Shurpali (1993,1998)
11	Mer Bleue Bog	-75.48	45.41	Temperate	Nonforested	Weekly, 2004-2007	Moore, et al. (2011)
12	Minnesota peatland2	-93.47	47.53	Temperate	Forested	Monthly,1988-1990	Dise (1993)
13	Stordalen1	19.05	68.33	Boreal	Nonforested	monthly, 1994-1995	Svensson et al. (1999)
14	Stordalen2	19.05	68.33	Boreal	Nonforested	Daily, 2006-2007	Jackowicz-Korczynski et al. (2010)
15	Degero Stormyr	19.55	64.18	Boreal	Nonforested	Daily, 1995-1997	Grandberg, et al. (2001)
16	Salmisue mire	30.93	62.78	Boreal	Forested	Daily, 1993	Saamio, et al. (1997)
17	Ruovesi	24.02	81.83	Boreal	Forested	Daily, 2005	Rinne, et al. (2007)

Table 4.1 continued

18	Quebec1	-78.77	53.90	Boreal	Nonforested	Daily, 2003	Pelletier, et al. (2007)
19	Quebec2	-77.72	53.63	Boreal	Nonforested	Daily, 2003	Pelletier, et al. (2007)
20	Quebec3	-76.13	53.57	Boreal	Nonforested	Daily, 2003	Pelletier, et al. (2007)
21	Sanjiang Plain1	133.52	47.58	Temperate	Nonforested	Annually, 2002-2005	Huang, et al. (2010); Song, et al. (2009)
22	Sanjiang Plain2	133.52	47.58	Temperate	Nonforested	Monthly, 1995-1996, 2001-2003	Want, et al. (2002); Cui, et al. (1997); Ding, et al. (2004); Yang, et al. (2006); Hao, et al. (2004)
23	Loch Vale	-105.65	40.28	Temperate	Nonforested	Daily, 1996-1998	Wichland, et al. (2001)
24	Ryans 1 Billagong	146.97	-36.12	Temperate	Nonforested	Monthly, 1993-1994	Boon and Mitchel (1995)
25	CA-SCB	-121.30	61.31	boreal	Nonforested	Hourly 2014-2017	Sonnentag and Quinton (2016)
26	US-A03	-149.88	70.50	boreal	Nonforested	Hourly 2014-2018	Cook (2016a)
27	US-A10	-156.61	71.32	boreal	Nonforested	Hourly 2011-2018	Cook (2016b)
28	US-DPW	-81.44	28.05	tropical	Nonforested	Hourly 2013-2017	Hinkle (2016)
29	US-EDN	-122.11	37.62	Temperate	Nonforested	Hourly 2018-2018	Oikawa (2016)
30	US-EML	-149.25	63.88	boreal	Nonforested	Hourly 2008-2018	Schuur (2018)
31	US-Ivo	-155.75	68.49	boreal	Nonforested	Hourly 2003-2016	Oechel and Zona (2016)
32	US-LA1	-90.44	29.50	tropical	Nonforested	Hourly 2011-2012	Krauss (2016a)
33	US-LA2	-90.29	29.86	tropical	Nonforested	Hourly 2011-2013	Krauss (2016b)
34	US-Los	-89.98	46.08	Temperate	Forested	Hourly2001-2018	Desai (2016a)

Table 4.1 continued

35	US-Myb	-121.76	38.05	Temperate	Nonforested	Hourly 2010-2018	Baldocchi (2016)
36	US-NGB	-156.61	71.28	boreal	Nonforested	Hourly 2012-2018	Torn (2018)
37	US-ORv	-83.02	40.02	Temperate	Nonforested	Hourly 2011-2016	Bohrer (2016)
38	US-OWC	-82.51	41.38	Temperate	Nonforested	Hourly 2015-2016	Bohrer (2018)
39	US-PFa	-90.27	45.95	Temperate	Forested	Hourly 1995-2018	Desai (2016b)
40	US-Sne	-121.75	38.04	Temperate	Nonforested	Hourly 2016-2018	Baldocchi (2018)
41	US-Srr	-122.03	38.20	Temperate	Nonforested	Hourly 2014-2017	Bergamaschi and Windham-Myers (2018)
42	US-StJ	-75.44	39.09	Temperate	Nonforested	Hourly 2016-2016	Vargas (2016)
43	US-Tw1	-121.65	38.11	Temperate	Nonforested	Hourly 2011-2018	Baldocchi (2016)
44	US-Uaf	-147.86	64.87	boreal	Forested	Hourly 2003-2018	Iwata, et al. (2016)
45	US-WPT	-83.00	41.46	Temperate	Nonforested	Hourly 2011-2013	Chen (2016)
46	Tobolsk	68.12	58.47	boreal	Forested/Nonforested	Few visits 2007	Glagolev, et al. (2011)
47	Surgut	73.33	61.43	boreal	Nonforested	Few visits 2007	Glagolev, et al. (2011)
48	Pangody	74.96	65.87	boreal	Nonforested	Few visits 2007	Glagolev, et al. (2011)
49	Plotnikovo	82.85	56.85	boreal	Forested/Nonforested	Monthly 1997, 2006-2010	Glagolev, et al. (2011)
50	Noyabrsk-Hills	74.49	63.12	boreal	Forested/Nonforested	Few visits 2008	Glagolev, et al. (2011)
51	Noyabrsk-Palsa	75.55	63.80	boreal	Nonforested	Few visits 2008	Glagolev, et al. (2011)
52	Vah	70.42	59.74	boreal	Forested	Few visits 2008	Glagolev, et al. (2011)

Table 4.1 continued

53	Muhrino	68.70	60.89	boreal	Forested/Nonforested	Monthly 2008-2010	Glagolev, et al. (2011)
54	Tazovsky	78.92	67.18	boreal	Nonforested	Monthly 2009-2010	Glagolev, et al. (2011)
55	Gyda	78.55	70.89	boreal	Forested/Nonforested	Few visits 2010	Glagolev, et al. (2011)
56	Skala	81.78	55.40	boreal	Forested	Few visits 2010	Glagolev, et al. (2011)

Table 4.2. Description of the parameters in the ANN model

Parameters	Description	Unit	Sources
PREC	Precipitation	mm $month^{-1}$	Site observation/CRU/ERA interim
TAIR	Surface air temperature	°C	Site observation/CRU/ERA interim
SOLAR	Surface downward solar radiation	W m^{-2}	Site observation/ERA interim
ELEV	Surface elevation	M	Site observation/GDEM
BULK	Bulk density of the soil	g cm^{-3}	Site observation/WISE30sec
CLPC	Clay content in soil	mass %	Site observation/WISE30sec
CNRT	Carbon/Nitrogen ratio in soil	mass/mass	Site observation/WISE30sec
ORGC	Organic carbon content in soil	g kg^{-1}	Site observation/WISE30sec
PHAQ	Soil reaction pH	pH unit	Site observation/WISE30sec
SDTO	Sand content in soil	mass %	Site observation/WISE30sec
STPC	Silt Content in soil	mass %	Site observation/WISE30sec

Table 4.3. Historical and future CH_4 emissions (Tg CH_4 yr^{-1}) estimated with the ANN model. The reference for other studies is Saunois et al. (2019).

Experiment	Period	Category	90S-60S	60S-30S	30S-0	0-30N	30N-60N	60N-90N	global
Historical	2000-2012	Emission_value	0	10.2	50.8	53.7	51.9	19.4	186.0
		Range	--	[8.4-10.7]	[44.7-51.6]	[48.2-57.3]	[47.4-52.9]	[17.4-19.8]	[168.5-190.1]
Historical	1979-2018	Emission_value	0	7.9	67.6	37.6	44.4	30.3	187.8
Other Studies	2008-2017	Range	[71-155]	[11-44]	[2-18]	[102-200]			
RCP2.6	2080-2099	Emission_value	0	8.0	72.7	41.0	45.9	31.3	198.9
		Range	--	[7.8-8.1]	[70.8-73.9]	[40.4-41.4]	[45.5-46.4]	[31.0-31.6]	[197.7-200.5]
RCP4.5	2080-2099	Emission_value	0	8.2	73.1	41.7	46.3	32.1	201.4
		Range	--	[8.1-8.3]	[70.9-75.7]	[41.4-41.9]	[45.4-46.8]	[31.3-32.9]	[199.4-205.2]
RCP6.0	2080-2099	Emission_value	0	8.3	74.1	42.0	46.8	32.6	203.8
		Range	--	[8.1-8.4]	[72.1-77.1]	[40.6-42.5]	[45.5-47.6]	[32.1-33.2]	[201.2-207.7]
RCP8.5	2080-2099	Emission_value	0	8.4	75.4	42.8	47.9	34.1	208.5
		Range	--	[8.2-8.5]	[72.8-79.0]	[41.1-43.5]		[46.8-49.0] [32.8-35.8]	[203.5-215.2]

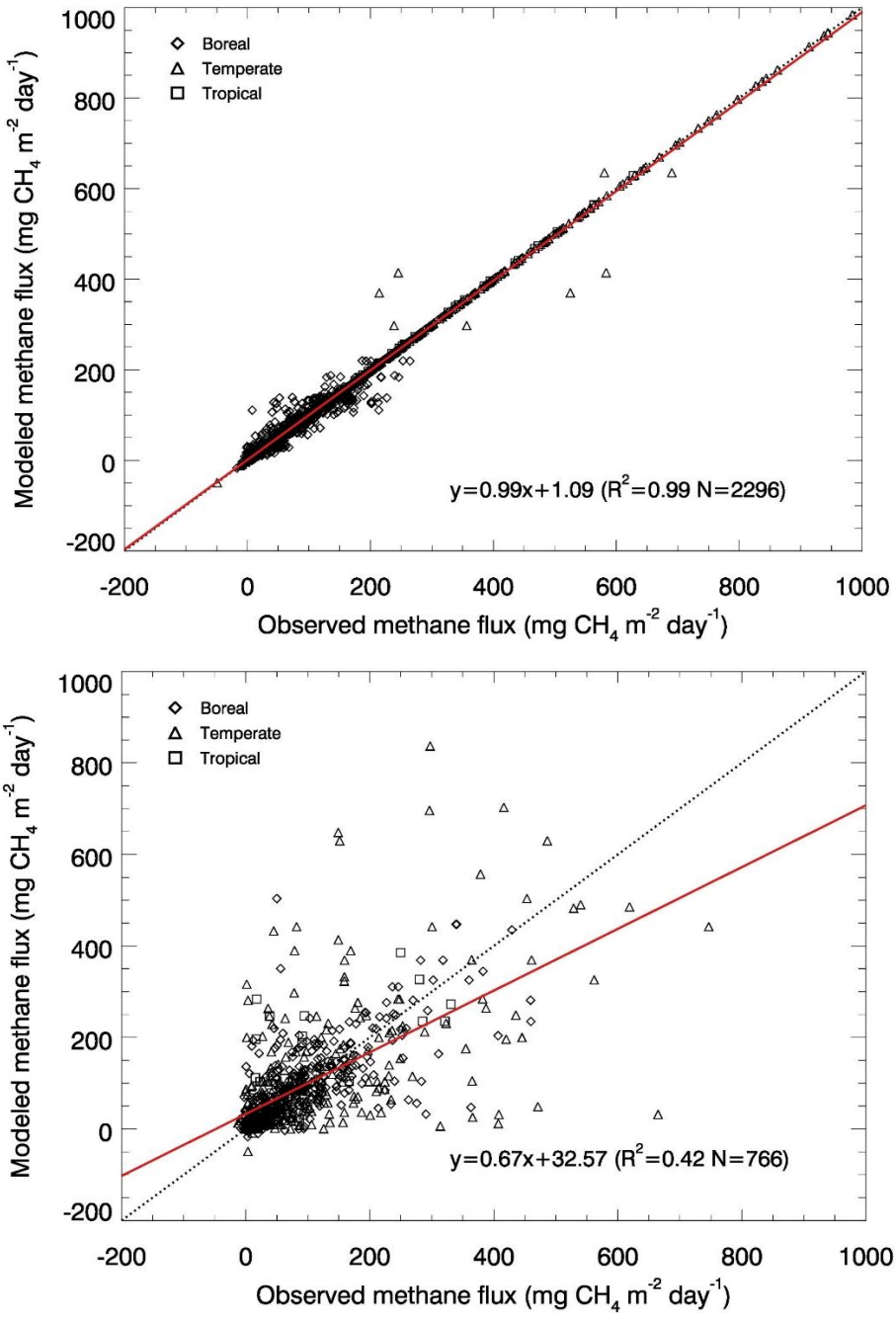

Figure 4.1. Comparisons between the measured and modeled monthly CH_4 emissions at all sites. Upper panel: The ANN models were constructed based on the training dataset; and lower panel: the validation dataset was used to test the performance of the model. Diamond symbol represents the boreal data. Triangle symbol represents the temperate data. Square symbols represent the tropical data. The dashed line is the 1:1 line, and the solid red line is the fitted line.

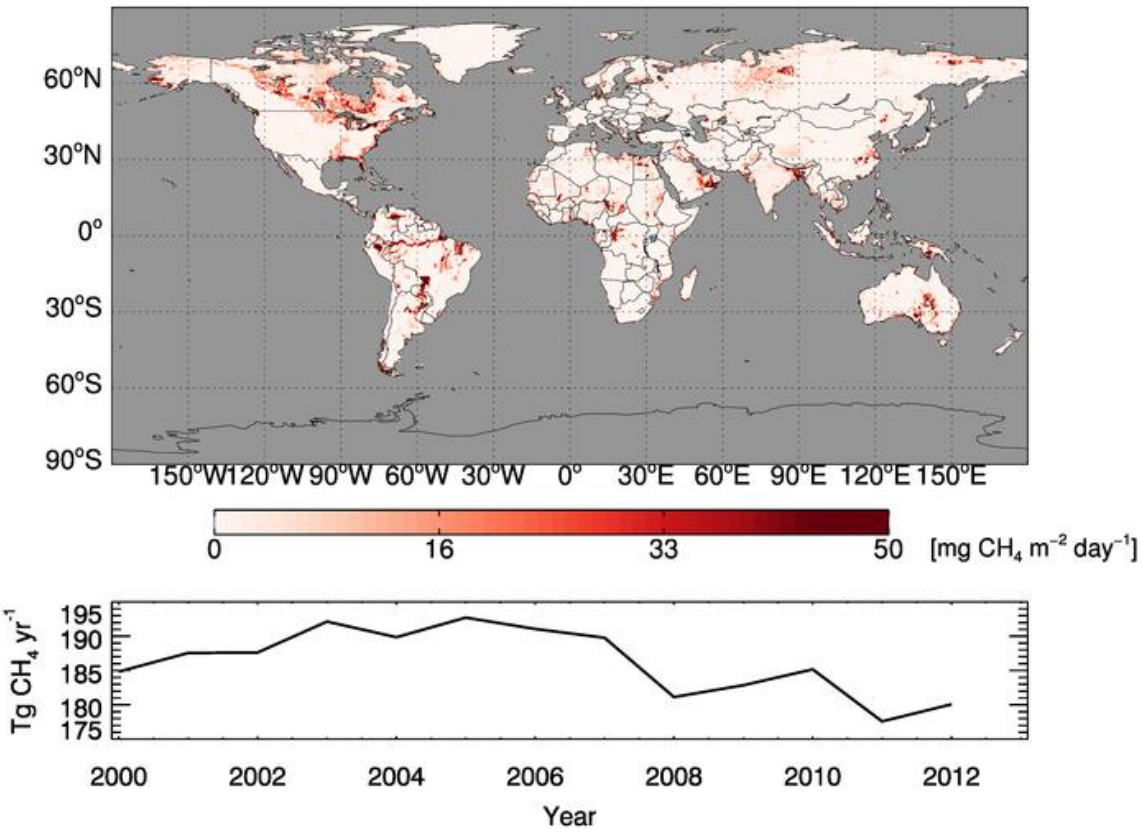

Figure 4.2. ANN model estimated global CH_4 wetland emissions with the transient wetland inundation map during 2000-2012. Upper panel is the global wetland mean fluxes distribution; Lower panel is the global annual wetland emission.

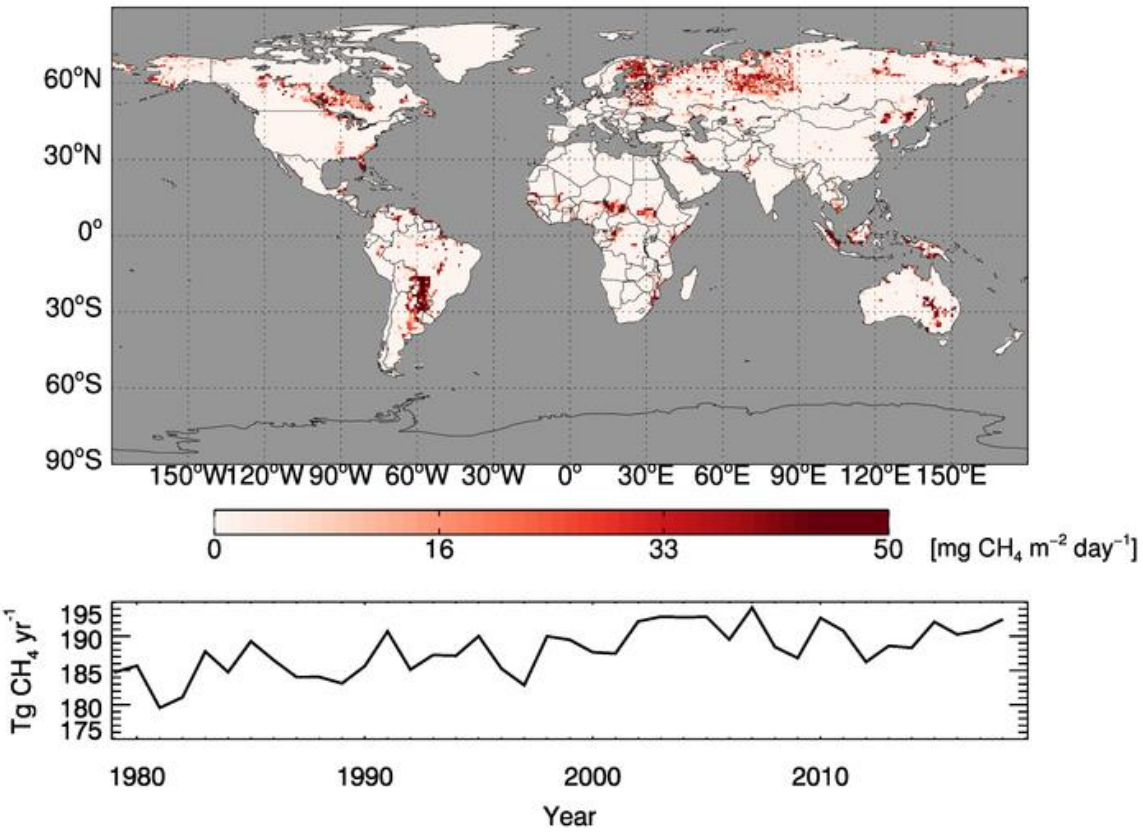

Figure 4.3. ANN model estimated global CH_4 wetland emissions with the static wetland inundation map during 1979-2018. Upper panel is the global wetland mean fluxes distribution; Lower panel is the global annual wetland emission

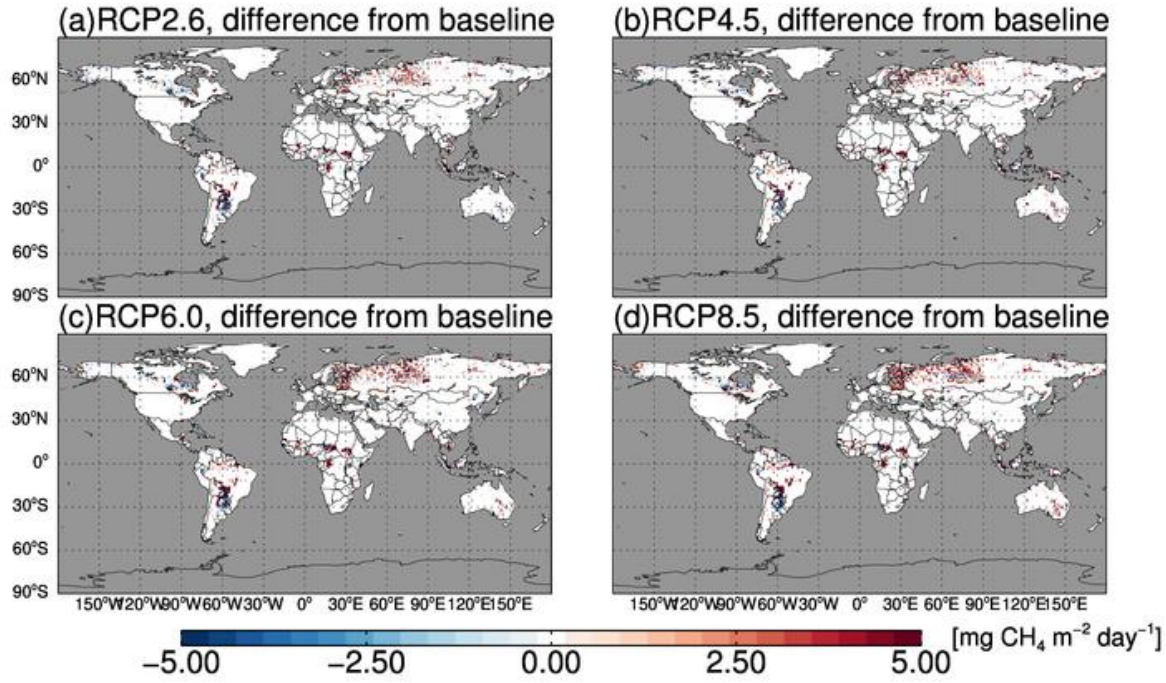

Figure 4.4. ANN model future predictions of global mean wetland CH_4 emission distribution during 2080-2099 comparing with historical estimates during 2000-2018 (positive value means increase). (a)-(d) presented results using future climate forcing of RCP2.6, 4.5, 6.0 and 8.5, respectively

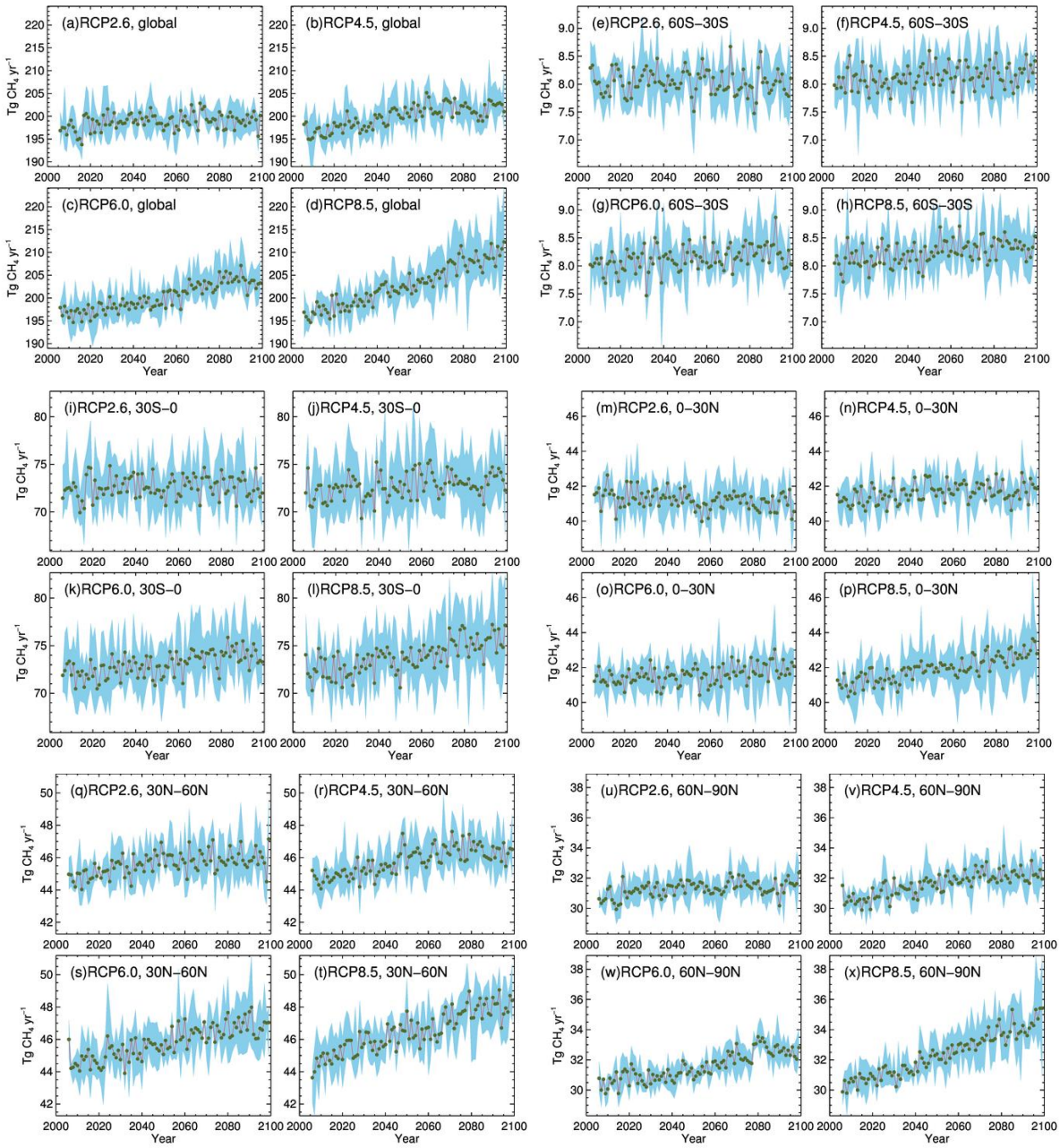

Figure 4.5. ANN model future predictions of annual wetland emissions from different regions. Green dots are interannual variation, red lines are fitted lines between years and blue shadows are uncertainties from four different GCMs in each RCP scenario

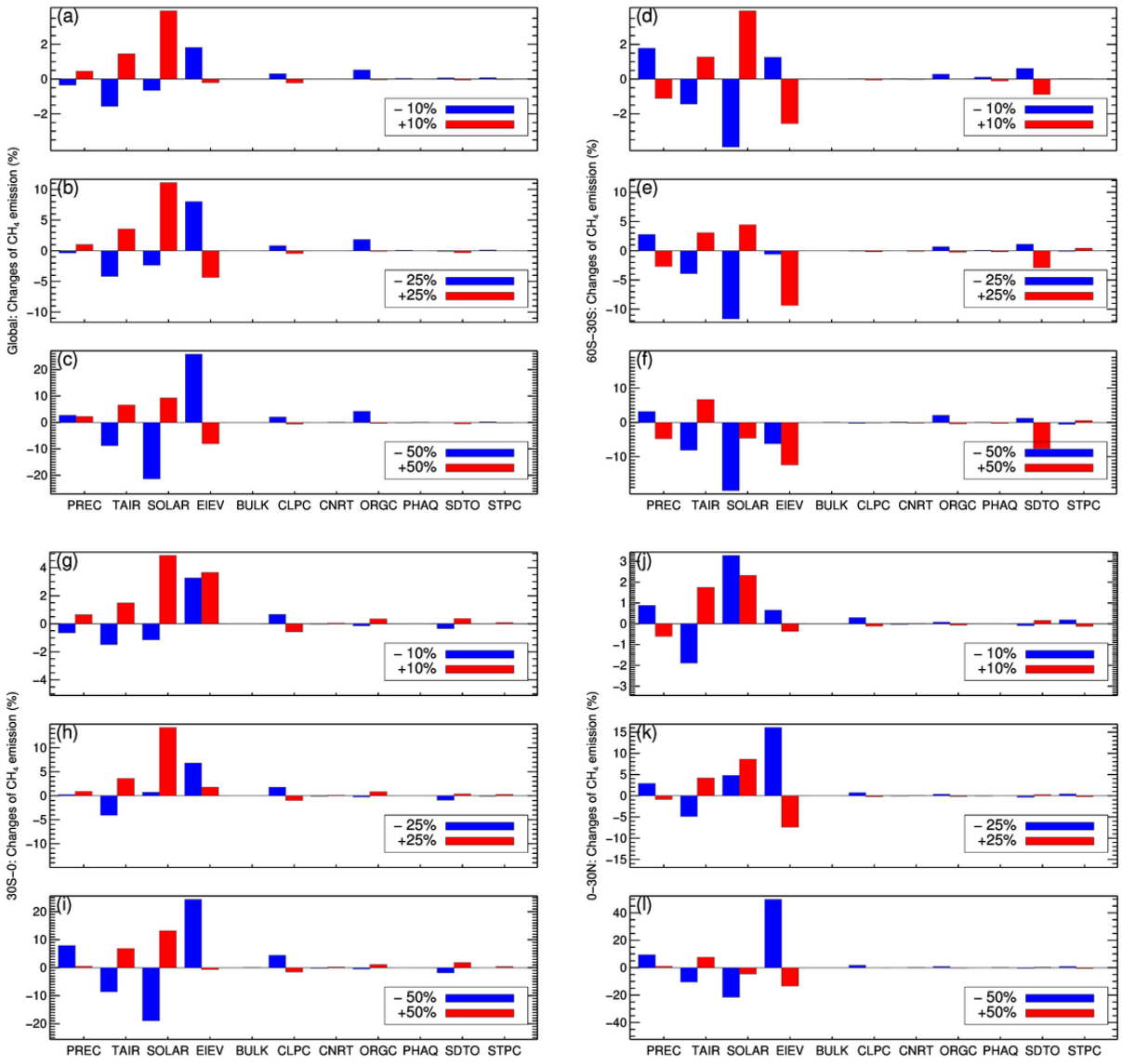

Figure 4.6. Sensitivity of the ANN model to changes in precipitation (PREC), surface air temperature (TAIR), surface solar radiation (SOLAR), elevation (ElEV), soil bulk density (BULK), soil clay content (CLPC), soil carbon/nitrogen ratio (CNRT), soil organic carbon (ORGC), soil pH (PHAQ), soil sand content (SDTO) and soil silt content (STPC). The values are for the period 2000-2012 and different regions. The changes are calculated based on the baseline simulation using the unchanged regional input data

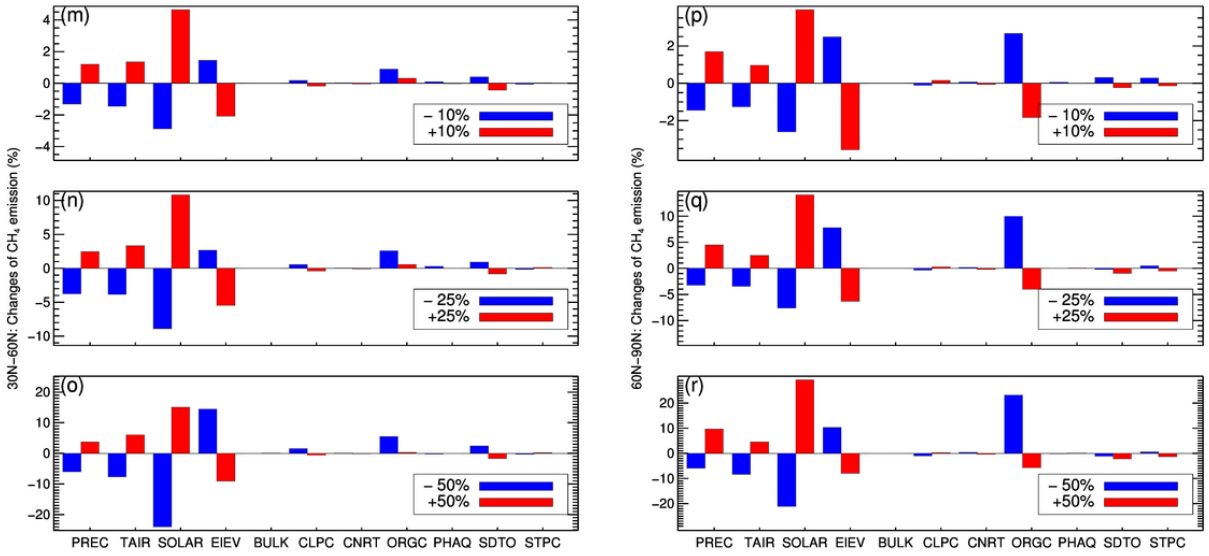

Figure 4.6.contd. Sensitivity of the ANN model to changes in precipitation (PREC), surface air temperature (TAIR), surface solar radiation (SOLAR), elevation (ElEV), soil bulk density (BULK), soil clay content (CLPC), soil carbon/nitrogen ratio (CNRT), soil organic carbon (ORGC), soil pH (PHAQ), soil sand content (SDTO) and soil silt content (STPC). The values are for the period 2000-2012 and different regions. The changes are calculated based on the baseline simulation using the unchanged regional input data

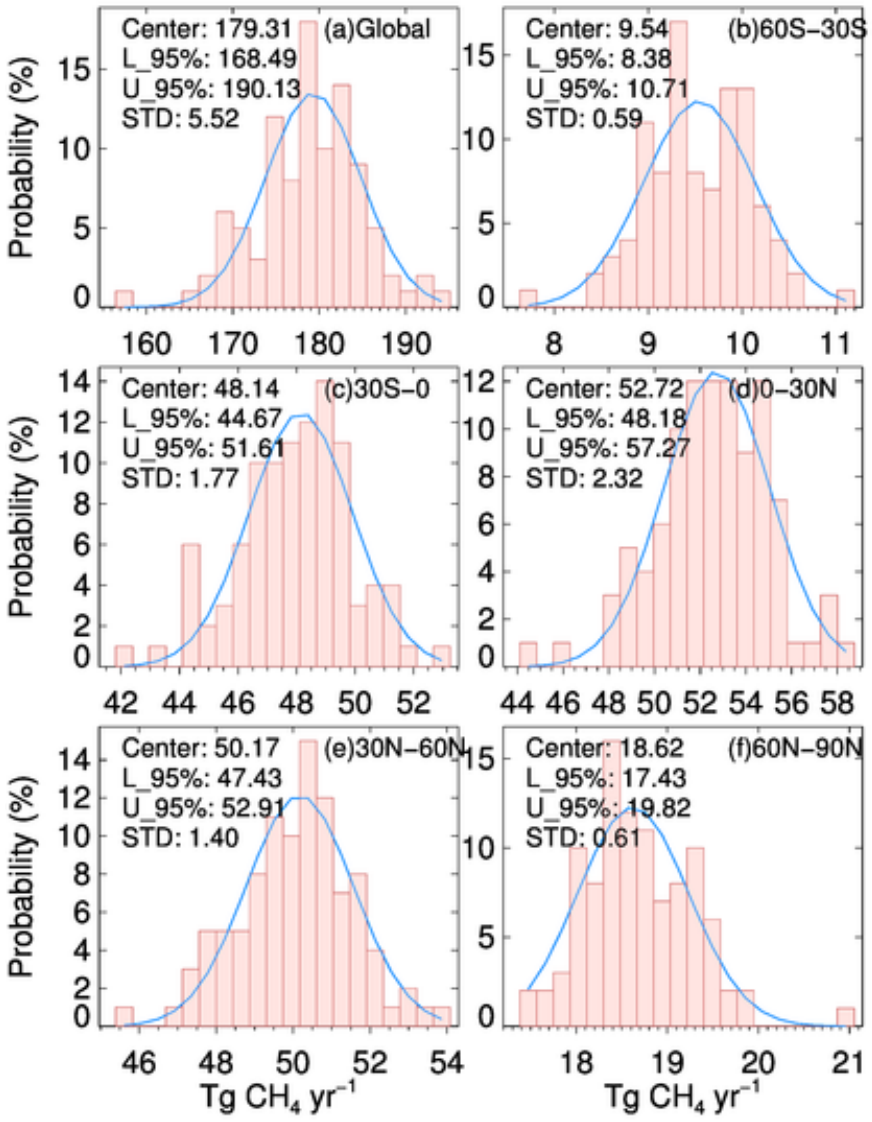

Figure 4.7. Uncertainties of the estimated wetland CH_4 emissions from the different region with 100 ANN models. Probability distribution (red histograms), fitted Gaussian distribution line (blue lines), the center of the distribution (Center), the 95% confidence intervals (L_95%: lower boundary of the distribution; U_95%: upper boundary of the distribution) and the standard deviation (STD) of mean annual CH_4 emissions during year 2000-2012 are presented

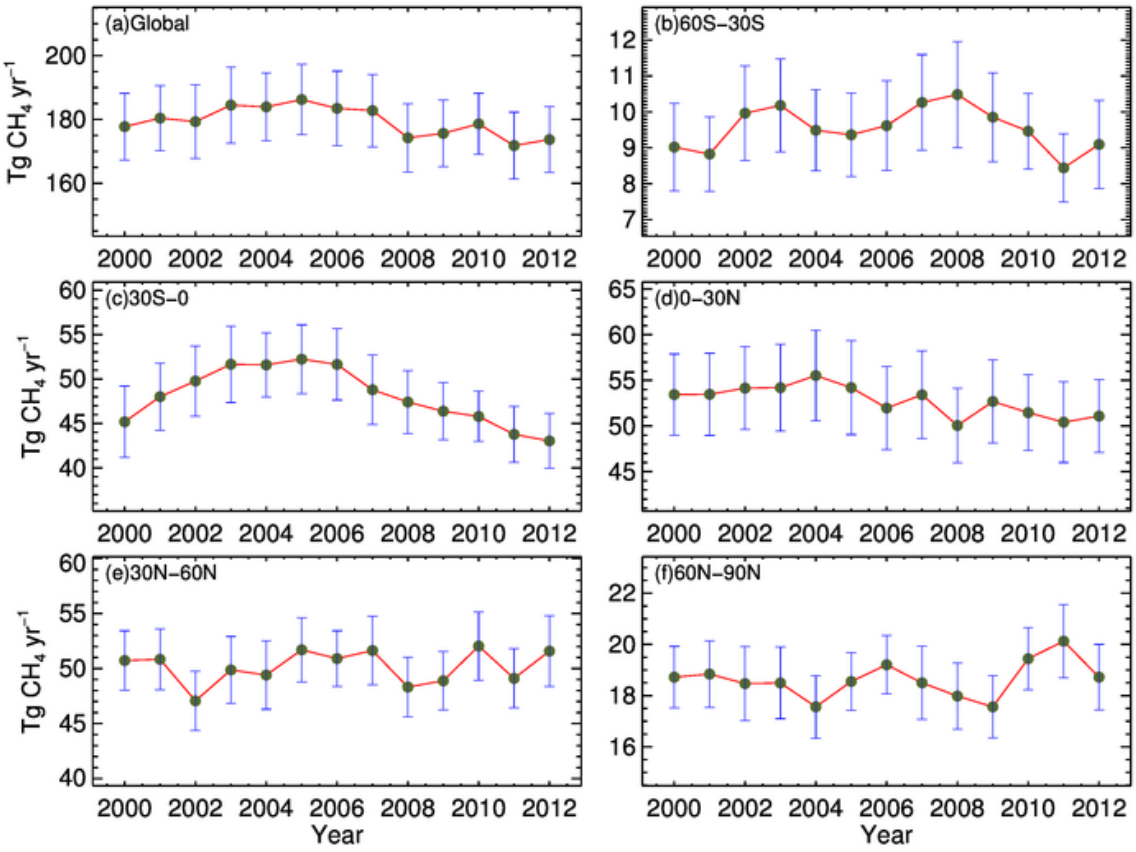

Figure 4.8. Uncertainties of the estimated annual wetland CH_4 emissions from the different region with 100 ANN models. Interannual variations of annual CH_4 emissions (black dots, fitted with red lines) and the 95% confidence intervals (blue error bars) from 2000 to 2012 are presented

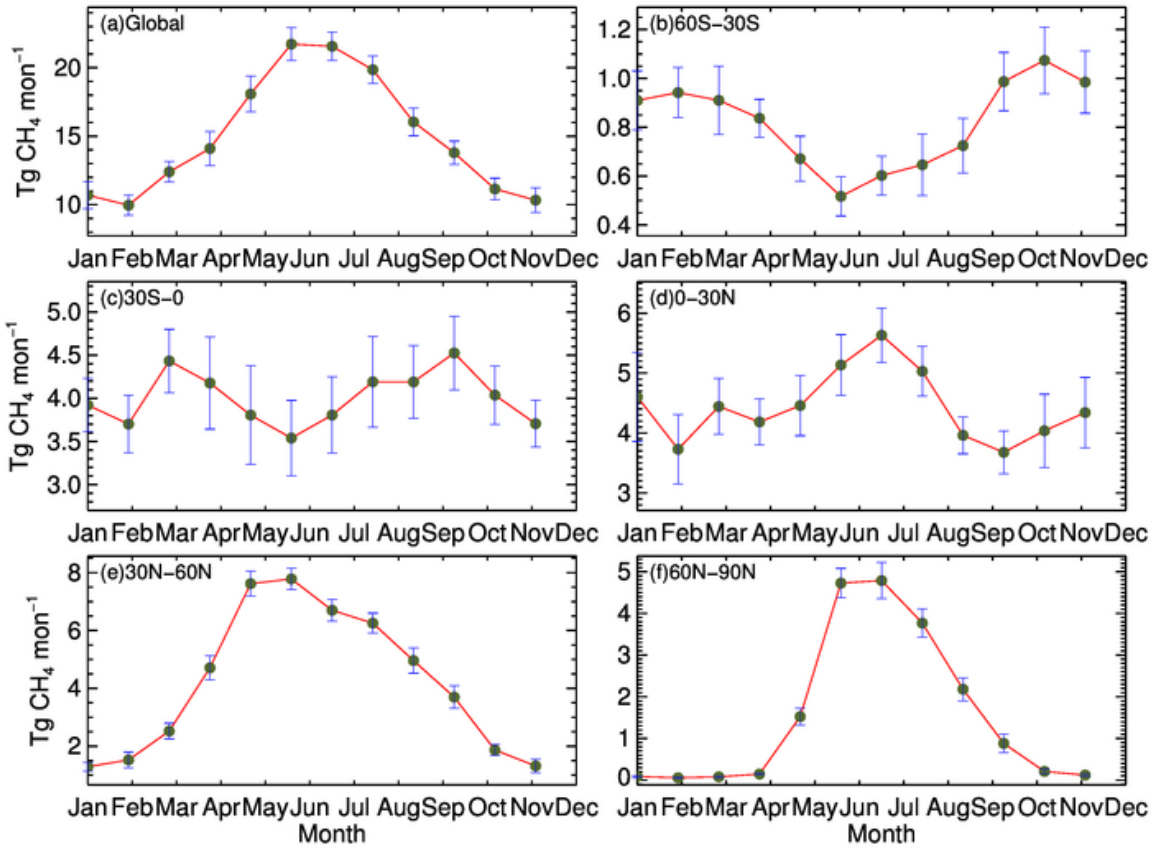

Figure 4.9. Uncertainties of the estimated wetland CH_4 emission seasonality from the different region with 100 ANN models. Seasonality of wetland CH_4 emissions (black dots, fitted with red lines) and the 95% confidence intervals (blue error bars) from 2000 to 2012 are presented

CHAPTER 5. LARGE METHANE EMISSIONS FROM PALM TREE STEMS IN AMAZONIAN BASIN

5.1 Abstract

Methane (CH_4) is the second powerful greenhouse gas behind atmospheric CO_2. Palm trees over peatlands in tropical regions have been found as a significant pathway to transport methane from soils to the atmosphere. This study used a two-dimensional diffusion model to quantify CH_4 emissions through this pathway. The model was optimized using field data of methane emissions from palm tree stems from 14 individual trees. Both model simulation and observation show 1000 times larger methane emissions (>150 mg C m^{-2} hr^{-1}) than that from other tree species. The model was then extrapolated to Pastaza-Marañón foreland basin (PMFB) in Peru by using a process-based biogeochemical model. We found that PMFB emits 1.1-3.0 Tg CH_4 yr^{-1} from Mauritia flexuos palm tree during 2000-2010, and methane fluxes have spatial patterns increasing from northwest to south east following surface atmosphere temperature patterns. To our knowledge, this is the first effort to quantify regional CH_4 emissions through this pathway. The estimates can be improved by considering the effects of changes in temperature, precipitation and radiation and using long-period continuous flux observations. Regional and global estimates of methane emissions through this pathway can be further constrained using more accurate palm swamp classification and spatial distribution data of palm trees at the global scale.

5.2 Introduction

Tropical wetlands play an important role in methane (CH_4) emissions, the second powerful greenhouse gas in the atmosphere (Kirschke, et al., 2013). Undisturbed tropical wetlands emit 85-184 Tg of methane each year, accounting for two thirds of the global emissions from wetlands (Sjögersten, et al., 2014). However, the estimates of fluxes from natural wetlands have at least 50%

uncertainty (Kirschke, et al., 2013). Plant stems are a particularly efficient means for releasing CH_4 from wetland soils because the pathway bypasses highly active populations of methanotrophic bacteria situated at the oxic-anoxic interface in the subsurface (Pangala, et al., 2013). Trees also have the capacity to cope with soil anoxia through development of morphological adaptations such as hypertrophied lenticels, adventitious roots and enlarged aerenchyma. These structures promote gas exchanges between the atmosphere and the rhizosphere (Kozlowski, et al., 1997; Megonigal, et al., 1992), in particular, entry of O2 to the root zone. (Pangala, et al., 2013) reported methane fluxes coming out from tree stems range from 17 to 185 µg CH_4 m^{-2} h^{-1}. A recent study also indicated 1000 times larger CH_4 emissions (150 mg C m^{-2} h^{-1} when height < 0.5 m) from stems of Mauritia flexuos, which is one of the dominated palm tree in palm swamp of Peru, than other tree species. Although tree stems are possible to play a significant role in CH_4 emissions from anoxic soils, most previous process-based models and ground-based flux chamber methods for estimating CH_4 emissions from forest wetlands have neglected this emission pathway (Pangala, et al., 2013).

There are three dominant wetland ecosystems in the tropics including forested peatlands, swamps and floodplains (Aselmann, et al., 1989). Palm swamp forests cover large regions of the Amazon Basin, estimated to be over 50,000 km2 (Eva, et al., 2002). The combination of permanently saturated soils, year-around warm temperature, and low oxygen in palm swamp soils can lead to a large amount of carbon release to the atmosphere, particularly as CH_4 (Erika, et al., 2011). Current models have not been able to predict the high concentrations of measured atmospheric CH_4 over some areas of tropical rainforests in the equatorial regions of South America and Africa (Bergamaschi, et al., 2007; Frankenberg, et al., 2005). Precise information on the extent and characteristics of palm swamps is difficult to gather because of their remoteness and difficult accessibility. Remote sensing is a unique tool to studying and monitoring these ecosystems

especially through the use of radar to acquire mages regardless of day/night conditions or the presence of clouds, which are especially prevalent in tropical regions. Remote sensing efforts on peatlands in the Peruvian Amazon include the work by (Lähteenoja, et al., 2011), who mapped the distribution of peatland forests, wetlands and other land covers in the Pastaza-Marañon basin through an unspecified supervised classification of Landsat images based on field observations. However, no classification accuracy assessment was performed. More recently, (Draper, et al., 2014) used data from the satellite sensors Landsat, ALOS-PALSAR and SRTM along with ground referencing points of known classes to map the spatial distribution of peatlands also in the Pastaza-Marañon foreland. Classification was performed using a supervised, support vector machine method. Land cover classes considered were pole forests, palm swamp and open peatlands as well as four non-peat-forming categories including terra firme forests or occasionally flooded forests, seasonally flooded forests, open water and urban areas. The overall classification accuracy was 95%. (Hergoualc, et al., 2016) combined field and remote sensing data from the satellites Landsat TM and ALOS/PALSAR to discriminate areas typifying dense palm swamp with low, medium and high degradation and terra firme, restinga and mixed palm swamp (not Mauritia flexuos dominated) forests, using a Random Forest machine learning classification algorithm. In addition, the Mauritia flexuos density was measured widely in Amazon Basin palm swamps (Hergoualc, et al., 2016). All efforts above give us possibility to estimate CH_4 emission from palm tree stem at the large scale, for example, for.the Pastaza-Marañón foreland basin (PMFB) in Peru.

Here we developed a two-dimensional (2D) diffusion model by considering horizontal and vertical transport of gases inside tree stem to quantify CH_4 fluxes from palm tree stem in Amazon Basin. The model was optimized using field observed methane fluxes from Mauritia flexuos tree stems, in the peatlands of Peru (unpublished data). We then extrapolated single tree fluxes estimate

to regions of PMFB by using a process-based biogeochemical model, the Terrestrial Ecosystem Model (TEM, Zhuang, et al., 2004; Tang, et al., 2010).

5.3 Method

5.3.1 Overview

We first develop a Palm Tree Methane fluxes Model using a 2D diffusion method (PTMM-2D) by quantifying the methane transport from soils to stem, and from stem to the atmosphere. We then conduct sensitivity test for all variables to identify the most significant variables. Third the model is then optimized using the Sequential Monte Carlo (SMC) method over Python (PySMC) (Bilionis, et al., 2015). Finally, a process-based biogeochemical model TEM is extrapolated to PMFB region to estimate regional palm tree stem emissions.

5.3.2 2D Diffusion Model

PTMM-2D considers vertical and horizontal diffusions between soils and stem and between stem and the atmosphere (Figure S1). We set 5 meters height as the top boundary for the tree since observations show very little emissions from tree stem above 5 meter (Figure S2). The tree stem is divided into small pixels with 2 cm width and 10 cm height, considering field observed diameter at breast height (DBH) ranging from 27 to 42 cm (field data unpublished). Methane can transport inside the tree stem horizontally (x direction) and vertically (y direction). The governing equation of these processes is:

$$\frac{\partial c(x,y,t)}{\partial t} = D\_x \frac{\partial^2 c(x,y,t)}{\partial x^2} + D\_y \frac{\partial^2 c(x,y,t)}{\partial y^2} \qquad (5.1)$$

Where, $c(x,y,t)$ is the methane concentration in each pixel, units are mg m^{-3}; D_x is the diffusivity at horizontal direction, D_y is the diffusivity at vertical direction, units are m^2 s^{-1}. Top and side boundaries are air methane concentrations, and we use average observed value of 2 ppm.

Bottom boundary is soil methane concentrations of 200-400 ppm (field data unpublished). With forward in time, central in space method (FTCS), we have:

$$c(x,y,t) = \alpha\big(c(x+1,y,t-1) + c(x-1,y,t-1)\big) + \beta\big(c(x,y+1,t-1) + c(x,y-1,t-1)\big) + (1-2\alpha-2\beta)c(x,y,t-1) \quad (5.2)$$

Where $\alpha = D\_x\Delta t/\Delta x^2$ and $\beta = D\_y\Delta t/\Delta y^2$; t is the time step. To get stable solution, we need to make sure that $\Delta t \le \Delta x^2\Delta y^2/2(D\_x\Delta x^2 + D\_y\Delta y^2)$, which leads to $\Delta t \le 5\,min$. All adjustable parameters are showed in table B.1.

5.3.3 Model Parameterization and Extrapolation

We first conduct 14 sensitivity tests to identify the most dominant parameters (Table B.1). Other parameters would be fixed during calibration and evaluation. Second, with a trial-and-error method, we run several forward simulations compared with observations to find priors of those dominant parameters, which are D_x and D_y (Table B.2; Figure B.2). Here we keep the soil methane concentration C_soil as constant of 200 ppmv. Finally, with initial ranges for these three parameters: C_soil (200-400ppmv), D_x (0.000001-0.00005 $m^2\ s^{-1}$), D_y (0.0001-0.004 $m^2\ s^{-1}$), we uniformly chose them for optimization using a PySMC method. We use PySMC to find 100 sets of optimized parameters, and for each set we run 5 times MCMC to get the posteriors (Figure 5.1) (Bilinois, et al., 2015).

After parameterization, we extrapolate the model to PMFB region using TEM model (Zhuang, et al., 2004; Tang, et al., 2010). To do this, we first calibrated the model soil methane concentration simulation using two temperate peat land sites Buck Hollow Bog and Big Cassandra Bog (Shannon and White, et al., 1994), and three boreal sites Bog Lake Fen, S1 Bog, Zim Bog (Figure B.3, B.4, unpublished ms) with the trial-and-error method. Then we incorporated PTMM-

2D with TEM model in PMFB for period 2000-2010 driven with reanalysis monthly climatic data from Climatic Research Unit (CRU, Harris et al., 2014). Vegetation type data was taken from Draper et al. (Draper, et al., 2014; Figure 5.2). We mainly used two types in this region, which are palm swamp and pole forest. All data was re-gridded to 1.69km x 1.69km. We used a uniform Mauritia flexuos palm tree density range which is 12-128 ha^{-1} for pole forest and 160-360 ha^{-1} for palm swamp (Draper, et al., 2014). Besides, we also estimate whole South America methane emissions from palm swamp by assuming soil methane concentrations are 200-400ppm, observed Mauritia flexuos palm tree density is 46-402 ha^{-1} (Hergoualc, et al., 2016) and the estimated total palm swamp area of South America is 5.39 million ha (Eva, et al., 2002).

5.3.4 Data Organization

Observed palm tree stem fluxes in Peru during August 2014 and August 2015 (field data unpublished) was used to parameterize PTMM-2D fluxes estimate. For regional study in PMFB, the climate data for the period 2000-2010 including surface atmosphere temperature, precipitation, cloud fraction and surface vapor pressure at monthly time step are from CRU database (Harris, et al., 2014) with resolution 0.5 degree x 0.5 degree. The CRU data together with the modern digital elevation (DEM) data at 1.69 km × 1.69 km were interpolated to a 1.69 km×1.69 km resolution using the interpolation software ANUPLIN4.4 (http://fennerschool.anu.edu.au/research/products/anusplin-vrsn-44) (Price, et al., 2000; Huutchinson, et al., 2009; McKenney, et al., 2011).

5.4 Results

5.4.1 Methane emissions from single palm tree stem

Two-Dimensional Palm Tree Methane fluxes Model (PTMM-2D) estimated vertical diffusivity of methane (D_y) ranges from 0.0005 to 0.003 m^2 s^{-1} and horizontal diffusivity (D_x) ranges from 0.000001 to 0.000042 m^2 s^{-1} (Table B.2). Forward model simulations capture the magnitude of methane fluxes along the tree stem at different heights (Figure B.2, 5.1), with uncertainty ranging from 1.0 to 20.94 mg CH_4 m^{-2} hr^{-1}. Calibration showed that, if no extra data (e.g., methane concentration in soils) was used to constrain the model, two sets of parameters did equally well in comparison to observations (Figure 5.1), with large fluxes (>150 mg C m^{-2} hr^{-1}) at tree height lower than 0.5 m (Figure 5.1). Model estimated methane emissions are 131-264 mg C hr-1 per tree, using D_y = 0.0028 m^2 s^{-1}, D_x = 0.0000079 m^2 s^{-1}, constant soil methane concentration (C_soil) of 200-400ppm and constant atmospheric methane concentrations (C_air) of 2 ppm. Optimized D_y (~10^{-3} m^2 s^{-1}) is always much larger than D_x (~10^{-5} m^2 s^{-1}) (Table B.2), suggesting that vertical gas transport is much faster than horizontal transport. This may be because of high plant water transpiration in tropical region under high temperature conditions and palm tree phytology structure.

5.4.2 Palm tree stem methane emissions from large regions

We estimated the methane emission from palm tree using a process-based biogeochemical model TEM (Zhuang, et al., 2004; Tang, et al., 2010). The TEM model has been parameterized using observation data from two temperate peatland sites and three boreal peatland sites (Shannon and White, 1994; SPRUCE unpublished manuscript, http://dx.doi.org/10.3334/CDIAC/spruce.043). For temperate sites, TEM model can capture the vertical trends and magnitude of observations (Figure B.3). For boreal sites, TEM model can

mostly capture the vertical trends and magnitudes, but underestimate in April 2014, which observation showed an extremely high soil methane concentration up to 3.3 mM. We then coupled PTMM-2D and TEM to estimate the methane emission from palm tree during 2000-2010 in PMFB (Figure 5.2, 5.3). The spatial distributions of methane fluxes from palm tree have a pattern increasing from northwest to south east of PMFB (Figure 5.3), similar to atmosphere temperature (Figure B.5). Estimated methane emissions are 0.007-0.2 Tg CH_4 yr^{-1} and 1.1-2.8 Tg CH_4 yr^{-1} for pole forest areas and palm swamp areas, respectively (Table 5.1; Figure 5.4). Time series of methane emission from PMFB have patterns high in summer and low in winter (Figure 5.4). Total emission from PMFB is 1.1-3.0 Tg CH_4 yr^{-1}. We also estimated the palm tree methane emission from all South America, which was previously estimated to have about 5.39 Million ha palm swamp area (Eva, 2002). If palm swamp has similar species and soil methane concentration to our calibration sites, the total methane emissions from palm swamp of South America will be 0.3-5.8 Tg CH_4 yr^{-1} (Table 5.1).

5.5 Discussion

5.5.1 Comparison with previous methane emission estimates

Both model estimates and observations showed there are much larger methane emissions from palm tree stem (>150 mg C m^{-2} hr^{-1} at height < 0.5m) compared to previous observations (up to 200 μg CH_4 m^{-2} hr^{-1}) (Pangala, et al., 2013). This indicates that Mauritia flexuos palm tree shall have special structure to facilitate the methane emissions from stem. The Amazon Basin emits 22-52 Tg CH_4 yr^{-1} (Ringeval, et al., 2014), while our model estimated 0.3-5.8 Tg CH_4 yr^{-1} from the South America palm swamp, and 1.1- 3.0 Tg CH_4 yr^{-1} from PMFB palm trees, accounting for up to 26% of the Amazon Basin emissions. Methane emissions from palm trees can be an important source to the atmospheric methane budget, even compared to the emissions from undisturbed

tropical wetlands of 85-184 Tg CH_4 yr^{-1} (Sjögersten, et al., 2014) and global total of 503-610 Tg CH_4 yr^{-1} (Aronson, et al., 2013).

5.5.2 Uncertainties and limitations

PTMM-2D simulations capture the trend and magnitude of methane fluxes along the tree stem (Figure 5.1), with an uncertainty ranging from 1.0 to 20.94 mg CH_4 m^{-2} hr^{-1}. In this study, the temperature effects were only considered on soil methane concentration since the observation period is short (only in August), and temperature variation is small (26.6-31.3 ℃). Hydrological dynamics and radiation effects on PTMM-2D were not considered either. When cooperated with TEM model in regional study, estimate uncertainty of methane emission is primarily due to following reasons: 1) soil methane concentration is only calibrated over temperate and boreal sites, and to our knowledge no tropical soil methane concentration data is available. However we conducted our simulation in tropical areas; 2) we used same root depth, soil texture, and other soil properties for whole PMFB palm swamp and pole forest areas since distributions of them are not available; 3) we used climate data of high resolution (1.6km x 1.6km) which are interpolated from coarse resolution (0.5 degree x 0.5 degree); 4) for palm tree density, we used the same density ranges for all regions because lacking of detailed distribution and density data. Thus, this study calls for experiments or observations of temperature, hydrology, radiation, tree species and tree sizes impacts on methane fluxes from palm tree stem over peatland; and also calls for observing more detailed palm tree distribution, palm tree density distribution, soil properties distribution and high resolution climate data to further constrain the regional simulation over the whole Amazon basin area.

5.6 Conclusions

Our model estimates show that methane emissions from palm tree stem are ~1000 times larger than other tree species in Amazon basin, up to 150 mg C m^{-2} hr^{-1}. A single tree can emit 131-264 mg CH_4 hr^{-1} and PMFB palm trees can emit 1.1-3.0 Tg CH_4 yr^{-1} during 2000-2010. To constrain these estimates, the effects of temperature, hydrology, radiation and tree size on tree fluxes shall be considered. In addition, more continuous field observations of stem fluxes and soil methane concentrations will be needed for tropical region. More accurate data of palm tree distribution and palm tree density distribution for the Amazon Basin and other tropical regions is also needed to further constrain our estimates

Table 5.1. Estimated palm swamp area, methane emissions per tree, trees per unit area and total emissions from the study regions. For South America palm swamp, we assume soil methane concentrations are from 200ppm to 400ppm. For Pastaza-Marañon foreland basin in Peru (PMFB), we used soil methane concentration product from TEM model. PMFB methane emissions are estimated using palm swamp classification from remote sensing data of Draper (2014).

Study Region	Area (Million ha)	Emission per tree (mg C hr^{-1})	Trees per area (ha^{-1})	Total emission (Tg CH_4 yr^{-1})	Reference
South America palm swamp	5.39	131-264	46-402	0.3-5.8	This study, Eva, 2002
PMFB: Pole Forest	0.37	250-276	12-128	0.007-0.2	This study, Draper, 2014
PMFB: Palm Swamp	2.77	250-276	160-360	1.1-2.8	This study, Draper, 2014
PMFB: Total Area	3.14	250-276	——	1.1-3.0	This study, Draper, 2014
Amazon Basin	——	——	——	22-52	Ringeval, 2014
Undisturbed tropical wetlands	——	——	——	85-184	Sjögersten, 2014
Total global methane emission	——	——	——	503-610	Aronson, 2013

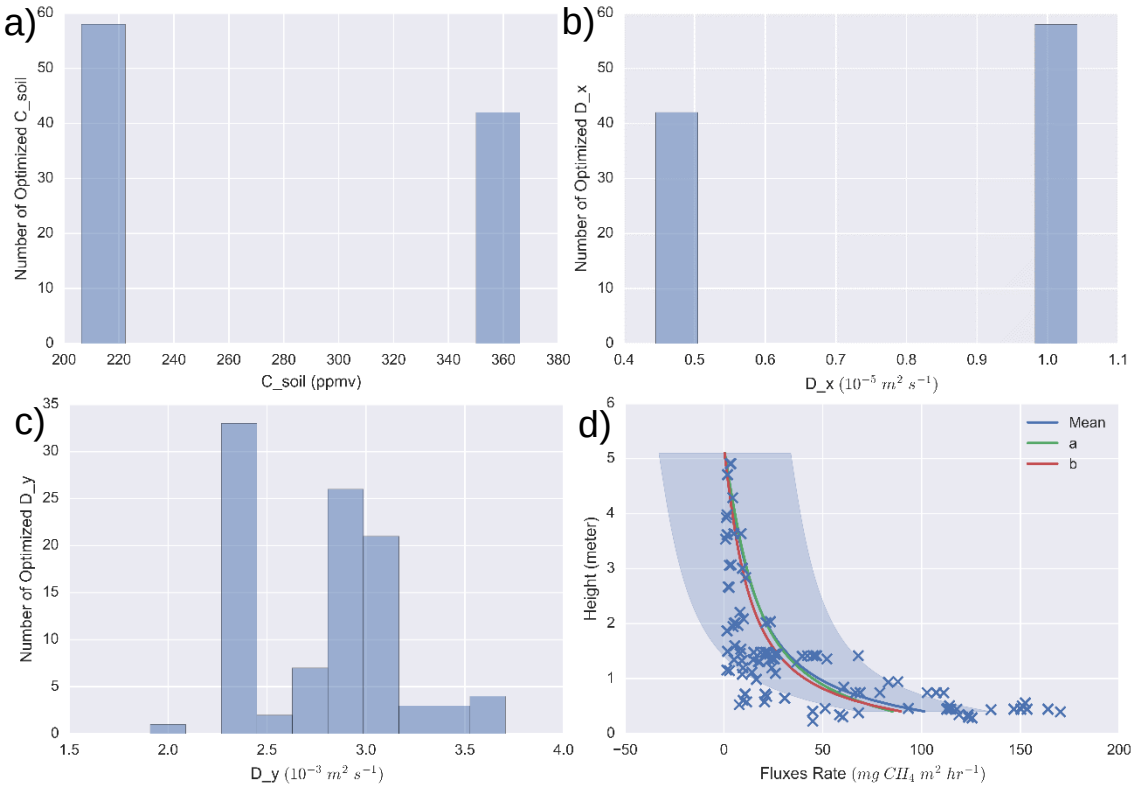

Figure 5.1. Parameter posteriors of (a)soil methane concentration C_soil, (b) diffusivity coefficients in x direction (D_x), and (c) diffusivity coefficients in y direction (D_y), using the PySMC method (Bilionis, 2015). Y-axis represents number of optimized C_soil, D_x or D_y located in a specific range of parameter values, which showed in X-axis; (d) is comparison between simulations (solid lines) and observations (blue "x"), and blue area is the standard deviation of the simulations. There are two modes of parameter posteriors: a and b mode showed in figure d. Each mode represents the average value of a group of parameter posteriors, and detailed values showed in Table S3.

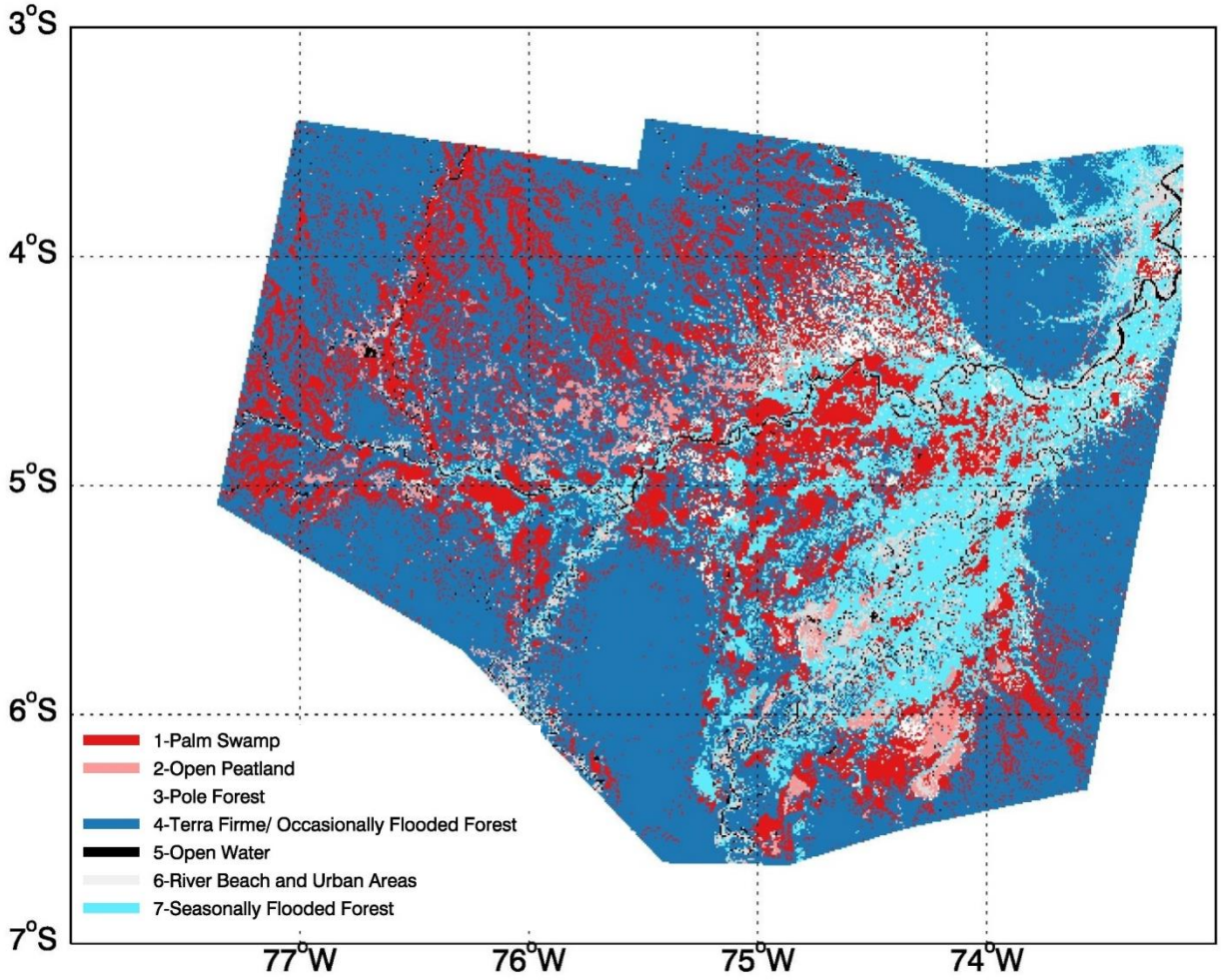

Figure 5.2. Ecosystem classification in PMFB in Peru. It is similar to the figure 5.4 in Draper (2015). Red areas represent distributions of palm swamp at a resolution of 90mx90m.

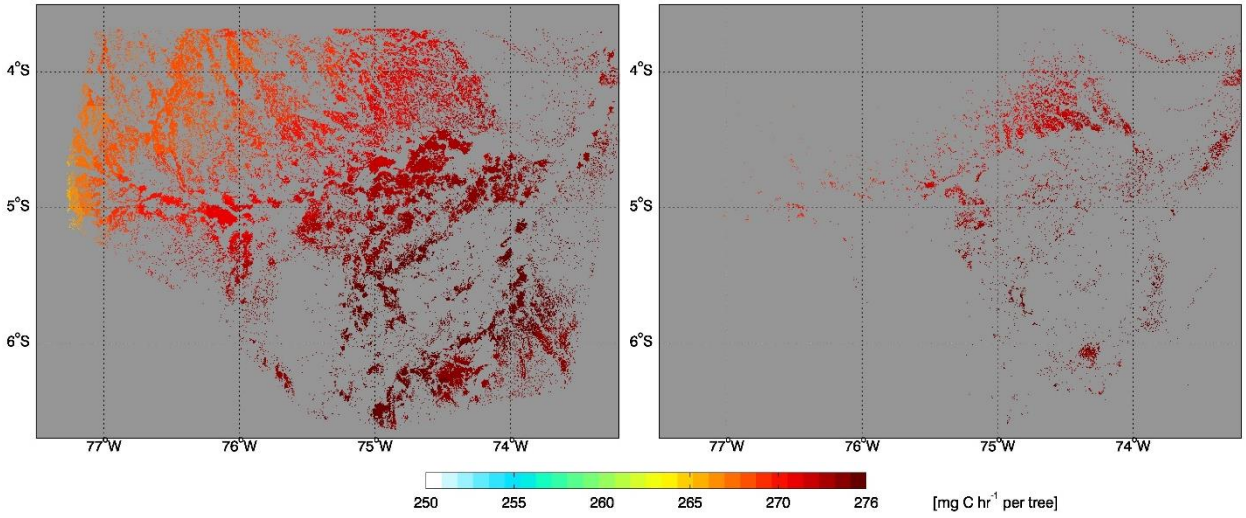

Figure 5.3. Mean methane flux distribution from palm tree stems in PMFB during 2000-2010: (a) the methane emission from palm swamp area and (b) the methane emission distribution from pole forest area.

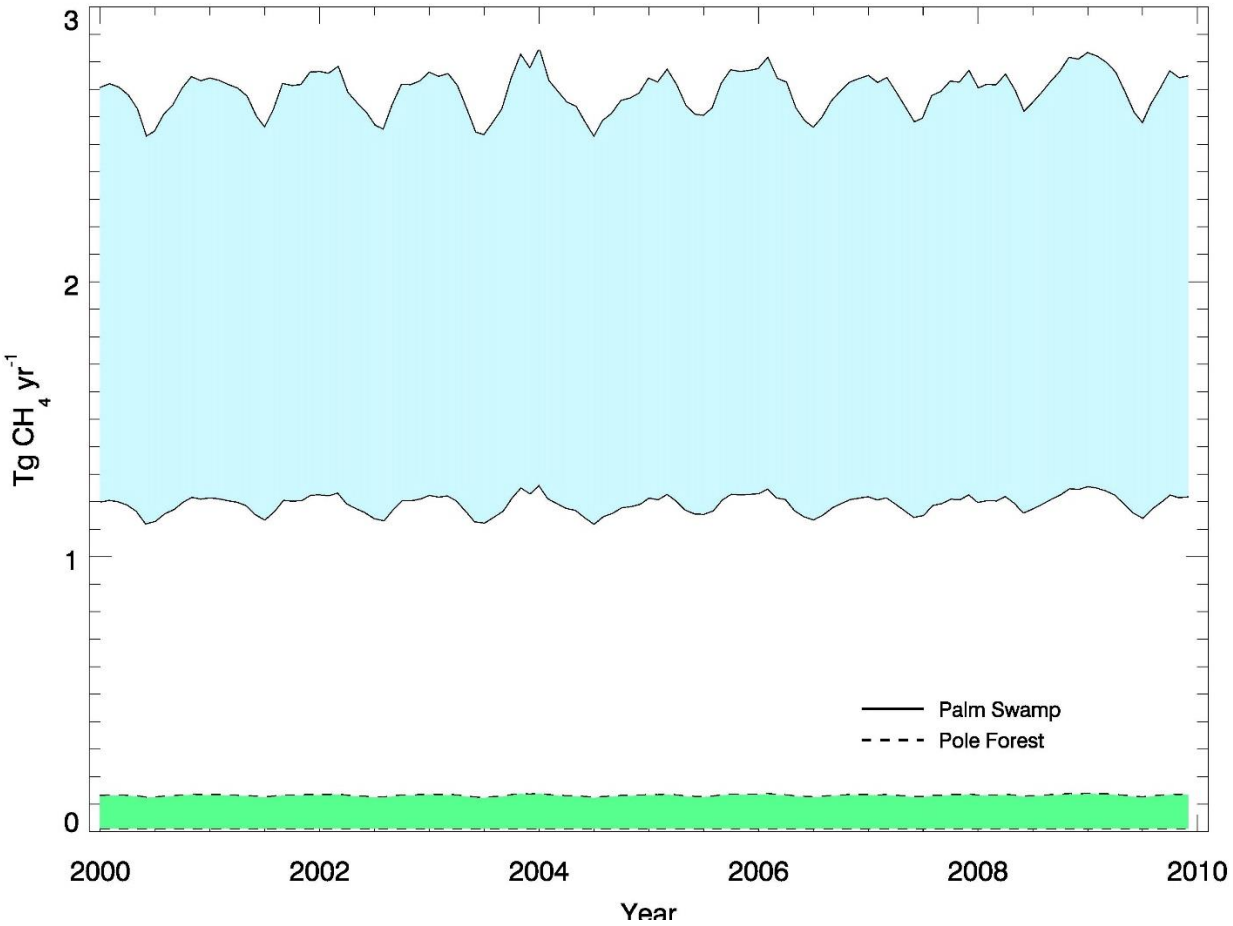

Figure 5.4. Monthly methane emissions from palm tree stems in PMFB from 2000 to 2010. Solid lines and blue shadow represent the temporal variations and ranges of methane emission from palm swamp in PMFB, respectively. Dash lines and green shadow represent the temporal variations and ranges of methane emissions from pole forest in PMFB, respectively.

CHAPTER 6. SUMMARY AND FUTURE WORK

6.1 Conclusions

In Chapter 2, I analyzed the magnitude, spatial pattern, and the controlling factors of the atmosphere-soil CO exchanges at the global scale for the 20th and 21st centuries using a process-based biogeochemistry model. Air temperature and soil temperature play a dominant role in determining the annual soil CO consumption and production while precipitation, air temperature, and soil temperature are the major controls for the monthly consumption and production. The atmospheric CO concentrations are important for annual CO consumption. This study calls for long-period observations of CO flux for various ecosystem types and better projection of atmospheric CO surface concentrations from 1901 to 2100 to improve estimates of global soil CO consumption. The effects of land-use change, agriculture activities, nitrogen deposition, photo-degradation and biological formation shall also be considered to improve quantification of soil CO fluxes.

Chapter 3 described the study quantifying the uncertainty sources and magnitudes of global land methane emissions and consumption using a process-based biogeochemical model. Results indicate that parameters, wetland type distribution and wetland area distribution are three major uncertainty sources for methane emissions. Climate forcing uncertainties also provide non-negligible uncertainties. Global methane emissions and consumption increase during El Niño events and decrease during La Niña events. Our estimates can be improved by using more in situ data in parameterization and more accurate dynamical wetlands and inundation distribution data to drive our model. This study provided an improved process-based methane biogeochemistry model to the research community and helped identify important uncertainty sources and controlling factors for quantifying global wetland methane emissions.

Chapter 4 used an artificial neural network approach and CH_4 flux measurements in wetland ecosystems and associated environmental data to inventory global wetland CH_4 emissions. The global wetland CH_4 emissions are most sensitive to variations in solar radiation and temperature. The large spatial variability in CH_4 emissions is due to variations in hydrology, climate, and soil conditions. This study calls for better characterizing variations of wetland areas and water table position and more long-term observations of CH_4 fluxes in tropical regions so as to improve future inventorying wetland CH_4 emissions at the global scale.

In Chapter 5, I developed and used a two-dimensional diffusion model to estimate the CH_4 emissions from palm tree stem in the Amazon basin. Both the model and observation indicate a huge amount of CH_4 can emit from the palm tree comparing to soil emissions. To constrain these estimates, the effects of temperature, hydrology, radiation and tree size on tree fluxes shall be considered in the future. In addition, more continuous field observations of stem fluxes and soil methane concentrations will be needed for tropical regions. More accurate data of palm tree distribution and palm tree density distribution for the Amazon Basin and other tropical regions is also needed to further constrain our estimates.

6.2 Limitations and Future Work

Firstly, as I mentioned in Chapters 2.5 and 3.5, the hydrology conditions significantly influence the simulation results of CH_4 and CO exchanges between land and the atmosphere. The hydrology conditions in our simulations come from two sources: the hydrology model of TEM simulated soil moisture and water table depth (influence CH_4 and CO production and consumption), and wetland distribution data from other models (e.g. SWAMPS-GLWD, influencing CH_4 emissions). In order to reduce the uncertainty from hydrology modelling, future studies can start from replacing the original hydrology component by the variable infiltration capacity (VIC) model,

for instance (Cherkauer & Lettenmaier, 1999; Cherkauer et al., 2003; Liang et al., 1994), a large-scale hydrological model and then use TOPMODEL-based formulation to represent subgrid variability in the soil moisture distribution (Beven & Kirkby, 1979). The VIC-TOPMODEL approach can help to determine not only the soil moisture but the inundation extent by soil moisture estimated from VIC simulation and local topographic information using a topographic wetness index in the TOPMODEL-based formulation (Lu and Zhuang, 2012; Lu et al., 2018). With this approach, we can further constrain the uncertainty of CH_4 and CO soil dynamics using process-based models. Besides, as mentioned in Chapters 2.2 and 3.2, there have been large disagreements among model simulations from recent model inter-comparison projects, which can be partially attributed to uncertain model algorithms (Kirschke et al., 2013; Melton et al., 2013; Saunois et al., 2016; Saunois et al., 2019). For each process in CH_4 dynamics, there usually exist several different methods to construct the algorithms. Therefore, a comprehensive evaluation of the mechanisms of different model algorithms is needed, in order to quantitatively examine the effects of different complexities of methane algorithms on estimating CH_4 emissions, consumptions and transport at the global scale.

Secondly, the ANN approach has been used to estimate global CH_4 wetland emissions in Chapter 4. However, we can find that the evaluation results are not ideal. More data, especially from tropical and temperate regions, can be collected from recent founded methane flux observation networks FLUXNET to train and evaluate the ANN model. A stratified sampling approach can be used instead of simple random sampling to ensure that the full range of CH_4 emissions in the measurement dataset is included in the training data. The ANN model structure can also be used to estimate CH_4 consumption into upland and CO soil consumption and production.

Thirdly, as mentioned in Chapter 5, the 2D diffusion model is still waiting for more tree stem flux data to further constrain the simulation results. As mentioned in Pangala et al. (2017), efforts have been made to observe CH_4 emitting from the tree stem and over 10 thousand data points can be obtained. Besides, detailed tree species distribution map and tree density map are needed for large scale simulations. Efforts will be made primarily on collecting and compiling data. Now only diffusion process has been considered. Future work can consider more processes including production inside the trees, consumption by the tree canopy, environmental influences on these process and feedbacks to soil CH_4 consumption and production.

Finally, I will feed the revised CO and CH_4 fluxes to a global three-dimensional chemistry transport model of atmospheric composition, GEOS-Chem (http://acmg.seas.harvard.edu/geos/), in order to examine the effects of the surface CO and CH_4 fluxes on atmospheric CH_4 trends in recent decades. This project will also extensively use trace-gas data from MOPITT (https://eosweb.larc.nasa.gov/project/mopitt/mopitt_table), GOME (https://earth.esa.int/web/guest/missions/esa-operational-eo-missions/ers/instruments/gome), and TES (https://eosweb.larc.nasa.gov/project/tes/tes_table) satellite missions, the NASA-AGAGE (http://agage.mit.edu/data/agage-data), NOAA-CMDL (ftp://aftp.cmdl.noaa.gov/-data/trace_gases/) in-situ trace-gas networks, Ameriflux (http://ameriflux.lbl.gov/) in-situ trace-gas networks, LBA (https://daac.ornl.gov/cgi-bin/dataset_lister.pl?p=11) in-situ gas networks, and aircraft and ship instruments. In addition, the adjoint biogeochemistry model TEM and inversion and transport model GEOS-Chem will also be used (Henze, D.K., 2007; Zhu and Zhuang, 2014; Tan et al., 2016).

APPENDIX A. SUPPORTING INFORMATION FOR CHAPTER 3

Text A.1. Model revision

Previous TEM-MDM details can be found in Zhuang et al. (2004). In the model, the methane production rate per day was used to represent the soil methane substrate concentration for most of the calculations and has not considered the effects of accumulated methane in soil columns on methane fluxes (Zhuang et al., 2004). In this revision, a new variable was added to the model to save the soil methane concentration at every time step for each 1cm soil layer. The effect on soil methane oxidation and transport are incorporated in the model:

1) The changes in CH_4 concentrations are governed by the following equation within each layer:

$$\frac{\partial C_M(z,t)}{\partial t} = M_P(z,t) - M_O(z,t) - \frac{\partial F_D(z,t)}{\partial z} - R_P(z,t) - R_E(z,t) \quad \text{… Equation A.1.}$$

The $C_M(z,t)$ now is the accumulated methane concentration at z depth of soil at time t. $\frac{\partial C_M(z,t)}{\partial t}$ is governed by Equation A.1, where $M_P(z,t)$, $M_O(z,t)$, $R_P(z,t)$ and $R_E(z,t)$ are methane production, oxidation, plant-mediated transport, and ebullition rates, respectively, and $\frac{\partial F_D(z,t)}{\partial z}$ represents flux divergence due to diffusion.

2) For oxidation calculation:

$$M_O(z,t) = O_{MAX}\boldsymbol{f}\left(\boldsymbol{C_M}(\boldsymbol{z},\boldsymbol{t})\right)f\left(T_{SOIL}(z,t)\right)f\left(E_{SM}(z,t)\right)F\left(R_{OX}(z,t)\right)f\left(N_{dp}(z,t)\right)f\left(D_{ms}(z,t)\right) \quad \text{…}$$

Equation A.2.

We used the Michaelis-Menten kinetics (Bender and Conrad, 1992) to simulate the effect:

$$f\left(C_M(z,t)\right) = \frac{C_M(z,t)}{K_{OCH_4} + C_M(z,t)} \quad \text{…Equation A.3.}$$

This equation is similar to B1 presented in Zhuang et al. (2004). The K_{OCH_4} is the methane ecosystem-specific half saturation constant, and units are μM (Table 3.1). $f\left(C_M(z,t)\right)$ is used as a multiplier for methane oxidation rate.

3) The plant-aided transport basic function is C4 in Zhuang et al. (2004):

$$R_P(z,t) = K_P \cdot TR_{VEG} \cdot f_{ROOT}(z) \cdot f_{GROW}(Tsoil(z,t)) \cdot C_M(z,t)$$

The $C_M(z,t)$ is directly used as a multiplier for plant-aided transport rate calculation. The ebullition transport is simulated in the model using equation C8a in Zhuang et al. (2004):

$$R_E(z,t) = K_e\, f\left(C_M(z,t)\right)$$

The ebullition happens when the $C_M(z,t)$ is over a threshold of 500 μM (Walter and Heimann, 2000). The $f\left(C_M(z,t)\right)$ is equal to the difference between $C_M(z,t)$ and the threshold.

In addition, instead of the previous daily time step, we used hourly timestep for methane dynamics simulation and 5 min time step for hydrology module simulation to reduce the error while solving partial differential equations (PDEs), following the suggestions from Land Surface Model (LSM version 1.0, Bonan, 1996).

Previous model is only developed for boreal regions (Zhuang et al., 2004). In order to extrapolate it to the global scale, we used the climate type and the classification method from Matthews and Fung (1987) to identify the wetland types for each site and pixel. Climate types were determined by site description (site level simulation) or its latitude (regional simulation, tropical <30°, 30°< temperate <60°, and boreal >60°). Wetland types were determined by the site description (site level simulation) or the classification method from Matthews and Fung (1987), using vegetation cover information and wetland inundation fraction information (regional simulation). With the 3 types of climate and 5 types of wetland, we totally have 15 types of

wetlands for model simulations. Each of them was calibrated using a representative site (Table 3.2, 3.3).

Text A.2. Model performance

Calibrations and evaluations were conducted for the revised model. The calibrated earlier version of TEM-MDM model (only for boreal regions, Zhuang, et al., 2004) was used for daily evaluation at boreal sites. Figure A.1 presents two sample sites of daily calibration comparisons. Figure A.2 presents 8 sites of evaluation results from the revised TEM-MDM and TEM-MDM. Firstly, the scatter plots of the calibration sites and evaluation sites in figure 1 show R^2 of 0.44 and 0.41, respectively. Most of the anomaly points in plots can be found as temperate site points (triangles). The reason is that during summer, some temperate sites can have large methane emissions (Figure A.1) due to the suitable soil hydrology and high temperature at few points, which are hardly captured by the model since it tries to fit the majority of the data points. Secondly, the scatter plots also show some points that observations show positive values, but simulations are near zero. The reason is that our model shuts down the methane production if the soil temperature is lower than 0 °C, but even during winter, some sites can still produce methane in field observations (Figure A.1 and A.2). The thermal model may also lead to a lower temperature than field data (Liu et al., 2018). The forcing data used in site level simulations can also induce errors, because some sites do not have sufficient observed forcing data, which are often based on Climatic Research Unit (CRU TS4.01, Harris et al., 2014) or ERA Interim data from European Centre for Medium-Range Weather Forecasts (ECMWF; Dee et al., 2011). Thirdly, the revised model performs poorly at monthly site 16 and annually site 24, due to coarse simulation time steps and using reanalysis forcing data or average forcing data instead of site meteorological data. The daily site 17 and site 22 evaluation results indicate that they have missed emission peaks (Figure A.2 a

and f). The reason is that the climate data from the nearest Global Summary of the Day (GSOD) station were used for these two sites but they may not represent the real environment conditions. Fourthly, the simulations using the earlier TEM-MDM on the daily sites were presented as blue lines in Figure A.2. This version often overestimates the methane emission from wetland during summer for boreal sites (Figure A.2a-g). The reasons are several folds. First, the earlier version does not consider the accumulated substrate methane concentration effects. The oxidation in the unsaturated zone will be underestimated using equation A.3. Second, the coarse time step for hydrology model causes too much water coming into soils, overestimating water table depth. In addition, the coarse time step for methane dynamics also may cause a large methane gradient between topsoil layer and the atmosphere, leading to overestimation of the diffusion rate moving from soils to the atmosphere. For temperate site 26, the earlier version underestimated the fluxes due to not including proper climate and wetland type.

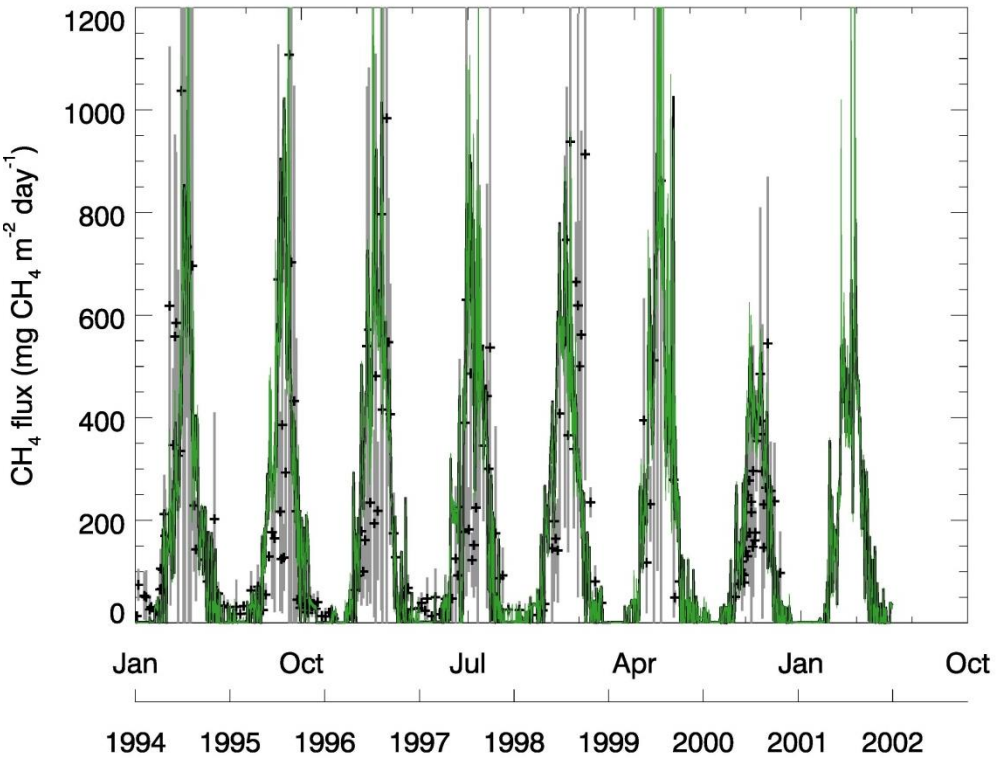

b) Site 7

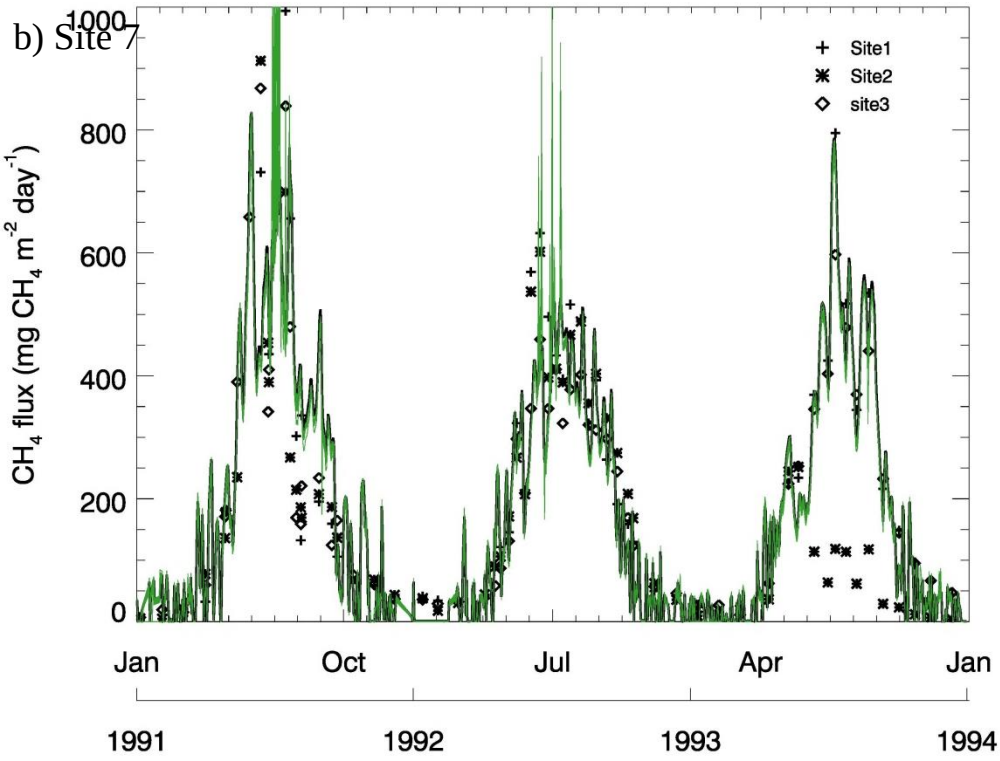

Figure A.1. Daily calibration results at two sites: a) site 6 and b) site 7. Symbols represent observed data while green lines represent the calibration results.

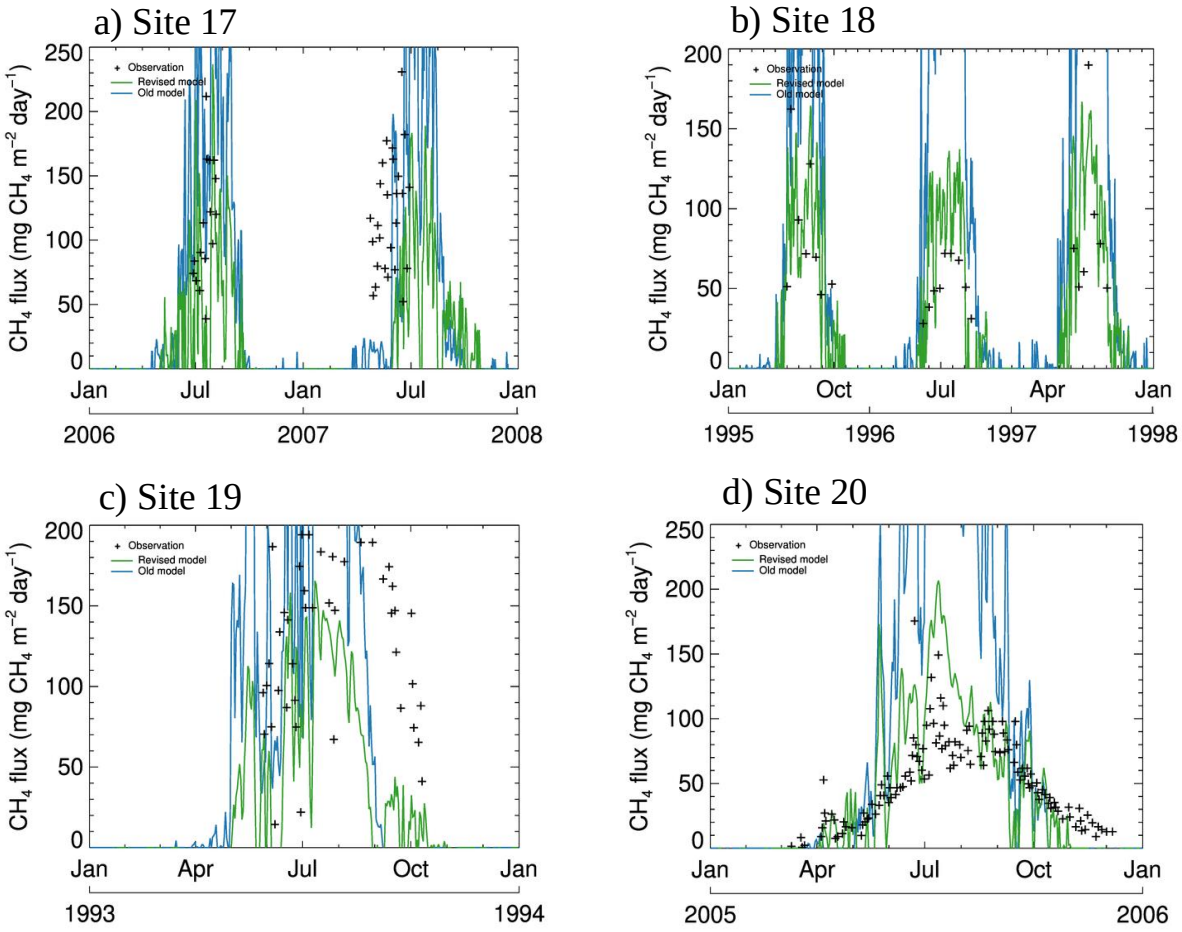

Figure A.2. Daily evaluation results of 8 sites at: a) site 17, b) site 18, c) site 19 and b) site 20. Symbols represent observed data while green lines represent the revised model simulations. Blue lines represent the earlier version model simulations.

Figure A.2. continued

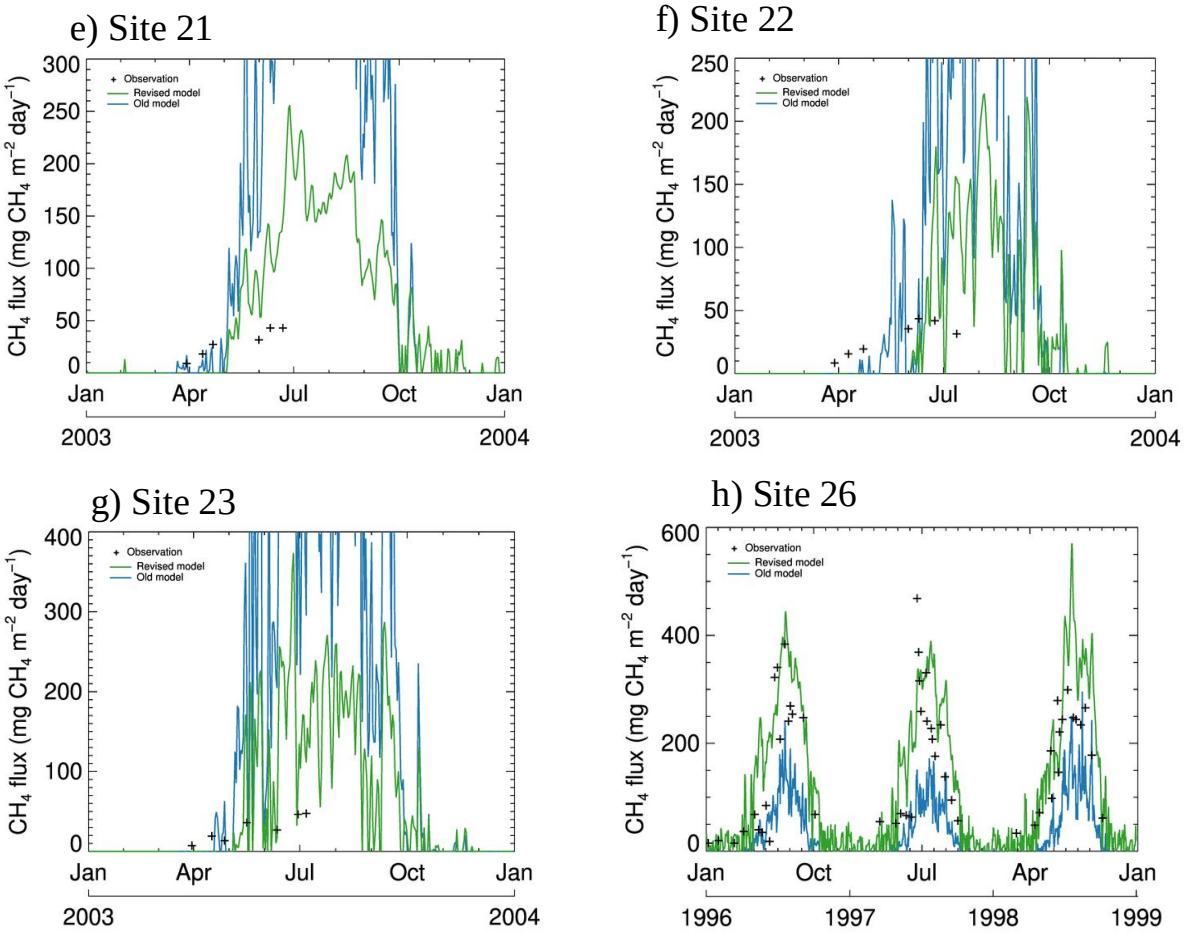

APPENDIX B. SUPPORTING INFORMATION FOR CHAPTER 5

Table B.1. Sensitivity test for all variables in the stem tree flux model. 16 tests are conducted for 8 variables. Changes after adjustment (normally ±20%, but different for dx and dy) are compared with baseline simulations. Fluxes of tree heights of 0.1m, 0.5m and 1.0m are showed. C_soil, D_x and D_y are three main variables.

Base line									Flux at:	(Units: mg CH_4 m^{-2} hr^{-1})	
Species	c_soil	c_air	dx	dy	D_x	D_y	DBH	Height	0.1m	0.5m	1.0m
Mauritia	200ppmv	2ppmv	0.02m	0.1m	0.00002 m^2/s	0.002 m^2/s	36.22cm	5m	259.13	90.55	43.04
Test Begin											
1	+20%								311.48 20.2%	108.85 20.2%	51.74 20.2%
2	-20%								206.78 -20.2%	72.26 -20.2%	34.35 -20.2%
3		+20%							258.61 -0.2%	90.37 -0.2%	42.95 -0.2%
4		-20%							259.65 0.2%	90.74 0.2%	43.13 0.2%
5			increase to 0.04						155.24 -40.1%	77.80 -14.1%	40.66 -5.5%
6			decrease to 0.01						381.27 47.1%	94.21 4.0%	43.19 0.3%
7				increase to 0.25					NAN NAN	93.08 2.8%	43.61 1.3%
8				decrease to 0.05					258.16 -0.4%	89.96 -0.7%	42.56 -1.1%
9					+20%				300.91 16.1%	99.55 9.9%	46.24 7.4%
10					-20%				215.15 -17.0%	80.34 -11.3%	39.21 -8.9%
11						+20%			267.18 3.1%	98.57 8.9%	47.88 11.3%
12						-20%			248.84 -4.0%	81.32 -10.2%	37.56 -12.7%
13							+20%		259.23 0.04%	91.03 0.53%	43.89 1.98%
14							-20%		258.79 -0.13%	88.95 -1.77%	40.30 -6.37%
15								+20%	259.13 0.001%	90.57 0.01%	43.07 0.06%
16								-20%	259.12 -0.005%	90.49 -0.070%	42.90 -0.318%

Table B.2. Priors for forward model simulations of stem tree methane emissions. The simulations are conducted for 14 individual trees, assuming soil concentrations of methane are 200 ppmv. D_x and D_y are diffusivity in x and y directions, units are $m^2\ s^{-1}$. Biases are mean squared error between modeled and observed fluxes.

C_soil (ppmv)	Tree #	D_x ($m^2\ s^{-1}$)	D_y ($m^2\ s^{-1}$)	Bias (mg $CH_4\ m^{-2}\ h^{-1}$)	DBH (cm)	Species
200	1	0.00002	0.0006	20.94	30.1	Mauritia
	2	0.000016	0.0024	13.47	31.6	Mauritia
	3	0.00001	0.00054	5.47	33.2	Mauritia
	4	0.00003	0.0006	21.55	32.7	Mauritia
	5	0.000001	0.0006	3.73	30.6	Mauritia
	6	0.000012	0.0006	0.76	30.0	Mauritia
	7	0.000024	0.002	17.84	30.0	Mauritia
	8	0.000001	0.0006	2.21	26.6	Mauritia
	9	0.000005	0.0005	2.10	31.4	Mauritia
	10	0.000021	0.0017	8.54	37.9	Mauritia
	11	0.000035	0.003	10.64	38.9	Mauritia
	12	0.000042	0.0017	9.90	39.8	Mauritia
	13	0.000011	0.001	12.43	41.4	Mauritia
	14	0.00001	0.0022	11.95	41.7	Mauritia

Table B.3. Parameter posteriors using the PySMC method.

	C_soil (ppmv)	D_x (10^{-5} m^2 s^{-1})	D_y (10^{-3} m^2 s^{-1})
Mode a	362.75	0.44	2.84
Mode b	211.64	1.04	2.76
Mean	275.11	0.79	2.80

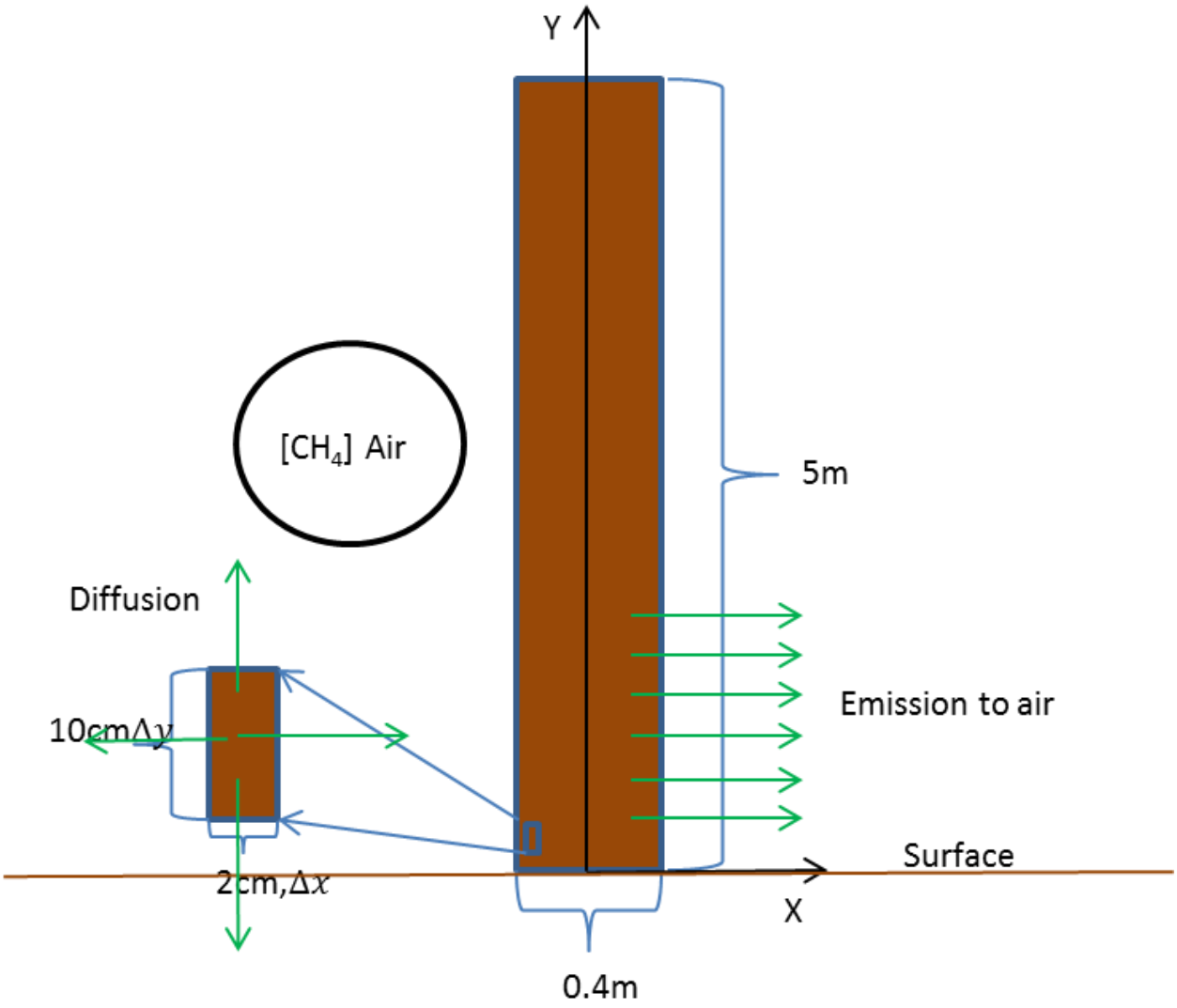

Figure B.1. Schematic diagram of 2D diffusion model for tree stem methane fluxes. The big rectangle represents the tree stem, small one represents the pixel size, and arrows represent fluxes.

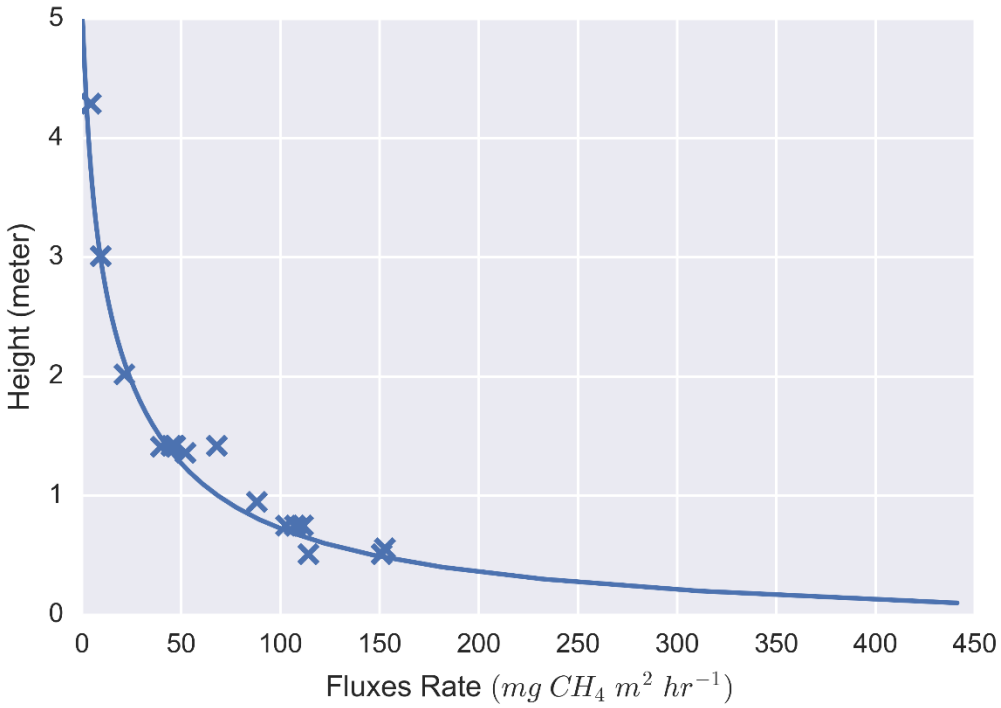

Figure B.2. Stem flux comparison between forward model simulations (solid line) and observed fluxes (blue x) for palm tree number 11, which showed in table B.2.

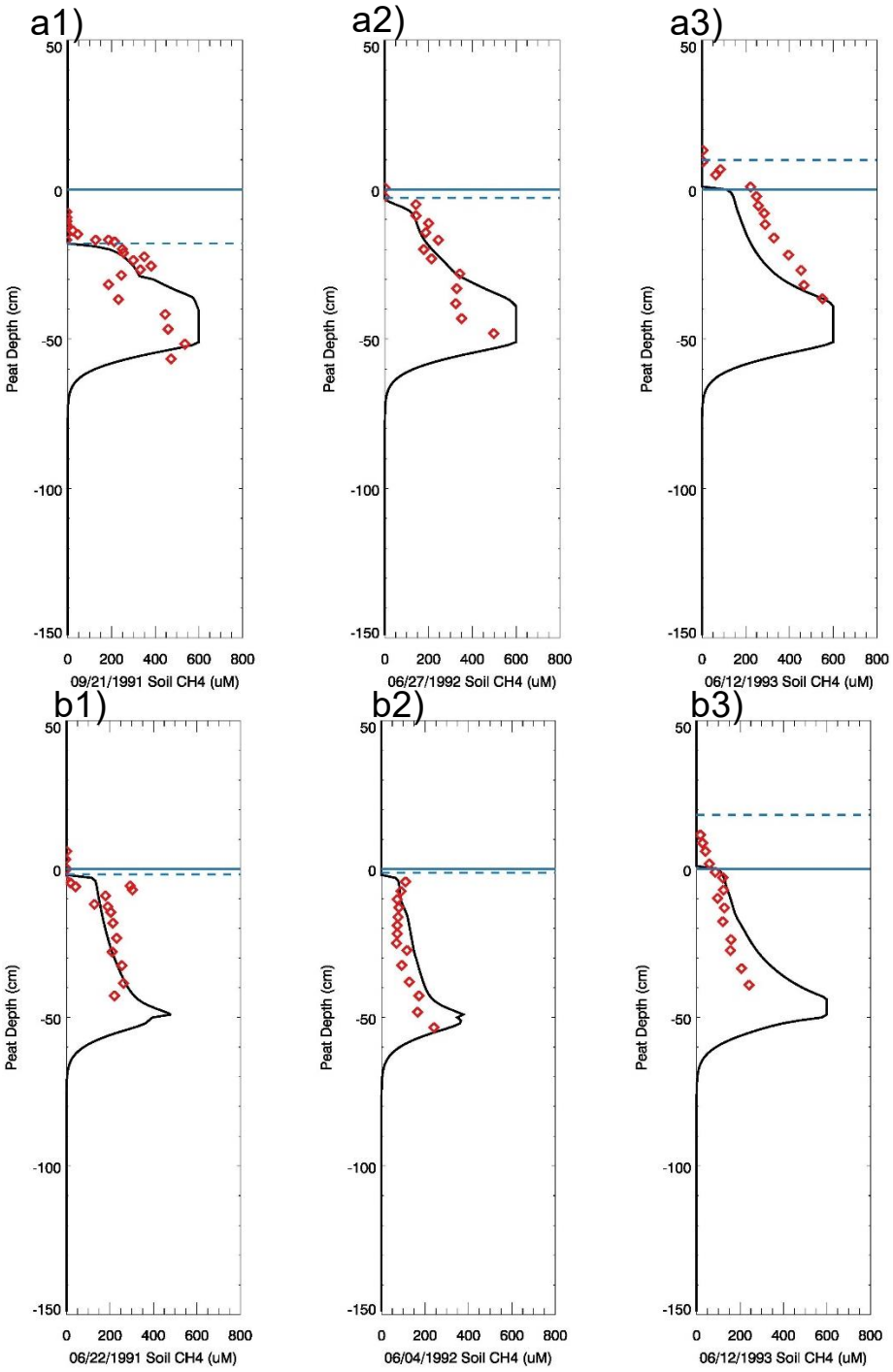

Figure B.3. Soil methane concentration comparison between TEM model and observations from a) Buck Hollow Site and b) Big Cassandra site (Shannon and White, 1994). Solid black lines are model estimate soil methane concentration; red dots are observed soil methane concentrations; blue solid lines are soil surface and dash lines are observed water table depth or standing water height.

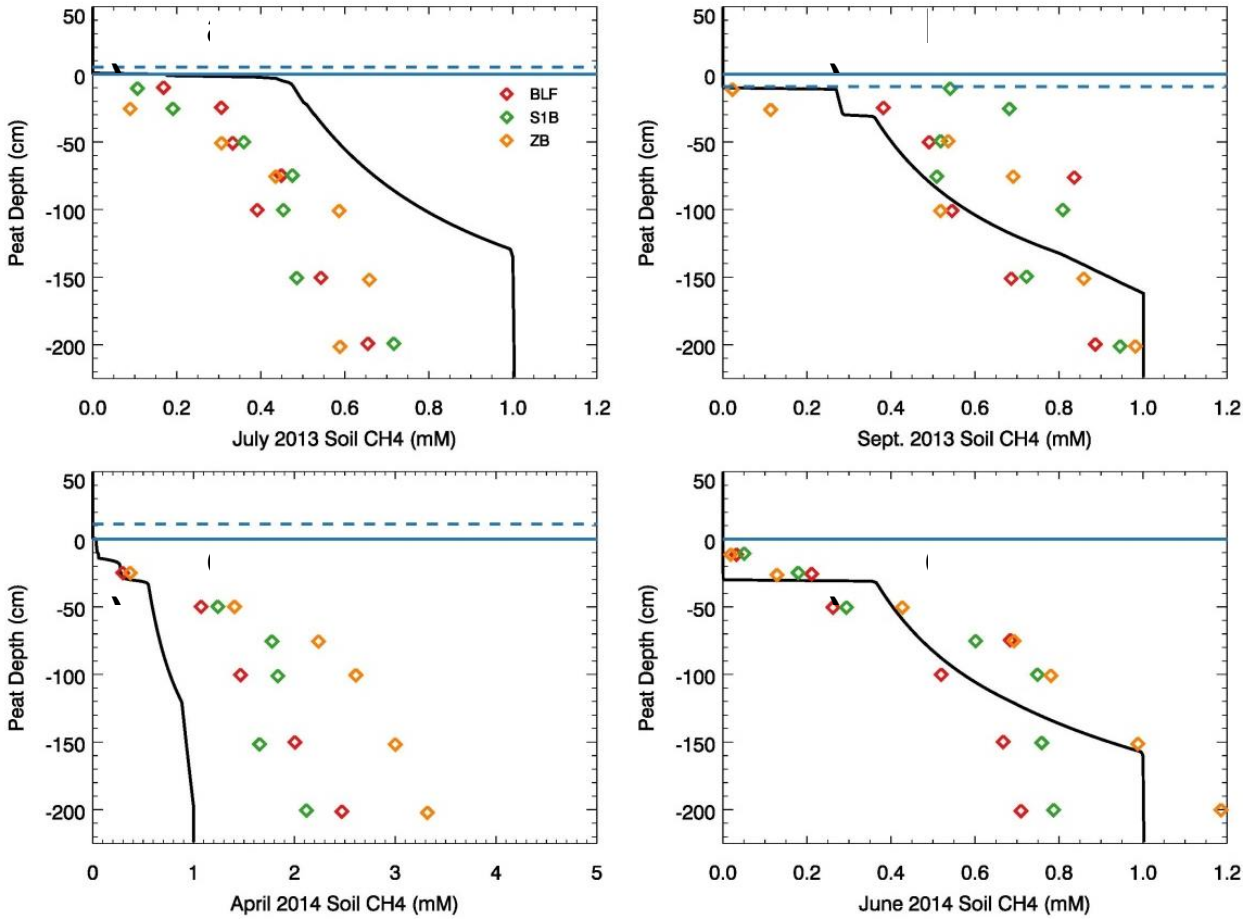

Figure B.4. Soil methane concentration comparison between TEM model simulations (solid black lines) and observations from SPRUCE sites: Bog Lake Fen (BLF, red dots), S1 Bog (S1B, green dots), Zim Bog (ZB, yellow dots) (Pending publication, http://dx.doi.org/10.3334/CDIAC/spruce.043). Blue solid lines are soil surface and dash lines are observed water table depth or standing water height.

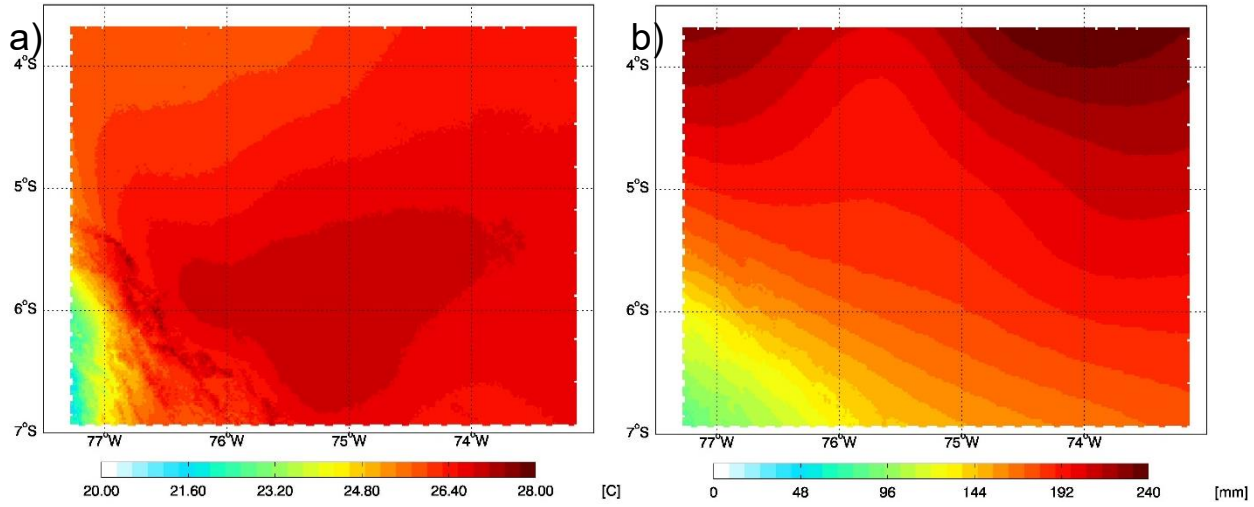

Figure B.5. Interpolated input data in PMFB area for TEM: (a) mean atmosphere temperature and (b) mean monthly precipitation from 2000 to 2010.

REFERENCES

Anderson, B., Bartlett, K. B., Frolking, S., Hayhoe, K., Jenkins, J. C., & Salas, W. A. (2010). Methane and nitrous oxide emissions from natural sources.

Arah, J. R. M., & Stephen, K. D. (1998). A model of the processes leading to methane emission from peatland. Atmospheric Environment, 32(19), 3257-3264.

Arneth, A., Sitch, S., Bondeau, A., Butterbach-Bahl, K., Foster, P., Gedney, N., ... & Wania, R. (2010). From biota to chemistry and climate: towards a comprehensive description of trace gas exchange between the biosphere and atmosphere. Biogeosciences, 7(1), 121-149.

Aronson, E. L., Allison, S. D. & Helliker, B. R. (2013). Environmental impacts on the diversity of methane-cycling microbes and their resultant function. Frontiers in Microbiology 4

Aselmann, I. & Crutzen, P. J. (1989). Global distribution of natural freshwater wetlands and rice paddies, their net primary productivity, seasonality and possible methane emissions. Journal of Atmospheric Chemistry 8, 307–358.

Badr, O., & Probert, S. D. (1994). Carbon monoxide concentration in the Earth's atmosphere. Applied Energy, doi:10.1016/0306-2619(94)90035-3

Badr, O., & Probert, S. D. (1995). Sinks and environmental impacts for atmospheric carbon monoxide, Applied Energy. doi:10.1016/0306-2619(95)98803-A

Baldocchi, D. (2016). AmeriFlux US-Myb Mayberry Wetland [Data set]. https://doi.org/10.17190/AMF/1246139

Baldocchi, D. (2016). AmeriFlux US-Tw1 Twitchell Wetland West Pond [Data set]. https://doi.org/10.17190/AMF/1246147

Baldocchi, D. (2018). AmeriFlux US-Sne Sherman Island Restored Wetland [Data set]. https://doi.org/10.17190/AMF/1418684

Bartholemew, G.W., Alexander, M. (1981). Soils as a sink for atmospheric carbon monoxide, Science 212, 1389-1391, doi:10.1126/science.212.4501.1389

Bartholomew, G. W., & Alexander, M. (1982). Notes. Microorganisms responsible for the oxidation of carbon monoxide in soil. Environmental Science & Technology. American Chemical Society (ACS), doi:10.1021/es00099a013

Bartlett, D. S., Bartlett, K. B., Hartman, J. M., Harriss, R. C., Sebacher, D. I., Pelletier-Travis, R., ... & Brannon, D. P. (1989). Methane emissions from the Florida Everglades: Patterns of variability in a regional wetland ecosystem. Global biogeochemical cycles, 3(4), 363-374.

Bartlett, K. B., Crill, P. M., Bonassi, J. A., Richey, J. E., & Harriss, R. C. (1990). Methane flux from the Amazon River floodplain: Emissions during rising water. Journal of Geophysical Research: Atmospheres, 95(D10), 16773-16788.

Bartlett, K. B., Crill, P. M., Sebacher, D. I., Harriss, R. C., Wilson, J. O., & Melack, J. M. (1988). Methane flux from the central Amazonian floodplain. Journal of Geophysical Research: Atmospheres, 93(D2), 1571-1582.

Batjes, N. H. (2016). Harmonized soil property values for broad-scale modelling (WISE30sec) with estimates of global soil carbon stocks. Geoderma, 269, 61–68. https://doi.org/10.1016/j.geoderma.2016.01.034

Belger, L., Forsberg, B. R., & Melack, J. M. (2011). Carbon dioxide and methane emissions from interfluvial wetlands in the upper Negro River basin, Brazil. Biogeochemistry, 105(1-3), 171-183.

Bender, M., & Conrad, R. (1994). Microbial oxidation of methane, ammonium and carbon monoxide, and turnover of nitrous oxide and nitric oxide in soils, Biogeochemistry, Springer Nature, doi:10.1007/bf00002813

Bergamaschi, B., & Windham-Myers, L. (2018). AmeriFlux US-Srr Suisun marsh - Rush Ranch [Data set]. https://doi.org/10.17190/AMF/1418685

Bergamaschi, P. et al. (2007). Satellite chartography of atmospheric methane from SCIAMACHY on board ENVISAT: 2. Evaluation based on inverse model simulations. Journal of Geophysical Research 112

Bergamaschi, P., Hein, R., Heimann, M., & Crutzen, P. J. (2000). Inverse modeling of the global CO cycle: 1. Inversion of CO mixing ratios, Journal of Geophysical Research: Atmospheres, doi:10.1029/1999jd900818

Bilionis, I., Drewniak, B. A. & Constantinescu, E. M. (2015). Crop physiology calibration in the CLM. Geosci. Model Dev. 8, 1071–1083

Bohrer, G. (2016). AmeriFlux US-ORv Olentangy River Wetland Research Park [Data set]. https://doi.org/10.17190/AMF/1246135

Bohrer, G. (2018). AmeriFlux US-OWC Old Woman Creek [Data set]. https://doi.org/10.17190/AMF/1418679

Bomers, A., van der Meulen, B., Schielen, R. M. J., & Hulscher, S. J. M. H. (2019). Historic flood reconstruction with the use of an Artificial Neural Network. Water Resources Research.

Bonan, G. (1996). A Land Surface Model (LSM Version 1.0) for Ecological, Hydrological, and Atmospheric Studies: Technical Description and User's Guide, UCAR/NCAR, doi:10.5065/d6df6p5x

Boon, P. I., & Mitchell, A. (1995). Methanogenesis in the sediments of an Australian freshwater wetland: comparison with aerobic decay, and factors controlling methanogenesis. FEMS Microbiology Ecology, 18(3), 175-190.

Bourgeau-Chavez, L.L., Garwood, G.C., Riordan, K., Koziol, B.W., Slawski, J. (2012). Development of calibration algorithms for selected water content reflectometry probes for burned and nonburned organic soils of Alaska. Int. J. Wildland Fire 19, 961e975, doi:10.1071/wf07175

Bruhn, D., Albert, K. R., Mikkelsen, T. N., & Ambus, P. (2013). UV-induced carbon monoxide emission from living vegetation. Biogeosciences, Copernicus GmbH, doi:10.5194/bg-10-7877-2013

Cao, M., Dent, J. B., & Heal, O. W. (1995). Modeling methane emissions from rice paddies. Global Biogeochemical Cycles, 9(2), 183-195.

Cao, M., Marshall, S., & Gregson, K. (1996). Global carbon exchange and methane emissions from natural wetlands: Application of a process-based model. Journal of Geophysical Research: Atmospheres, 101(D9), 14399-14414.

Castellanos, P., Marufu, L. T., Doddridge, B. G., Taubman, B. F., Schwab, J. J., Hains, J. C., … Dickerson, R. R. (2011). Ozone, oxides of nitrogen, and carbon monoxide during pollution events over the eastern United States: An evaluation of emissions and vertical mixing, Journal of Geophysical Research Atmospheres, 116(16), doi:10.1029/2010JD014540

Chan, A. S. K., & Steudler, P. A. (2006). Carbon monoxide uptake kinetics in unamended and long-term nitrogen-amended temperate forest soils. FEMS Microbiology Ecology, 57(3), 343–354, doi:10.1111/j.1574-6941.2006.00127.x

Chen, H., Zhu, Q. A., Peng, C., Wu, N., Wang, Y., Fang, X., ... & Yu, G. (2013). Methane emissions from rice paddies natural wetlands, lakes in China: synthesis new estimate. Global change biology, 19(1), 19-32.

Chen, J. (2016). AmeriFlux US-WPT Winous Point North Marsh [Data set]. https://doi.org/10.17190/AMF/1246155

Chen, Y. H., & Prinn, R. G. (2005). Atmospheric modeling of high-and low-frequency methane observations: Importance of interannually varying transport. Journal of Geophysical Research: Atmospheres, 110(D10).

Christensen, T. R., S. Jonasson, T. V. Callaghan, and M. Havström (1995), Spatial variation in high-latitude methane flux along a transect across Siberian and European tundra environments, J. Geophys. Res., 100(D10), 21,035–21,021

Ciais, P., Sabine, C., Bala, G., Bopp, L., Brovkin, V., Canadell, J., ... & Jones, C. (2013). Carbon and other biogeochemical cycles. Climate change 2013: the physical science basis. Contribution of Working Group I to the Fifth Assessment Report of the Intergovernmental Panel on Climate Change. Cambridge University Press Cambridge United Kingdom and New York NY USA, 465-570.

Clement, R. J., Verma, S. B., & Verry, E. S. (1995). Relating chamber measurements to eddy correlation measurements of methane flux. Journal of Geophysical Research: Atmospheres, 100(D10), 21047-21056.

Conrad, R., & Seiler, W. (1980). Role of Microorganisms in the Consumption and Production of Atmospheric Carbon Monoxide by Soil. Appl. Environ, Microbiol., 40(3), 437–445. Retrieved from http://aem.asm.org/cgi/content/abstract/40/3/437

Conrad, R., & Seiler, W. (1982). Arid soils as a source of atmospheric carbon monoxide, Geophysical Research Letters, doi:10.1029/gl009i012p01353

Conrad, R., & Seiler, W. (1985). Characteristics of abiological carbon monoxide formation from soil organic matter, humic acids, and phenolic compounds, Environmental Science & Technology, American Chemical Society (ACS), doi:10.1021/es00142a004,

Conrad, R., Meyer, O., & Seiler, W. (1981). Role of carboxydobacteria in consumption of atmospheric carbon monoxide by soil, Applied and Environmental Microbiology, 42(2), 211–215

Cook, D. (2016a). AmeriFlux US-A03 ARM-AMF3-Oliktok [Data set]. https://doi.org/10.17190/AMF/1498752

Cook, D. (2016b). AmeriFlux US-A10 ARM-NSA-Barrow [Data set]. https://doi.org/10.17190/AMF/1498753

Crutzen, P. J., & Giedel, L. T. (1983). A two-dimensional photochemical model of the atmosphere. 2: The tropospheric budgets of anthropogenic chlorocarbons CO, CH_4, CH3Cl and the effect of various NOx sources on tropospheric ozone, J. Geophys. Res., 88(Cll), 6641−6661. doi:10.1029/JC088iC11p06641

Crutzen, P.J. (1987). Role of the tropics in atmospheric chemistry, The Geophysiology of Amazonia Vegetation Climate Interaction (Dickinson RE, ed.), pp 107–131. John Wiley, New York

Cui, B (1997).: Estimation of CH_4 emission from Sanjiang plain, scientia Geographica Sinica, 17, 93–95 (in Chinese with English abstract).

Daniel, J. S., & Solomon, S. (1988) On the climate forcing of carbon monoxide, Journal of Geophysical Research-Atmospheres, 103(D11), 13249–13260. doi:10.1029/98JD00822

Dee, D. P., Uppala, S. M., Simmons, A. J., Berrisford, P., Poli, P., Kobayashi, S., … Vitart, F. (2011). The ERA-Interim reanalysis: configuration and performance of the data assimilation system, Quarterly Journal of the Royal Meteorological Society, doi:10.1002/qj.828

Dee, D. P., Uppala, S. M., Simmons, A. J., Berrisford, P., Poli, P., Kobayashi, S., ... & Bechtold, P. (2011). The ERA-Interim reanalysis: Configuration and performance of the data assimilation system. Quarterly Journal of the royal meteorological society, 137(656), 553-597.

Delon, C., D. SerCa, C. Boissard, R. Dupont, A. Dutot, P. Laville, P. de Rosnay, and R. Delmas (2007), Soil NO emissions modelling using artificial neural network, Tellus, Ser. B, 59(3), 502–513

Dentener, F., Drevet, J., Lamarque, J. F., Bey, I., Eickhout, B., Fiore, A. M., … Wild, O. (2006). Nitrogen and sulfur deposition on regional and global scales: A multimodel evaluation, Global Biogeochemical Cycles, 20(4), doi:10.1029/2005GB002672

Derendorp, L., Quist, J. B., Holzinger, R., & Röckmann, T. (2011). Emissions of H2 and CO from leaf litter of Sequoiadendron giganteum, and their dependence on UV radiation and temperature, Atmospheric Environment, 45(39), 7520–7524. doi:10.1016/j.atmosenv.2011.09.044

Desai, A. (2016a). AmeriFlux US-Los Lost Creek [Data set]. https://doi.org/10.17190/AMF/1246071

Desai, A. (2016b). AmeriFlux US-PFa Park Falls/WLEF [Data set]. https://doi.org/10.17190/AMF/1246090

Devol, A. H., Richey, J. E., Clark, W. A., King, S. L., & Martinelli, L. A. (1988). Methane emissions to the troposphere from the Amazon floodplain. Journal of Geophysical Research: Atmospheres, 93(D2), 1583-1592.

Ding, W., Cai, Z., & Wang, D. (2004). Preliminary budget of methane emissions from natural wetlands in China. Atmospheric Environment, 38(5), 751-759.

Dise, N. (1993). Methane emission from Minnesota peatlands: Spatial and seasonal variability. Global Biogeochemical Cycles, 7(1), 123-142.

Dlugokencky, E. J., Bruhwiler, L., White, J. W. C., Emmons, L. K., Novelli, P. C., Montzka, S. A., ... & Gatti, L. V. (2009). Observational constraints on recent increases in the atmospheric CH_4 burden. Geophysical Research Letters, 36(18).

Draper, F. C. et al. (2014). The distribution and amount of carbon in the largest peatland complex in Amazonia. Environ. Res. Lett. 9, 124017

Duan, Q. Y., Gupta, V. K., & Sorooshian, S. (1993). Shuffled complex evolution approach for effective and efficient global minimization, Journal of Optimization Theory and Applications, 76(3), 501–521. doi:10.1007/BF00939380

Duggin, J. A., & Cataldo, D. A. (1985). The rapid oxidation of atmospheric CO to CO2 by soils, Soil Biology and Biochemistry, 17(4), 469–474, doi:10.1016/0038-0717(85)90011-2

Dupont, R., K. Butterbach-Bahl, C. Delon, N. Bruggemann, and D. Serça (2008), Neural network treatment of 4 years long NO measurement in temperate spruce and beech forests, J. Geophys. Res., 113, G04001, doi:10.1029/2007JG000665

Emmons, L. K., Walters, S., Hess, P. G., Lamarque, J.-F., Pfister, G. G., Fillmore, D., … Kloster, S. (2010). Description and evaluation of the Model for Ozone and Related chemical Tracers, version 4 (MOZART-4), Geoscientific Model Development, 3(1), 43–67. doi:10.5194/gmd-3-43-2010

Erika, P. et al. (2011). Microwave remote sensing of palm swamp distribution and flooding status over a sub-region in the upper amazon basin. 34th Int. Symp. Remote Sens. Environ. - GEOSS Era Towar. Oper. Environ. Monit. 2003–2006

Etheridge, D. M., Steele, L., Francey, R. J., & Langenfelds, R. L. (1998). Atmospheric methane between 1000 AD and present: Evidence of anthropogenic emissions and climatic variability. Journal of Geophysical Research: Atmospheres, 103(D13), 15979-15993.

Etminan, M., Myhre, G., Highwood, E. J., & Shine, K. P. (2016). Radiative forcing of carbon dioxide, methane, and nitrous oxide: A significant revision of the methane radiative forcing. Geophysical Research Letters, 43(24), 12-614.

Eva, H. et al. (2002). a Vegetation Map of South America. doi:10.2307/633834

Fenchel, T., King, G. M., & Blackburn, T. H. (1988) Bacterial biogeochemistry: the ecophysiology of mineral cycling, Bacterial biogeochemistry (p. 307 pp). doi:10.1016/B978-0-12-415836-8.00012-8

Ferenci, T., Strom, T., & Quayle, J. R. (1975) Oxidation of carbon monoxide and methane by Pseudomonas methanica, Journal of General Microbiology, 91(1), 79–91. doi:10.1099/00221287-91-1-79

Fisher, M. E. (2003). Soil-atmosphere Exchange of Carbon Monoxide in Forest Stands Exposed to Elevated and Ambient CO2 (Doctoral dissertation)

Frankenberg, C. (2005). Assessing Methane Emissions from Global Space-Borne Observations. Science 308, 1010–1014

Fraser, W. T., Blei, E., Fry, S. C., Newman, M. F., Reay, D. S., Smith, K. A., & McLeod, A. R. (2015). Emission of methane, carbon monoxide, carbon dioxide and short-chain hydrocarbons from vegetation foliage under ultraviolet irradiation, Plant, Cell and Environment, 38(5), 980–989. doi:10.1111/pce.12489

Frieler, K., Lange, S., Piontek, F., Reyer, C. P., Schewe, J., Warszawski, L., ... & Geiger, T. (2017). Assessing the impacts of 1.5 C global warming–simulation protocol of the Inter-Sectoral Impact Model Intercomparison Project (ISIMIP2b). Geoscientific Model Development.

Funk, D. W., Pullman, E. R., Peterson, K. M., Crill, P. M., & Billings, W. D. (1994). Influence of water table on carbon dioxide, carbon monoxide, and methane fluxes from Taiga Bog microcosms, Global Biogeochem. Cycles, 8(3), 271–278. doi:10.1029/94gb0122

Galbally, I., Meyer, C. P., Wang, Y. P., & Kirstine, W. (2010) Soil-atmosphere exchange of CH_4, CO, N2O and NOx and the effects of land-use change in the semiarid Mallee system in Southeastern Australia, Global Change Biology, 16(9), 2407–2419, doi:10.1111/j.1365-2486.2010.02161.x

Gille, J. (2013). MOPITT Gridded Monthly CO Retrievals (Near and Thermal Infrared Radiances) - Version 6 [Data set], NASA Langley Atmospheric Science Data Center. doi:10.5067/TERRA/MOPITT/DATA301

Glagolev, M., Kleptsova, I., Filippov, I., Maksyutov, S., & Machida, T. (2011). Regional methane emission from West Siberia mire landscapes. Environmental Research Letters, 6(4), 045214.

Gödde, M., Meuser, K., & Conrad, R. (2000). Hydrogen consumption and carbon monoxide production in soils with different properties, Biology and Fertility of Soils, 32(2), 129–134, doi:10.1007/s003740000226

Granberg, G., Ottosson-Löfvenius, M., Grip, H., Sundh, I., & Nilsson, M. (2001). Effect of climatic variability from 1980 to 1997 on simulated methane emission from a boreal mixed mire in northern Sweden. Global Biogeochemical Cycles, 15(4), 977-991.

Guthrie, P. D. (1989). The CH_4- CO - OH conundrum: A simple analytic approach, Global Biogeochemical Cycles, doi:10.1029/gb003i004p00287

Hanson, R. S., and T. E. Hanson (1996), Methanotrophic bacteria, Microbiol. Mol. Biol. Rev., 60(2), 439–471

Hao, Q. J., Wang, Y. S., Song, C. C., Liu, G. R., Wang, Y. Y., & Wang, M. X. (2004). Study of CH_4 emission from wetlands in Sanjiang Plain. Journal of Soil and Water Conservation, 18(3), 194-199.

Hardy, K. R., & King, G. M. (2001). Enrichment of High-Affinity CO Oxidizers in Maine Forest Soil. Applied and Environmental Microbiology, 67(8), 3671–3676, doi:10.1128/AEM.67.8.3671-3676.2001

Harris, I. P. D. J., Jones, P. D., Osborn, T. J., & Lister, D. H. (2014). Updated high-resolution grids of monthly climatic observations–the CRU TS3. 10 Dataset. International journal of climatology, 34(3), 623-642.

Harriss, R. C., Sebacher, D. I., Bartlett, K. B., Bartlett, D. S., & Crill, P. M. (1988). Sources of atmospheric methane in the south Florida environment. Global Biogeochemical Cycles, 2(3), 231-243.

He, H., & He, L. (2014). The role of carbon monoxide signaling in the responses of plants to abiotic stresses, Nitric Oxide : Biology and Chemistry / Official Journal of the Nitric Oxide Society, 42, 40–3. doi:10.1016/j.niox.2014.08.011

Heichel, G. H. (1973). Removal of Carbon Monoxide by Field and Forest Soils1, Journal of Environment Quality, American Society of Agronomy, doi:10.2134/jeq1973.00472425000200040001x

Hergoualc, K., Gutierrez-velez, V. H., Lent, J. Van & Verchot, L. V. (2016). Characterizing peat palm forest degradation in the Peruvian Amazon from space and on the ground. For. Ecol. Manage. 18, 9431

Hess, L. L. et al. (2015). Wetlands of the Lowland Amazon Basin: Extent, Vegetative Cover, and Dual-season Inundated Area as Mapped with JERS-1 Synthetic Aperture Radar. Wetlands 35, 745–756

Hinkle, C. R. (2016). AmeriFlux US-DPW Disney Wilderness Preserve Wetland [Data set]. https://doi.org/10.17190/AMF/1562387

Hodson, E. L., Poulter, B., Zimmermann, N. E., Prigent, C., & Kaplan, J. O. (2011). The El Niño–Southern Oscillation and wetland methane interannual variability. Geophysical Research Letters, 38(8).

Hopcroft, P. O., Valdes, P. J., O'Connor, F. M., Kaplan, J. O., & Beerling, D. J. (2017). Understanding the glacial methane cycle. Nature communications, 8, 14383.

Huang, Y. A. O., Sun, W., Zhang, W. E. N., Yu, Y., Su, Y., & Song, C. (2010). Marshland conversion to cropland in northeast China from 1950 to 2000 reduced the greenhouse effect. Global Change Biology, 16(2), 680-695.

Hutchinson, M. F. et al. (2009). Development and testing of Canada-wide interpolated spatial models of daily minimum-maximum temperature and precipitation for 1961-2003. Journal of Applied Meteorology and Climatology, 48(4), 725-741

Ito, A., & Inatomi, M. (2012). Use of a process-based model for assessing the methane budgets of global terrestrial ecosystems and evaluation of uncertainty. Biogeosciences, 9(2), 759-773.

Iwata, H., Ueyama, M., & Harazono, Y. (2016). AmeriFlux US-Uaf University of Alaska, Fairbanks [Data set]. https://doi.org/10.17190/AMF/1480322

Jackowicz-Korczyński, M., Christensen, T. R., Bäckstrand, K., Crill, P., Friborg, T., Mastepanov, M., & Ström, L. (2010). Annual cycle of methane emission from a subarctic peatland. Journal of Geophysical Research: Biogeosciences, 115(G2).

Jobbagy, E. G., & Jackson, R. (2000). The vertical Distribution of soil organic carbon and its relation to climate and vegetation, Ecological Applications, 10:2(April), 423–436, doi:10.2307/2641104

Jones, R. D., & Morita, R. Y. (1983). Carbon monoxide oxidation by chemolithotrophic ammonium oxidizers, Canadian Journal of Microbiology, 29(11), 1545–1551, doi:10.1139/m83-237

Kalnay, E., Kanamitsu, M., Kistler, R., Collins, W., Deaven, D., Gandin, L., ... & Zhu, Y. (1996). The NCEP/NCAR 40-year reanalysis project. Bulletin of the American meteorological Society, 77(3), 437-472.

Karkalos, N. E., Efkolidis, N., Kyratsis, P., & Markopoulos, A. P. (2019). A comparative study between regression and neural networks for modeling Al6082-T6 alloy drilling. Machines, 7(1), 13.

Khalil, M. A. ., Pinto, J. ., & Shearer, M. (1999). Atmospheric carbon monoxide, Chemosphere - Global Change Science, Elsevier BV, doi:s1465-9972(99)00053-7

Khalil, M. A. K., & Rasmussen, R. A. (1990). The global cycle of carbon monoxide: Trends and mass balance, Chemosphere, 20(1–2), 227–242, doi:10.1016/0045-6535(90)90098-E

King, G. M. (1999). Attributes of Atmospheric Carbon Monoxide Oxidation by Maine Forest Soils, Appl. Environ. Microbiol., 65(12), 5257–5264

King, G. M. (1999a). Characteristics and significance of atmospheric carbon monoxide consumption by soils, Chemosphere, 1, 53–63, doi:10.1016/S1465-9972(99)00021-5

King, G. M. (2000). Land use impacts on atmospheric carbon monoxide consumption by soils, Global Biogeochemical Cycles, 14(4), 1161–1172, doi:10.1029/2000GB001272

King, G. M., & Crosby, H. (2002). Impacts of plant roots on soil CO cycling and soil-atmosphere CO exchange, Global Change Biology, 8(11), 1085–1093, doi:10.1046/j.1365-2486.2002.00545.x

King, G. M., & Hungria, M. (2002). Soil-atmosphere CO exchanges and microbial biogeochemistry of CO transformations in a Brazilian agricultural ecosystem, Applied and Environmental Microbiology, 68(9), 4480–4485, doi:10.1128/AEM.68.9.4480-4485.2002

King, G. M., & Weber, C. F. (2007). Distribution, diversity and ecology of aerobic CO-oxidizing bacteria, Nature Reviews, Microbiology, 5(2), 107–18, doi:10.1038/nrmicro1595

King, J. Y., Brandt, L. A., & Adair, E. C. (2012). Shedding light on plant litter decomposition: advances, implications and new directions in understanding the role of photodegradation, Biogeochemistry, 111(1–3), 57–81, doi:10.1007/s10533-012-9737-9

Kirschke, S., Bousquet, P., Ciais, P., Saunois, M., Canadell, J. G., Dlugokencky, E. J., ... & Cameron-Smith, P. (2013). Three decades of global methane sources and sinks. Nature geoscience, 6(10), 813.

Kisselle, K. W., Zepp, R. G., Burke, R. A., De Pinto, A. S., Bustamante, M. M. C., Opsahl, S., … Viana, L. T. (2002). Seasonal soil fluxes of carbon monoxide in burned and unburned Brazilian savannas, Journal of Geophysical Research Atmospheres, 107(20), doi:10.1029/2001JD000638

Kleinen, T., Brovkin, V., & Schuldt, R. J. (2012). A dynamic model of wetland extent and peat accumulation: results for the Holocene. Biogeosciences, 9(1), 235-248.

Knox, S. H., Jackson, R. B., Poulter, B., McNicol, G., Fluet-Chouinard, E., Zhang, Z., ... & Papale, D. (2019). FLUXNET-CH_4 Synthesis Activity: Objectives, Observations, and Future Directions. Bulletin of the American Meteorological Society,

Kozlowski, T. T. (1997). Responses of woody plants to flooding and salinity. Tree Physiology 17, 490–490

Krauss, K. (2016a). AmeriFlux US-LA1 Pointe-aux-Chenes Brackish Marsh [Data set]. https://doi.org/10.17190/AMF/1543386

Krauss, K. (2016b). AmeriFlux US-LA2 Salvador WMA Freshwater Marsh [Data set]. https://doi.org/10.17190/AMF/1543387

Kuhlbusch, T. A., Zepp, R. G., Miller, W. L., & A BURKE, R. (1998). Carbon monoxide fluxes of different soil layers in upland Canadian boreal forests, Tellus B. Informa UK Limited, doi:10.1034/j.1600-0889.1998.t01-3-00003.x

Lähteenoja, O. et al. (2011). The large Amazonian peatland carbon sink in the subsiding Pastaza-Marañón foreland basin, Peru. Global Change Biology 18, 164–178

Lamarque, J. F., Emmons, L. K., Hess, P. G., Kinnison, D. E., Tilmes, S., Vitt, F., … Tyndall, G. K. (2012). CAM-chem: Description and evaluation of interactive atmospheric chemistry in the Community Earth System Model, Geoscientific Model Development, 5(2), 369–411, https://doi.org/10.5194/gmd-5-369-2012

Lange, S. (2016). EartH2Observe, WFDEI and ERA-Interim data Merged and Bias-corrected for ISIMIP (EWEMBI) [Data set]. https://doi.org/10.5880/PIK.2016.004

Lee, H., Rahn, T., & Throop, H. (2012). An accounting of C-based trace gas release during abiotic plant litter degradation, Global Change Biology, 18(3), 1185–1195, doi:10.1111/j.1365-2486.2011.02579.x

Lehner, B., & Döll, P. (2004). Development and validation of a global database of lakes, reservoirs and wetlands. Journal of Hydrology, 296(1-4), 1-22.

Li, C. S. (2000). Modeling trace gas emissions from agricultural ecosystems. In Methane Emissions from Major Rice Ecosystems in Asia (pp. 259-276). Springer, Dordrecht.

Liu, L., Zhuang, Q., Zhu, Q., Liu, S., van Asperen, H., & Pihlatie, M. (2018). Global soil consumption of atmospheric carbon monoxide: an analysis using a process-based biogeochemistry model. Atmospheric Chemistry and Physics (Online), 18(11).

Liu, S., Zhuang, Q., He, Y., Noormets, A., Chen, J., & Gu, L. (2016). Evaluating atmospheric CO2 effects on gross primary productivity and net ecosystem exchanges of terrestrial ecosystems in the conterminous United States using the AmeriFlux data and an artificial neural network approach. Agricultural and forest meteorology, 220, 38-49.

Logan, J. A., Prather, M. J., Wofsy, S. C., & McElroy, M. B. (1981). Tropospheric chemistry - A global perspective, J. Geophys. Res., doi:10.1029/JC086iC08p07210

Lu, Y., & Khalil, M. A. K. (1993). Methane and carbon monoxide in OH chemistry: The effects of feedbacks and reservoirs generated by the reactive products, Chemosphere. Elsevier BV, doi:10.1016/0045-6535(93)90450-j

Luo, M., Read, W., Kulawik, S., Worden, J., Livesey, N., Bowman, K., & Herman, R. (2013). Carbon monoxide (CO) vertical profiles derived from joined TES and MLS measurements, Journal of Geophysical Research Atmospheres, 118(18), 10601–10613, doi:10.1002/jgrd.50800

MacDonald, J. A., D. Fowler, K. J. Hargreaves, U. Skiba, I. D. Leith, and M. B. Murray (1998), Methane emission rates from a northern wetland; response to temperature, water table and transport, Atmos. Environ., 32(19), 3219–3227.

MacFarling Meure, C., Etheridge, D., Trudinger, C., Steele, P., Langenfelds, R., Van Ommen, T., ... & Elkins, J. (2006). Law Dome CO_2, CH_4 and N_2O ice core records extended to 2000 years BP. Geophysical Research Letters, 33(14).

Matthews, E., & Fung, I. (1987). Methane emission from natural wetlands: Global distribution, area, and environmental characteristics of sources. Global biogeochemical cycles, 1(1), 61-86.

McKenney, D. W. et al. (2011). Customized spatial climate models for North America. Bulletin of the American Meteorological Society, 92(12), 1611

Megonigal, J. P. & Day, F. P. (1992). Effects of Flooding On Root and Shoot Production of Bald Cypress in Large Experimental Enclosures. Ecology 73, 1182–1193

Melack, J. M., Hess, L. L., Gastil, M., Forsberg, B. R., Hamilton, S. K., Lima, I. B., & Novo, E. M. (2004). Regionalization of methane emissions in the Amazon Basin with microwave remote sensing. Global Change Biology, 10(5), 530-544.

Melillo, J. M., McGuire, A. D., Kicklighter, D. W., Moore, B., Vorosmarty, C. J., & Schloss, A. L. (1993). Global climate change and terrestrial net primary production. Nature, 363(6426), 234.

Melton, J. R., & Arora, V. K. (2016). Competition between plant functional types in the Canadian Terrestrial Ecosystem Model (CTEM) v. 2.0, Geosci. Model Dev., 9, 323–361.

Melton, J., Wania, R., Hodson, E. L., Poulter, B., Ringeval, B., Spahni, R., ... & Eliseev, A. (2013). Present state of global wetland extent and wetland methane modelling: conclusions from a model inter-comparison project (WETCHIMP).

Meng, L., Hess, P. G. M., Mahowald, N. M., Yavitt, J. B., Duan et al., 1993, W. J., Subin, Z. M., ... & Fuka, D. R. (2012). Sensitivity of wetland methane emissions to model assumptions: application and model testing against site observations. Biogeosciences, 9(7), 2793-2819.

Moore, T. R., De Young, A., Bubier, J. L., Humphreys, E. R., Lafleur, P. M., & Roulet, N. T. (2011). A multi-year record of methane flux at the Mer Bleue bog, southern Canada. Ecosystems, 14(4), 646.

Moxley, J. M., & Smith, K. A. (1998). Factors affecting utilisation of atmospheric CO by soils, Soil Biology and Biochemistry, 30(1), 65–79, doi:10.1016/S0038-0717(97)00095-3

Myhre, G., Shindell, D., Bréon, F. M., Collins, W., Fuglestvedt, J., Huang, J., ... & Nakajima, T. (2013). Anthropogenic and Natural Radiative Forcing. In: Climate Change 2013: The Physical Science Basis, Contribution of Working Group 1 to the Fifth Assessment Report of the Intergovernmental Panel on Climate Change. Table, 8, 714

Nahlik, A. M., & Mitsch, W. J. (2011). Methane emissions from tropical freshwater wetlands located in different climatic zones of Costa Rica. Global Change Biology, 17(3), 1321-1334.

Nakai, T., Kim, Y., Busey, R. C., Suzuki, R., Nagai, S., Kobayashi, H., … Ito, A. (2013). Characteristics of evapotranspiration from a permafrost black spruce forest in interior Alaska. Polar Science, 7(2), 136–148. doi:10.1016/j.polar.2013.03.003

Nisbet, E. G., Dlugokencky, E. J., & Bousquet, P. (2014). Methane on the rise—again. Science, 343(6170), 493-495.

Nisbet, E. G., Dlugokencky, E. J., Manning, M. R., Lowry, D., Fisher, R. E., France, J. L., ... & Bousquet, P. (2016). Rising atmospheric methane: 2007–2014 growth and isotopic shift. Global Biogeochemical Cycles, 30(9), 1356-1370.

Oechel, W., & Zona, D. (2016). AmeriFlux US-Ivo Ivotuk [Data set]. https://doi.org/10.17190/AMF/1246067

Oikawa, P. (2016). AmeriFlux US-EDN Eden Landing Ecological Reserve [Data set]. https://doi.org/10.17190/AMF/1543381

Pangala, S. R., Enrich-Prast, A., Basso, L. S., Peixoto, R. B., Bastviken, D., Hornibrook, E. R., ... & Bastos, W. R. (2017). Large emissions from floodplain trees close the Amazon methane budget. Nature, 552(7684), 230.

Pangala, S. R., Moore, S., Hornibrook, E. R. C. & Gauci, V. (2013). Trees are major conduits for methane egress from tropical forested wetlands. New Phytol. 197, 524–531

Pelletier, L., Moore, T. R., Roulet, N. T., Garneau, M., & Beaulieu-Audy, V. (2007). Methane fluxes from three peatlands in the La Grande Riviere watershed, James Bay lowland, Canada. Journal of Geophysical Research: Biogeosciences, 112(G1).

Petrescu, A. M. R., Van Beek, L. P. H., Van Huissteden, J., Prigent, C., Sachs, T., Corradi, C. A. R., ... & Dolman, A. J. (2010). Modeling regional to global CH_4 emissions of boreal and arctic wetlands. Global Biogeochemical Cycles, 24(4).

Philip, R., & Novick, K. (2016) AmeriFlux US-MMS Morgan Monroe State Forest [Data set]. AmeriFlux; Indiana University, doi:10.17190/AMF/1246080

Pihlatie, M., Rannik, Ü., Haapanala, S., Peltola, O., Shurpali, N., Martikainen, P. J., … Mammarella, I. (2016). Seasonal and diurnal variation in CO fluxes from an agricultural bioenergy crop, Biogeosciences. Copernicus GmbH, doi:10.5194/bg-13-5471-2016

Potter, C. S., Klooster, S. A., & Chatfield, R. B. (1996). Consumption and production of carbon monoxide in soils: A global model analysis of spatial and seasonal variation, Chemosphere, 33(6), 1175–1193, doi:10.1016/0045-6535(96)00254-8

Poulter, B., Bousquet, P., Canadell, J. G., Ciais, P., Peregon, A., Saunois, M., ... & Joos, F. (2017). Global wetland contribution to 2000–2012 atmospheric methane growth rate dynamics. Environmental Research Letters, 12(9), 094013.

Prather, M., and Ehhalt, D. (2001). Atmospheric chemistry and greenhouse gases. Climate Change, 2001: The Scientific Basis (Houghton JT, Ding Y, Griggs DJ, Noguer M, van der Linden PJ, Dai X, Maskell K & Johnson CA, eds), pp. 239–288, Cambridge University Press, Cambridge, UK

Prather, M., Derwent, R., Ehhalt, D., Fraser, P., Sanheeza, E. and Zhou, X. (1995). Other trace gases and atmospheric chemistry, Climate Change, 1994. Radiative Forcing of Climate Change (Houghton JT, Meira Filho LG, Bruce J, Hoesung Lee BA, Callander E, Haites E, Harris N & Maskell K, eds), pp. 76–126, Cambridge University Press, Cambridge, UK

Price, D. T. et al. (2000). A comparison of two statistical methods for spatial interpolation of Canadian monthly mean climate data. Agricultural and Forest meteorology, 101(2), 81-94

Quiquet, A., Archibald, A. T., Friend, A. D., Chappellaz, J., Levine, J. G., Stone, E. J., ... & Pyle, J. A. (2015). The relative importance of methane sources and sinks over the Last Interglacial period and into the last glaciation. Quaternary Science Reviews, 112, 1-16.

Riley, W. J., Subin, Z. M., Lawrence, D. M., Swenson, S. C., Torn, M. S., Meng, L., ... & Hess, P. (2011). Barriers to predicting changes in global terrestrial methane fluxes: analyses using CLM4Me, a methane biogeochemistry model integrated in CESM. Biogeosciences, 8(7), 1925-1953.

Ringeval, B. et al. (2014). Methane emissions from floodplains in the Amazon Basin: Challenges in developing a process-based model for global applications. Biogeosciences 11, 1519–1558

Ringeval, B., Friedlingstein, P., Koven, C., Ciais, P., de Noblet-Ducoudré, N., Decharme, B., & Cadule, P. (2010). Climate-CH 4 feedback from wetlands and its interaction with the climate-CO 2 feedback. Biogeosciences, 8(8), 2137-2157.

Rinne, J., Riutta, T., Pihlatie, M., Aurela, M., Haapanala, S., Tuovinen, J. P., ... & Vesala, T. (2007). Annual cycle of methane emission from a boreal fen measured by the eddy covariance technique. Tellus B: Chemical and Physical Meteorology, 59(3), 449-457.

Rull, V. & Montoya, E. (2014). Mauritia flexuosa palm swamp communities: Natural or human-made? A palynological study of the Gran Sabana region (northern South America) within a neotropical context. Quat. Sci. Rev. 99, 17–33

Saarnio, S., Alm, J., Silvola, J., Lohila, A., Nykänen, H., & Martikainen, P. J. (1997). Seasonal variation in CH 4 emissions and production and oxidation potentials at microsites on an oligotrophic pine fen. Oecologia, 110(3), 414-422.

SALESKA, S. R., DA ROCHA, H. R., HUETE, A. R., NOBRE, A. D., ARTAXO, P. E., & SHIMABUKURO, Y. E. (2013). LBA-ECO CD-32 Flux Tower Network Data Compilation, Brazilian Amazon: 1999-2006, ORNL Distributed Active Archive Center, doi:10.3334/ORNLDAAC/1174

Sanderson, M. G., Collins, W. J., Derwent, R. G., & Johnson, C. E. (2003). Simulation of global hydrogen levels using a Lagrangian three-dimensional model, Journal of Atmospheric Chemistry, 46(1), 15–28, doi:10.1023/A:1024824223232

Sanhueza, E., Dong, Y., Scharffe, D., Lobert, J. M., & Crutzen, P. J. (1998). Carbon monoxide uptake by temperate forest soils: The effects of leaves and humus layers, Tellus, Series B: Chemical and Physical Meteorology, 50(1), 51–58, doi:10.1034/j.1600-0889.1998.00004.x

Saunois, M., Bousquet, P., Poulter, B., Peregon, A., Ciais, P., Canadell, J. G., ... & Janssens-Maenhout, G. (2016). The global methane budget 2000–2012. Earth System Science Data, 8(2), 697-751.

Saunois, M., Stavert, A. R., Poulter, B., Bousquet, P., Canadell, J. G., Jackson, R. B., ... & Dlugokencky, E. J. (2019). The global methane budget 2000–2017. Earth System Science Data.

Savage, K. E., & Davidson, E. A. (2001). Interannual variation of soil respiration in two New England forests. Global Biogeochemical Cycles, 15(2), 337-350.

Schade, G. W., & Crutzen, P. J. (1999). CO emissions from degrading plant matter (II). Estimate of a global source strength, Tellus, Series B: Chemical and Physical Meteorology, 51(5), 909–918, doi:10.1034/j.1600-0889.1999.t01-4-00004.x

Schaefer, H., Fletcher, S. E. M., Veidt, C., Lassey, K. R., Brailsford, G. W., Bromley, T. M., ... & Lowe, D. C. (2016). A 21st-century shift from fossil-fuel to biogenic methane emissions indicated by $^{13}CH_4$. Science, 352(6281), 80-84.

Scharffe, D., Hao, W. M., Donoso, L., Crutzen, P. J., & Sanhueza, E. (1990). Soil fluxes and atmospheric concentration of CO and CH_4 in the northern part of the Guayana shield, Venezuela, Journal of Geophysical Research-Atmospheres, 95(90), 22475–22480, doi:10.1029/JD095iD13p22475

Schroeder, R., McDonald, K., Chapman, B., Jensen, K., Podest, E., Tessler, Z., ... & Zimmermann, R. (2015). Development and evaluation of a multi-year fractional surface water data set derived from active/passive microwave remote sensing data. Remote Sensing, 7(12), 16688-16732.

Schuur, T. (2018). AmeriFlux US-EML Eight Mile Lake Permafrost thaw gradient, Healy Alaska. [Data set]. https://doi.org/10.17190/AMF/1418678

Seiler, W. (1987). In: Krumbein, W.E. (Ed.), Environmental Biogeochemistry and Geomicrobiology, Methods, Metals and Assessment, vol. 3, Ann Arbor Science, Ann Arbor, MI, pp. 773-810

Seinfeld, J. H., & Pandis, S. N. (1998). Atmospheric Chemistry and Physics: From Air Pollution to Climate Change, Atmospheric Chemistry and Physics from Air Pollution to Climate Change Publisher New York NY Wiley 1998 Physical Description Xxvii 1326 p A WileyInterscience Publication ISBN 0471178152, 51, 1–4, doi:10.1080/00139157.1999.10544295

Sellers, P. J., Hall, F. G., Kelly, R. D., Black, A., Baldocchi, D., Berry, J., ... & Margolis, H. (1997). BOREAS in 1997: Experiment overview, scientific results, and future directions. Journal of Geophysical Research: Atmospheres, 102(D24), 28731-28769.

Shannon, R. D. & White, J. R. (1994). A Three-Year Study of Controls on Methane Emissions from Two Michigan Peatlands A three-year study of controls on methane emissions from two Michigan peatlands Introduction Estimates of methane emissions from northern. Biogeochemistry 27, 35–60

Shurpali, N. J., & Verma, S. B. (1998). Micrometeorological measurements of methane flux in a Minnesota peatland during two growing seasons. Biogeochemistry, 40(1), 1-15.

Shurpali, N. J., Verma, S. B., Clement, R. J., & Billesbach, D. P. (1993). Seasonal distribution of methane flux in a Minnesota peatland measured by eddy correlation. Journal of Geophysical Research: Atmospheres, 98(D11), 20649-20655.

Sjögersten, S. et al. (2014). Tropical wetlands: A missing link in the global carbon cycle? Global Biogeochem. Cycles 28, 1371–1386

Song, C., Xu, X., Tian, H., & Wang, Y. (2009). Ecosystem–atmosphere exchange of CH_4 and N_2O and ecosystem respiration in wetlands in the Sanjiang Plain, Northeastern China. Global Change Biology, 15(3), 692-705.

Sonnentag, O., & Quinton, W. L. (2016). AmeriFlux CA-SCB Scotty Creek Bog [Data set]. https://doi.org/10.17190/AMF/1498754

Spahni, R., Wania, R., van Velthoven, P., Neef, L., van Wheele, M., Pison, I., ... & Prentice, I. C. (2011). Constraining global methane emissions and uptake by ecosystems.

Specht, D. F. (1991), A general regression neural network, IEEE Trans. Neural Networks, 2(6), 568–576.

Stein, O., Schultz, M. G., Bouarar, I., Clark, H., Huijnen, V., Gaudel, A., … Clerbaux, C. (2014). On the wintertime low bias of Northern Hemisphere carbon monoxide found in global model simulations, Atmospheric Chemistry and Physics, 14(17), 9295–9316, doi:10.5194/acp-14-9295-2014

Stevenson, D. S., Dentener, F. J., Schultz, M. G., Ellingsen, K., van Noije, T. P. C., Wild, O., … Szopa, S. (2006). Multimodel ensemble simulations of present-day and near-future tropospheric ozone, Journal of Geophysical Research Atmospheres, 111(8), doi:10.1029/2005JD006338

Suzuki, R. (2016). AmeriFlux US-Prr Poker Flat Research Range Black Spruce Forest [Data set], AmeriFlux; Japan Agency for Marine-Earth Science and Technology, doi:10.17190/AMF/1246153

Svensson, B. H., Christensen, T. R., Johansson, E., & Öquist, M. (1999). Interdecadal changes in CO 2 and CH 4 fluxes of a subarctic mire: Stordalen revisited after 20 years. Oikos, 22-30.

Tan, Z., & Zhuang, Q. (2012). An analysis of atmospheric CH_4 concentrations from 1984 to 2008 with a single box atmospheric chemistry model, Atmospheric Chemistry and Physics Discussions, Copernicus GmbH, doi:10.5194/acpd-12-30259-2012

Tang, J., Zhuang, Q., Shannon, R. D., & White, J. R. (2010). Quantifying wetland methane emissions with process-based models of different complexities. Biogeosciences, 7(11), 3817-3837.

Tarr, M. a., Miller, W. L., & Zepp, R. G. (1995). Direct carbon monoxide photoproduction from plant matter, Journal of Geophysical Research, 100, 11403, doi:10.1029/94JD03324

Taylor, J. A., Zimmerman, P. R., & Erickson, D. J. (1996). A 3-D modelling study of the sources and sinks of atmospheric carbon monoxide, Ecological Modelling, 88(1–3), 53–71, doi:10.1016/0304-3800(95)00069-0

Tian, H., Chen, G., Lu, C., Xu, X., Ren, W., Zhang, B., ... & Zhang, C. (2015). Global methane and nitrous oxide emissions from terrestrial ecosystems due to multiple environmental changes. Ecosystem Health and Sustainability, 1(1), 1-20.

Tian, H., Xu, X., Liu, M., Ren, W., Zhang, C., Chen, G., & Lu, C. (2010). Spatial and temporal patterns of CH 4 and N 2 O fluxes in terrestrial ecosystems of North America during 1979–2008: application of a global biogeochemistry model. Biogeosciences, 7(9), 2673-2694.

Torn, M. (2018). AmeriFlux US-NGB NGEE Barrow [Data set]. https://doi.org/10.17190/AMF/1436326

Toutin, T. (2002). Three-dimensional topographic mapping with ASTER stereo data in rugged topography. IEEE Transactions on geoscience and remote sensing, 40(10), 2241-2247.

van Asperen, H., Warneke, T., Sabbatini, S., Nicolini, G., Papale, D., & Notholt, J. (2015). The role of photo- and thermal degradation for CO₂ and CO fluxes in an arid ecosystem, Biogeosciences, 12(13), 4161–4174, doi:10.5194/bg-12-4161-2015

Van Huissteden, J., van den Bos, R., & Alvarez, I. M. (2006). Modelling the effect of water-table management on CO 2 and CH 4 fluxes from peat soils. Netherlands Journal of Geosciences, 85(1), 3-18.

Varella, R. F., Bustamante, M. M. C., Pinto, A. S., Kisselle, K. W., Santos, R. V., Burke, R. A., … Viana, L. T. (2004). Soil fluxes of CO2, CO, NO, and N2O from an old pasture and from native Savanna in Brazil, Ecological Applications, 14(4 SUPPL.), doi:10.1890/01-6014

Vargas, R. (2016). AmeriFlux US-StJ St Jones Reserve [Data set]. https://doi.org/10.17190/AMF/1480316

Vreman, H. J., Wong, R. J., & Stevenson, D. K. (2011). Quantitating carbon monoxide production from heme by vascular plant preparations in vitro, Plant Physiology and Biochemistry, 49(1), 61–68, doi:10.1016/j.plaphy.2010.09.021

Wagner, D., A. Lipski, A. Embacher, and A. Gattinger (2005), Methane fluxes in permafrost habitats of the Lena Delta: Effects of microbial com- munity structure and organic matter quality, Environ. Microbiol., 7(10), 1582–1592.

Walter, B. P., & Heimann, M. (2000). A process-based, climate-sensitive model to derive methane emissions from natural wetlands: Application to five wetland sites, sensitivity to model parameters, and climate. Global Biogeochemical Cycles, 14(3), 745-765.

Walter, B. P., Heimann, M., & Matthews, E. (2001a). Modeling modern methane emissions from natural wetlands: 1. Model description and results. Journal of Geophysical Research: Atmospheres, 106(D24), 34189-34206.

Walter, B. P., Heimann, M., & Matthews, E. (2001b). Modeling modern methane emissions from natural wetlands: 2. Interannual variations 1982–1993. Journal of Geophysical Research: Atmospheres, 106(D24), 34207-34219.

Wang, D. X., Lu, X. G., Ding, W. X., Cai, Z. C., & Wang, Y. Y. (2002). Comparison of methane emission from marsh and paddy field in Sanjiang Plain. Scientia Geographica Sinica, 22(4), 500-503.

Wania, R., Ross, I., & Prentice, I. C. (2010). Implementation and evaluation of a new methane model within a dynamic global vegetation model: LPJ-WHyMe v1. 3.1. Geoscientific Model Development, 3(2), 565-584.

Wesely, M. L. (1989). Parameterization of surface resistances to gaseous dry deposition in regional-scale numerical models. Atmospheric Environment (1967), Elsevier BV, doi:10.1016/0004-6981(89)90153-4

Wesely, M., & Hicks, B. (2000). A review of the current status of knowledge on dry deposition. Atmospheric Environment, 34, 2261–2282, doi:10.1016/S1352-2310(99)00467-7

Whalen, S. C., & Reeburgh, W. S. (2001). Carbon monoxide consumption in upland boreal forest soils, Soil Biology and Biochemistry, 33(10), 1329–1338, doi:10.1016/S0038-0717(01)00038-4

Wickland, K. P., Striegl, R. G., Mast, M. A., and Clow, D. W. (2001). Interannual variation of soil respiration in two New England forests, Global Biogeochemistry Cycle., 15, 321–335, doi:10.1029/2000gb001325.

Woodward, F. I., & Lomas, M. R. (2004). Vegetation dynamics–simulating responses to climatic change. Biological reviews, 79(3), 643-670.

Xu, X., Riley, W. J., Koven, C. D., Billesbach, D. P., Chang, R. Y. W., Commane, R., ... & McDonald, K. C. (2016). A multi-scale comparison of modeled and observed seasonal methane emissions in northern wetlands. Biogeosciences (Online), 13(17).

Yang, J. S., Liu, J. S., Wang, J. D., Yu, J. B., Sun, Z. G., & Li, X. H. (2006). Emissions of CH_4 and N2O from a wetland in the Sanjiang Plain. Journal of Plant Ecology, 30(3), 432-440.

Yonemura, S., Kawashima, S., & Tsuruta, H. (2000). Carbon monoxide, hydrogen, and methane uptake by soils in a temperate arable field and a forest, Journal of Geophysical Research, 105(Dll), 14347, https://doi.org/10.1029/1999JD901156

Yoon, J., & Pozzer, A. (2014). Model-simulated trend of surface carbon monoxide for the 2001-2010 decade, Atmospheric Chemistry and Physics, 14(19), 10465–10482, doi:10.5194/acp-14-10465-2014

Zepp, R. G., Miller, W. L., Tarr, M. A., Burke, R. A., & Stocks, B. J. (1997). Soil-atmosphere fluxes of carbon monoxide during early stages of postfire succession in upland Canadian boreal forests, Journal of Geophysical Research-Atmospheres, 102(D24), 29301–29311, doi:10.1029/97jd01326

Zhang, Y., Li, C., Trettin, C. C., Li, H., & Sun, G. (2002). An integrated model of soil, hydrology, and vegetation for carbon dynamics in wetland ecosystems. Global Biogeochemical Cycles, 16(4), 9-1.

Zhang, Z., Zimmermann, N. E., Calle, L., Hurtt, G., Chatterjee, A., & Poulter, B. (2018). Enhanced response of global wetland methane emissions to the 2015–2016 El Niño-Southern Oscillation event. Environmental Research Letters, 13(7), 074009.

Zhang, Z., Zimmermann, N. E., Stenke, A., Li, X., Hodson, E. L., Zhu, G., ... & Poulter, B. (2017). Emerging role of wetland methane emissions in driving 21st century climate change. Proceedings of the National Academy of Sciences, 114(36), 9647-9652.

Zhu, Q., Liu, J., Peng, C., Chen, H., Fang, X., Jiang, H., ... & Zhou, X. (2014). Modelling methane emissions from natural wetlands by development and application of the TRIPLEX-GHG model. Geoscientific Model Development, 7(3), 981-999.

Zhu, Q., Peng, C., Chen, H., Fang, X., Liu, J., Jiang, H., ... & Yang, G. (2015). Estimating global natural wetland methane emissions using process modelling: spatio-temporal patterns and contributions to atmospheric methane fluctuations. Global ecology and biogeography, 24(8), 959-972.

Zhu, Q., Peng, C., Ciais, P., Jiang, H., Liu, J., Bousquet, P., ... & Chen, H. (2017). Interannual variation in methane emissions from tropical wetlands triggered by repeated El Niño Southern Oscillation. Global change biology, 23(11), 4706-4716.

Zhu, X., Q. Zhuang, M. Chen, A. Sirin, J. Melillo, D. Kicklighter, A. Sokolov, and L. Song (2011), Rising methane emissions in response to climate change in Northern Eurasia during the 21st century, Environ. Res. Lett., 6, 045211, doi:10.1088/1748-9326/6/4/045211

Zhu, X., Zhuang, Q., Qin, Z., Glagolev, M., & Song, L. (2013). Estimating wetland methane emissions from the northern high latitudes from 1990 to 2009 using artificial neural networks. Global Biogeochemical Cycles, 27(2), 592-604.

Zhuang, Q. and Crill, P. (2008): NCEAS 10645: Toward an adequate quantification of CH_4 emissions from land ecosystems: Integrating field and in-situ observations, satellite data, and modeling. Sallies Fen NH CH_4 Flux 1994–2001, National Center for Ecologi- cal Analysis and Synthesis and Stockholm University.

Zhuang, Q., Chen, M., Xu, K., Tang, J., Saikawa, E., Lu, Y., ... & McGuire, A. D. (2013). Response of global soil consumption of atmospheric methane to changes in atmospheric climate and nitrogen deposition. Global Biogeochemical Cycles, 27(3), 650-663.

Zhuang, Q., McGuire, A. D., Melillo, J. M., Clein, J. S., Dargaville, R. J., Kicklighter, D. W., … Hobbie, J. E. (2003). Carbon cycling in extratropical terrestrial ecosystems of the Northern Hemisphere during the 20th century: A modeling analysis of the influences of soil thermal dynamics, Tellus, Series B: Chemical and Physical Meteorology, 55(3), 751–776, doi:10.1034/j.1600-0889.2003.00060.x

Zhuang, Q., Melillo, J. M., Kicklighter, D. W., Prinn, R. G., McGuire, A. D., Steudler, P. A., … Hu, S. (2004). Methane fluxes between terrestrial ecosystems and the atmosphere at northern high latitudes during the past century: A retrospective analysis with a process-based biogeochemistry model, Global Biogeochemical Cycles, 18(3), doi:10.1029/2004GB002239

Zhuang, Q., Melillo, J. M., McGuire, A. D., Kicklighter, D. W., Prinn, R. G., Steudler, P. A., ... & Hu, S. (2007). Net emissions of CH_4 and CO_2 in Alaska: Implications for the region's greenhouse gas budget. Ecological Applications, 17(1), 203-212.

Zhuang, Q., Romanovsky, V. E., & McGuire, a. D. (2001). Incorporation of a permafrost model into a large-scale ecosystem model: Evaluation of temporal and spatial scaling issues in simulating soil thermal dynamics, Journal of Geophysical Research, 106, 33649, doi:10.1029/2001JD900151

Zhuang, Q., Y. Lu, andM. Chen (2012), An inventory ofglobal N2O emissions from the soils ofnatural terrestrial ecosystems, Atmos. Environ., 47,66–75

VITA

Licheng Liu

Department of Earth, Atmospheric and Planetary Sciences
Purdue University
550 Stadium Mall Dr

Education

- Purdue University, West Lafayette, IN USA 08/2014 – 05/2020
  -Ph.D. in earth and atmospheric sciences
- Peking University, Beijing, China 09/2009 - 07/2013
  -B.Sc. in atmospheric sciences

Employment

- Purdue University, West Lafayette, US 08/2014 - 01/2018, 06/2018 – 05/2020
  -Research Assistant in Prof. Qianlai Zhuang's group, Dept. of Earth, Atmospheric, and Planetary Sciences
- Purdue University, West Lafayette, US 02/2018 - 05/2018
  -Teaching Assistant in class Earth Science, EAPS 10000, Dept. of Earth, Atmospheric, and Planetary Sciences
- Peking University, Beijing, China 07/2013 - 08/2014
  -Research Assistant in Prof. Lin Zhang's group, Dept. of Atmospheric and Oceanic Sciences

Publications

Liu, L., Li C., Zhuang Q., Yao Y., Qu Y., Liu L., Shurpali N. (2020), Inventorying Global Wetland Methane Emissions Using In Situ Data and an Artificial Neural Network Approach. Biogeosciences, under review.

Liu, L., Zhuang, Q., Oh Y., Shurpali, N. J., Kim S., Poulter B. (2019). Uncertainty Quantification of Global Net Methane Emissions from Terrestrial Ecosystems Using a Mechanistically-based Biogeochemistry Model. Journal of Geophysical Research – Biogeoscience, under review.

Liu, L., Zhuang, Q., Zhu, Q., Liu, S., van Asperen, H., & Pihlatie, M. (2018). Global soil consumption of atmospheric carbon monoxide: an analysis using a process-based biogeochemistry model. Atmospheric Chemistry and Physics, 18(11), 7913.

Oh, Y., Zhuang, Q., **Liu, L**., Lisa, R. W., Maggie, C.Y. L., Tullis, C. O., … & Bo E. (2020) Microbial methane oxidation projects reduced net methane emissions in a warmer Arctic. Nature Climate Change. https://doi.org/10.1038/s41558-020-0734-z

Saunois, M., Stavert, AR., Poulter, B., Bousquet P., … & **Liu, L.**, … & Zhuang, Q. (2019) The Global Methane Budget 2000-2017. Earth System Science Data discussion

Liu, L., Zhang, L. (2014). The parameterization of N2O5 Hydrolysis and the impact of NOx content in the atmosphere. (final dissertation in Peking University)

Yun, H., Wu, Q., Zhuang, Q., Chen, A., Yu, T., Lyu, Z., ... & **Liu, L.** (2018). Consumption of atmospheric methane by the Qinghai–Tibet Plateau alpine steppe ecosystem. The Cryosphere, 12(9), 2803-2819.

Zhang, L., **Liu, L.**, Zhao, Y., Gong, S., Zhang, X., Henze, D. K., ... & Wang, Y. (2015). Source attribution of particulate matter pollution over North China with the adjoint method. Environmental Research Letters, 10(8), 084011.

Conference Presentations

Liu, L., Zhuang, Q., Oh, Y., Kim, S., & Poulter, B. (2018, December). Uncertainty Quantification of Global Net Methane Emissions from Land Ecosystems Using Mechanistically-Based Biogeochemistry Models. In American Geophysical Union (AGU) Fall Meeting, Washington, D.C., US

Research Experience

- Using VIC-TOPMODEL approach to further constrain the global methane estimates in the past and future 09/2019-present

-Advisor: Prof. Qianlai Zhuang, Dept. of Earth, Atmospheric and Planetary Sciences, Purdue University, US

- Using multiple in situ data and neural network approach to investigate the special and temporal distribution of wetland methane emission in global scale 01/2019-12-2019
  -Advisor: Prof. Qianlai Zhuang, Dept. of Earth, Atmospheric and Planetary Sciences, Purdue University, US
- Extended the Methane Dynamics Model (MDM) from Arctic region to global scale by considering multiple ecosystem types, estimated the global methane fluxes from soil in recent two decades and analyzed the model uncertainties 08/2017-09/2019
  -Advisor: Prof. Qianlai Zhuang, Dept. of Earth, Atmospheric and Planetary Sciences, Purdue University, US
- Developed a 2D diffusion model for methane emission from palm tree stem and estimated the total methane emission from palm swamp in Amazon region 02/2016-08/2017
  -Advisor: Prof. Qianlai Zhuang, Dept. of Earth, Atmospheric and Planetary Sciences, Purdue University, US
- Developed and used a biogeochemistry model (TEM) to simulate net soil CO fluxes in global scale 08/2014-01/2016
  -Advisor: Prof. Qianlai Zhuang, Dept. of Earth, Atmospheric and Planetary Sciences, Purdue University, US
- Simulated PM2.5 sensitivities of Beijing using Geos-Chem-Adjoint Model 06/2013-08/2014
  -Advisor: Prof. Lin Zhang, Dept. of Atmospheric & Oceanic Sciences, Peking University, China
- Investigated the impact of N2O5 Hydrolysis on global NOx concentration 02/2013-06/2013
  -Advisor: Prof. Lin Zhang, Dept. of Atmospheric & Oceanic Sciences, Peking University, China
- Updated the parameterization of N2O5 Hydrolysis in Geos-Chem 09/2012-01/2013
  -Advisor: Prof. Lin Zhang, Dept. of Atmospheric & Oceanic Sciences, Peking University, China

- Explored oxalic acid formation mechanism in ambient aerosols 07/2011-09/2012
  -Advisor: Prof. Tzung-May Fu, Dept. of Atmospheric & Oceanic Sciences, Peking University, China

Awards

First Prize of China National Mathematic Olympiad 01/2009

Skills

- Solid skill of using IDL, Fortran, MATLAB, C, C++, R, Python.
- Atmospheric and biogeochemistry model simulation and development
- Statistical analysis